Scuola Internazionale Superiore Studi Avanzati (SISSA)

Department of Neuroscience

Characterization of the conformational space of the murine prion protein using single-molecule force spectroscopy techniques

Candidate: Andrea Raspadori

Supervisors:

Prof. Giuseppe Legname, D.Phil.
Prof. Bruno Samorì

A thesis submitted for the degree of
Doctor of Philosophy
in Functional and Structural Genomics
October 2014

Declaration

The work described in this thesis has been carried out at Scuola Internazionale Superiore di Studi Avanzati (SISSA), Trieste, Italy from November 2010 to October 2014, in collaboration with the laboratory of Nanobioscience at the University of Bologna, Bologna, Italy.

The work has been funded by the Human Fronteer Science Program (HFSP).

During my Ph.D course I have contributed to one publication. The results described in this thesis will be published in the near future.

List of publications

Biljan*, I., Ilc*, G., Giachin*, G., **Raspadori, A.**, Zhukov, I., Plavec, J., and Legname, G. (2011) Toward the molecular basis of inherited prion diseases: NMR structure of the human prion protein with V210I mutation, *J Mol Biol 412*, 660-673.

Index

Part III: Results and discussion

List of abbreviations

3D = three-dimensional
aa = aminoacid
AFM = atomic force microscope
ANS = 8-anilinonaphthalene-1-sulfonate
Aβ = amyloid beta precursor
BSE = bovine spongiform encephalopaties
CC1 = charged aminoacid cluster 1 (residues 23-27 mouse numeration)
CC2 = charged cluster 2 (residues 94-109 mouse numeration)
CD = circular dichroism
CJD = Creutzfeldt-Jakob disease
CNS = central nervous system
cryoEM = cryo electron microscopy
DFS = dynamic force spectroscopy
DRM = detergent resistant domains
EPR = electron paramagnetic resonance
ER = endoplasmatic reticulum
FEC = force-extension curve
FJC = freely jointed chain
FS = force spectroscopy
FTIR = Fourier-transform infrared spectra
GB1 = Streptococcal protein G domain B1
GndHCl = guanidinium hydrochloride
GPI = glycophosphatidilinositol
H-bonds = hydrogen bonds
HD = hydrophobic domain (residues 111 to 128 mouse numeration)
Hu = human
HX-MS = hydrogen-deuterium exchange mass spectrometry
I27 = 27th immunoglobulin binding domain of the band I of titin
IDP = intrinsically disordered protein
IQR = interquartile range (from the 1st to the 3rd quartile)
MD = molecular dynamic
Mo = mouse
NMR = nuclear magnetic resonance
nN = nanonewton
^{Ctm}PrP = C-terminal transmembrane PrP form
^{Ntm}PrP = N-terminal transmembrane PrP form
OR = octpeptide repeat region (from residues 50 to 89 mouse numeration)
ORF = open reading frame
OT = optical tweezers
PK = proteinase K
pN = pico newton
Prnp or PRNP = prion protein gene
PrP = prion protein
PrP* = partially destabilized folding intermediate of PrP^{C}
PrP^{C} = cellular prion protein
PrP^{Sc} = misfolded, infective form of PrP^{C}, denoted also as “prion”
SAXS = small angle X-ray scattering

SDSL = site-directed spin labeling
Sha = syrian hamster
SM = single-molecule
SMFS = single-molecule force spectroscopy
ssNMR = solid-state NMR
TEM = transmission electron microscopy
ThT = thioflavin T
TSEs = transmissible spongiform encephalopathies
WLC = worm-like chain
WT = wild type, reffered to protein primary structure
ZAM = sipping-and-assembly model of protein folding
α-Syn = α-synuclein
Δ_{cl} = delta contour length

Abstract

The conversion of the cellular prion protein (PrP^{C}) to its infectious counterpart (PrP^{Sc}) is the initial step of prion diseases. These neurodegenerative disorders are characterized by different incubation times, sympthoms and disease phenotypes. Structural heterogenity of PrP aggregates is responsible for this biological diversity. Understanding the structural rearrangements of PrP at the monomeric and oligomeric level is essential to gain insights into its aggregation processes. However traditional "in-bulk" techniques can only provide ensemble-averaged information for monomer and oligomer structures. We applied single-molecule force spectroscopy to characterize the heterogeneous structural ensemble of the murine PrP at the monomeric and at the oligomeric level. By stretching chimeric protein construct carrying one MoPrP molecule we found that the protein folds with a two state mechanism. Less frequently the protein can adopt more extended conformations that encompass also the N-terminal domain. These structures might be involved in subsequent aggregation processes. We also developed an assay to characterize the oligomerization processes using multiple PrP constructs. By analyzing the extension of these constructs under tension we characterized the structure between different PrP moieties, under different conditions. We found that reciprocal PrP orientation affects the length and mechanical resistance of these structures but their events frequency. Comparing the structures observed from monomers, dimers, trimers and tetramers we found that their frequency of events and their average length increased by increasing the number of PrP moieties. Remarkably, decreasing pH to more acidic values resulted in a higher frequency of events that involved structures between PrP moieties only in multimeric constructs. Instead, increasing the ionic strength significantly diminished their frequency, indicating how solution conditions can strongly alter the conformational transitions. These results provide a new scenario on PrP misfolding and aggregation processes, characterizing their early aggregation steps under different reaction conditions.

Part I: Introduction

1.1 Protein folding and misfolding

During and immediately following its translation on the ribosome, nascent protein meets the first major hurdle of its life: to fold into the conformation it requires in order to fulfill its *raison d'être*. This is not a trivial task because the number of theoretical interactions between each of its amino acid side chains far exceeds the total number of protein molecules within the cell and establishing the correct interactions is vital for proper folding. Moreover the crowded environment of the cell, in which the intracellular concentration of proteins can be as high as 350 mg/mL [1], increases the chances of making non-specific contacts with other proteins. Nevertheless the driving force that pushes the protein to attain its lowest free energy state ensures that most proteins fold spontaneously and rapidly (in the order of micro- to milliseconds depending on the protein size and complexity). Thus folding occurs correctly most of the time [2,3,4]. Interestingly, many proteins never attain a defined conformation, but remain intrinsically disordered even in their biologically active state, without well-defined secondary and tertiary structures in their native state [5,6]. For other proteins, folding does not occur unassisted and instead the folding process is guided by a number of auxiliary proteins, denoted as chaperones. Although occurring quickly, the folding pathway of a protein typically does not occur in one step but instead proceeds through a number of intermediately folded states (each with lower energy than the unfolded protein). This process is well described by the *zipping and assembly* model (ZAM), were on fast timescales a few key initial contacts are established that are crucial in directing the correct protein structure (reviewed in [7]). Hydrogen bonding and hydrophobic interactions enable the protein to attain its fully folded form. Despite cellular machineries checkpoints in place to ensure proper folding of proteins, undesired interactions during folding might shift the protein folding into an "off-folding" pathway (**figure 1.1**).

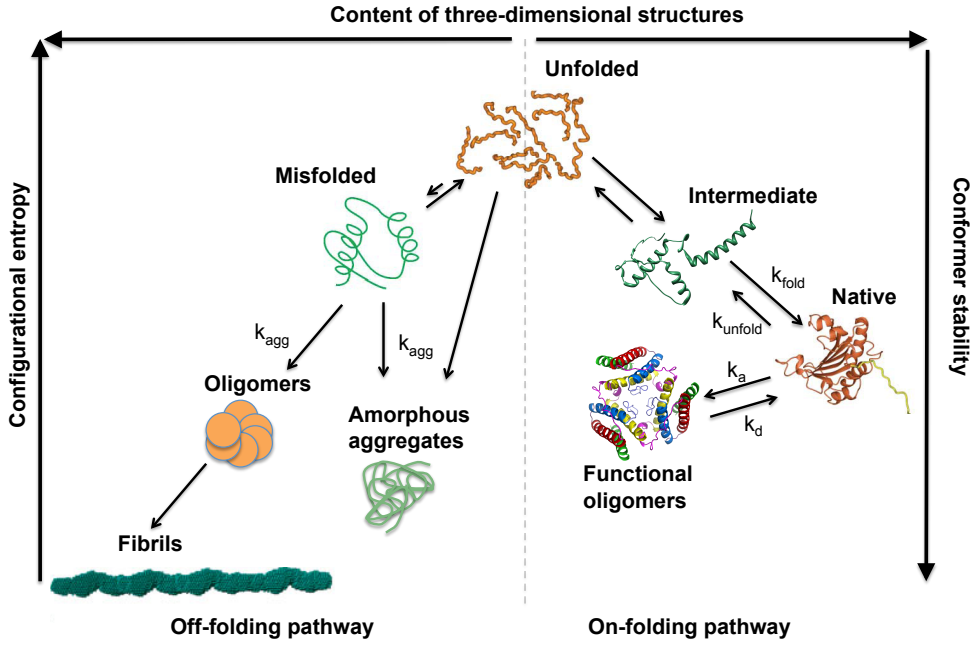

Figure 1.1 Protein on- and off-folding pathway scheme. The scheme is general and may vary depending on the protein primary sequence and environmental conditions. Adapted from [12].

1.1.1 Protein misfolding: a common mechanism for amyloidogenic diseases

Since the discovery that several amyloidogenic disorders are related to protein misfolding and aggregation, increasing interest and efforts have been employed to understand these common mechanism in the last 20 years. There are now approximately 50 disorders, with a multitude of disparate symptoms, which are associated with the misfolding of normally soluble, functional peptides and proteins (**table 1.1**). Protein conversion to insoluble aggregates is related to loss of functions with the generation of often toxic, gain-of-function intermediates in the process of self-assembly [8,9].

Interestingly, almost half of the proteins involved in these diseases do not possess globular structures (unless in presence of specific interactors), classifying them as "intrinsically disordered protein" (IDP). Others present partially unstructured fold, with a structured domain and an intrinsically disordered domain [10,11].

Disease	Related protein/peptide	Polypeptide length (number of residues)	Protein/peptide structure
Neurodegenerative diseases			
Alzheimer's disease	Amyloid-β-peptide	37-43	Intrinsically disordered
Transmissible spongiform encephalopathies	Prion protein	~230	Intrinsically disordered and α-helical
Parkinson's disease	α-synuclein	140	Intrinsically disordered
Amyotrophic lateral sclerosis	Superoxide dismutase 1	153	β-sheet, Ig-like
Huntington's disease	Hungtingtin fragments	variable	Intrinsically disordered
Familial amyloidotic polyneuropathy	Transthyretin (mutants)	127	β-sheet
Non-neuropathic systemic amyloidosis			
Amyloid light chain amyloidosis	Immunoglobulin (Ig) light chains or its fragments	~90	β -sheet and Ig like
Amyloid A amyloidosis	Serum amyloid A1 protein fragments	76–104	α -helical
Senile systemic amyloidosis	Wild-type transthyretin	127	β -sheet
Haemodialysis-related amyloidosis	β2-microglobulin	99	β -sheet and Ig like
Lysozyme amyloidosis	Lysozyme mutants	130	α -helical and β-sheet
Non-neuropathic localized amyloidosis			
Apolipoprotein A1 amyloidosis	Apo A-1 fragments	80–93	Intrinsically disordered
Type II diabetes	Amylin	37	Intrinsically disordered
Injection-localized amyloidosis	Insulin	21 and 30	α-helical and insulin-like

Table 1.1 Diseases related to extracellular depositions or intracellular inclusions of amyloid-like aggregates. Adapted from [12].

These proteins may fold into structures different from the ones present in the on-folding pathway, a process common addressed as "misfolding". In this process, the individual molecules may form new interactions and are then kinetically trapped in local energy minima.

The polypeptide chain in case of misfolding fails to attain its closely packed three-dimensional structure, by loss of native residue contacts [13] and as a result of that partially folded states start to populate.
These states can be associated to so-called *molten-globule* or *pre-molten globule* intermediate states, depending on the percentage of secondary structures and tertiary contacts that are still present, with respect to the native state [14]. The *molten-globule* state is characterized by an increase of 15% in the hydrodynamic radius compared with the native state, which corresponds to a volume increase of ~ 50% [14]. Small angle X-ray scattering (SAXS) is a technique used to measure the shape and size of macromolecules as result of their X-ray scattering. Studies using this technique have revealed that protein molecules in the *molten-globule* state, have a globular structure typical of ordered globular proteins [15,16,17,18]. An increased affinity to hydrophobic fluorescence probes such as 8-anilinonaphthalene-1-sulfonate (ANS) is observed when proteins attain this structural ensemble. In the *pre-molten globule* state a protein is still able to interact with ANS, but it does not exhibit a globular structure [18,19]. The *pre-molten globule* state probably represents a partially ordered form of the random coil or unfolded state [19,20].

These partially unfolded conformations favor reciprocal and specific intermolecular interactions, including electrostatic attraction, hydrogen bonding and hydrophobic contacts, which are necessary for further oligomerization and fibrillation [21,22,23]. On the other hand, the primary step in the fibrillation of IDPs represents partial folding, like stabilization of a partially folded conformation [24,25], making them more prone to aggregation. Under such conditions intermolecular contacts with other misfolded proteins can occur [26,27]. Mutations, environmental conditions such as stress or ageing play major roles in modulating the conformational equilibra between these states, increasing the evidence on the complex folding dynamics and conformational heterogeneity of these proteins [28,29,30].

1.1.2 Aggregation and oligomerization

Once entered in a *off-folding* pathway, the misfolded protein can follow two different paths: unordered or high-ordered aggregation routes. Depending on environmental conditions and primary sequence of the protein, one route will be preferred to the other [31,32]. In both cases, due to the association of hydrophobic surfaces, the heat effects associated with protein aggregation are often exothermic, analogous to the release of heat upon protein folding [33,34]. While in some cases, thermally induced aggregation is reversible, more often aggregation is at least partially irreversible. For irreversible systems, models of unfolding such as the Lumry-Eyring model may be applicable, where a reversible unfolding/misfolding transition is followed by an irreversible aggregation step [35].

The formation of amorphous aggregates is characterized by individual monomers adding to the growing clump of aggregated protein through a random process. The accumulation of recombinant proteins inside bacterial inclusion bodies is a typical example of amorphous aggregates. Once purified from bacteria, inclusion bodies present sphere-like or rod-like shapes with diameters ranging from 0.2 μm to 1.2 μm [36,37]. Fourier-transform infrared spectroscopy (FTIR) has been extensively used to characterize macromolecules secondary structure contents by measuring their absorbance at different wavelengths. The technique is very useful since it can be applied also to unsoluble samples. Using this technique it has been shown that inclusion bodies present newly formed β-sheet structures with respect to the protein monomeric native state [38,39]. On the other hand, some proteins maintained some β-sheet and α-helical structures of their soluble form [40,41].

The second route is the formation of high ordered structures, such as soluble proto-fibrils or oligomers, depending if they are on-pathway to fibril formation [42,43] or off-

pathway, respectively [44,45]. Oligomers and protofibrils are composed of a variable number of monomers, usually indicated as *n*-mer, where *n* is the number of monomers. The size of the oligomers may vary from 2-mer to 4-mer, in case of β2-microglobulin [46], up to 8-20 mer like Aβ peptide and PrP [9,47]. These molecules in turn assemble into chains with straight, curved or circular shapes [47,48]. The structure of oligomers need not to share β-sheet structures that are found in amyloid fibrils, nevertheless oligomers may be precursors of amyloid fibrils and may present a large β-sheet content. Interestingly, antibodies raised against pre-fibrillar aggregates of Aβ peptides cross-react with similar aggregates of other peptides or proteins (such as amylin, α-synuclein, and the amyloidogenic prion fragment), but not with mature fibrils [49]. These observations suggest common structural features of oligomers, differing from those found in the mature fibrils. In fact, an oligomer with a spherical shape of 20 nm diameter has been found to be a common trait of many amyloidogenic proteins [50]. Unlike the formation of amorphous protein aggregates, high ordered oligomer formation occurs more slowly through a highly ordered, nucleation-dependent mechanism in which partially folded forms of the protein associate to form a stable nucleus (rate-determining step). This nucleus acts as a template to sequester other intermediates adding them to the growing thread of aggregated protein (protofibril). The sequential addition of free monomers to the ends of the chain leads to the formation of the highly structured, insoluble amyloid fibrils. Such a mechanism explains the observed kinetics of fibril formation as monitored using amyloidogenic dyes such as thioflavin T (ThT) or Congo red. Both the length of the lag phase (*i.e.* the time required to form a stable nucleus) and the rate of elongation are highly dependent on the concentration of partially folded intermediates present at any given time [51]. Recently, a general mathematical model for fibrillation kinetics has been proposed [52]. In this model, in addition to the classical nucleation step, where monomer concentration is critical, also fragmentation and monomer-dependent elongation processes are taken into account (**figure 1.2**).

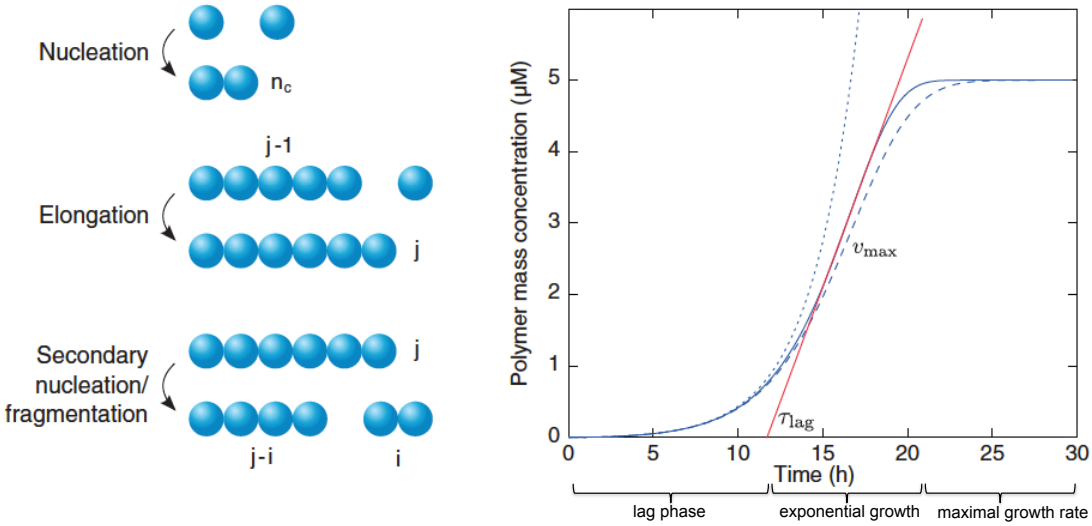

Figure 1.2 Mechanism of fibril formation (taken from [52]). On the left the three processes described for fibrillation: nucleation, monomer-dependent elongation and fragmentation. On the right a typical example of fibrillation curve, with three distinct phases. During the lag-phase, a stable nucleus is building-up to initiate the growth of fibrils. At this point exponential growth of fibers occurs until it reaches its maximal growth rate. Depending on the protein, the contribution of the three above-mentioned processes may vary, leading to different fibrillation curves.

1.1.3 Amyloid fibrils morphology and structure

Diseases related to the misfolding of proteins are often referred as proteopathies or proteinopathies. Perhaps the most distinctive hallmark of proteopathies is the accumulation of amyloid fibrils in specific tissues. Structural characterization of such molecules is very challenging because they are inherently noncrystal-forming, which precludes them to structural elucidation by X-ray crystallography. This technique can attain structural information of a crystallized protein sample at the atomic level from its X-ray diffraction pattern. In addition, because of the large size and particulate nature, they are not amenable to solution NMR spectroscopy. Historically, X-ray fiber diffraction has been the first technique used to characterize amyloid filaments [53]. The physical principle behind this technique is the same as X-ray crystallography but experiments are performed on fibrillar macromolecules instead. Studies using this technique showed that amyloid fibrils from different proteins presented similar diffraction cross-β pattern, which is indicative of β-strands component being oriented perpendicularly to the fibril axis [23,54,55,56,57,58]. As shown in **figure 1.3, A** the distinctive diffraction pattern shows a strong meridional intensity at about 4.75 Å resolution (corresponding to the inter-β strand spacing), and an equatorial reflection at about 10 Å resolution (corresponding to the distance between stacked β-sheets).

Transmission electron microscopy (TEM) and atomic force microscopy (AFM) have been used to obtain qualitative structural information on amyloid fibrils. The former technique requires staining of the sample with heavy metals, which will absorb and reflect the electrons from an electron beam. The latter is better described in **paragraph 1.3.1**. Using these two techniques, amyloid polymorphisms were characterized, in which different structural elements are propagated along the length of the fibril. Protofilaments assemble as fibrils by twisting in a helix fashion into rope-like structures 5-20 nm wide [59,60] or by jointing in ribbon-like structures that can be up to 30 nm wide [61,62]. Such morphological diversity is a common characteristic of amyloids, reflecting the protein structural heterogeneity.

Recently, a highly detailed perspective of several amyloid structures has begun to emerge, employing techniques such as site-directed spin labeling (SDSL), solid state NMR (ssNMR) and cryo-electron microscopy (cryoEM). SDSL requires the reaction of spin labels with amino acids of the proteins. Labels can give information on its local dynamics, conformational dynamics of protein domains, and global protein tumbling. In ssNMR methodology amyloid fibrils are obtained from protein samples labeled with carbon-13 and nitrogen-15 isotopes. Structural information of the labeled residues is obtained from their resonance frequency. Finally cryoEM share the same physical principles of TEM, but the sample is not stained and is studied at cryogenic temperatures. It is important to point out that these techniques require labeling of protein residues, requiring their heterologous expression. Thus is it possible that synthetic amyloid fibrils may not reflect the physiological ones [63].

Parallel in-register β-sheet structure is the most common underlying architecture observed for pathological amyloid (**figure 1.3, B**). These fibrils are composed of stacked polypeptide strands that lie perpendicular to the fibril axis and form backbone hydrogen bonds with the adjacent strands aligned in-register and parallel. SDSL studies on recombinant fibres of α-synuclein [64,65] and β2-microglobulin [66] revealed a parallel in-register β-sheet structure, which, for example, involved the whole 99 residue sequence of the latter protein. ssNMR studies, combined with EM mass-per-length measurements revealed that also recombinant Aβ fibrils present such structure [67,68,69], with the monomer shaped as a pair of β-strands, encompassing residues 12-24 and 30-40 respectively. This model has also been proposed for prion protein *in vitro* generated amyloids [70].

Several small peptides that form amyloid fibrils, including fragments of Aβ, arrange in antiparallel β-sheets, which is also the most common β-sheet arrangement in globular proteins (**figure 1.3, C**). Using ssNMR, $A\beta_{16-22}$, $A\beta_{11-25}$ and $A\beta_{32-42}$ fragments were shown to adopt antiparallel alignment of the peptides [71,72,73]. Regardless, no full-length protein up to now has shown such a fibrillar structure. The only exception is the $A\beta_{1-40}$ peptide, associated to early onset familiar Alzheimer's disease, which adopts an anti-parallel fold [74].

The strands in a β-helix (or solenoid) align to form parallel β-sheets, but the strands wrap around an axis in a helical arrangement, and unlike parallel in-register β-sheets, parallel strands in helices have intramolecular backbone hydrogen bonds (**figure 1.3, D**). NMR data from HET-s(218-289) prion protein of *Podospora anserina* revealed that each monomer makes two helical turns around the filament axis, and the strands form parallel β-sheets [75]. A similar structure has been proposed for PrP 27-30 fibrils (discussed in **paragraph 1.2.4**).

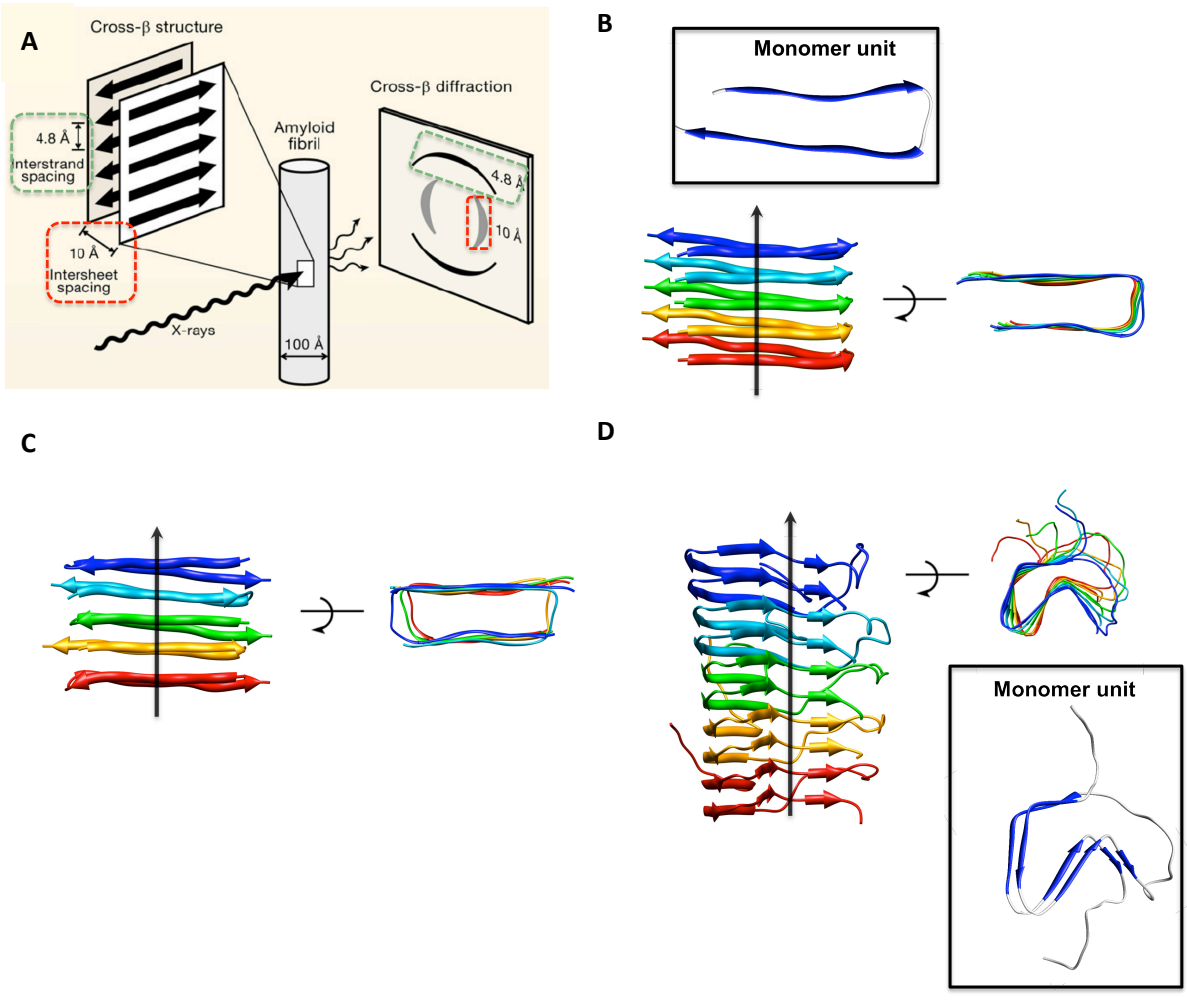

Figure 1.3 Amyloid fibers structures. (**A**) Schematic diagram of diffraction pattern from amyloid fibrils adapted from [8]. The green dashed box indicates the band relative to monomers interstrand spacing of ~ 5 Å, while the red dashed box indicates the equatorial band relative to intersheet spacing of ~ 10 Å. (**B**) NMR structure of parallel in-register β-sheet $A\beta_{1-42}$ amyloid fibril (PDB entry: 2BEG). In the black box the structure of single monomer. (**C**) Model of anti-parallel β-sheet fibril of Abeta1-40. The model is based on [74] using 2BEG PDB entry as reference structure. (**D**) NMR structure of β-solenoid HET-s 218-289 amyloid fibril (PDB entry: 2RNM); random coiled residues are not shown for clarity. Lateral and top views are shown for B, C and D.

1.2 Prion diseases as a model for neurodegenerative disorders

Prion diseases correspond to anatomo-pathologically defined transmissible spongiform encephalopathies (TSEs) of infectious, genetic, or sporadic etiology. They are characterized by neurodegeneration and protein aggregation. These diseases include kuru and Creutzfeldt-Jakob disease (CJD) in humans, scrapie in sheep and bovine spongiform encephalopathy (BSE) in cattle. In humans, these diseases can affect subjects at distinct age groups, course with a variety of motor or cognitive symptoms. Although their prevalence is relatively low, TSEs are still incurable and invariably fatal [76].
The pathogenesis of prion diseases is attributed to major changes in the metabolism of the cellular prion protein (PrP^{C}). Current understanding of TSEs evolved from the concept of prions, proteinaceous, nucleic acid-free, infectious particles [77]. A wide body of data now supports the idea that prions consist principally or entirely of an abnormal isoform of a host-encoded protein, the prion protein (PrP), designated PrP^{Sc}. PrP^{Sc} is derived from PrP^{C} by a post-translational mechanism [78,79]. Neither amino acid sequencing nor systematic study of known covalent post-translational modifications have shown any consistent differences between PrP^{C} and PrP^{Sc} [80]. PrP^{Sc} acts as a template that promotes the conversion of PrP^{C} to PrP^{Sc} and this conversion involves only conformational change. In fact, while PrP^{C} is α-helical with low β-sheet content (~3%), PrP^{Sc} is mainly β-sheet rich (~43%) [81]. Full understanding of prion propagation requires knowledge both of the structure of PrP^{C} and PrP^{Sc} and of the mechanism of conversion between them.

1.2.1 Biogenesis and function of PrP^{C}

PrP is a highly conserved among mammals, and it has been also identified in marsupials [82] and birds [83]. The protein is encoded by the *PRNP* (human) or *Prnp* (other animals) gene and its open reading frame (ORF) is encoded within a single exon, even if the gene itself contains either two (in hamster, humans, tamar wallaby) or three exons (in rat, mouse, bovine, sheep) [84,85,86,87,88,89]. *Prnp* is often considered as a housekeeping gene, based on the absence of a TATA box, the identification of several Sp1 binding sites and the presence of CpG islands [90,91,92]. It is expressed during early embryogenesis, increasing postnatally with distinct time courses for various regions of the hamster, rat, and mouse brains [93,94,95,96,97,98]. The highest levels of expression are observed in the central nervous system, in particular in association with synaptic membranes.
After protein synthesis, PrP^{C} is translocated to the endoplasmatic reticulum (ER) due to the presence of a 22 amino acid N-terminal signal peptide. Remarkably, PrP^{C} can be synthesized with at least three forms in the ER: a secreted form that reflects the main pathway for PrP^{C} synthesis *in vivo*, plus C- and N-terminal transmembrane forms (^{Ctm}PrP and ^{Ntm}PrP respectively). These latter two forms are characterized by transmembrane insertion of the hydrophobic pocket between amino acids 110–134 and their relative membrane orientation [99,100]. The role of these two forms is still not fully clarified, but they are related to neurotoxicity especially in inherited prion diseases [101].
In the ER cellular compartment the pre-pro-prion protein is post-translationally modified by glycosylation at residues Asn180 and Asn196, cleaving the N-terminal signal peptide and a GPI-anchor is covalently linked to its C-terminal [102,103]. Full-length PrP^{C} has been found in non-, mono- and di-glycosylated forms [104], with a different variety of N-glycans [105], which may be differently distributed in the CNS [106].
Regarding the sub-cellular environment organization, PrP^{C} molecules are found attached to lipid rafts: low-density, detergent-insoluble membrane domains (DRM), rich in cholesterol and sphingolipids [107]. Like other GPI-linked proteins PrP^{C} can be internalized, and it has

been shown that in neuronal cells this mechanism is mediated via clathrin-coated vesicles [108,109]. It has been proposed that the N-terminal, a positively charged domain of PrP^C (KKRPKP), is responsible for the constitutive endocytosis of PrP^C by clathrin-coated vesicles, perhaps by interacting with a transmembrane protein [110]. The internalization occurs with a $t_{1/2}$ of 5 minutes [108]. While in non-neuronal internalization occurs via non-clathrin-coated vesicles [111].
A small fraction of endocytosed PrP^C is degraded by lysosomes, but large fractions return to the cell surface. Previous studies originally intended to understand the intercellular transfer of PrP^{Sc} have led to evidence that part of the recycled PrP^C may be secreted to the extracellular medium associated with exosomes [112]. Thus, it is possible that such a mechanism could be one of the possible pathways to spread PrP^{Sc} in the extracellular environment, leading to cell death and neurodegeneration.

Defining PrP^C function is one of the major issues in prion biology. The first attempt to understand the possible function of the prion protein was done by generating a PrP-null mouse strain in a mixed C57BL/6J 129/Sv(ev) background, by replacement of codons 4–187 with a neomycin phosphotransferase (neo) expression cassette. These animals, designated $Prnp^{0/0}$ or Zurich I (ZrchI), showed no remarkable anatomical abnormalities. Also, cognitive tests revealed no defects in behavior or learning [113]. Remarkably, grafting *Prnp*-knockout mice with PrP^{Sc} material from PrP^C-expressing tissue, did not result in neuronal damage [114]. Also progressive accumulation of PrP^{Sc} in glial cells around PrP^C-null neurons did not induce cell death in the knockout neurons, suggesting that PrP^{Sc} does not mediate a direct cytotoxic effect [115,116]. It is likely that conversion of PrP^C to PrP^{Sc} results in both a loss-of-function of the cellular form and, in parallel, a gain-of-function of the infectious one.

The presence of PrP^C in both pre- and post-synaptic structures raised the hypothesis that PrP^C plays a role in neuronal communication [117,118]. A functional role of PrP^C in synapses was suggested on the basis of the ability of PrP^C to bind copper released into the synaptic cleft during depolarization [119]. Since high extracellular levels of Cu^{2+} could induce the endocytosis of PrP^C to intracellular organelles and the Golgi apparatus [120,121,122], it was proposed that presynaptic PrP^C may buffer Cu^{2+} levels in the synaptic cleft and ensure its transport back into the presynaptic cytosol. This mechanism could also have a protective role against reactive oxygen species generated by Fenton-type redox reactions.

On the other hand, several experimental studies suggest that PrP^C could play a role in synaptic structure, function and maintenance. In particular, these studies have shown that PrP^C is distributed on all portions of neurons, without any preferential synaptic targeting [123]. The observation that PrP^C is important for synapse formation and function is supported by a wealth of evidence on synapse loss and PrP^{Sc} deposition in synaptic terminals during prion diseases [124,125]. PrP^C expression in defined brain regions seems to corroborate the importance of these findings. Indeed, during brain early postnatal development PrP^C is strongly expressed in the hippocampus. Within this brain region, the stratum lacunosum-moleculare revealed the highest PrP^C expression. Since this is a synapse rich region where hippocampal interneurons and afferent neuronal inputs make connections, it has been inferred that the relatively high expression of PrP^C in this region could possibly be necessary for the correct development of synapses [96].

1.2.2 Structure of PrP^C

Structural information on PrP^C is mainly derived from recombinant protein expressed in bacterial cells. Although post-translational modifications like N-glycosylation and GPI-anchoring were lacking, it has been shown that native structure and stability [126] were

comparable to PrP^C extracted directly from healthy calf brains [127]. In general, PrP^C is composed of an N-terminal unstructured domain and a C-terminal globular folded domain.

More in detail the N-terminal domain can be divided into four different consecutive sub-domains: a first charged cluster (CC1), the octapeptide repeat (OR), a second charge cluster (CC2), and a hydrophobic domain (HD) (**figure 1.5, A**). The high degree of conservation of this unstructured domain between species, suggests a strong functional significance [128,129]. The flexibility and little secondary structure characterizing the N-terminal moiety in solution render PrP^C as a partially intrinsically unstructured or disordered protein. Under acidic conditions, the N-terminal region encopassing residues 23-120, does not fold spontaneously into a folded domain [130,131,132]. On the other hand, it has been observed that the OR region acquires transient structures at neutral pH [133], and Cu^{2+} is able to induce the formation of beta enriched structures in two different regions [134,135].

CC1 and CC2 domains seem to be involved in the binding of glycosaminoglycans (GAGs) [105] and nucleic acids [136,137], but evidence at the cellular level are lacking. The CC1 region was also identified as polypeptide sequence involved in endosome internalization of PrP^C [110].

The octapeptide region (OR) contains four or five repeats of eight residues (PHGGGWGQ), binds Cu^{2+} [138,139]. Coordination of Cu^{2+} likely occurs with residues HGGGW [140,141]; histidine and amide-nitrogen coordination from the Gly residues were detected, making the coordination site likely composed of three nitrogen and one oxygen atoms (**figure 1.5, A**, upper panel). *In vitro*, the octarepeats appear to strictly prefer Cu^{2+} over Cu^{1+} and other metal ions, but lower affinity binding of other metals has also been detected in full-length PrP^C (reviewed in [142]). Cooperative binding of four Cu^{2+} was shown to occur in these octarepeats. A range of binding affinities for interactions of PrP^C and Cu^{2+} were estimated in the low micromolar range. Binding efficiency of Cu^{2+} to PrP^C was higher at neutral pH, with reduced affinity at lower pH (reviewed in [143]). This enhances the hypothesis that PrP^C acts as a copper transporter, from the extracellular matrix to the endosomes. Two extra copper coordination sites were identified at His-96 [144] and His-111 [135] in $HuPrP^C$, and it is possible that up to six copper ions can be present in a fully copper-loaded PrP^C [145]. These can bind two Cu^{2+} with an estimated affinity in the nanomolar range, which has been proposed to be the biologically relevant mode of Cu^{2+} coordination, given the affinity of other proteins for copper [146]. Interestingly, pathological mutations in the C-terminal domain changed drastically the coordination geometry in the non-octapeptide region [147], suggesting an alteration of PrP^C-mediated copper homeostasis in pathological conditions.

The palindromic sequence (AGAAAAGA) encompassing residues 112-119 is also denoted as “toxic peptide”, because short peptides corresponding to this segment form fibrils in solution with β-sheet structure that are toxic to cultured mouse hippocampal cells [148,149,150]. During the conversion, the region encompassing the CC2 and HD is not accessible to antibodies recognizing this epitope in PrP^C [151], indicating that this segment undergoes profound conformational changes. These data suggest that such a sequence is essential for PrP^C to PrP^{Sc} transition.

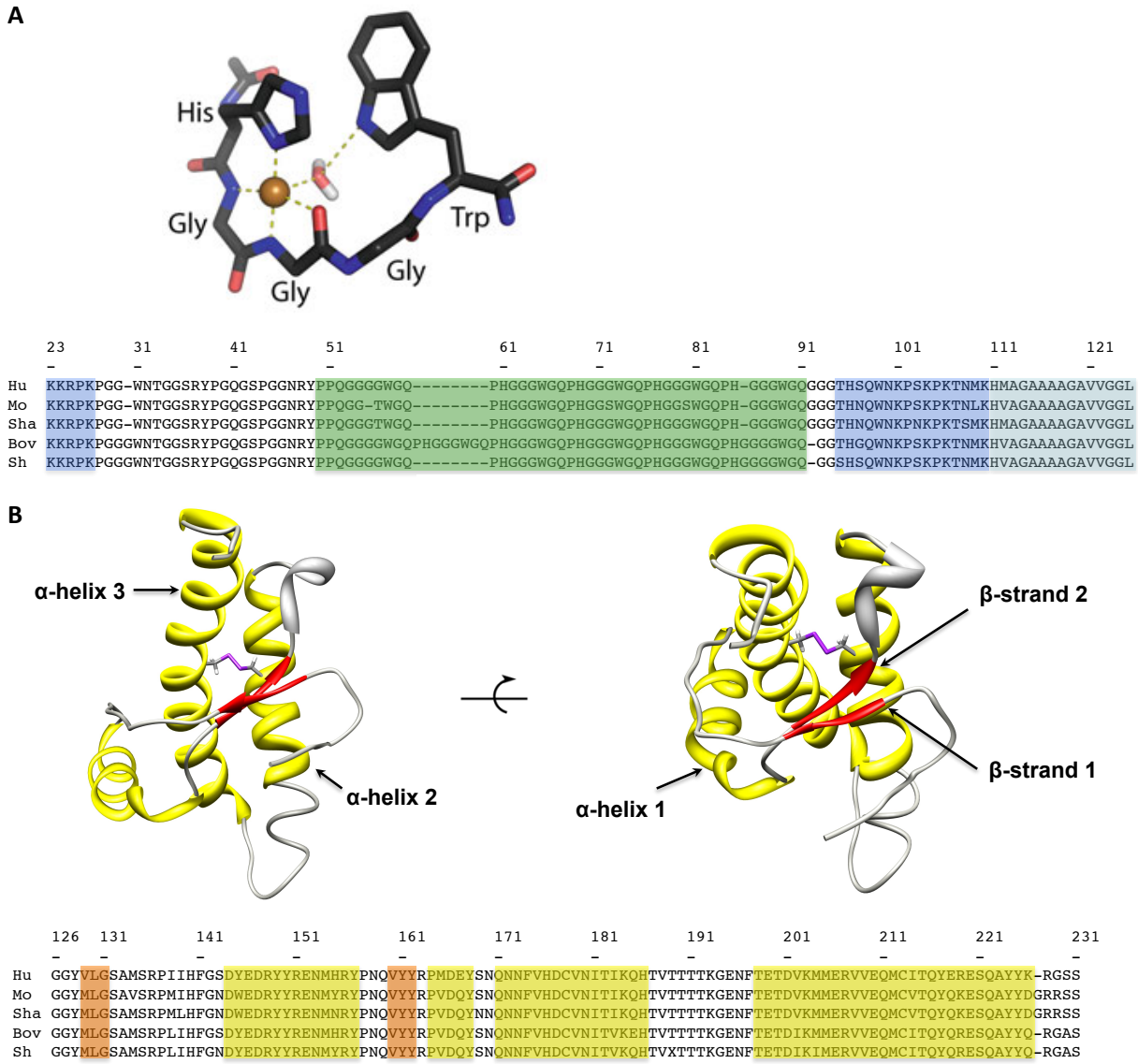

Figure 1.5 (**A**) Structure of the N-terminal domain. On top the coordination geometry of HGGGT peptide of the OR region (modified from [172]). On bottom alignment of human (Hu), mouse (Mo), syrian hamster (Sha), bovine (Bov) and sheep (Sh) N-terminal region protein sequences; in the purple box the CC1 and CC2 regions, in green the OR region and in grey the HD region. (**B**) On top NMR structure of MoPrP C-terminal globular domain from residue 121 to 230 (PDB entry: 2L39), with the disulfide bond highlighted in purple. On bottom alignment of the C-terminal domain sequences with beta strands in red and alpha helices in yellow.

The structure of the PrP C-terminal region has been obtained mainly by NMR experiments, from several mammalian species [126,152,153,154]. It is composed by three α-helices, corresponding to aa 143-153, 172-193 and 199-227, interspersed with an antiparallel β-sheet, formed by β-strands at residues 129-131 and 161-163 (**figure 1.5, B**). A single disulfide bond between Cys179 and Cys214 bridges α2 with α3. This type of structure is conserved also in non mammalian species [155], regardless there is ~30% identity and 50% conservation of the primary sequence.

The structured C-domain folds and unfolds reversibly in response to chaotropic denaturants [156]. The protein displays unusually rapid rates of folding and unfolding without populated intermediates in the folding reaction [157]. Moreover, hydrogen/deuterium exchange measurements on the human protein, showed that the overall equilibrium constant describing the distribution of folded and unfolded states was the same

as the protection factor [158]. This shows that no partially unfolded forms or intermediates have a population greater than the unfolded state. These data suggest that PrP^{Sc} is unlikely to be formed from a kinetic folding intermediate, as has been hypothesized in the case of amyloid formation in other systems, rather PrP^{Sc} conformers are formed from the unfolded state of the molecule. On the other hand, recent studies claim that folding intermediates are present [159]. The disulfide bridge is essential for protein stability [160], reducing the conformational entropy of the unfolded state [161]. Moreover, it has been shown that Cu^{2+} had a destabilizing effect on the folding reaction of recombinant full-length mouse PrP [162].

Prion protein stability is strongly related to pH. Several studies, which employed different biophysical techniques, have pointed out that mild-acidic and acidic pH values (~5.5-3) have a destabilizing effect on the protein [159,163,164,165]. Molecular-dynamics (MD) simulations support this hypothesis [166]. These results are consistent with the hypothesis that structural conversion of PrP into PrP^{Sc} taking place at acidic pH, along the endosomic pathway, making this environmental factor a key element in prion structural biology (see **paragraph 1.2.4**).

Mutations have been invaluable tools for understanding prion protein stability, and its possible effect on subsequent conversion to PrP^{Sc}. It has been shown that some mutation located in the C-terminal domain, involved in inherited prion diseases in humans, did not change the prion protein folding, rather they had a destabilizing effect on the native state [167]. This was confirmed by NMR studies on human PrP V210I and Q212P mutants [168,169], supported by MD simulations [170]. Interestingly, deletion mutants in the 114-121 region, encompassing the toxic peptide, have a stabilizing effect on the folded domain without affecting its structure [171].

1.2.3 The protein-only hypothesis

According to the protein-only hypothesis the central molecular event in the replication of prions is the self-propagating conversion of PrP^{C} to PrP^{Sc} [173]. Two different mechanisms have been proposed (**figure 1.6**).

The nucleation-polymerization model states that PrP^{C} and PrP^{Sc} are at equilibrium, but that the latter is less stable, shifting the equilibrium toward the cellular form. Stabilization occurs only when a stable oligomeric nucleus appears [174]. After this passage, PrP^{C} can adopt the scrapie conformation. The rate-limiting step is the formation of the stable nucleus. This step of stable nucleus reflects the lag phase of spontaneous conversion and it is accelerated by adding preformed PrP^{Sc} seeds.

The template assisted model instead expects that PrP^{C} can rarely adopt the PrP^{Sc} conformer, which is more thermodynamically stable but kinetically inaccessible [175]. Whenever PrP^{Sc} occurs spontaneously or is provided exogenously, it can template the misfolding of PrP^{C} with a direct interaction. The rate-limiting state in this model is represented by the dimerization between PrP^{C} and PrP^{Sc} monomers, or the formation of a less stable folding intermediate denoted PrP^{*}.

The two models are mutually exclusive; in fact the nucleation-polymerization model could explain the initial formation of the seed, while the template-assisted model could be involved in the elongation of fibrils. However, in both cases the formation of oligomeric structures or amyloid fibrils represents thermodynamic minima, with respect to PrP^{C} and PrP^{Sc}, making this process spontaneous.

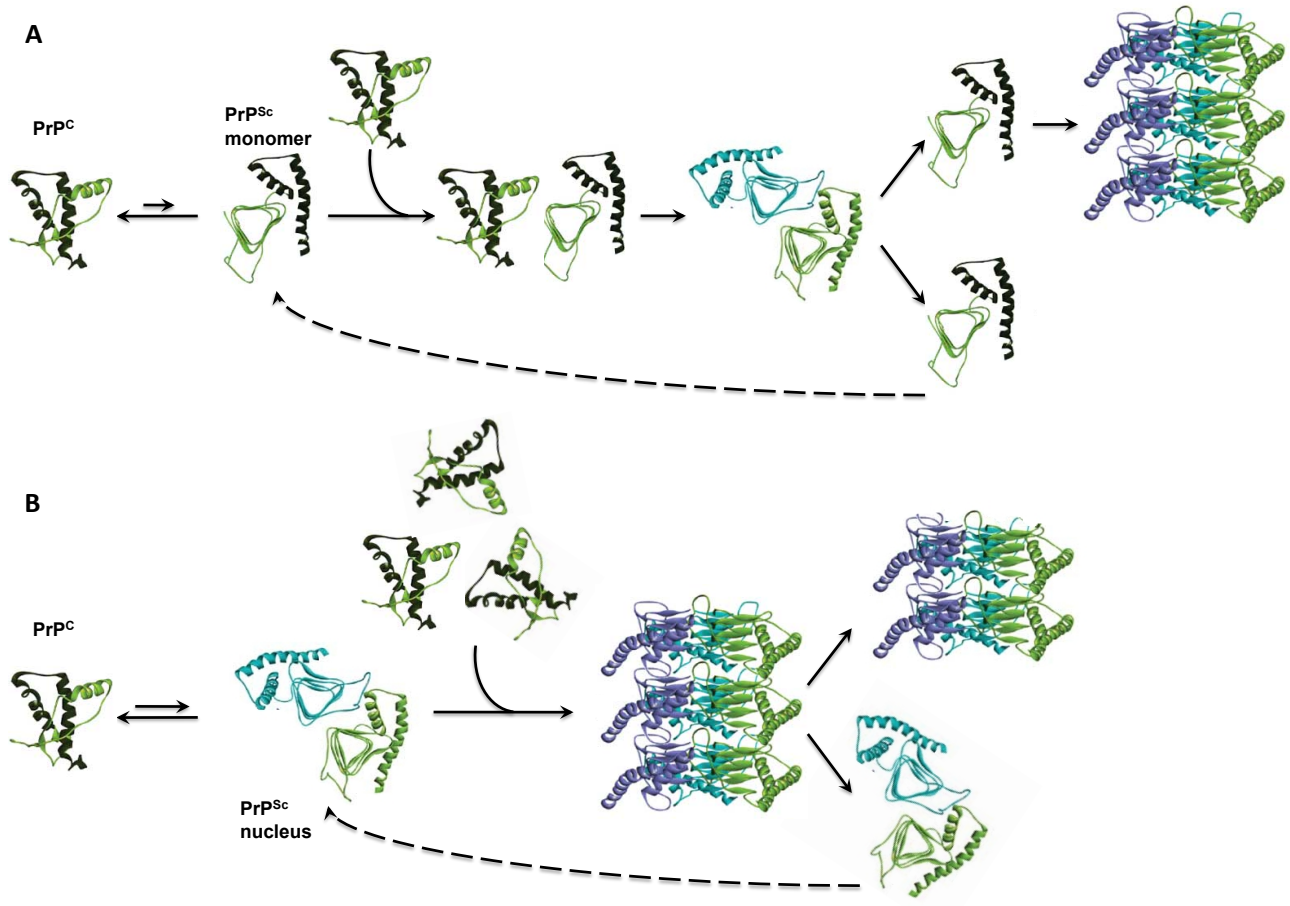

Figure 1.6. A) template-assisted model and **B)** nucleation-polymerization model. Images captured and adapted from [172].

1.2.4 PrP misfolding, oligomers and fibrils: a structural point of view

Structural characterization of PrP aggregation events is essential to gain insights in the disease development. Several studies have focused at the different stages of this process, from the misfolding of the monomer, to the oligomerization processes and to the resulting amyloid fibers formation.

The structure and stability of the monomer is strongly dependent on the environment. In fact, alternative folding pathway is observed at acidic pH. Studies on recombinant human PrP residues 90–231 (HuPrP(90–231)) [176] and mouse PrP encompassing residues 121–231 (MoPrP(121–231)) have identified a distinct, detergent-stabilized equilibrium folding intermediate at pH 4.0. Circular dichroism spectroscopy has indicated that this intermediate was structured with predominantly β-sheet topology and it has been proposed that this may be an intermediate on the pathway to PrP^{Sc} formation [165]. Studies on the truncated human prion protein (HuPrP(91–231)) have shown that PrP can fold to a soluble β-sheet enriched monomer in the presence of acidic pH conditions and in the absence of denaturants [177]. Reduction of the native disulfide bond is a prerequisite for β-sheet formation, and these observations of alternative folding pathways dependent on solvent pH and redox potential could have important implications for the mechanism of conversion to PrP^{Sc}. Indeed, this monomeric β-sheet state is prone to aggregation into fibrils with partial resistance to proteinase K digestion, characteristic markers of PrP^{Sc}. Although unusual for a protein with a predominantly helical fold, the majority of residues in PrP(90–231) have a preference for β-

conformation (55% of non–glycine/proline residues). In view of this property, it is possible that the PrP molecule is delicately balanced between radically different folds with a high-energy barrier between them: one dictated by local structural propensity (β-conformation), and one requiring the precise docking of side chains (native α-conformation).

Many efforts have been carried out aiming at characterize PrP oligomers. Such structures can be easily generated *in vitro* and due to their small size, ranging from 8 to 20-mer, they are soluble [178]. In presence of copper and oxidizing environment, oligomers showed a high heterogeneity in their radius and sedimentation coefficient [179], making their structural characterization challenging. This is expected since depending on the solution conditions of the initial state, the folding trajectories of a protein can be extremely different [180,181]. Nevertheless, all *in vitro* generated PrP oligomers presented β-rich spectra [182,183] and they co-existed with the monomeric soluble form at low pH. NMR studies on HuPrP(91–231) have pointed out that the monomeric soluble form, present in the oligomeric mixture, showed characteristic molten-globule state features, with a partial unfolding of the native structure [184]. On the other hand, it has been shown that such a molten-globule state is rich in α-helices [185]. Recent studies using 19F-labeled HuPrP(90–231) showed that association of monomers is entropically driven, suggesting burial of hydrophobic groups that have been exposed following the loss of native structure, and a concomitant desolvation of the oligomer [186]. Subsequent formation of the larger oligomers is enthalpically driven, indicating that this process represents addition of octamers and monomers to a stable β-sheet core. Despite the evidence, it is still debated whether the formation of such oligomers are on the pathway to fibrillization [185,187] or are off-pathway intermediates, requiring dissociation and conformational rearrangement of the monomer before fibril assembly can take place [47,188,189].

A defining feature of PrP^{Sc} is the unusual high resistance to degradation by proteolytic enzymes such as the proteinase K (PK). Limited proteolysis on PrP^{Sc} usually generates a smaller C-terminal PK-resistant molecule composed by approximately 142 residues starting from residue ~90 to 230. These residues are involved in the formation of the hydrophobic core of prion fibrils. Historically, PK-resistant PrP^{Sc} is denoted also as PrP27-30 because of its electrophoretic mobility, which encompasses a molecular weight from 27 to 30 kDa [190]. In the presence of either anionic detergents or nonionic detergents PrP27-30 polymerizes into rod-shaped particles, which present tintorial and morphological features typical of amyloids [191]. The unique properties of prion aggregates pose challenges for X-ray crystallization and NMR.

Three models of PrP^{Sc} amyloids have been described.

1. The β-helix model has been proposed on the basis of EM data from 2D crystals [192]. A model of a left handed β-helix was constructed by threading the PrP sequence through a known β-helix motif from uridyltransferase of *S. pneumoniae* [192]. In this model, a trimeric arrangement constitutes the basic symmetrical unit for PrP^{Sc}, with the N-terminal residues of PrP27-30 (~90–175) forming left-handed β-helices that are horizontally stacked and include a long unstructured loop encompassing residues 145–163 (**figure 1.7, A**). Larger aggregates are formed by vertically stacking PrP trimers along the β-helical axis. In addition to a major refolding within the N-terminal region of PrP27-30, the model is characterized by only minor structural rearrangements in the C-terminal part of the protein, which retains most of its native secondary structure, except for the first small α-helix that switches to a loop. Interestingly, the β-helical motif has been observed in other proteins that exhibit biochemical features reminiscent of PrP^{Sc}, such as partial resistance to protease degradation and aggregation propensity [193,194]. Remarkably, the fungal prion HET-s was shown to form a β-solenoid arrangement of β-sheets that is structurally similar to β-helices [75]. On the other hand, the β-helix model is not consistent with antibody mapping studies, enzyme cleavage

sites and unit cell packing dimension of the EM data [195].

2. The β-spiral model (**figure 1.7, B**) consists of a spiraling core of extended sheets, comprising three short β-strands (spanning residues 116–119, 129–132 and 160–164) and an isolated strand (residues 135–140). It has been proposed from MD simulations of PrP conformational fluctuations under low pH, using the natively folded structure as the starting point [196]. As with the β-helical model, formation of β-strands involves the natively unfolded N-terminal region of PrP27-30, whereas most of the C-terminal remains intact, preserving the three α-helices characteristic of PrP^{C}. The model does not fit well with experimental proteolysis experiments and the HX-MS data.

3. The extended in-register β-sheet consists of β-strands and relatively short turns and/or loops, with no α-helices present (**figure 1.7, C**). Therefore, PrP conversion would involve refolding of the entire protein, and PrP^{Sc} would not preserve any of the structural motifs of PrP^{C}. This model is based on structural constraints obtained by HX-MS studies from recPrP fibrils [197] and with PrP^{Sc} derived from prion infected transgenic mice expressing PrP lacking GPI anchor [198]. The major weakness of this model is the absence of α-helical structures, which is in conflict with CD and FTIR data [81,199].

Recently, X-ray diffraction data from both natural and synthetic prions was obtained [200], including the Syrian hamster (SHa) Sc237 PrP27-30 strain (SHaSc237), the mouse RML prion (MoRML), the mouse adapted synthetic prion (MoSP1), mouse truncated recombinant PrP(89-230) and truncated recombinant SHa(90-231) amyloids. Fiber diffraction patterns of SHaSc237, MoRML and MoSP1 exhibited a marked intensity maximum at 4.8 Å resolutions, confirming the presence of β-strands running perpendicular with respect to filament axis, typical for amyloid structures. Equatorial maxima, diminished in intensity with increasing resolution. Equatorial diffraction from natural brain isolates and synthetic prions also included an intense, moderately sharp, low-angle reflection (63.3 Å), characteristic of fibers with poorly ordered para-crystalline packing. These data are more consistent with β-helical model. Contrarily, diffraction patterns from both recombinant MoPrP(89-230) and recombinant SHa(90-231) showed a well-defined 4.8 Å meridional layer line, but with an equatorial broad maximum at 10.5 Å. This diffraction pattern is consistent with a stacked β-sheet structure for the major component of recPrP amyloids. These differences imply that recPrP fibrils do not have the same amyloid structure as brain adapted prions. This structural information might also explain the substantial differences in their infectivity.

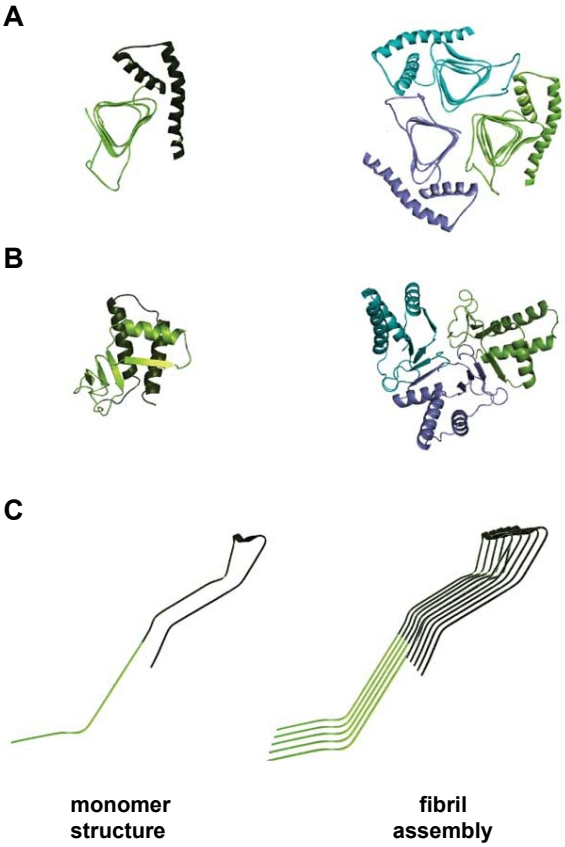

Figure 1.7 (**A**) The PrP^{Sc} monomer and the β-helical model. Residues ~90-175 are shown to form left-handed β-helices that associate into trimers, leaving the α-2 and α-3 helices of PrP^{C} intact. (**B**) In the spiral model the two native β-sheets elongate in a longer single β-strand, which forms intermolecular β-sheets with other PrP^{Sc} molecules. **(C**) Parallel and in-register β-structure model including a continuum of short β-strands from residue ~90 to the entire C-terminal region.

1.3 Single-molecule force spectroscopy

The pioneering work of Rosalind Franklin and Maurice Wilkins on X-ray diffraction on dsDNA molecules, and the subsequent double-helix model proposed by Watson and Crick, initiated the characterization of bio-molecules at the atomic level. A few years later the first tridimensional structure of a protein molecule, the myoglobin, was obtained by Kendrew using X-ray crystallography [201]. In the mid-80's Williamson and Wuthrich employed nuclear magnetic resonance (NMR) to calculate the structure of proteinase inhibitor IIA [202], expanding the structural biology field using this technique. In 2014 more than 100000 structures of bio-molecules have been deposited on the Protein Data Bank, most of which are proteins. Although in these cases the actual object of study was not the molecule itself, rather the average properties of billions of individual molecules. Protein molecules are dynamic objects, continuously shifting from stable states to intermediate or misfolded ones, which can be rarely populated. It is therefore obvious that using *in-bulk* techniques, such aspects could not be investigated. The invention of the atomic force microscope in 1986 initiated the era of manipulation of single molecules, expanding our knowledge in the nanometer scale.

1.3.1 Single-molecule techniques

In the last 30 years, there have been an increasing number of studies aimed at characterizing bio-molecules using single-molecule (SM) techniques. The three major single-molecule techniques are atomic force microscopy (AFM) imaging, SM fluorescence resonance energy transfer (SM-FRET) and SM force spectroscopy (SMFS). The first uses a probe to obtain topographical images of the sample deposited on a surface [203,204], but it can also be used to measure physico-chemical parameters such as axial elastic modulus [205]. Usually little or no modification of the sample is required, and experiments can be performed in air, in liquid or in vacuum. In SM-FRET the intesity of the energy transfer between fluorophores is measured, obtaining information on their respective distance. Usually, if the sample is a protein, two cysteines are added in specific positions and fluorophores are added via cysteine chemistry. By calculating the relative distance between fluorophores, information regarding proteins structural changes can be obtained.

In SMFS experiments, the molecule of interest is directly manipulated, applying mechanical force to it in real time, inducing some form of structural transition. Depending on the time derivative of applied force, the observed event can occur in quasi-equilibrium conditions or in out-of-equilibrium conditions. Structural, thermodynamic, and kinetic information about the transition can be inferred from the force required to induce it [206,207]. The two most used SMFS techniques are AFM based SMFS (AFM-SMFS) and optical-tweezers based SMFS (OT-SMFS), and their application is mainly focused on DNA or protein molecules.

In SMFS experiments, performed with laser optical tweezers, the protein molecule is modified by adding covalently long molecular handles. These handles are usually double stranded DNA molecules, which are attached to protein termini (or in other specific positions of the primary sequence) using cysteine chemistry [208]. The termini of the handles that are not bound to the protein are linked to polystyrene beads. The beads are then “trapped” using a near-infrared laser beam with a Gaussian intensity, and when the spherical particles become subject to radiation pressure from the beam, their trajectories are modified due to conservation of momentum [209]. The small variation of position induced by the bead, is directly applied to the protein molecule, applying a stretching force (or a torque). For small displacements the restoring force has an approximately linear dependence on displacement and the optical trap can be modeled as a Hookean spring. The spring constant of the trap in typical OT apparatuses has a range of 0.01−0.2 pN nm^{-1}, increasing the signal-to-noise ratio dependent on thermal fluctuations and allowing the clear detection of mechanical events occurring at tenths of pN [210]. Therefore OT-SMFS is well suited for studies under near-equilibrium conditions due to the low force applied to the molecule [211,212]. On the other hand, the functionalization using dsDNA poses the experimental limitation of forces lower than 65 pN, due to overstretching transition of the DNA double helix [213].

In AFM based SMFS an interaction of the analyte between a probe and a surface is employed. During the AFM-SMFS experiment, the relative position of the cantilever tip (probe) and the surface is controlled via a piezo-electric actuator, while the analyte molecule bridges the gap and distributes the mechanical stress between the two. Measuring the deflection induced by the flexible cantilever tip with known mechanical characteristics can continuously monitor the force applied on the analyte. The behavior of the cantilever is usually approximated to that of a single Hookean spring, and its single elastic constant parameter can be measured with the thermal noise method [214]. Several possible sample preparations can be used to perform AFM SMFS. Different chemical functionalization of tip and/or surface can be employed, in order to control orientation, position and area density of the molecules of interest [215,216,217]. Another method is adding well-known mechanical

"markers" or "fingerprints" as handles of the analyte, the so called "polyprotein approach" (discussed in **paragraph 1.3.3**). Commercial cantilevers used in AFM FS experiments have elastic constant values with 50–150 pN nm^{-1} range, which for $k_bT \approx 4$ pN nm correspond to thermal force fluctuations of around 15–25 pN. This makes the measurement of mechanical events reliable above 20 pN, due to a low signal-to-noise (SN) ratio [218], with a millisecond time resolution [210]. AFM-SMFS is well suited for far-from-equilibrium transitions, like folding/unfolding of structured protein domains [210].

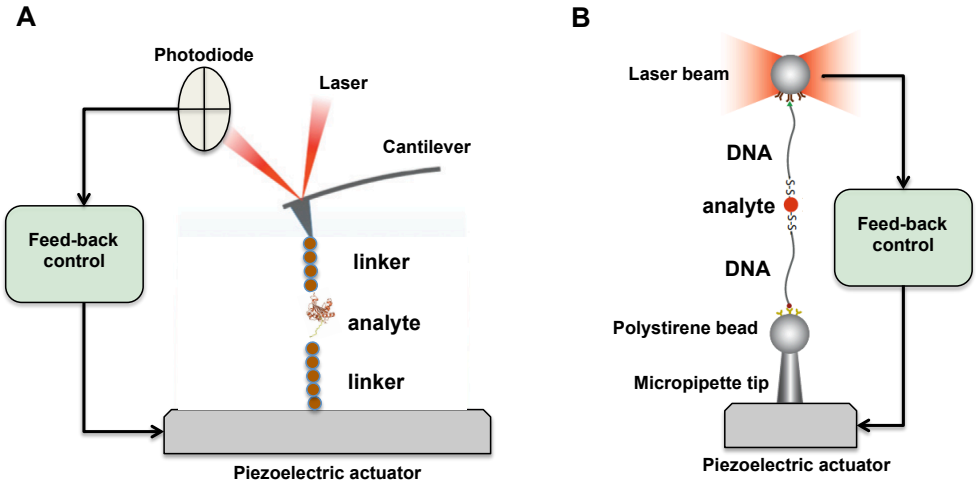

Figure 1.8 Single-molecule force spectroscopy techniques. (**A**) Main components of AFM based SMFS apparatus. The analyte is tethered to a surface and a sharp tip present on a flexible cantilever. The surface is mounted on a piezoelectric stage. A laser beam is focused on the tip, which reflects the light to a photodiode. When the surface is retracted away from the tip, the tethered molecule will be put under tension. The applied force and its variation are measured by tip deflection. (**B**) OT force spectroscopy apparatus main components. The analyte is tethered between two microbeads. At least one of the beads is optically trapped via a focused laser beam, while the other is usually attached by suction to a micropipette tip. The micropipette is usually mounted on a piezoelectric stage. Position of AFM surface and OT micropipette tip are both controlled via active feed-back loop. One micro image captured and adapted from [208,219].

1.3.2 Protein mechanical stability

With respect to traditional chemical unfolding experiments, mechanical unfolding follows a different pathway, with a different unfolding barrier [220]. This has been shown using the 27th immunoglobulin domain (Ig) of the band I of titin (I27): in SMFS experiments the protein presented an intermediate unfolding transition [221], which could not be detected using standard "in-bulk" chemical unfolding experiments. Mechanical stability of proteins depends on their folding and pulling geometry.

In general, β-sheet rich structures are more mechanically resistant compared to α-helix rich ones. This has been investigated using coarse grain Gō models on several PDB entries [222] and *in silico* calculations [223]. The orientation of the force vector, with respect to the hydrogen bond involved in these secondary structures, is responsible of the force required to break such structures. Two general classes of geometries are identified: zipping and shearing geometries [223,224,225].

In zipping geometry the two force vectors lie orthogonal with respect to the protein strands and, therefore, parallel to the hydrogen bonds (**figure 1.9, A**). In this case, in every moment, only a single bond between residues of the two strands is under tension, making their rupture sequential, "unzipping" the two strands. Therefore the force required to unfold such structure would be comparable to the force required to break a single hydrogen bond. In

shearing geometry (**figure 1.9, B**), the force vector lies parallel with respect to the strand, putting all the hydrogen bonds under tension. Thus, unfolding the protein requires that many bonds have to break at the same time. Such an event is exponentially less probable to happen at a given force, with respect to the breaking of a single bond, therefore a higher force is required to break all the structure. However, using molecular dynamics (MD) simulations it has been calculated that even in this case the rupture can occur in a sequential manner, but the discrete number of hydrogen bonds broken is 3-4, instead of one as in unzipping geometry [224].
However, taking into account only secondary structure in protein mechanical unfolding is reductive, since hydrogen bonds, hydrophobic interactions and Van der Waals forces of tertiary and quaternary structures are involved in the formation and maintenance of the native fold as well. AFM SMFS studies have shown that even α-helix rich protein such as T4 lysozyme [226] and Notch-1 [227], which in theory should unfold at very low forces compared to β-enriched structures, are still able to unfold at considerable force values (~ 50 - 150 pN). Myosin α-helices in a coiled-coil topology could elicit considerable force in AFM SMFS experiments [228], with a plateau-like force extension curves (FEC) similar to dsDNA overstretching [213,229]. In contrast, studies on α-helix spectrin heterodimers [230] revealed a sawtooth like pattern, similar to β-sheet rupture events but with lower unfolding forces. Single α-helix domains (SAH) unfolded at forces lower than 30 pN instead, without unfolding peaks [231].

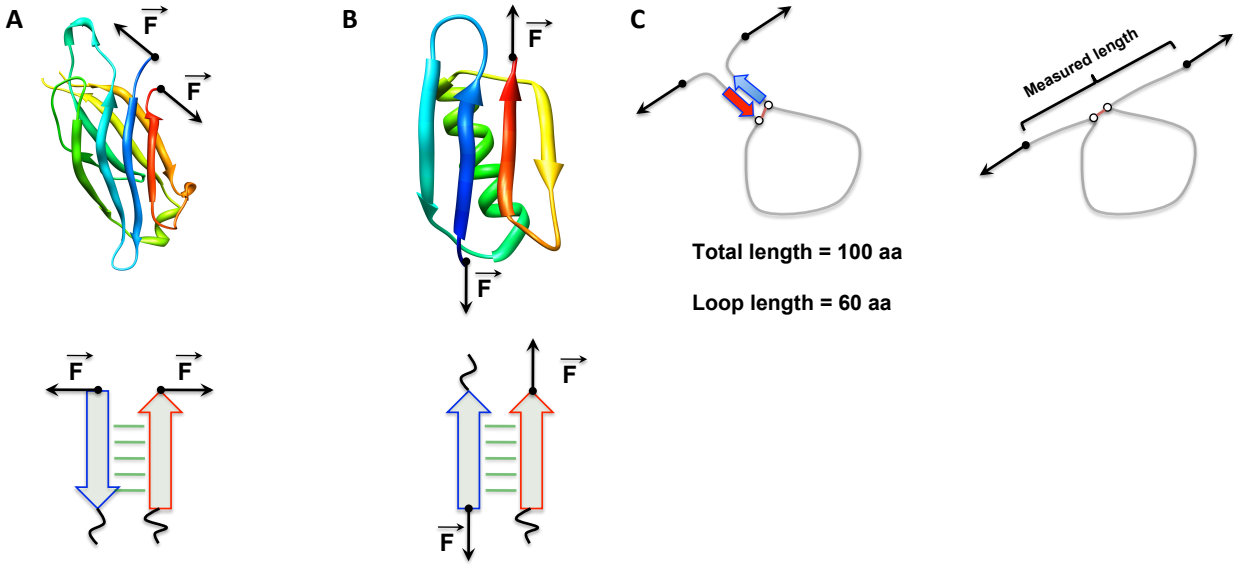

Figure 1.9 (**A**) On top zipping pulling geometry of an antiparallel β-sheet of C2A domain (PDB entry: 3F04); on bottom the schematic representation of the force vector, which is parallel respect to the H-bonds of the β-sheet (green lines). (**B**) On top shearing pulling geometry of a parallel β-sheet of GB1 domain (PDB entry: 2J52); on bottom the schematic representation of the force vector, which in this case is perpendicular respect to the H-bonds of the β-sheet (green lines). (**C**) Schematic representation of unfolding a domain containing a disulfide bridge. Considering a total length of the folded domain (L_{tot}) of 100 aa, upon stretching it the loop inside the disulfide bridge (L_{loop}) is not under tension. The resulting elongation $L_m = L_{tot} - L_{loop} + L_{SS}$, where L_{SS} is the length of the disulfide bond, which is ~ 0.4 nm.

Disulfide bonds alter the mechanical unfolding of protein molecules. Since they are covalent bonds, the force required to break them is 1-1.5 nN, five to hundred times higher compared to ones necessary to unfold folded domains. Usually the detachment of the bridged molecule between the tip and the surface occurs simultaneously or before the disulfide bond breakage. Therefore the disulfide bond "hides" the encompassed loop, preventing the application of

force to it. This means that the apparent length of unfolding is shorter than the theoretical unfolding length of the whole protein or domain (**figure 1.9, C**). The presence of reducing agents can lead to the reduction of the disulfide bridge, and concomitant extension of the hidden loop. This behaviour has been observed on mammalian Ig protein domains such as V-CAM [232], on angiostatin [233,234], and on engineered I27 domains with an artificial disulfide bond [235]. Further studies have shown that the reduction of disulfide bridge is force dependent [236], and that different reducing agents have different energy activation barriers (E_a), depending on their solvation and their structure [237].

1.3.3 Mechanical unfolding of proteins with AFM-SMFS

In AFM single-molecule force spectroscopy experiments the unfolding processes previously described are, with a certain approximation, thermodynamically reversible. Hysteresis is a measure of the energy dissipated in the process, which can be identified in force-extension curves as the difference between the approach and retraction curve of a stretched molecule. Only few proteins have a true Hookean elastic nature, with little heat dissipation; some examples are PEVK and N2B domains of cardiac titin [238,239] and elastin [240] (**figure 1.10, A**).
Most proteins analyzed by AFM-SMFS display equilibration transition rates slower than timescales of SMFS experiments, making virtually impossible to discern the collapse of tertiary structures, followed by the unfolding of secondary ones. Usually the unfolding is cooperative, seen as a single global collapse of all the bonds involved in the structure. With this assumption it is possible to describe the unfolding process as a bond, with an energy profile where the barrier separates the associated (native) and the dissociated state (unfolded). Applying a force f that induces dissociation of the bond, diminishes the bond lifetime as described by:

$$t_{off}(f) = \frac{1}{k_{off}(f)} = t_D \cdot e^{\frac{E_b(f)}{k_b T}} \qquad [6.1]$$

where k_{off} is the diffusive relaxation time and E_b is the height of the energy barrier between the two states. As described by Evans and Richtie [206], on the basis of Bell's model [241], the energy barrier between the two states is reduced by the application of the external force. The energy distorsion is quantitatively change in an exponential way (**eq. 6.1**), with an E_b decrease in function of the work performed by force f along the distance x_b on the reaction coordinate (x_b is the distance of the barrier from the minimum). This can be described by:

$$t_{off}(f) = t_D \cdot e^{\frac{E_b(f)}{k_b T}} = t_D \cdot e^{\frac{E_b(0) - f \cdot x_b}{k_b T}} = t_D \cdot e^{-\frac{f \cdot x_b}{k_b T}} \qquad [6.2]$$

The effective result is a tilt of the energy landscape. In order to relate the bond lifetime with the force of dissociation, it is necessary to consider the dissociation equation of an isolated pair of reacting molecules:

$$\frac{dp_b}{dt} = -k_{off}(t) \cdot p_b(t) + k_{on}(t) \cdot p_0(t) \qquad [6.3]$$

with $p_b(t)$ is the likehood of being in the bound state and $p_0(t) = 1 - p_b(t)$ is the likehood of being dissociated; k_{off} and k_{on} are the dissociation and association constants. By the

application of a force the second term of the sum goes to zero, due to the reduction of binding probability, giving:

$$\frac{dp_b}{dt} = -k_{off}(t)\cdot\ p_b(t) \qquad [6.4]$$

When an elastic probe acts as a pulling spring at constant speed, the applied force increases as a function on time:

$$r_f(f) = \frac{df}{dt} = k_s(f)\cdot v_s \qquad [6.5]$$

where k_s is the spring constant of the fetched molecule and of the probe, and v_s is the pulling speed. By introducing the force dependent expression $k_{off}(f)$ in **eq 6.5**, and solving the resulting differential equation, the probability density of the dissociation/unfolding force is:

$$\omega(f) = \frac{k_{off}(0)}{r_f}\cdot \exp\left(\frac{f\cdot\ xb}{k_bT} + \frac{k_{off}(0)}{r_f}\frac{k_bT}{x_b}\left(1 - e^{\frac{f\cdot x_b}{k_bT}}\right)\right) \qquad [6.6]$$

By calculating the maximum value of the distribution, the most probable unfolding force can be obtained:

$$f(r) = \omega(f) = \frac{k_bT}{x_b}\ln\left(\frac{r_f}{k_{off}(0)}\frac{x_b}{k_bT}\right) \qquad [6.7]$$

The unfolding force is directly dependent on loading rate (the speed at which molecule stretching is performed), so that at higher loading rates higher dissociations forces are more frequent.

It is important to notice that the unfolding force is a thermally driven probabilistic process. The force applied to the molecule, by tilting it's energy landscape, shifts the barrier of unfolding in the order of k_bT or less. The distribution of unfolding forces are not Gaussian, with a skewed distribution towards lower force values [206]. It is possible to extrapolate x_b and k_{off}, with experiments performed at different loading rates. This approach is also named dynamic force spectroscopy (DFS) [242].

Considering an ideal random chain molecule, its deformability is controlled by entropic elasticity. By stretching the polymer the total number of degrees of freedom diminishes, until ideally only the straight line conformation is possible. Ideally, every polymer could be described as several monomers joined one to another, with a certain flexibility. In the freely-jointed chain (FJC) model monomers are randomly oriented it the space, without taking into account any forces acting between them. This model is not used for stiffer polymers, such as biological macromolecules. The worm-like chain (WLC) model instead is widely used since segments are correlated. The chain is treated as an isotropic, homogeneous elastic rod whose trajectory varies continuously and smoothly through space, opposed to the jagged contours of the FJC polymer chains. Therefore the polymer behaviour can be considered intermediate between a rigid rod and a flexible coil [229]. The force F at a given extension x is described as:

$$F = \frac{k_bT}{p}\left(\frac{x}{L} + \frac{1}{4}\left(1 - \frac{x}{L}\right)^{-2} - \frac{1}{4}\right) \qquad [6.8]$$

where *L* is the contour length, and *p* is the persistence length. The latter represents the length at which correlations between the direction of two segments are lost; basically for lengths longer than *p* the polymer can be described statistically as a random walk. As long as *L* >> *p*, the WLC model describes with a good approximation the entropic elasticity of the polymer. The precise value of persistence length is not known, since it depends on polymer unit and other factors. In general, in SMFS experiments of proteins *p* is considered between 0.3 nm and 0.5 nm, which is approximately the length of a peptide bond [243]. Calculating the difference between the L values of two separated rupture events, the delta contour length (Δ_{cl}) can be obtained. This parameter gives the exact length of an unfolded protein module.

The WLC describes only the entropic elasticity of the polymer, but enthalpic contributions can be involved in the rupture of protein structures. In practice, a deviation from the WLC can be considered as a result of enthalpic interactions. Typical examples are dsDNA overstretching transition [244] and polysaccharides [245] (**figure 1.10, B**). In proteins such events were observed in few cases as a "hump" transition, over the WLC profile of I27 domains [221] and GFP protein [246] (**figure 1.10, C**).

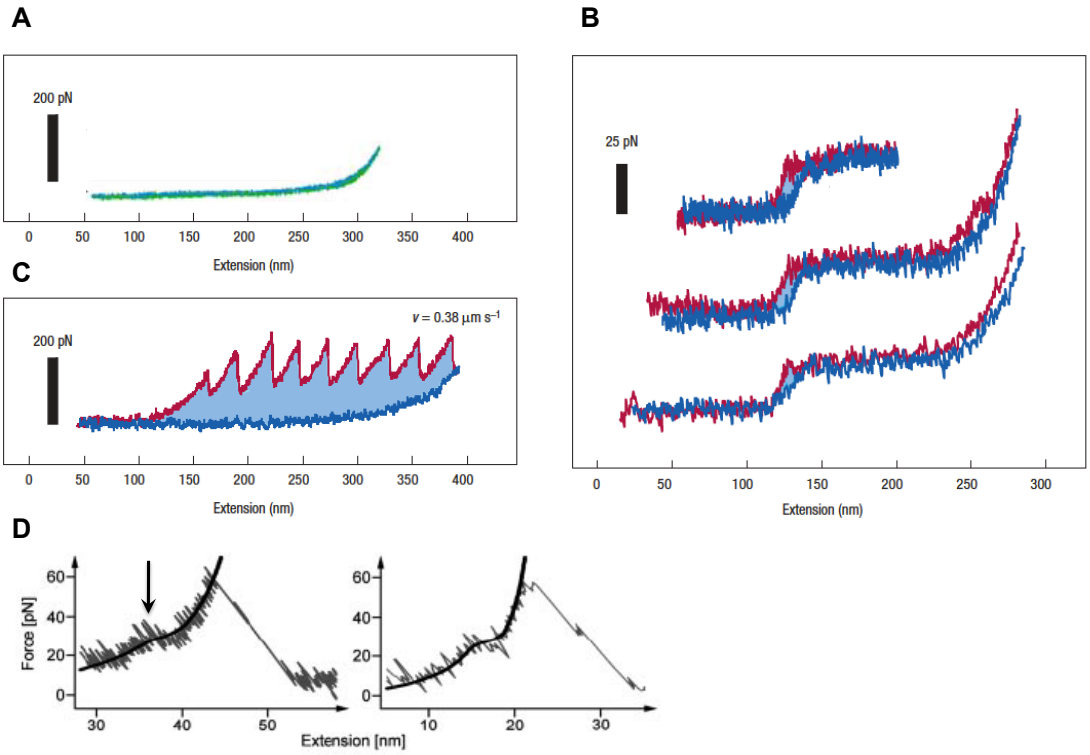

Figure 1.10 Different type of AFM FECs from protein unfolding experiments. (**A**) Unfolding of elastin results in a typical entropic spring behaviour, with complete superimposition of retraction (green) and approach (blue) curves. Adapted from [247]. (**B**) Superimposition of retraction (red) and approach (blue) curves, as result of an equilibrium unfolding transition of coiled-coil myosin II. Three FEC of the same molecule at different extensions are showed. (**C**) Typical sawtooth pattern obtained from the non-equilibrium unfolding of tandem repeats of I27 domains. It is possible to notice the hysteresis between the retraction (red) and the approach (blue) traces, as a result of heat dissipation upon protein unfolding. Images captured and adapted from [228]. (**D**) Unfolding intermediate of GFP indicated by the "hump" transition (indicated by the black arrow), as result of enthalpic contribution over the WLC. The solid line over the trace is the fitting of the experimental data with a three state unfolding model. Image captured and adapted from [246].

1.3.4 Heteropolyprotein strategy for AFM-SMFS

AFM-SMFS is a "blind" single-molecule technique. In the simplest experimental setup, the sample is adsorbed on a surface. The tip is then ramped in order to push first on it and then is retracted, resulting in a force extension curve (FEC) like the one shown in **figure 1.12**. During the retraction a molecule may be bridged between the surface and the probe, but this is an infrequent event since most of the curves (70-90%) do not contain any relevant signal. While this type of events can be easily discarded automatically by appropriate software, the interpretation of the remaining curves can be very challenging. In general this experimental approach has several weaknesses:

1- The bridged molecule can be bound between two (or more) random points of its chain, making the guess whether it has been pulled from the two termini not trivial.

2- Usually protein molecules are very small objects when folded, with length ranging from a few nanometers up to ten nanometers. The typical curvature radius of an AFM FS probe is 10 – 100 nm (depending on the cantilever tip). Thus it is possible that more than one molecule could be picked by the tip, giving a "double featured" force extension curve, which is theoretically indistinguishable from a single molecule curve.

3- The region proximal to the surface often shows non-specific signals due to the interaction between the tip and the surface.

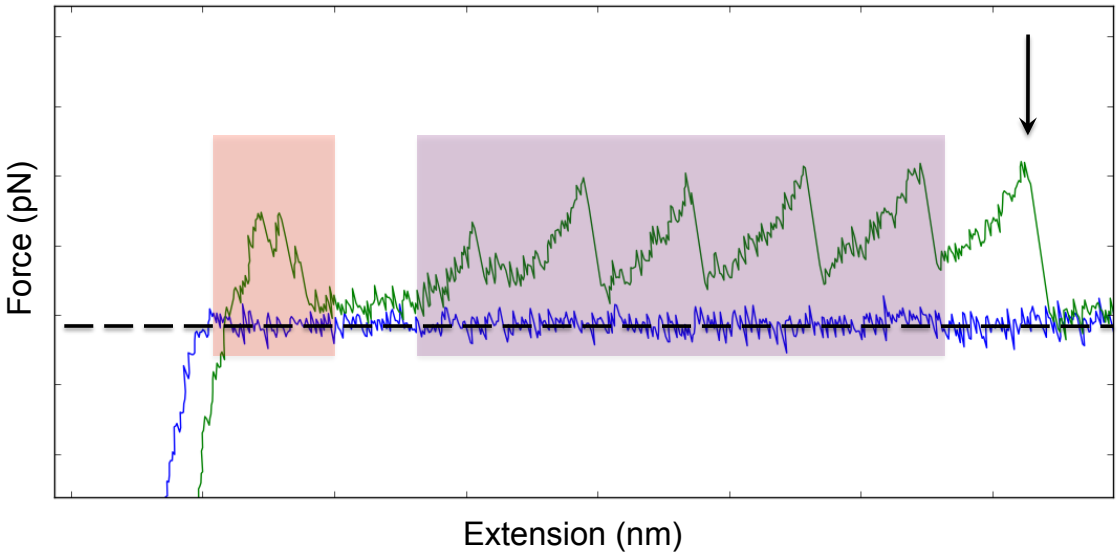

Figure 1.12 Typical force-extension curve (FEC) from AFM SMFS unfolding experiments. The black dashed line indicates the baseline, at zero force. During the approach (blue trace) the cantilever encounters the surface and starts pushing over it, indicated by the sudden increase of negative force. The tip is then retracted (green trace) and, after it stops pushing over then surface, molecules may be tethered to it. Usually non-specific interaction between the tip and the surface is present as result of irregular signals in the first tens of nanometers of retraction from the surface (red box); signals from the tethered molecule will follow (purple box). The molecule is stretched until it finally detaches from the tip (black arrow).

To overcome these experimental limitations, two major approaches are employed. The first one is the "functionalization" approach, where the surface is covalently modified with molecules that act as linkers, spacing the analyte and the surface [215,217]. This method has

the main advantage that the analyte requires little modifications. Cysteine chemistry is widely used to cross-link the analyte with the spacers, by simply adding one or two cysteine residues in specific positions of the protein primary sequence [248]. Amide cross-linking chemistry can also be used but since amide groups are present not only in the protein backbone, but also in side chains of some amino acids (i.e arginine), the selectivity of the binding geometry is drastically reduced. Double functionalization of tip and surface with the same protein is also employed to characterize dimerization processes, but the orientation of the two proteins involved in the complex could not be controlled [249,250].

The second approach is the "polyprotein" approach which requires a drastic modification of the analyte, but it also includes major benefits. The simplest polyprotein is the homopolymeric protein, where a protein domain is repeated in tandem over the same polypeptide sequence. Proteins used in this approach have a related *in vivo* mechanical function, like the domain I27 of titin protein [251] or the fibronectin domain III [252]. These two proteins are arranged in tandem repeats in titin protein of cardiac muscle cells, acting as molecular mechanical shock absorbers [252,253]. Other proteins instead have been found to have mechanical properties, despite their different function, such as ubiquitin [254] and small ubiquitin-like modifier protein (SUMO) [255]. Polyproteins of prokaryotic streptococcal protein G immunoglobulin-binding domain B1 showed mechanical performances than surpassed the ones from I27 protein domain [256]. Interestingly, all the above mentioned protein share the α/β fold structure, where an α-helical region creates an hydrophobic pocket with a β-sheet composed of 4-5 β-strands. The β-sheet has a shearing pulling geometry. Stretching this construct result in a typical "sawtooth" pattern, where every single domain unfolding event is characterized by a peak (**figure 1.12**). The delta contour length (Δ_{cl}) from adjacent peaks fits very well with the theoretical unfolding length of the folded domain. These protein modules are usually mechanically strong, with unfolding forces in the order of hundreds of pN. The unfolding of protein domains within the polypetide chain follows a memoryless markovian process, since the unfolding of one domain is not dependent on previous unfolding events [257]. Thus, it is not possible to correlate the rupture events with their specific unfolded domains by simply looking at the unfolding pattern.

In the heteropolymeric protein approach the protein under investigation is added to the polypeptide chain of a homopolymeric protein construct, and is "sandwiched" between marker domains. Therefore every signal that could not be associated to the marker, is related to the analyte. In general two types of patterns between the analyte and the marker can be adopted using this approach:

1- Sandwiched pattern (**figure 1.13, A**): one analyte moiety is flanked generally by two to four marker domains. It is possible to know that the analyte have been stretched by counting the number of marker unfolding events [227,231,238,258,259].
2- Alternate pattern (**figure 1.13, B**): analyte and marker are repeated in tandem [231,260]. The advantage is that more than one unfolding event of the analyte is present. If the analyte has a weak mechanical resistance, it can be seen at the beginning of the FEC as multiple independent unfolding event.

Usually the most used approach is the first one. These approaches have the advantage that FEC of protein construct can be easily distinguished; also by increasing protein size, signals from domains unfolding are located distantly from the non-specific interaction at the beginning of the retraction curve respect to functionalization approaches. Recently, a third approach was established where the analyte protein is inserted inside a loop region of the marker named "carrier" [261], based on a previous work by Li *et al.* [262]. In this construct the force can be applied to the analyte prior the unfolding of the "carrier", which acts as a spacer that bypass the non-specific interaction noisy region (**figure 1.13, C**). On the other

hand, in this approach, guest's termini are extremely near to each other, imposing structural constraints which are much less pronounced in the alternate and sandwiched patterns.

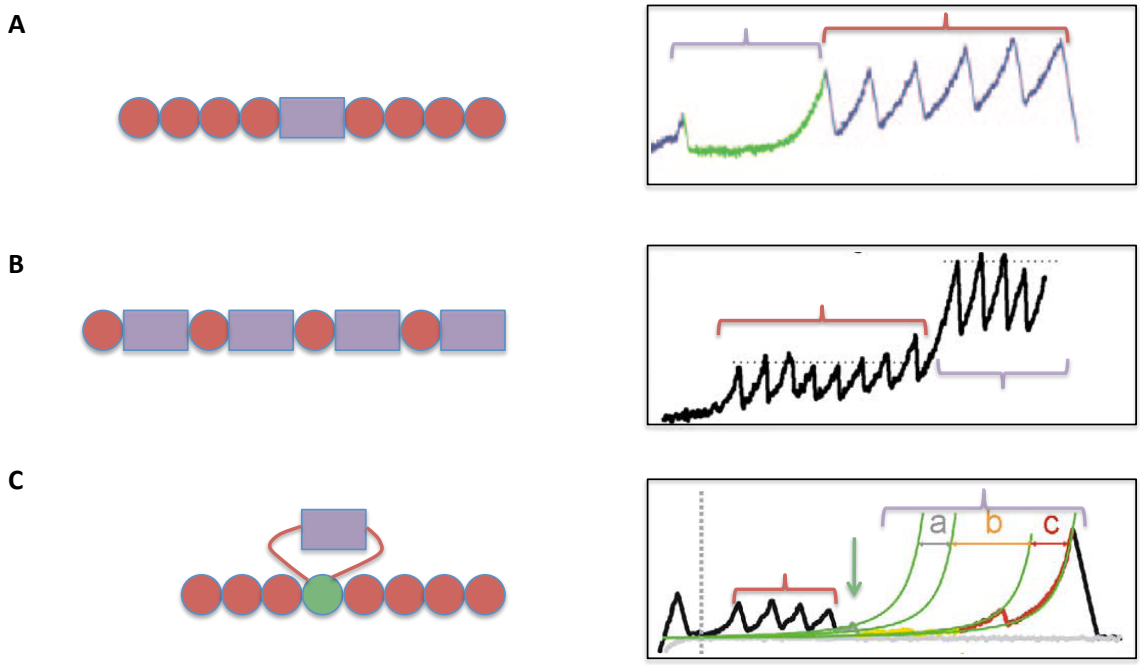

Figure 1.13 Three different heteropolymeric protein constructs employed in AFM SMFS. On the left the schematic representation of the polymeric constructs, where red circles are marker units, and the purple box represents the analyte. On the right a FEC using the corresponding construct, with red and purple parenthesis that indicate unfolding events from marker and analyte moieties respectively. (**A**) Sandwich pattern, with GFP (analyte) flanked by three I27 domains (marker). The unfolding of the analyte in this case occurs at the beginning of the FEC as a single peak at low force, followed by five I27 rupture events. Adapted from [246]. (**B**) Alternate pattern, with fibronectin domain III (FNIII) and I27 as marker and analyte respectively. It is possible to notice that multiple FNIII unfolding events occur at the beginning of the FEC at lower forces, followed by I27 domains; this indicates that rupture events are dependent on the force required to unfold the domain, regardless of its position inside the protein construct. Also, low force events are located at the beginning of the curve, while high force ones at the end. Adapted from [260]. (**C**) "Carrier/guest" approach, with α-synuclein (analyte/guest) inserted inside a loop of a structured carrier (green circle), which is flanked by standard marker domains (red circles). Before the carrier unfolds, it "hides" the guest protein from the applied force. In the FEC markers unfold first, followed by the rupture of the carrier (green arrow) that exposes the guest to the mechanical stress; the guest then unfolds, as indicated by the presence of long peaks. The main advantage is that low force unfolding events from the guest, can be located far away from the non-specific interaction region. Adapted from [263].

In general, to distinguish the analyte signal respect to the marker, contour length of unfolding events are used, since forces have a broader distribution. It follows that, regardless of the heteropolyprotein constructs approach is used, a "blind window" of the delta contour length from unfolding events of the marker will be present; while it is possible that the analyte can unfold with the same delta contour length of the marker, it is virtually impossible to distinguish them. Finally, another advantage of the sandwich constructs is the possibility to follow their folding/refolding kinetics, using double or multi pulse refolding protocols [246,256,260]. In these experiments the fetched molecule is extended without detaching it from the surface/tip. Subsequently, iterative cycles of approach and retraction without pushing the surface are performed. The ratio between the number of refolded domains with respect to the total unfolded domains in function of time, gives the kinetic parameters of folding transition with an acceptable approximation. In turn, force-clamp experiments can be

performed as well [237,254]. In these experiments the protein is kept under constant force via feed-back loop on piezo actuator, following molecule elongation over time. Each unfolding event is seen as a "jump" in height, with the same delta contour length of velocity-clamp experiments.

1.3.5 State of the art in SMFS of amyloidogenic proteins

Despite single-molecule force spectroscopy techniques have been employed to study bio-molecules since the mid 90's, they have only been used for analysis of amyloidogenic proteins less than ten years ago. The first insights were obtained using AFM SMFS on α-synuclein molecule, at the monomeric level by Sandal *et al.* [258]. Using the heteropolymeric protein approach authors have found that α-synuclein, is able to adopt at least three conformations, namely "random coil", "weak" and "strong". Weak interaction conformers were extremely heterogeneous, while strong conformers showed up as a homogeneous class of conformations having SMFS signals compatible with extensive acquisition of β structure. Surprisingly, the strong compact conformers were present in a high proportion. The authors proposed that this observation showed the ability of the α-synuclein monomer to sporadically populate a β-containing form that could be relevant in fibrillation processes. The same approach was used to show that factors linked to enhanced Parkinson pathogenicity, such as the presence of metal ions or familial α-synuclein point mutations, substantially increased the amount of observed compact structures [259]. In parallel, an experimental SMFS approach previously employed to characterize intermolecular interactions between fragments of α-synuclein was modified by Lyubchenko and co-workers and applied to the same protein [250]. This approach required the covalent tethering of α-synuclein molecules via their flexible C-termini to both the AFM cantilever tip and the mica surface, using silane chemistry. The velocity clamp SMFS data collected by repeating approach/retraction cycles revealed an occasionally enhanced interprotein interaction attributed by the authors to the acquisition of structure by the transiently formed α-synuclein dimers. DFS allowed them to observe two different lifetimes for the transient interactions, both of which were measured to fall in the seconds time range. Since these values are much higher than is characteristic for the dynamics of monomeric α-synuclein, one interpretation of these results could be that occasionally formed stable α-synuclein dimers might function as nuclei for amyloidogenic aggregation. Interestingly, these associations were observed only at acidic pH (2.7–5.1). Using the same experimental approach, the authors evaluated the impact of metal ions on the phenomenon [264,265].
Taking advantage of the *carrier/guest* approach, Hervàs *et al.* [263] probed the mechanical features of several amyloidogenic IDPs: polyglutamine (polyQ) stretches of three different lengths, β-amyloid 1–42 (Aβ42), α-synuclein , and a yeast prion extensively used as a human prion model (Sup35NM). While the percentage of different kinds of conformers was comparable to previous studies on monomeric α-synuclein mentioned above, differences in Δ_{cl} distributions of mechanically β-sheet like structures were observed. Moreover, a small population of hyper mechanostable conformers, with unfolding forces higher than 400 pN, were detected using the *carrier/guest* approach. This suggests that using different construct strategies could lead to a different behaviour of the protein.
AFM SMFS experiments performed on the polyQ-containing pFS construct allowed the authors to show that the Q19 tract, which has a length considered to be sub-threshold for the triggering of polyQ diseases, showed no detectable mechanostable conformations. Conversely, the Q35 (near-threshold) and Q62 (super-threshold) tracts showed increasingly common mechanostable and hyper mechanostable conformations whose unfolding required the application of forces in excess of 400 pN. On the basis of these results, the authors propose

that polyQ tracts with lengths of more than 35 amino acids can undergo a transient, sporadic acquisition of structure that might correspond to β-sheet-containing conformations. In contrast AFM SMFS studies of polyQ tracts performed by Dougan *et al.* [266] showed that irrespective of their lengths, all polyQ tracts offered significant resistance to mechanical elongation under applied load, with total inextensibility of Q50 traits up to 800 pN. The authors suggest that polyQ peptides can form a heterogeneous ensemble of mechanically stable collapsed structures and with an extensive network of intrachain interactions, which should cause the distribution of the applied force over several points simultaneously.
Even Aβ42 showed a high degree of conformational heterogeneity, characterized by a broad distribution of unfolding Δ_{cl} from mechanostable conformers. Familial-disease Arc Aβ42 (E22G) mutant was observed to assume mechanostable and even hyper-mechanostable conformations more than its wild-type (WT) counterpart, while the double mutant F19S/L34P, known to be less prone to fibrillogenesis, showed complete absence of mechanical events. Recently Lv *et al.* have further investigated the dimerization process of Aβ42, Aβ40 and corresponding [*VPV*] mutants [249], using the functionalization approach as previously described [250]. Data showed that different type of dimers could be obtained, due to a broad distribution of Δ_{cl} rupture events. Surprisingly, the force distribution for Aβ40 and [*VPV*] Aβ40 dimers was quite narrow for both proteins, 63.4 ± 3.2 pN and 79.3 ± 1.5 pN, respectively, showing that [*VPV*] mutation could adopt more stable structures.
Recently an alternative approach to study oligomerization processes was introduced by Woodside and co-workers [267], where multiple α-synuclein molecules were arranged *in tandem* over the same polypeptide chain and analyzed by OT SMFS. Analysis of the monomeric form of α-synuclein led to different results compared to previous works with AFM SMFS [258,263], since the presence of mechanically relevant signals could be observed only in 15% of the overall FEC. Also, the distribution of Δ_{cl} from these structures was different (**figure 1.14**), suggesting that different constructs could lead to different conformational transitions of the same analyte. Analysis of two and four tandem α-synuclein moieties revealed that the frequency of mechanical unfolding events was still 15%, regardless of the number of analyte moieties. Authors concluded that these structures were not thermodynamically stable, but rather of kinetically-trapped conformations that were only metastable. Such states should form transiently as the protein underwent thermally-driven conformational fluctuations, with a frequency and duration determined by the relative free energy of the state and the height of the energy barrier. The unfolding force of the overall events increased by increasing the number of α-synuclein moieties, with average values of 9 pN, 10 pN and 14 pN for monomer, dimer and tetramer respectively. Moreover the rate at which structures of a given total contour length change occurred is similar for all constructs, but declines roughly exponentially with increasing length.

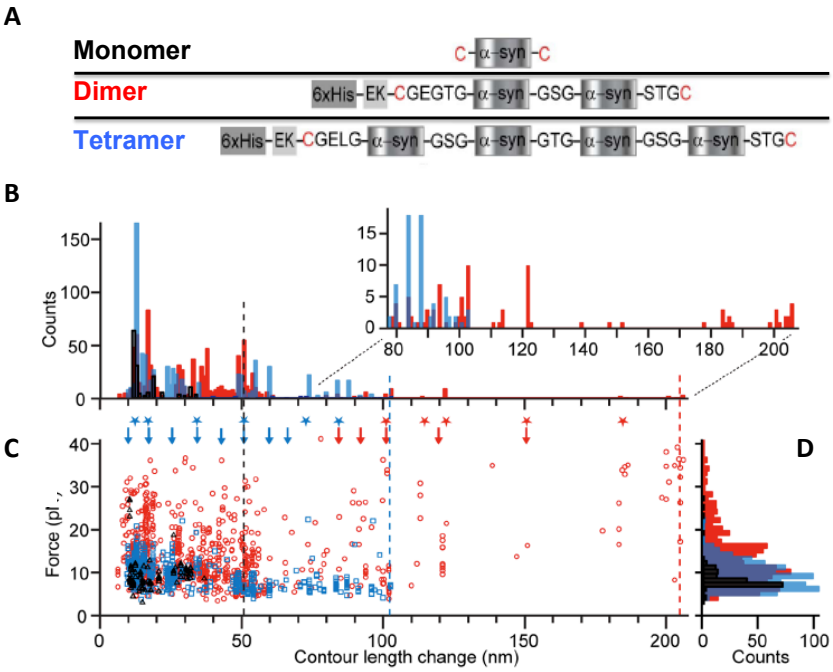

Figure 1.14 OT SMFS studies on α-Syn from [267]. (**A**) Schematic illustration of the three constructs employed, carrying one (monomer), two (dimer) and four (tetramer) tandem repeats of α-Syn molecules. (**C**) Scatterplot of all rupture events recorded from the constructs, with (**B**) relative histograms of Δ_{cl} rupture events and (**D**) corresponding unfolding force.

While SMFS experiments were extensively carried out on IDPs, few experiments were performed on the prion protein. In 2008 Ganchev *et al.* performed AFM-SMFS experiments in order to gain structural insights on the monomer structure inside prion synthetic fibrils [248]. To achieve that, $HuPrP_{90\text{-}231}$ was modified adding a cysteine residue in position 103 or at position 90, and fibrils were obtained *in vitro* at acidic pH [268]. Fibrils were deposited on mica surface and a gold-coated tip was ramped over the fibrils in order to establish a gold-thiol bond with the exposed cysteine residues of monomers. Subsequent retraction would have "extracted" single monomer units from the fibril. The distribution of monomer extraction of both types of constructs, led to the mapping of the hydrophobic core between residues 164-166, while residues 90-160 where supposed to be unstructured. This model is in contrast with all previous structural models of PrP^{Sc} (see **paragraph 1.2.4**), but a possible explanation could be related to the strong structural heterogeneity of amyloid fibrils. In fact, as discussed in **paragraph 1.2.4**, prion fibrils may present different structures, making their comparison between them not a trivial task. The average unfolding force was 115 ± 5 pN at loading rate of 150 nm s^{-1}, which is comparable to β-sheet proteins unfolding. A similar experiment was carried out by Dong *et al.*, on Sup35NM fibrils with a modified OT SMFS setup [269]. Prion fibrils from Sup35NM protein were immobilized on one terminus through inclusion in the fibril of free Sup35NM monomers, which were linked terminally to the surface. The other terminus of the fibril was bound in the same fashion to polystyrene beads functionalized with protein covalently linked monomers. Interestingly, fibrils were able to sustain high forces (~ 200 pN) without showing any "jump" in height due to unfolding of monomers, which occurred with a complex pattern only in presence of 1.2 M of GndHCl. Interestingly some height jumps were longer than 91 nm, the theoretical unfolding length of the whole Sup35NM protein, indicating that multiple monomers unfolded simultaneously.
More recently, analysis of the conformational space of monomeric ShaPrP was carried out

using OT SMFS by Yu *et al.* [270]. Almost 3000 FEC recorded from the unfolding of nine molecules showed that the prion protein folded and unfolded with a two state mechanism, as a result of single transition of 34.1 ± 0.4 nm. The energy-landscape was reconstructed, including diffusion constants for barrier crossing and the transition path times across the barriers [271]. Using force-clamp mode and signal-pair correlation analysis [272], the authors managed to identify three rarely populated states, named M1, M2 and M3, that were accessible only from the unfolded state (**figure 1.15, B**). M1 and M2 states were 3 and 5 kcal/mol more stable than the unfolded state, with 45 aa and 65 aa folded, while M3 was approximately stable as the unfolded state, with 35 aa folded (**figure 1.15, A**). The combined calculated values for the formation rates of such off-pathway intermediates implied that around 90% of the structure acquisition attempts by unfolded PrP led to non-native, transient conformations. A PrP double mutant (C179A/C214A), known to form oligomers rich in β structure, was also investigated with the same methodology, revealing an increased occupancy of the same off-pathway misfolded states respect to WT PrP, suggesting that they could act as intermediates leading to oligomerization.
Finally, the authors employed the same approach used for oligomeric constructs of α-synuclein [267] with ShaPrP, showing a similar pattern of unfolding transitions due to monomer associations (**figure 1.15, C**) [211].
These data taken together shows how SMFS can directly investigate the complex and rugged energy landscape of amyloidogenic proteins, both at the monomeric and at the oligomeric level.

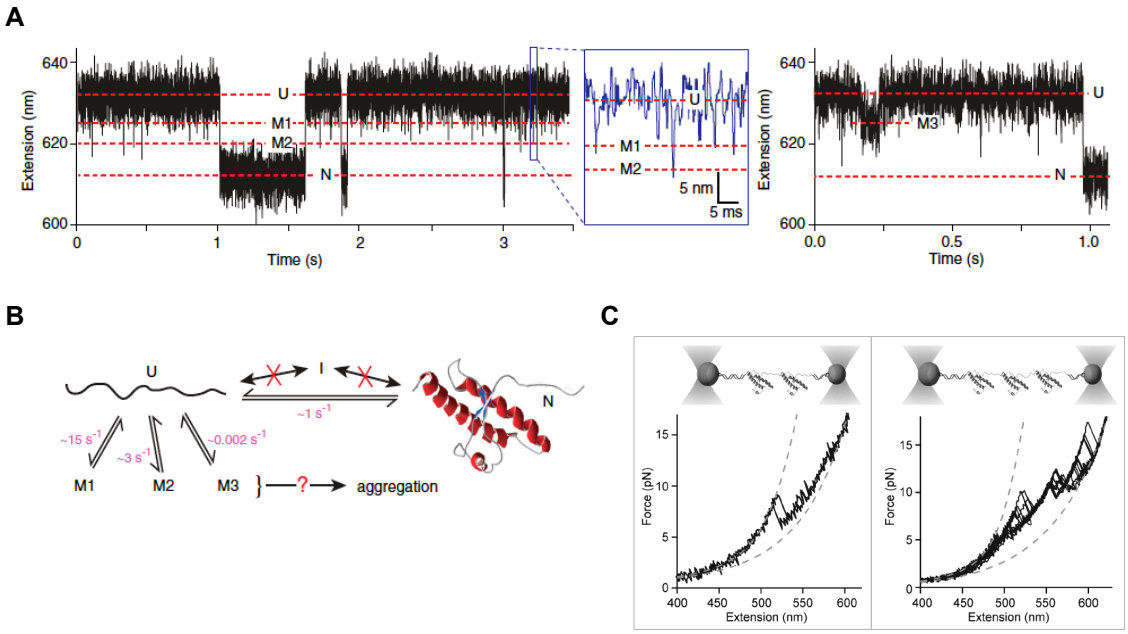

Figure 1.15 OT SMFS studies on ShaPrP$_{90-231}$ from [211,270]. (**A**) Passive force-clamp at 9 pN on ShaPrP. The protein populates mostly the unfolded state (named "U", at ~ 630 nm extension) and the native state (named "N", at ~ 615 nm extension); from the U state the protein explores ~ 90% of the time three metastable states (M1, M2 and M3), indicated by small jumps towards extensions with values between N and U. (**B**) Model obtained from OT experiments of the folding/unfolding transition of ShaPrP showing no intermediates between N and U, and three metastable states accessible only from U. (**C**) OT SMFS experiments on two (left) and three (right) tandem repeats of ShaPrP$_{90-231}$ molecules, revealing rupture events longer than the theoretical length of a fully stretched monomer, as a result of associations between PrP molecules.

2. Aim of the research

Neurodegenerative disorders, including prion diseases, are associated with protein aggregation. Considerable evidence indicates that the extent of neurotoxicity or infectivity of the oligomeric or aggregated proteins is strictly dependent on their structures. The proteins involved in these diseases are conformationally heterogeneous and, according to an emerging view, can switch back-and-forth between functional and various amyloidogenic conformations (strain conformations). Since the various conformations present in these heterogeneous ensembles lead to different aggregated forms, characterizing the monomer conformational space is critical to understand their pathogenicity. However, the characterization of the conformational heterogeneity of monomeric proteins by standard structural biological methods has proven to be extremely challenging. Single-molecule methodologies offer exciting opportunities to increase our understanding of protein conformational equilibria. This project is aimed at using a novel approach that combines the two main methods for single-molecule force spectroscopy manipulation, Optical Tweezers and Atomic Force Microscopy, to map the conformational energy landscapes of the truncated mouse prion protein (PrP), as well as their monomer conformations that promote the aggregation process. Truncated mouse PrP is an ideal candidate for prion conformational studies due to the possibility of creating different infectious conformations in a test tube and of introducing them in mice to develop novel prion diseases. The protein also represents the minimal unit to generate a prion. The synergic integration of these single-molecule techniques will make it possible to explore conformational properties of mammalian PrP that are inaccessible to more classical in-bulk ensemble-averaged methods, and to study the nature of the energy surfaces over which these molecules diffuse as they move between their different strain conformations and towards those that are responsible for triggering the aggregation processes and pathogenesis.
Specifically, we attempted to address here the following questions:

1. How does the conformational polymorphism of the monomer is related to the structures of oligomers and amyloid species?

2. How do various reaction conditions such as the polarity of the interaction between monomers (C-to-C terminus vs. N-to-C terminus), their relative concentration, and their rate of refolding and contact, affect the structure, yield, minimum size, and propagation of the early aggregation nucleus at the beginning of polymerization?

Ultimately, this proposal aims at relating conformational space, folding intermediates, and protein dynamics to the oligomer structure, amyloid conformation and strain phenotype.

Part II: Materials and Methods

3.1 Molecular biology

Omopolymeric $GB1_{x8}$ constructs and heteropolymeric $GB1_{x4}$-$(MoPrP(89-230))_{x1}$-$GB1_{x4}$ constructs cloning strategy was adapted from previous protocol [256].

3.1.1 Cloning

Plasmid vector pQE-80L :: $GB1_{x4}$ was kindly provided by the group of Prof. Bubacco (University of Padua). Cloning of $GB1_{x4}$-$(MoPrP(89-230))_{x1}$-$GB1_{x4}$ was performed by Dr. Federico Benetti and Eleonora Carboni.
Plasmid vectors were amplified by transforming 50µl aliquots of DH5α *E.coli* cells with 0.5µl of plasmid; after incubating competent cells in ice for 30', heat-shock was performed at 42°C for 90 seconds, followed by other 5' in ice. Transformed cells were grown at 37°C for 45 minutes in 900µl of LB medium, then plated on LB agar plates with ampicillin (100µl/ml). Single colonies were expanded in 5ml LB + Amp (100µg/ml) and the plasmid was purified using QIAGEn Plasmid Mini Kit (QIAGEN).
pQE-80L::$GB1_{x8}$ construct (**figure 3.1**) was obtained by adding $GB1_{x4}$ sequence to the pQE-80L::$GB1_{x4}$ linearized plasmid. Plasmid and insert were obtained by enzymatic cleavage and isolated (**table 3.1**) using QIAquick Gel Extraction Kit (QIAGEN).

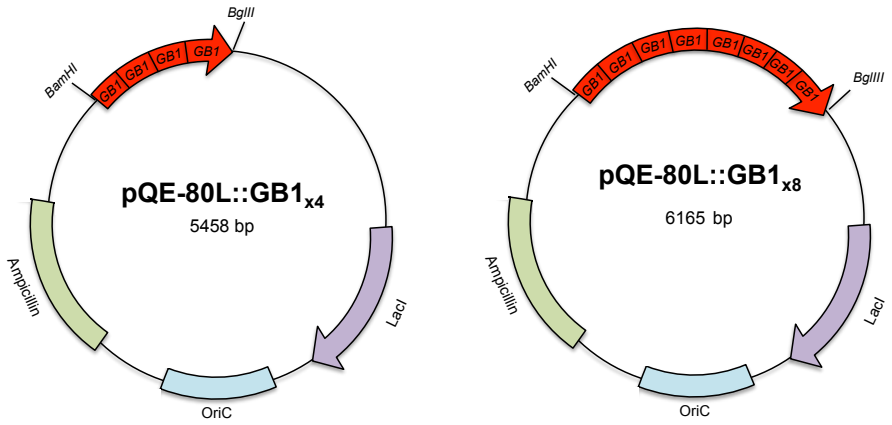

Figure 3.1 Cloning of pQE-80L::$GB1_{x8}$ from pQE-80L::$GB1_{x4}$**.** The $GB1_{x4}$ sequence was cut and inserted on the plasmid after linearization. BglII and BamHI sites can anneal and generate BstYI as new restriction site.

The insert and the linearized vector were quantified and mixed in 5:1 and 7:1 molar ratios for the subsequent ligase reaction (**table 3.2**). The ligation reaction was carried out at +4°C o/n and inactivated at 65°C for 20 minutes.

Reagents	Final concentration or volume	Final concentration or volume
	Linearization	Excision
pQE-80L::GB1$_{x4}$	100-300 ng	100-300 ng
BglII	1 µl	1 µl
BamHI	-	1 µl
NEB buffer 3 (10X)	2 µl	2 µl
MilliQ water	until 20 µl	until 20 µl

Table 3.1 Enzymatic restriction reaction used for cloning. The first reaction was used to linearize the plasmid, the second was used for isolating the insert sequence, which was inserted in the linearized plasmid.

Reagents	Final concentration or volume	Final concentration or volume
	5:1	7:1
Linearized plasmid	100 ng	100 ng
Insert	25 ng	40 ng
T4 DNA ligase (Roche)	1 µl	1 µl
Ligase buffer (10X)	1 µl	1 µl
MilliQ water	until 10 µl	until 10 µl

Table 3.2 Ligation reactions. 5:1 and 7:1 refers to insert:linearized plasmid molar ratios respectively.

For GB1$_{x4}$-MoPrP(89-230)-GB1$_{x4}$ plasmid, specific primers were designed on the nucleotide sequence NM_011170.2 (NCBI accession number) to amplify the MoPrP(89-230) (MoPrP Tr) gene while adding Bgl II and Bam HI restriction sites. The gene was subcloned into the pGEM-T vector (Promega), amplified and double digested with both restriction enzymes. A first round of ligation of the linearized pQE-80L::GB1$_{x4}$ plasmid with MoPrP(89-230) gene was performed (**figure 3.2**).

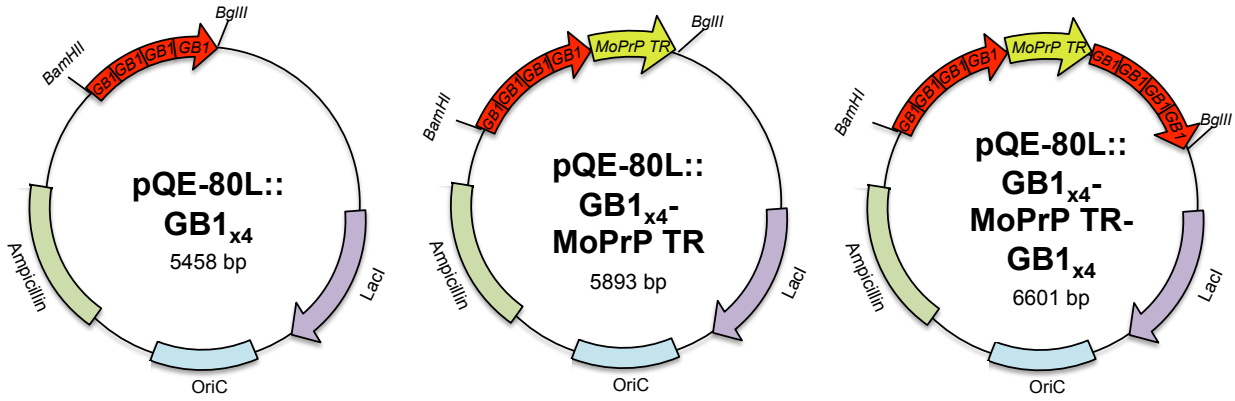

Figure 3.2: schematic representation of cloning strategy for the heteropolymeric construct GB1$_{x4}$-MoPrP(89-230)-GB1$_{x4}$ carrying one copy of the MoPrP(89-230) gene: firstly the MoPrP(89-230) sequence is added after the BglII restriction site of pQE-80L::GB1$_{x4}$ plasmid; then the GB1$_{x4}$ sequence is added after the GB1$_{x4}$-MoPrPTr sequence.

A second round of linearization of the resulting plasmid and ligation with GB1$_{x4}$ insert led to the formation of the GB1 flanking heteropolymeric construct. An His$_6$ tag was added to the 5' of GB1$_{x4}$, GB1$_{x8}$ and GB1$_{x4}$-(MoPrP(89-230))$_{x1}$-GB1$_{x4}$ sequences to facilitate purification steps. Cysteine mutant of GB1$_{x4}$-(MoPrP(89-230))$_{x1}$-GB1$_{x4}$ a cysteine was added at position 3 using

QuikChange Site Directed Mutagenesis kit (Agilent). For OT experiments pET11a::MoPrP(89-230) and pET11a::MoPrP(23-230) plasmids were mutated adding two cysteine residues at positions 91, 229 and 25, 229, respectively, using primers in **table 3.3**.
Correct construct formation and gene orientation was checked by restriction reactions and sequencing.

Construct	Mutation	Sequence
$GB1_{x4}$-(MoPrP(89-230))$_{x1}$-$GB1_{x4}$	**Fwd**	**5' GAAATTAACTATGAGATGCGGATCGCATCACCATC 3'**
	R2_G3InsC	
"	**Rev**	**5' GATGGTGATGCGATCCGCATCTCATAGTTAATTTC 3'**
	R2_G3InsC	
MoPrP(89-230)	**Fwd Q91_G92InsC**	**5' GATATACATATGGGCCAATGCGGAGGGGGTACCCATAATC 3'**
"	**Rev Q91_G92InsC**	**5' GATTATGGGTACCCCCTCCGCATTGGCCCATATGTATATC 3'**
MoPrP(23-230)	**Fwd K24_R25InsC**	**5' GATATACATATGAAAAAGTGCCGGCCAAAGCCTGGAGG 3'**
"	**Rev**	**5' CCTCCAGGCTTTGGCCGGCACTTTTTCATATGTATATC 3'**
	K24_R25InsC	
MoPrP(89-230) & MoPrP(23-230)	**Fwd R228_S229InsC**	**5' CTATTACGACGGGAGAAGATGCTCCAGCTAATAGGATCCG 3'**
"	**Rev R228_S229InsC**	**5' CGGATCCTATTAGCTGGAGCATCTTCTCCCGTCGTAATAG 3'**

Table 3.3: Primer sequences for mutagenensis. For each mutation forward (Fwd) and reverse (Rev) primers are annotated. Aminoacid numbers for optical tweezers constructs are referred to the pre-maturation sequence of MoPrP protein.

3.1.2 Sequence design

Plasmids of heteropolymeric constructs carrying multiple copies of MoPrP(89-230)have been designed, optimized and synthesized by GenScript. The synthetic genes were cloned inside pET-11a plasmid (Addgene) and an His_6 tag was added to the C terminus of the construct to facilitate purification steps. In **figure 3.3** a schematic representation of all protein constructs used for SMFS AFM experiments.

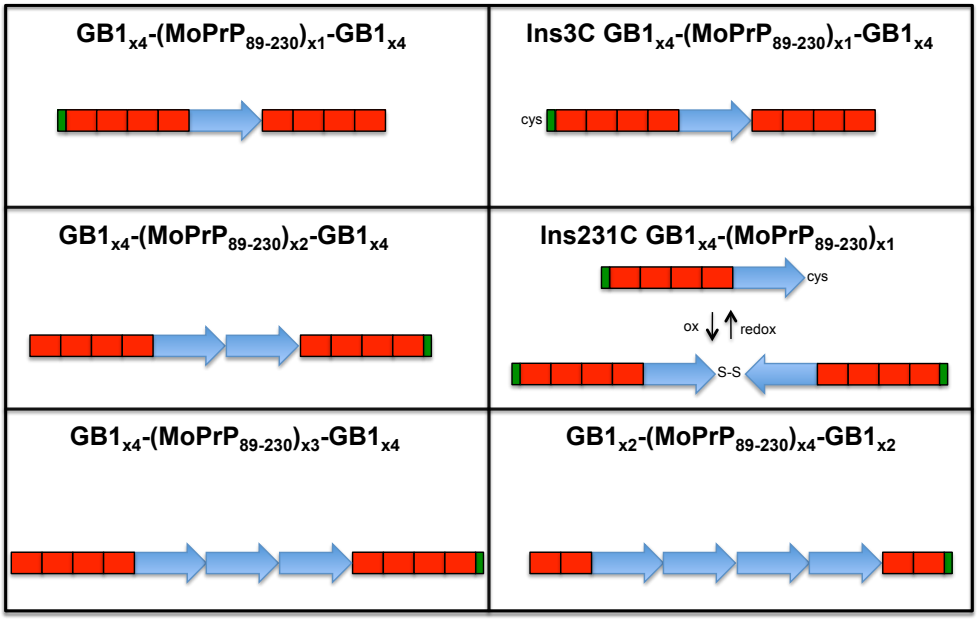

Figure 3.3: Representation of polypeptide sequence of SMFS AFM constructs. The green rectangle is the His_6 tag, the red rectangles are GB1 domains and the light blue arrow is MoPrP(89-230); the arrow direction indicates the orientation of the peptide bond from N-terminal to C-terminal. Insertion of cysteines for two protein mutants are showed. For the Ins231C $GB1_{x4}$-(MoPrP(89-230))$_{x1}$ the black arrows indicate the resulting protein in presence of oxidative or reducing conditions.

AFM protein constructs expressed from respective plasmids are named depending on the number of MoPrP moiety/moieties for clarity. Constructs with one MoPrP moiety are named MoPrP Tr_{x1} while the cysteine insertion mutant name is MoPrP Tr_{x1}-PEG. Dimeric constructs with two MoPrP moieties are named depending on the orientation of the two prion molecules. In MoPrP Tr_{x2} H-T the C-terminal globular domain of the first MoPrP moiety contacts the N-terminal domain of the following MOPrP moiety, while in MoPrP Tr_{x2} H-H the C-terminal domains of the two MoPrP moieties are adjacent. The production of the latter was achieved by dimerization through a terminal cysteine added in position 231 of Ins231C $GB1_{x4}$-$(MoPrP(89-230))_{x1}$ protein (**figure 3.3**). Finally constructs with three and four prion protein moieties are named MoPrP Tr_{x3} and MoPrP Tr_{x4} respectively.

3.2 Protein expression

The expression of all the constructs was carried out in BL21 (DE3) *E.coli* cells. After transformation, colonies were resuspended in LB media + Amp (100µg/ml) and inoculated directly in the flask for standard growth. For fermentation, a pre-inoculum of 200 mL of the same medium was prepared.

3.2.1 E.coli cells growth: flasks

Cells were grown in Luria Bertani medium (**table 3.4**) with ampicillin as antibiotic (final concentration of 100µg/ml) at +37°C, 150 rpm until O.D was ~ 0.6. Cells were induced with Isopropyl β-D-1-thiogalactopyranoside (IPTG) and culture was grown at 30°C o/n. To harvest, cells were centrifuged at 3500 g, 45' at +4°C, washed twice with 200ml of Lysis buffer (Trizma Base 25mM, sodium deoxycholate w/v 0.4%, Triton X-100 v/v 0.5% pH 8.0) to remove growth medium; and resuspended in 100mL of the same buffer.

3.2.2 E.coli cells growth: fermentation

The pre-inoculum was inoculated in 10L vessels of BioStat-Plus (Sartorius) containing autoclavated Zym-5052 autoinduction medium (**table 3.4**) [273]; with feed-back controls oxygen levels were kept between 26-32% modifying stirrer velocity, while with acetic acid/ammonium hydroxide pH was kept at ~7.2. Growth was carried out at 37°C for 16 hours, cells were then harvested, washed and resuspended as indicated in paragraph 3.2.1.

Luria-Bertani medium		Zym-5052 autoinduction medium	
Yeast extract	5g	NZ Amine	w/v 1%
Bacto Tryptone	10g	Bacto Yeast extract	w/v 0.5%
NaCl	10g	Glycerol	v/v 0.5%
ddH_2O	until 1L	Glucose	w/v 0.05%
		Lactose	w/v 0.2%
		Macroelements	1 X
		Microelements	0.2 X

Table 3.4 Expression media recipes for bacteria cell cultures. Zym-5052 macro and microelements composition are indicated in detail in [273].

Cells were lysed using Panda Homogenizer (GEA Niro Soavi) at 1500 bar for 3', added EDTA free Protease Inhibitor cocktail (Roche) and separated supernatant from inclusion bodies by centrifugation at 15000g, 60' at +4°C.

3.3 Protein purification

Protein purity after each purification step was checked on SDS-PAGE gel with corresponding acrylamide concentration depending on the molecular weight of the protein. Wild type MoPrP(89-230) and MoPrP(23-230) were purified with a protocol adapted from previous works [147,274] therefore this will not be described in this thesis.

3.3.1 Purification of soluble proteins

Supernatant from lysed cells was loaded slowly (0.5 mL/min) onto HisTrap crude FF (GE Healthcare) nickel affinity column mounted on Akta Purifier system (GE Healthcare) previously equilibrated with binding buffer (Trizma-Base 25 mM pH 8.0). The column was washed with washing buffer (Trizma-Base 25 mM, NaCl 150 mM, pH 8.0) to remove non specifically bound proteins and then elution was performed with a linear or a step-wise gradient of elution buffer (Trizma-Base 25 mM, NaCl 150 mM, Imidazole 500 mM, pH 8.0). A second purification step was performed using Sephacryl S-300 10/60 (GE Healthcare) size exclusion column for multimeric MoPrP AFM constructs or Superdex 200 26/60 HiPrep (GE Healthcare) for monomeric MoPrP AFM constructs. Both columns were equilibrated in washing buffer. Mutant Ins3C MoPrP Tr_{x1} construct was purified as MoPrP Tr_{x1} except that 1 mM DTT was added in each buffer to prevent protein concatenation.
The purification of MoPrP Tr_{x2} H-H was performed with a first step on HisTrap column. The purified protein was allowed to spontaneously dimerize in an oxidizing environment at +4°C for 24-48 hrs. Separation of reaction products was performed by Sephacryl S-300 10/60 size-exclusion chromatography column.

3.3.2 Purification from inclusion bodies

Proteins that were not localized in the supernatant fraction accumulated in inclusion bodies. A common inclusion bodies extraction protocol was developed. The pellet from lysed cells was resuspended in Tris-HCl 25mM, 5mM EDTA, 0.8% Triton X-100, pH 8.0, pelleted again and washed several times with distilled water. Pure inclusion bodies were solubilized 12 hrs at 37°C in 5 volumes of Tris-HCl 25mM GndHCl 8M pH 8.0 and centrifuged 30 min, 10000 g, 4°C to remove bacterial debris.
Solubilized inclusion bodies were loaded on Superdex 200 26/60 HiPrep (GE Healthcare) SEC column equilibrated with washing buffer (Trizma-Base 25 mM, NaCl 150 mM, GndHCl 6 M pH8.0). Refolding and purification was adapted from [275] and achieved in a single step using 5mL HisTrap crude FF (GE Healthcare) nickel affinity column as follows. Protein was loaded on the column equilibrated washing buffer, then a linear gradient of 200 minutes at 1mL/min to refolding buffer (Trizma-Base 25 mM, NaCl 150 mM, pH 8.0) was used to remove guanidine and refold the protein while keeping it attached to the resin. Finally the protein was eluted with a linear gradient with elution buffer (Trizma-Base 25 mM, NaCl 150 mM, Imidazole 500 mM, pH 8.0).
OT proteins inclusion bodies were washed and size-exclusion chromatography was carried out as previously described in this paragraph, except that inclusion body resuspension and SEC equilibration buffers were MOPS 10 mM Urea 8 M NaCl 150 mM DTT 1 mM pH 8.0. After

24 hrs fresh DTT was added to buffers to a final concentration of 1 mM to maintain the reducing environment. A second step of purification was achieved by diluting protein fractions from SEC 1:10 in MOPS 10 mM, Urea 8 M, DTT 1 mM then loading the sample on HiPreP Q FF (GE Healthcare) cation exchange chromatography. Elution was achieved using a linear gradient to equilibration buffer with NaCl 1 M. Fractions containing pure protein were pooled, dialyzed to MilliQ water using 3.5 kDa dialysis membranes (SpectraPore) and finally lyophilized for -80°C storage.

3.4 Sample preparation and characterization

Purified proteins were concentrated using Amicon Ultra 30-50kDa MWCO (Merck-Millipore) tubes until desired concentration and dialyzed with buffer of choice. Typically, AFM experiment storage buffer was Trizma Base 20mM pH7.4 NaN_3 0.05% while that for circular dichroism experiments was Na_2HPO_4/NaH_2PO_4 20mM pH 7.4. or NaOAc 20 mM pH 5.5

3.4.1 Protein refolding

Two milligrams of OT lyophilized samples were resuspended in Trizma-Base 25 mM, GndHCl 6 M DTT 1 mM, pH 8.0. Then a rapid dilution to 0.1 mg/mL in Trizma-Base 25 mM, DTT 1mM pH 8.0 was performed followed by dialysis with 5 L of NaOAc 20 mM, DTT 1 mM pH 5.5. The pellet was separated by centrifugation 50', 2000 g, 4°C. Supernatant was concentrated as previously described.

3.4.2 Protein concentration measurements

Concentration was calculated measuring absorbance at 280 nm with theoretical molar extinction coefficient calculated from ProtParam Tools software (**table 3.5**).

Protein	N° residues	Molecular weight (kDa)	ε_0 ($M^{-1} \times cm^{-1}$)
$GB1_{x4}$	**250**	**27.767**	**40005**
$GB1_{x8}$	**486**	**53.912**	**79885**
$GB1_{x4}$-(MoPrP(89-230))$_{x1}$-$GB1_{x4}$	**631**	**70.423**	**107400**
$GB1_{x4}$-(MoPrP(89-230))$_{x2}$-$GB1_{x4}$	**770**	**86.357**	**134915**
$GB1_{x4}$-(MoPrP(89-230))$_{x3}$-$GB1_{x4}$	**915**	**102.813**	**162430**
$GB1_{x2}$-(MoPrP(89-230))$_{x4}$-$GB1_{x2}$	**824**	**93.125**	**150065**
$GB1_{x4}$-(MoPrP(89-230))$_{x1}$ cys_{231}	**387**	**43.487**	**67395**

Table 3.5 Protein constructs with relative parameters. Parameters were derived from the amino acid sequence. Cysteine residues were assumed to be oxidized.

3.4.3 Protein functionalization

Ins3C $GB1_{x4}$-MoPrP(89-230)-$GB1_{x4}$ protein was dialyzed with Tris-HCl 10 mM TCEP 1 mM pH 7.4, added 10k Mal-PEG (Nanocs) with 1:50 molar ratio and incubated at room temperature for 4 hrs. Excess PEG was removed using Superdex 200 Increase 10/300 GL (GE Healthcare) size-exclusion chromatography.
Optical tweezers MoPrP constructs were activated by reacting with DTDP as previously described [208]: proteins were loaded three times on Zeba Spin Desalting Columns 7 MWCO

(Thermo-Pierce) previously equilibrated with Na_2HPO_4/NaH_2PO_4 100 mM, DTDP 2 mM, Acetonitrile 15% v/v, pH 5.5. Excess DTDP was removed by dialysis with NaOAc 20 mM pH 5.5 and protein was stored at +4°C.
DNA handles 1000 bp long were obtained by PCR from pET11a empty plasmid (amplifying position 1 to 1000) using 5' thiol conjugated primers, purified using QIAGEN Plasmid Maxi kit (QIAGEN), concentrated using Amicon Ultra 10 MWCO devices. Finally DNA handles were stored in buffer Na_2HPO_4/NaH_2PO_4 100 mM, TCEP 1 mM pH 7.4.

3.4.4 SDS-PAGE and Western-blot

Protein purity was assessed by SDS-PAGE gel as well as by Western-blot (WB). Briefly, protein was boiled in loading buffer (Tris-HCl 50 mM, glycerol 10% v/v, SDS 2% w/v, 5 mM DTT, 0.005% bromophenol blue, pH 6.8) and loaded on SDS-PAGE gel with different acrylamide concentration depending on protein molecular weight. Gels were stained 20 minutes with staining buffer (MilliQ water 45 % v/v, methanol 45 % v/v, acetic acid 10% v/v, Comassie Brilliant blue R 0.04% w/v) and destained with destaining buffer (MilliQ water 45 % v/v, methanol 45 % v/v, acetic acid 10% v/v). Images were acquired with ChemiDoc XRS system (BioRad).
Western-blotting (WB) was performed by transferring proteins onto nitrocellulose, blocked with blocking solution (TBST + milk 2% w/v) and incubated o/n at +4°C with primary antibody. Typically, HisProbe-HRP (ThermoScientific) was used for GB1 only constructs and 1 µg/mL anti-PrP Fab D18 (InPro Biotech) for PrP bearing constructs. Membranes were washed with TBST, incubated 45 minutes with secondary antibodies conjugated with HRP, developed using ECL detection reagent (GE Healthcare) and images acquired with digital imaging system Alliance 4.7 (UVITEC).

3.4.5 Circular dichroism

Typically 200 µl of protein samples were loaded inside 0.1 cm quartz cuvettes (Hellma Analytics) and mounted on Jasco J-715 CD spectrometer (Jasco). Spectra of protein samples and blanks were acquired with wavelength intervals between 190 and 260 nm at 20 nm/s scan rate. The resulting spectra were an average of three subsequent scans. Blank subtraction and smoothing using Savitzkey-Golay filter with 25 nm smoothing window, were performed using SpectraManager software (Jasco). Normalized spectra were obtained using Dichroweb software (http://dichroweb.cryst.bbk.ac.uk/html/home.shtml) with CDSSTR 7 or K2D as reference set.

3.5 Protein-protein and protein-DNA interaction

3.5.1 Size-exclusion chromatography

Purified $GB1_{x4}$ and WT MoPrP(89-230) were incubated with a 1:10 molar ratio concentration in Trizma-base 20mM pH7.4 and NaOAc 20 mM pH 5.5 buffer for 1 hour, at room temperature, in protein low-binding tubes (Eppendorf). Samples of 100µl volume were injected in Superdex 200 Increase 10/300 GL (GE Healthcare) column equilibrated in the same protein incubation buffer with NaCl 150 mM.
Fractions were then analyzed by western-blot, developing first using the HisProbe-HRP. Then the membrane was stripped for 4 hrs with TBST + NaN_3 0.05% and developed using Fab D18 antibody

3.5.2 Co-immunoprecipitation

Pure Proteome Protein A Magnetic beads (Millipore) were previously washed with PBS pH 7.4 and then incubated with 102 µl of washing buffer (PBS pH7.4, Tween 20 0.1% v/v) with 10 µl of anti Histidine 6 tag 1:1000 (AbD Serotec) antibody on rotating mixer for 10' at RT. Beads were washed three times with washing buffer and added 500 µl of protein mixture: 0.5 µg of $GB1_{x4}$ and MoPrP were mixed together, while negative controls were prepared without adding $GB1_{x4}$. Protein mixtures were incubated 1 hour at +4°C, removed and washed 3 times with washing buffer. Samples were then loaded on SDS-PAGE gel and WB was developed using Fab D18 antibody.

3.5.3 ELISA

Nunc-Immuno Microwell 96 well solid plates (Falcon) were coated o/n at +4°C with 100µl of WT MoPrP(89-230) or $GB1_{x4}$ proteins in PBS. Wells were then washed five times with PBS and blocked with PBS + milk 2% w/v for 2 hours at room temperature. After washing wells five times with PBS, $GB1_{x4}$ in PBS buffer was added to MoPrP(89-230) coated wells at increasing molar concentrations and incubated for 1 hr at RT. Rinsed with PBS + Tween-20 0.05% v/v, incubated 1 hr with Fab D18 for PrP or anti Histidine 6 tag 1:1000 (AbD Serotec) for $GB1_{x4}$. Secondary antibody goat anti human HRP or rabbit anti mouse AP were used for PrP and GB1 respectively. The former secondary antibody was developed using 2mg/mL p-nitrophenyl phosphate (Thermo-Scientific) in developing buffer (Tris-HCl 100 mM, MgCl 5 mM, NaCl 100 mM, pH 9.2) while the latter with 3,3',5,5'-tetramethylbenzidine (Sigma) and stopped with 100µl 0.16 M H_2SO_4. Plates were read on Spectramax M5 (Molecular Devices) at 405 nm and 450 nm wavelengths respectively.

3.5.4 Electrophoretic mobility shift assay

DNA handles were incubated with increasing stoichiometric amounts of wild type MoPrP(89-230) and MoPrP(23-230) for 1 hr at RT in buffer Hepes 10 mM, KCl 500 mM, $MgCl_2$ 5 mM pH 7.4. Samples were loaded on agarose 1% w/v gel with 2 µl ethidium bromide and checked DNA migration. dsDNA used will be the handles for OT experiments.

3.6 Single-molecule force spectroscopy

Constant velocity mechanical unfolding experiments were performed with a Veeco Picoforce AFM on a Multimode Nanoscope IIIa (Bruker) equipped with PicoForce 196 PF (Bruker) piezo-stage. Gold-coated triangular silicon nitride cantilevers (NPG, Bruker) with nominal spring constants of 0.06 N/m were used. The effective spring constant was determined for each of them by their thermal noise spectrum [276]. All the experiments were carried out at room temperature, with an estimated fluid-cell temperature of 28°C.

3.6.1 Sample preparation

Ten microliters of protein specimen were deposited for 30 minutes on a flame-cleaned glass coverslip or freshly peeled TSG surface and mounted on a fluid cell. The buffers used were Trizma-base 20 mM pH 7.4, Trizma-base 20 mM NaCl 150 mM pH 7.4, NaOAc 20 mM pH 5.5 and NaOAc 20 mM pH 4.0. A double inlet device was used to switch from neutral to acidic buffer, directly inside the fluid cell in the case of experiments with pH lower than 7.4.

3.6.2 Unfolding experiments

Velocity-clamp experiments were carried out by iterating approach/retraction cycles of the tip (**figure 3.4**) with fixed 500 nm ramp and 10 nm push on the surface. Protein sample concentration was usually 0.5-7 μM. Pulling velocities were 2180, 4360 and 8720 nm/s in order to compare results with previous studies [299, 300]. Typically ~30-100k curves were obtained from each experimental setup but, on the average, only 0.03% of them normally could be associated to an interpretable FEC and therefore only these were considered and analyzed.

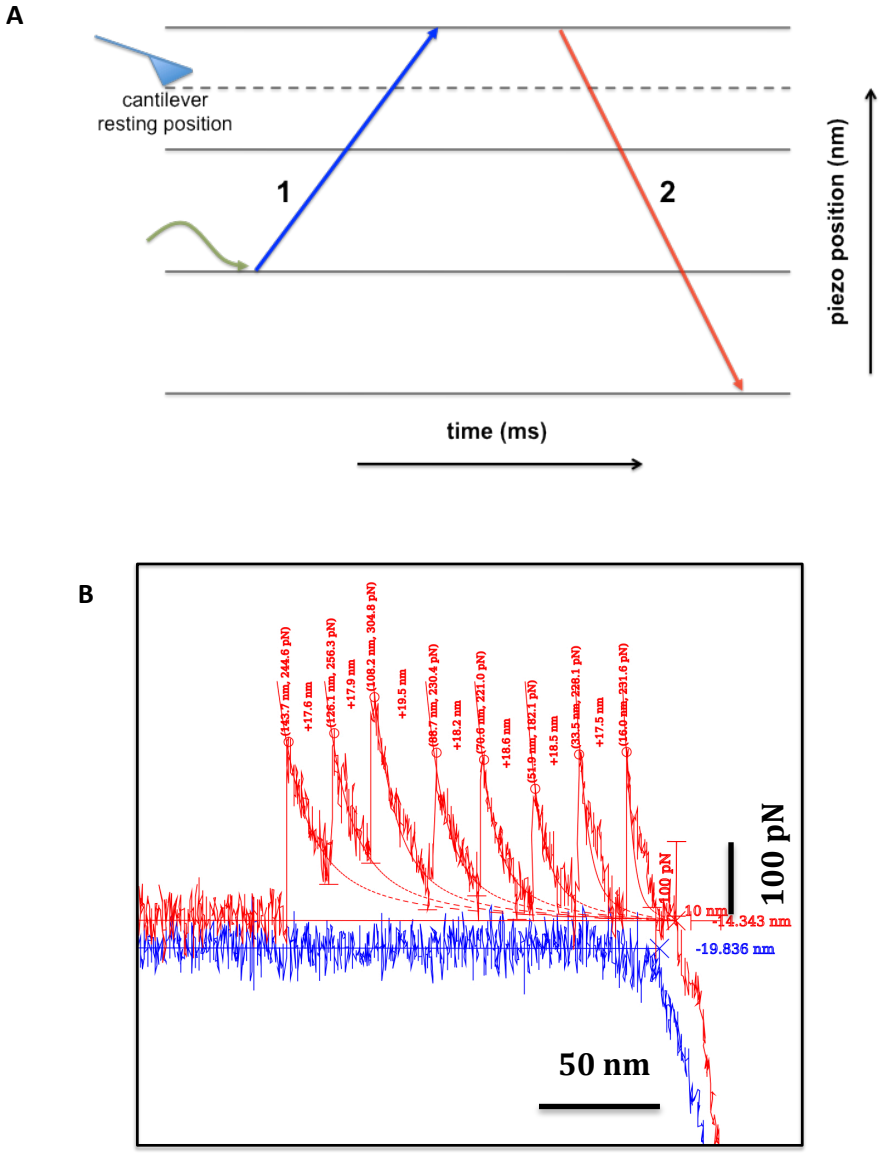

Figure 3.4 Constant velocity unfolding experiments scheme. (**A**) representation of piezo-electric actuator position over time. (**B**) Example of unfolding curve. Colours in panel A of piezo-electric stage movements correspond to traces in panel B. During step 1 the piezo was approached to the cantilever until it pushed onto it for a predetermined distance and time. During step 2 the piezo retracted from the surface and started pulling the molecule. Eight peaks resulting from unfolding events are present. Each peak is fitted with WLC model and the Δ_{cl} is showed. The contact point in the approach and retraction traces is indicated by a blue and a red cross respectively. The blue/red line starting from the contact point indicates the baseline.

3.6.3 Double-pulse refolding experiments

Double-pulse refolding experiments (**figure 3.5**) were performed using in-house developed software [277] in conjunction with Nanoscope v6 software. Experimental ramping parameters were set according to the theoretical length of protein constructs, using crystallographic contour length of an amino acid L_c^{aa} = 0.36 nm/aa [243], as shown in **table 3.6**. A fixed fetch distance was chosen in order to be sure that the MoPrP domain/s within the fetched molecules were stretched.
A refolding time of 50 ms was chosen because it is sufficient to refold all GB1 domains [256] and to refold alfa-helix rich proteins [7]. Refolding took place at ~5-10 nm distance from the surface. Retraction velocity for fetch and break-away traces was set at 2180 nm/s whereas the velocity for the refolding approach trace was set at 8720 nm/s. Protein sample concentration was 10-15µM, to increase the probability of protein fetching. Usually 10-30k curves were obtained from each experimental setup, with an average efficiency of ~0.008%.

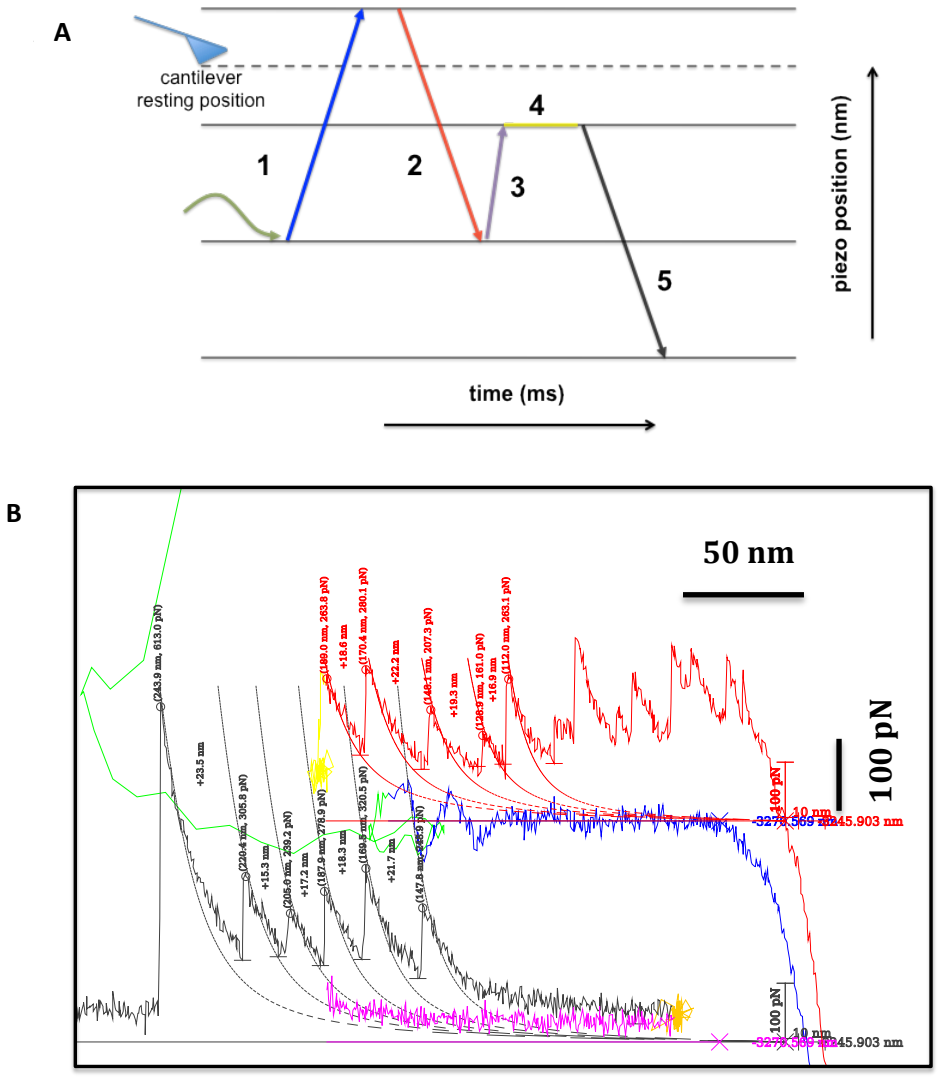

Figure 3.5 Double-pulse refolding scheme. (**A**) Piezo position over time. (**B**) Example of double-pulse refolding curve, the two pulses are separated for clarity. Colors in panel A of piezo movements and curves in panel B are the same. During step 1 the piezo was approached to the cantilever until it pushed onto it for a predetermined distance and for a predetermined time. During step 2 the piezo moved back faster to a predetermined position to unfold but not to detach the molecule (*fetch*). On step 3 the piezo moved near to the cantilever without touching it, lowering the force and allowing the fetched protein to refold for a given time 4. Then in step 5 it moves away from the tip stretching the molecule and detaching it from the tip (*break away*). It is possible to notice that non-specific interaction is absent in the *break away* trace.

3.6.4 Multi-pulse refolding experiments

Multi-pulse refolding experiments were performed using a home-built software as in the previous paragraph. Initially, molecules were picked and stretched to a fixed length indicated in **table 3.6** ("*fetch*" curve, **figure 3.6 B**). Subsequently 10 approach/retraction cycles were performed to unfold and refold the tethered molecule ("*refold*" curves, **figure 3.6 C**). This step was iterated up to six times, each time the extension was increased by 10 nm only if the force of the last peak was lower than 500 pN. Finally, the protein was detached from the tip/surface with a 1 µm retraction ramp ("*loose*" curve, **figure 3.6 D**). Retraction velocity for *fetch*, *refolding* and *loose* curves was set at 2180 nm/s, while velocity for refolding approach trace at 8720 nm/s. Protein sample concentration was ~20 µM, as to increase the probability of protein fetching. Usually 2-6k curves were obtained from each experimental setup, with an average efficiency of 0.00014%.

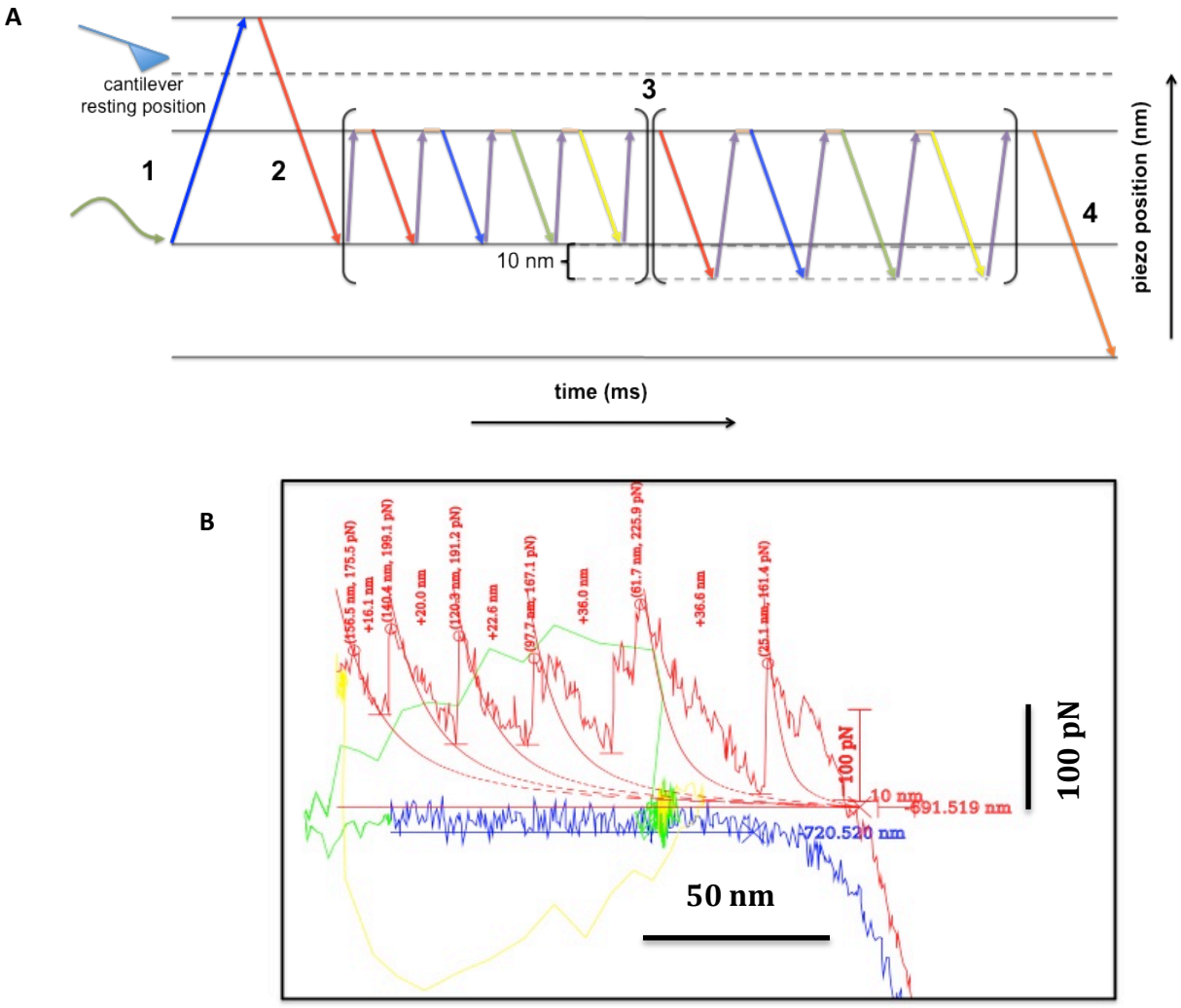

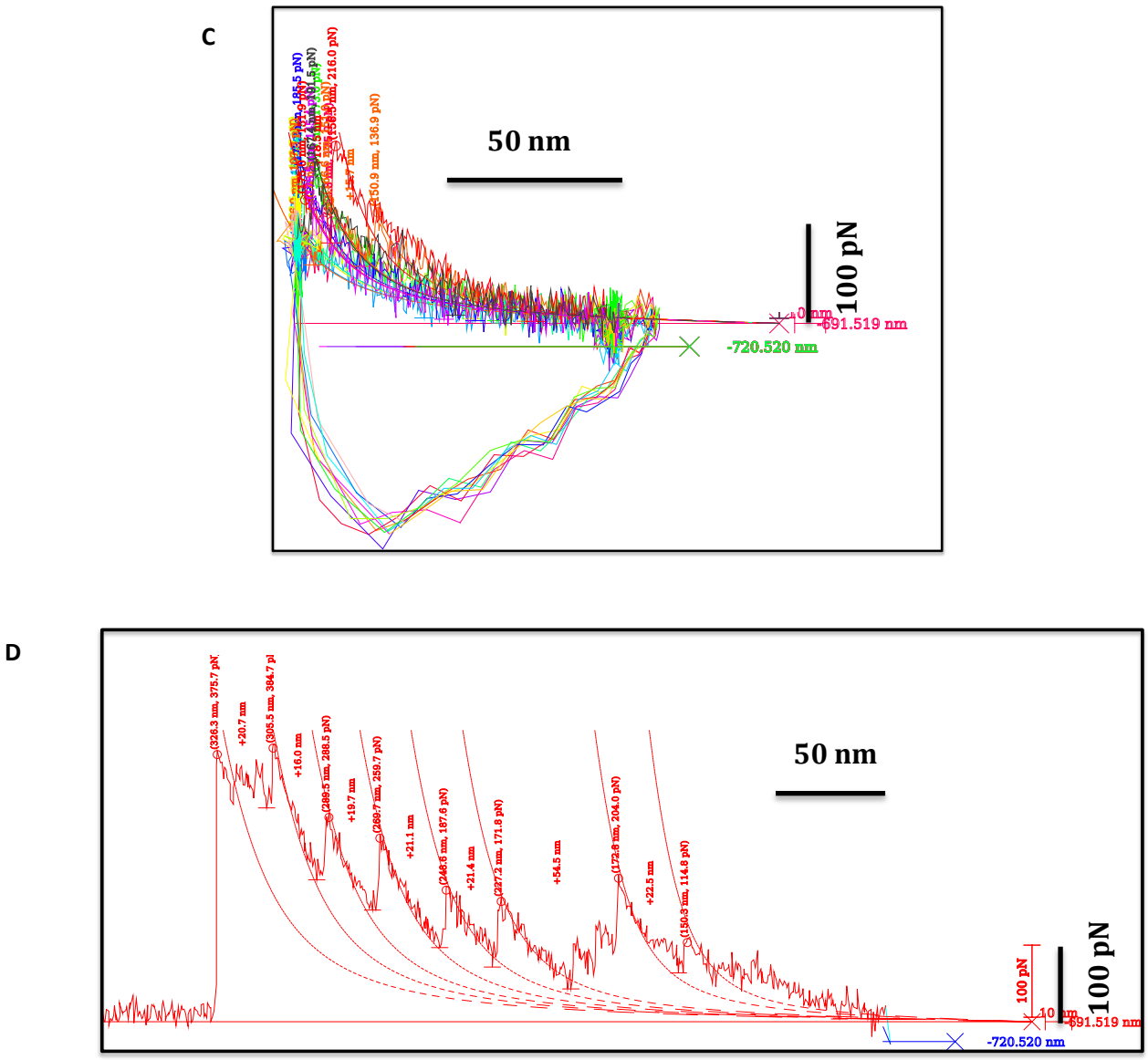

Figure 3.6 Multi-pulse refolding scheme. (**A**) Piezo position over time. (**B**) *fetch* curve; (**C**) *refolding* curve; (**D**) *loose* curve. Colours in panel A of piezo movements and curves in panel B, C, D are the same. Step 1 and 2 are identical to the double-pulse refolding. On step 3 the piezo moved repeatedly 10 times from the refolding position to the fetching position (*refold*). This cycle was iterated N times and each time the fetching position was increased of 10 nm only if the last peak force was lower than 500 pN. In step 4 the piezo stage moves away from the tip, fully stretching the molecule and detaching it from the tip (*loose*).

3.7 Data analysis

Curve filtering and peak fitting was performed by in-house developed software [277]. Briefly, curve peaks were fitted using the Worm Like Chain (WLC) model [229]:

$$F = \frac{k_b T}{p}\left(\frac{x}{L} + \frac{1}{4}\left(1 - \frac{x}{L}\right)^{-2} - \frac{1}{4}\right)$$

where k_b is Boltzman constant, T is temperature and L is contour length and p is the persistence length. In our studies we set p = 0.4 nm. We considered 1 nm spatial sensitivity, as

result of an overestimation by a factor of two the sum of the experimental error and WLC fitting.
Curves were first selected automatically on the basis of the three parameters reported in **table 3.6**. The first is the minimum and maximum number of unfolded GB1 modules (*n*) in the retraction trace, sufficient to claim that also the MoPrP moiety/ies in the construct was/were stretched:

$$\frac{M}{2}+1 \le n \le M$$

where M is the number of GB1 modules on the construct polypeptide chain.
The other two parameters are the maximum and minimum length of the fetched molecules, depending on *n*, in retraction traces. Selection was performed in the retraction trace for unfolding experiment, whereas for double-pulse and multi-pulse refolding curves the selection was applied on the *break away* and *refolding* traces respectively.
A second round of manual selection was carried out as to save only FEC that were unequivocally related to single-molecule stretching events with the typical sawtooth pattern and with low or absent non-specific interaction. WLC peak fitting adjustment was performed where needed, outside the non-specific interaction region. Delta contour length (Δ_{cl}) and force values of every peak from FEC where used for subsequent analysis.

Protein	*n*	Min. molecule length (nm)	Max. molecule length (nm)
$GB1_{x8}$	**5/8**	**110.52**	**174.96**
$GB1_{x4}$-$(MoPrP(89-230))_{x1}$-$GB1_{x4}$	**5/8**	**150.48**	**214.92**
$GB1_{x4}$-$(MoPrP(89-230))_{x2}$ H-T-$GB1_{x4}$	**5/8**	**185.38**	**254.88**
$GB1_{x4}$-$(MoPrP(89-230))_{x2}$ H-H-$GB1_{x4}$	**5/8**	**185.38**	**258.48**
$GB1_{x4}$-$(MoPrP(89-230))_{x3}$-$GB1_{x4}$	**5/8**	**225.26**	**294.84**
$GB1_{x2}$-$(MoPrP(89-230))_{x4}$-$GB1_{x2}$	**3/4**	**222.84**	**247.68**

Table 3.6 Molecule fetching and selection parameters. Fetching curves of double and multi-pulse refolding were set as the minimum molecule length. A variable error of 5-20 nm (depending on the individual experiment) was introduced due to the presence of protein layer on the surface. These parameters were used also for curve selection. Cysteine residues were assumed to be oxidized.

Analysis of force and Δ_{cl} distributions were performed using custom made software in Matlab R2012b (Mathworks). Specifically, Δ_{cl} distributions were fitted automatically with Kernel density estimator, while gaussian mixture distribution was performed using a curve fitting tool. Statistical analysis of length intervals was performed using standard bidimensional boxplots, calculating median values and interquartile ranges (IQR) between the first and third quartile. Bootstrapping was performed where indicated, by generating hypothetical randomized data sets with the same size of target data set; this procedure was repeated 500 times calculating mean and standard deviation of relative intervals values.

Part III: Results and discussion

4.1 Cloning, expression, purification and characterization of $GB1_{x4}$ and $GB1_{x8}$ constructs

In our studies we decided to take advantage of the heteropolymeric protein approach [246,249,258,263] to investigate structural properties of MoPrP(89-230) using AFM single-molecule force spectroscopy. We used streptococcal protein G domain B1 as a mechanical fingerprint and to build up a protein-handle flanking the MoPrP moieties under investigation.
pQE-80L::$GB1_{x8}$ was obtained as indicated in **paragraph 3.1** by using pQE-80L::$GB1_{x4}$ as the starting cloning vector. BglII and BamHI restriction enzymes produced 5' overhanging filaments that were complementary and their ligation generated a BstI restriction site, leaving the Bgl II and Bam HI sites at the 3' and 5' termini of the gene. Enzymatic cleavage of resulting clones using BglII and BamHI restriction enzymes was used to check if concatenation of two $Gb1_{x4}$ DNA sequences occurred (see **figure 4.1**).

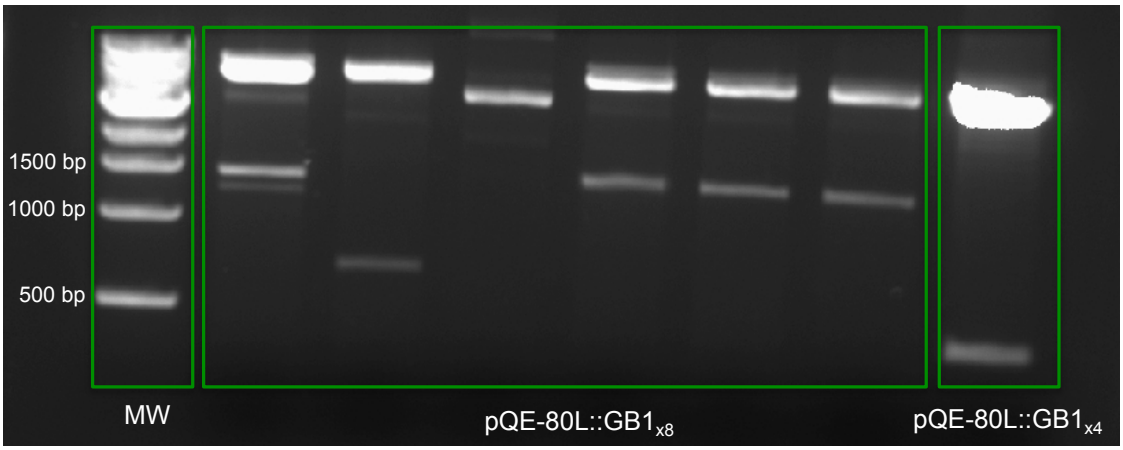

Figure 4.1: Agarose 1% gel of double enzymatic digestion of pQE-80L::$GB1_{x8}$ positive clones; on the right the control using pQE-80L::$GB1_{x4}$. The positive clones show a band at 1440 bp.

Orientation of insertion in the positive clones was checked by sequencing. Expression of both constructs was achieved by adapting to a previous protocol [256]. Bacterial cells were induced at ~0.5-0.6 $O.D_{600nm}$ with 1mM IPTG and grown at 37°C o/n. After cell disruption, both proteins were localized in the soluble fraction, and purification was carried out under native conditions. The first step of purification was achieved using Ni^{2+}-affinity columns (**figure 4.2**) which yielded a large amount of protein Major contaminants included lower molecular weight protein bands and a band at twice the theoretical molecular weight of the protein construct. The latter was likely due to dimerization of the construct by C-terminal cysteine residues. A second step of purification was carried out by size exclusion chromatography (**figure 4.3**) which increased the purity of $GB1_{x4}$ and $GB1_{x8}$ to ~97% and ~94%, respectively.
Circular dichroism data showed that both proteins had a typical α-β spectra (**figure 4.4**), comparable to previous studies [278]. Normalized spectra of the two proteins were not superimposable, with an intensity of ~2000 deg×cm^2/dmol (208 nm wavelength) lower for the octameric construct.

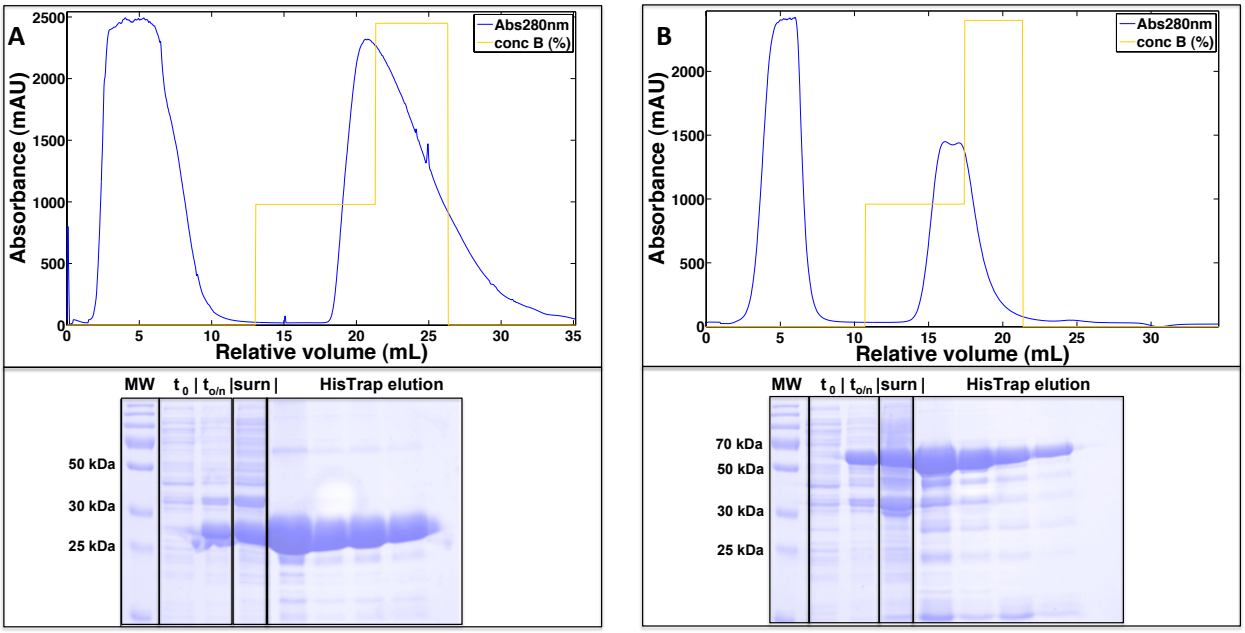

Figure 4.2: Top panel: HisTrap chromatography of (**A**) $GB1_{x4}$ and (**B**) $GB1_{x8}$. Bottom panel: SDS-PAGE 12% gel of t_0 and $t_{o/n}$ LB culture of $GB1_{x4}$ and $GB1_{x8}$, supernatant fraction and HisTrap elution fractions.

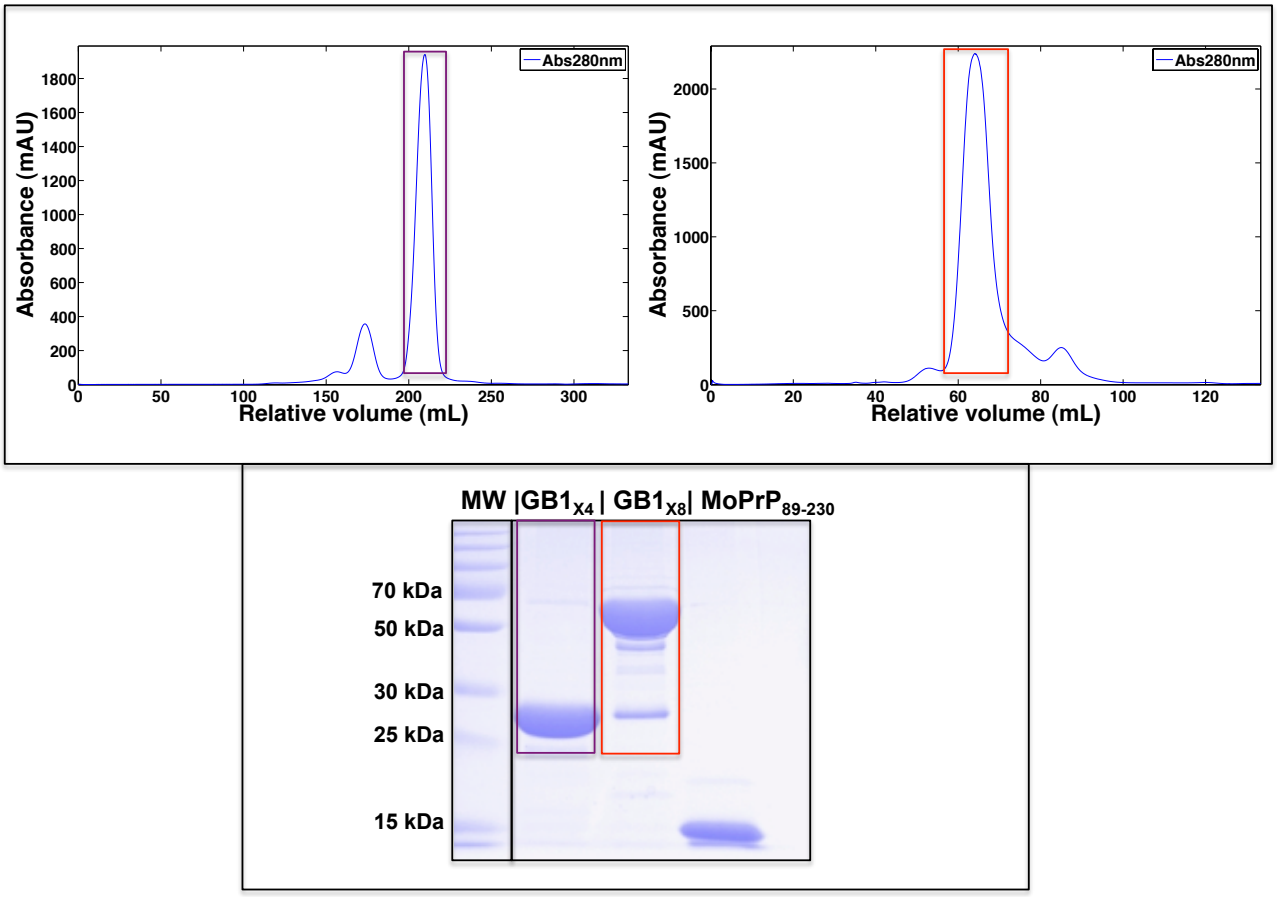

Figure 4.3: Top panel: HisTrap chromatography of (**A**) $GB1_{x4}$ and (**B**) $GB1_{x8}$. Bottom panel: SDS-PAGE 12% gel of t_0 and $t_{o/n}$ LB culture of $GB1_{x4}$ and $GB1_{x8}$, supernatant fraction and HisTrap elution fractions.

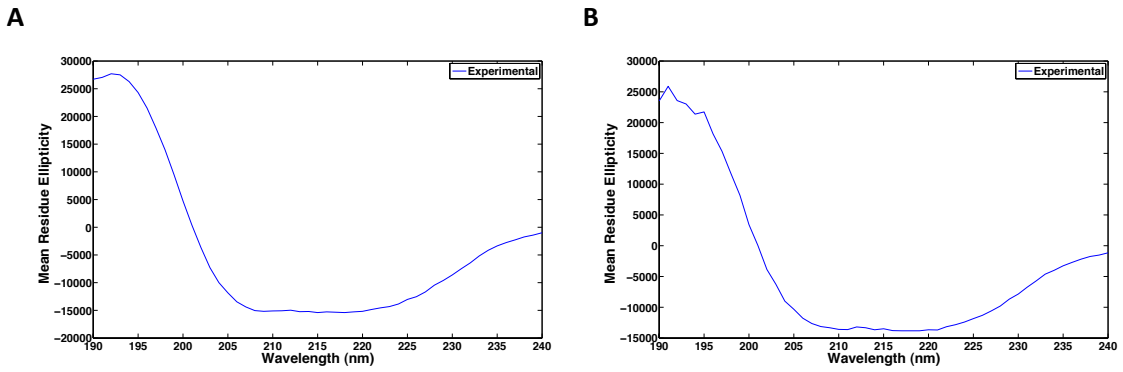

Figure 4.4: Normalized Far-UV CD spectra of (**A**) $GB1_{x4}$ and (**B**) $GB1_{x8}$ in $Na_2HPO^{4-}/NaH_2PO^{4-}$ 20 mM pH 7.4.

4.2 Expression and purification of MoPrP Tr_{x1}, MoPrP Tr_{x2}H-T and MoPrP Tr_{x3}

Since expression of truncated recombinant PrP in *E. coli* cells usually results in the accumulation of the recombinant protein in inclusion bodies, it is necessary to purify the protein under denaturing conditions [274,279]. Strikingly, the MoPrP Tr_{x1} recombinant protein was localized only in the soluble fraction and not in the inclusion bodies, suggesting that flanking the prion protein with GB1 domains increased the solubility of the fusion protein. This behaviour was previously described for other insoluble proteins [280,281]. Previous work done by Dr. Federico Benetti and Eleonora Carboni showed that the 73 kDa band was immunoreactive toward Fab-D18 and Anti His_6 tag antibodies, showing that MoPrP(89-230) moiety was present. Protein purification was carried out under native conditions. Major contaminants were lower molecular weight products recognized by His_6 tag antibody, suggesting premature translation ending of the protein or low mRNA stability [282].

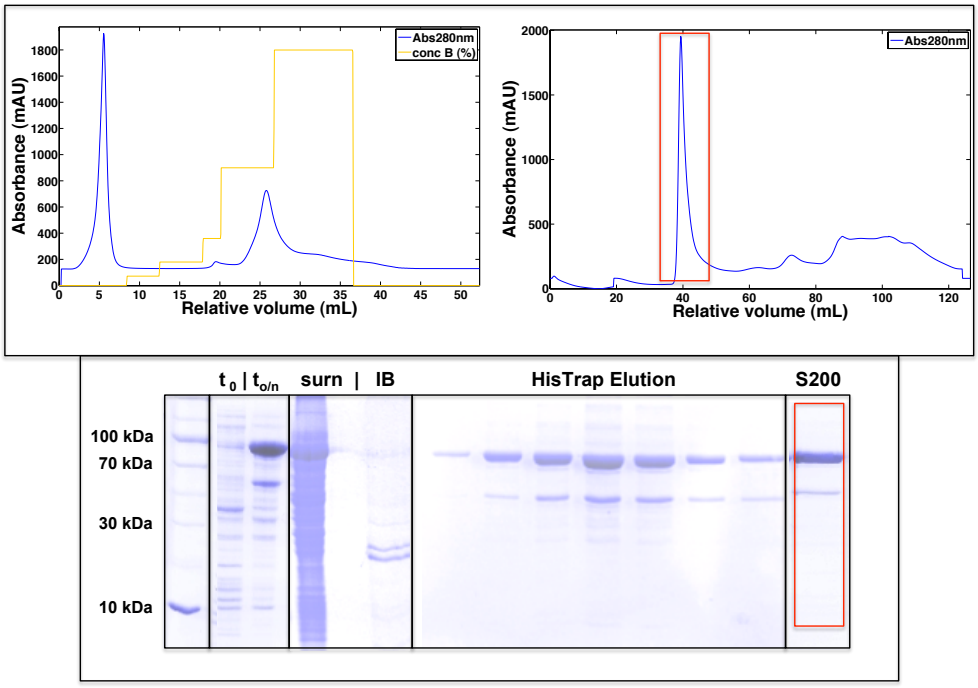

Figure 4.5: Top panel: HisTrap chromatography on the left and HiPrep S300 16/60 on the right of MoPrP Tr_{x1}. Bottom panel: SDS-PAGE showing expression of the protein construct and its localization in the soluble fraction, as well as protein purification steps.

During size-exclusion chromatography, the recombinant protein eluted at void volume, probably due to its non-globular shape (**figure 4.5**). SDS-PAGE gel of the corresponding peak revealed a protein purity of ~90%. Purification of MoPrP TR_{x1}-PEG performed with the same protocol under reducing conditions, reacted with PEG and unreacted molecules were separated with size-exclusion chromatography.
Since low molecular weight contaminants were still able to bind to the Ni^{2+}-affinity column, for the multimeric MoPrP constructs the His_6 tag was placed on the C-terminus. In case premature translation occurred, only the complete translated molecules would have had the tag.

Expression trials on dimeric MoPrP Tr_{x2} H-T and trimeric MoPrP Tr_{x3} were carried out in order to find the best conditions that resulted in high over-expression (**figure 4.6**). Protein expression was then performed in 250 ml LB-medium flasks.

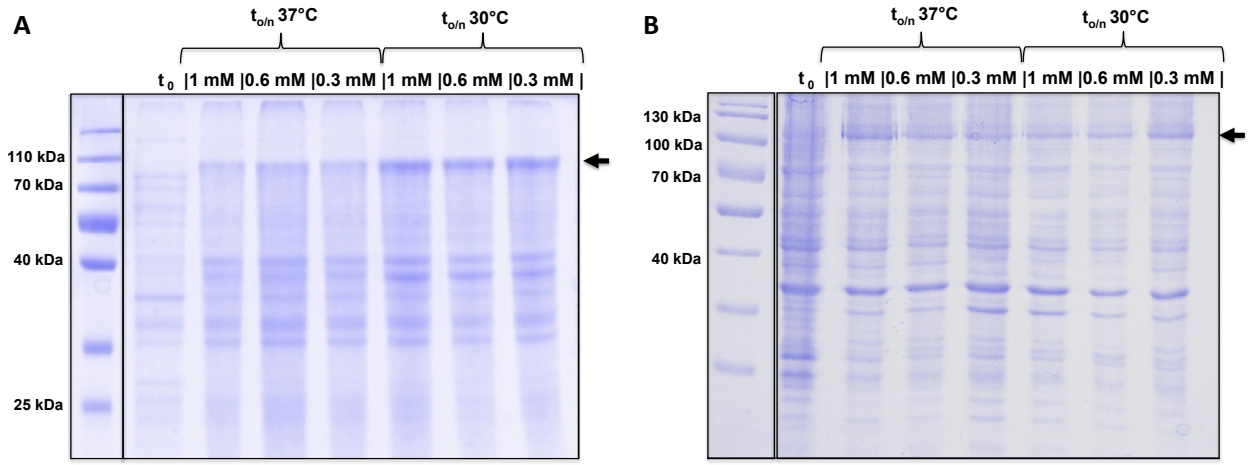

Figure 4.6: Expression trials at different temperatures and different IPTG concentrations of (**A**) MoPrP Tr_{x2} H-T and (**B**) MoPrP Tr_{x3}. Arrows indicate the appearance of the protein band after induction, respect to t_0.

In both cases the protein was localized in the supernatant fraction and native purification was performed, similarly to MoPrP Tr_{x1}. During affinity chromatography lower molecular weight products were still present but during the second step of purification they were removed. Both proteins in size-exclusion chromatography eluted in two different fractions. One at void volume (~ 41 ml) and one at retention volume of ~ 60 ml and ~ 62 ml for MoPrP Tr_{x2} H-T (**figure 4.7**) and MoPrP Tr_{x3} (**figure 4.8**) respectively. No clear difference between these two fractions on SDS-PAGE was detected. Nevertheless, circular dichroism experiments were carried out on both fractions of MoPrP Tr_{x3} revealing no differences in the overall fold (**figure 4.10**).

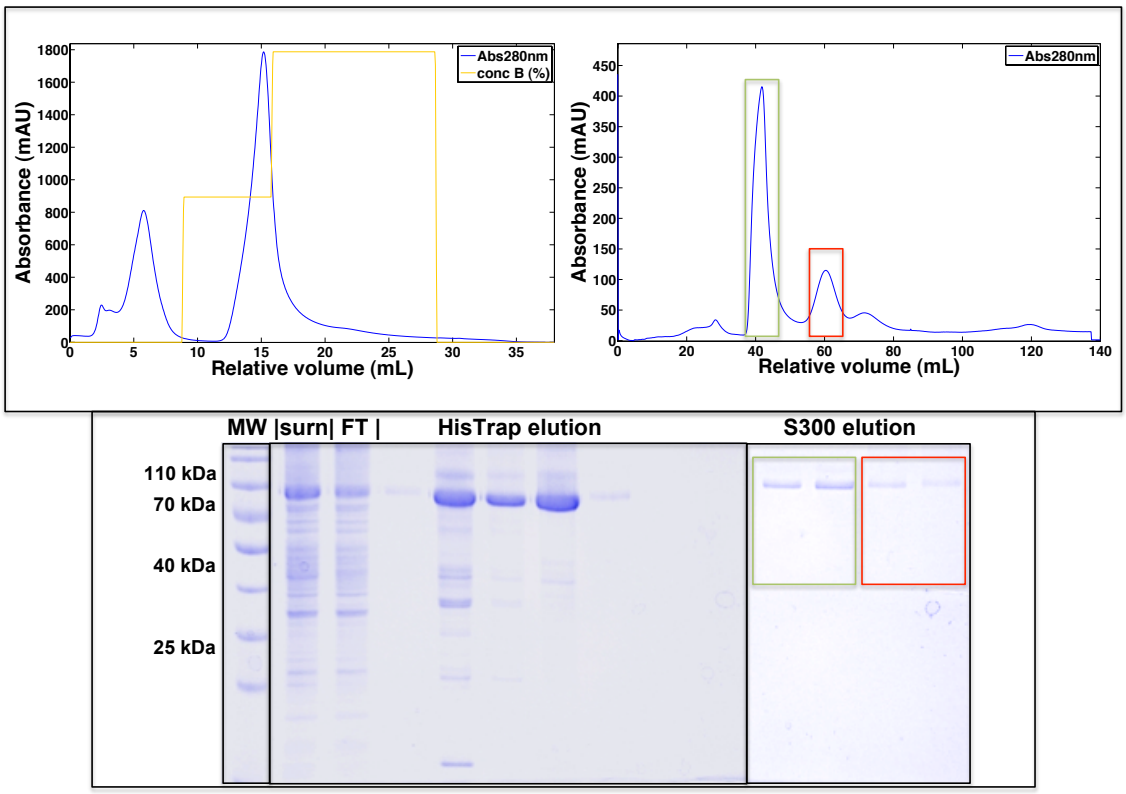

Figure 4.7: On top panel HisTrap chromatography on the left and HiPrep S300 16/60 on the right of MoPrP Tr_{x2}. On bottom panel SDS-PAGE showing expression of the protein construct, its localization in the soluble fraction and purification steps; the green and red box refers to the elution peaks of size-exclusion chromatography.

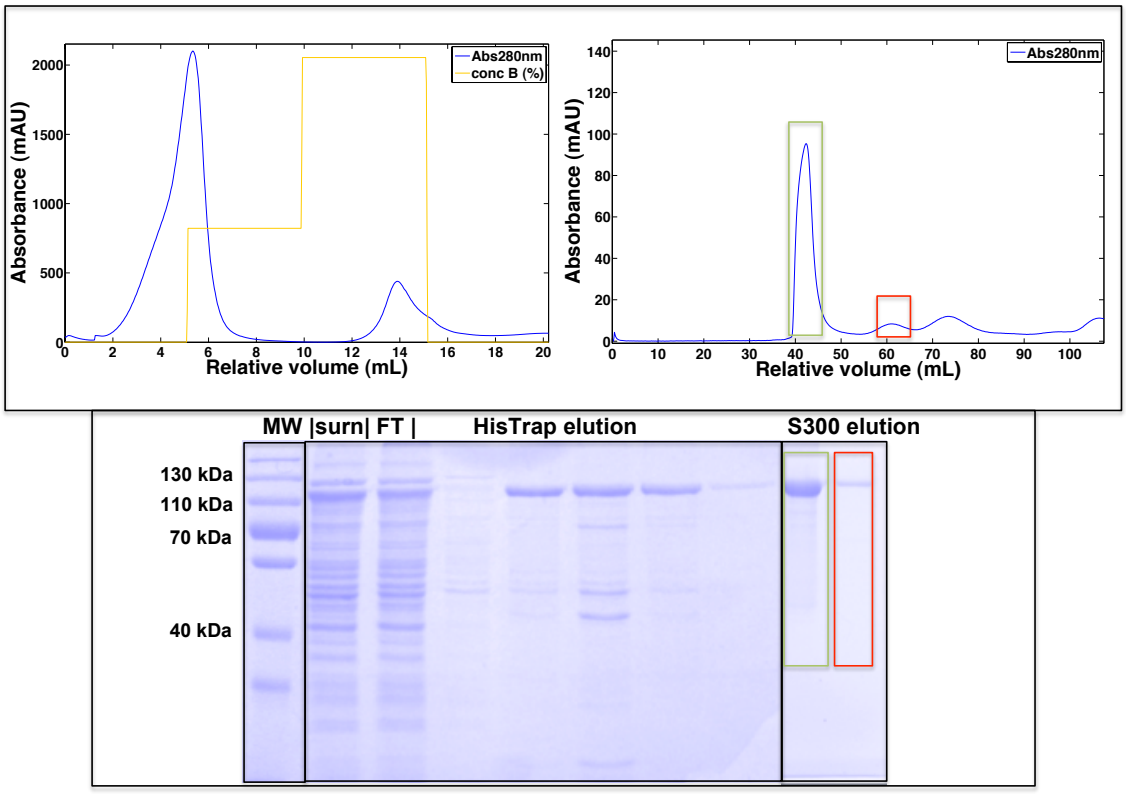

Figure 4.8: On top panel HisTrap chromatography on the left and HiPrep S300 16/60 on the right of MoPrP Tr_{x3}. On bottom panel SDS-PAGE showing expression of the protein construct and its localization in the soluble fraction, as well as protein purification steps; the green and red box refers to the elution peaks of size-exclusion chromatography.

Protein purity of MoPrP Tr_{x2} H-T and MoPrP Tr_{x3} was assessed by SDS-PAGE and WB (**figure 4.9**) and it was estimated ~ 90%.

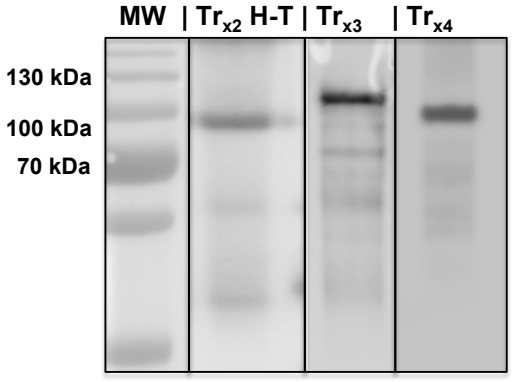

Figure 4.9: Western blot of purified samples of MoPrP Tr_{x2}H-T, MoPrP Tr_{x3} and MoPrP Tr_{x4} using Fab D18 antibody.

Circular dichroism spectra of the three constructs showed that both proteins were structured with similar secondary structure contents (**figure 4.10**).

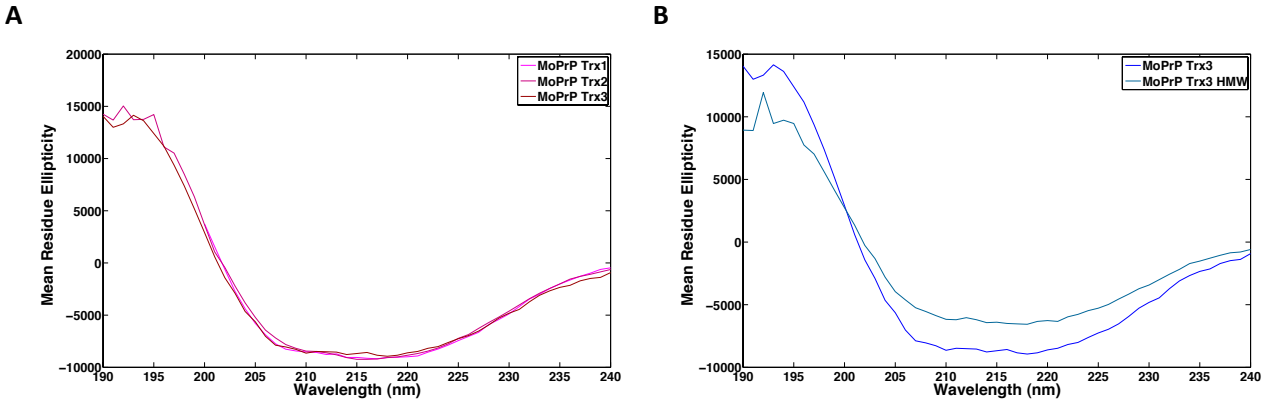

Figure 4.9: Normalized Far-UV CD spectra acquired in phosphate buffer 20 mM, pH7.4. (**A**) Overlay of MoPrP Tr_{x1}, MoPrP Tr_{x2}H-T, MoPrP Tr_{x3}. (**B**) Overlay between MoPrP Tr_{x3} from 60 ml (MoPrP Tr_{x3}) and 40 ml (MoPrP Tr_{x3} HMW) peaks: the latter shows similar secondary structure content but lower MRE.

4.3 Expression, purification and assembly of MoPrP Tr_{x2} with Head-to-Head orientation

The dimeric MoPrP construct with the two C-terminal globular domains facing each other (MoPrP Tr_{x2}H-H) was obtained by purification of Ins231C GB1x4-$(MoPrP(89\text{-}230))_{x1}$ protein. Ins231C GB1x4-$(MoPrP(89\text{-}230))_{x1}$ over-expression was checked under different growth temperature and IPTG concentrations. Protein was initially purified by affinity chromatography (**figure 4.11**): two bands at 44 kDa and ~90 kDa were present in the eluate, presumably the monomer and the homo-dimer respectively.

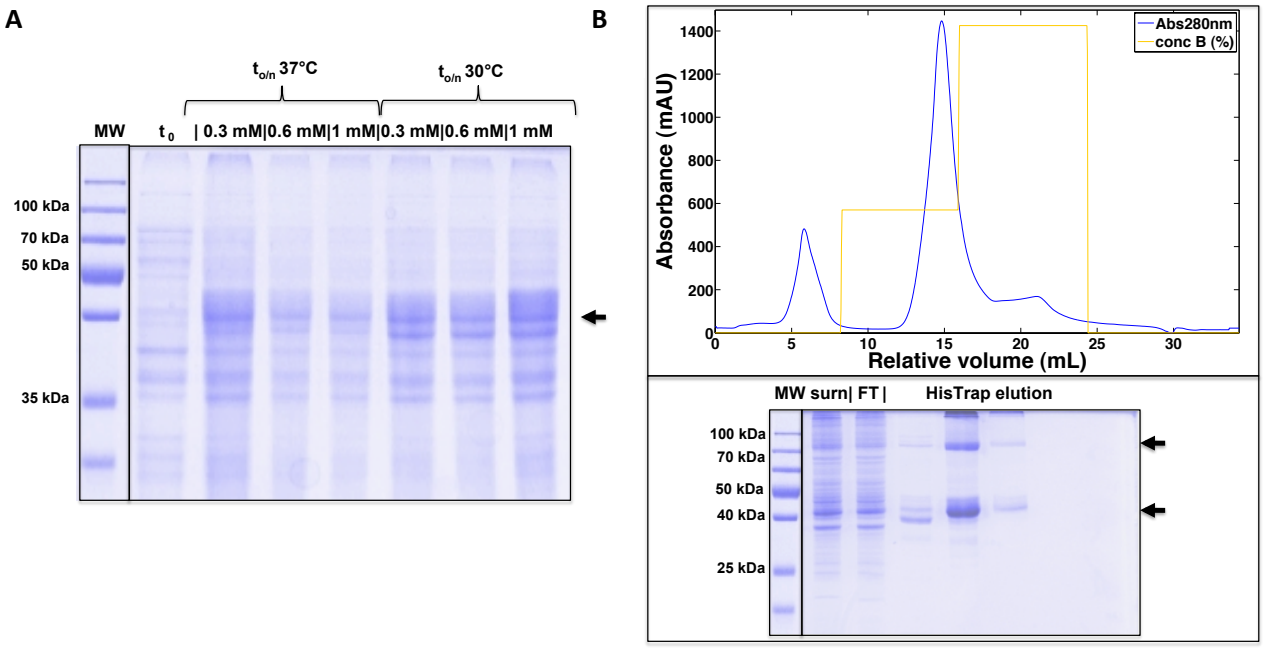

Figure 4.11: (**A**) Expression trials of Ins231C GB1x4-(MoPrP(89-230))$_{x1}$. (**B**) HisTrap chromatography of soluble fraction of induced bacteria, the arrows indicate the monomer and the dimer.

After the first purification passage, the protein was left oxidizing spontaneously, then products of the reaction were separated depending on their size (**figure 4.12, A**). Three species eluted from the column at void volume, at 60 ml and at 75 ml respectively. On SDS-PAGE the first peak showed two bands corresponding to the theoretical MW of unreacted monomer and dimer respectively. The second showed only a band of the protein dimer. The third peak presented unreacted monomer and small amounts of dimer.

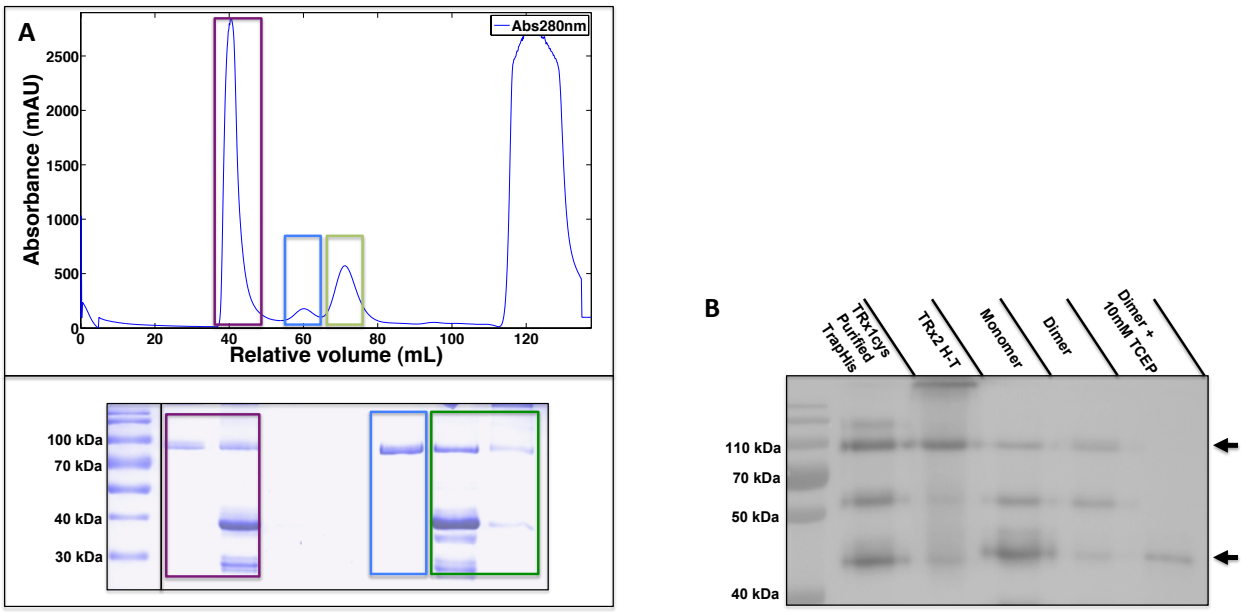

Figure 4.12: (**A**) Purification of oxidized Ins231C GB1$_{x4}$-(MoPrP(89-230))$_{x1}$ and corresponding SDS-PAGE: the colored boxes reflect the chromatographic fractions. (**B**) WB of Ins231C GB1$_{x4}$-(MoPrP(89-230))$_{x1}$ after S300 purification: in presence of excess TCEP, the dimer (upper arrow) reverted to unreacted monomer (lower arrow).

Fractions from relative elution peaks were analyzed on WB with Fab D18 antibody confirming the presence of MoPrP moiety. Incubating the purified dimer with reducing agents resulted in the appearance of the monomer band only, indicating that the disulfide bridge between two monomeric molecules was disrupted (**figure 4.12, B**). The overall yield of the purification was very low (0.06 µg/L culture). CD spectra were acquired from the unreacted monomer and dimer (**figure 4.13**). Secondary structure contents were similar to MoPrP Tr_{x1}, MoPrP Tr_{x2} H-T and MoPrP Tr_{x4} protein constructs.

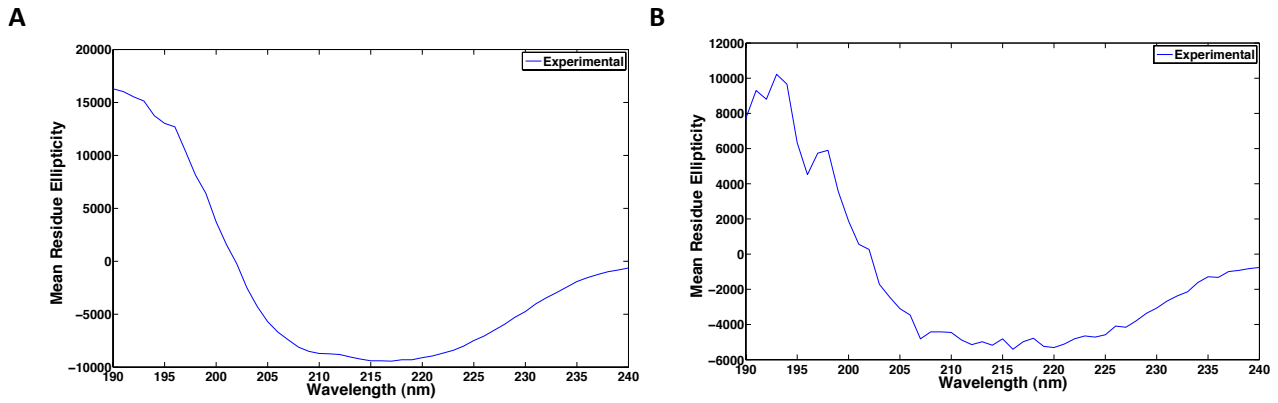

Figure 4.13: Normalized far-UV CD spectra acquired in phosphate buffer 20 mM, pH7.4. (**A**) Unreacted monomer of $GB1_{x4}$-$(MoPrP(89\text{-}230))_{x1}$cys231. (**B**) MoPrP Tr_{x2}H-H spectra: the scattered signal was due to the low concentration of the protein sample.

4.4 Expression and purification of MoPrP Tr_{x4}

Since very large proteins (>100 kDa) are poorly expressed in *E. coli* cells, the construct containing four tandem copies of MoPrP(89-230) was flanked only by two GB1 domains. It has been shown that such number of marker domain was still sufficient for correct identification of molecules in AFM SMFS [227].
Expression trials and fermentation were carried out in Zym5052 autoinduction medium: unlike previous discussed proteins, MoPrP Tr_{x4} expression always led to the accumulation of the recombinant protein in inclusion bodies (**figure 4.14, A**). Purification was performed under non-native conditions with size-exclusion as first step (**figure 4.14, B**) and refolding/purification with affinity chromatography as second step (**figure 4.14, C**). The advantage of using on-column refolding was reducing molecular crowding by binding protein molecules to the resin, giving them enough time to refold autonomously.
Interestingly the purified protein showed a strong pH-dependence solubility. Aliquots of 100µl MoPrP Trx4 were dialyzed with four different buffers (Tris 20 mM pH 7.4, Tris 20 mM pH 6.5, NaOAc 20 mM pH 5.5 and NaOAc 20 mM pH 4.0). Samples were centrifuged and the pellet was resuspended in Loading Buffer 1X Urea 8M, while the supernatant was lyophilized and resuspended in the same buffer. Samples were analyzed on SDS-PAGE (**figure 4.16**). At neutral pH the protein was completely soluble, while decreasing pH to 5.5 diminished its solubility as protein aggregated and precipitated. At pH 4.5 the protein maintained its solubility similarly to neutral pH. Protein purity was very high (~97%) and the MoPrP moiety presence was confirmed by WB (**figure 4.9**).
Analysis of the secondary structure content revealed that protein is folded similarly to the other heteropolymeric protein constructs (**figure 4.15**)

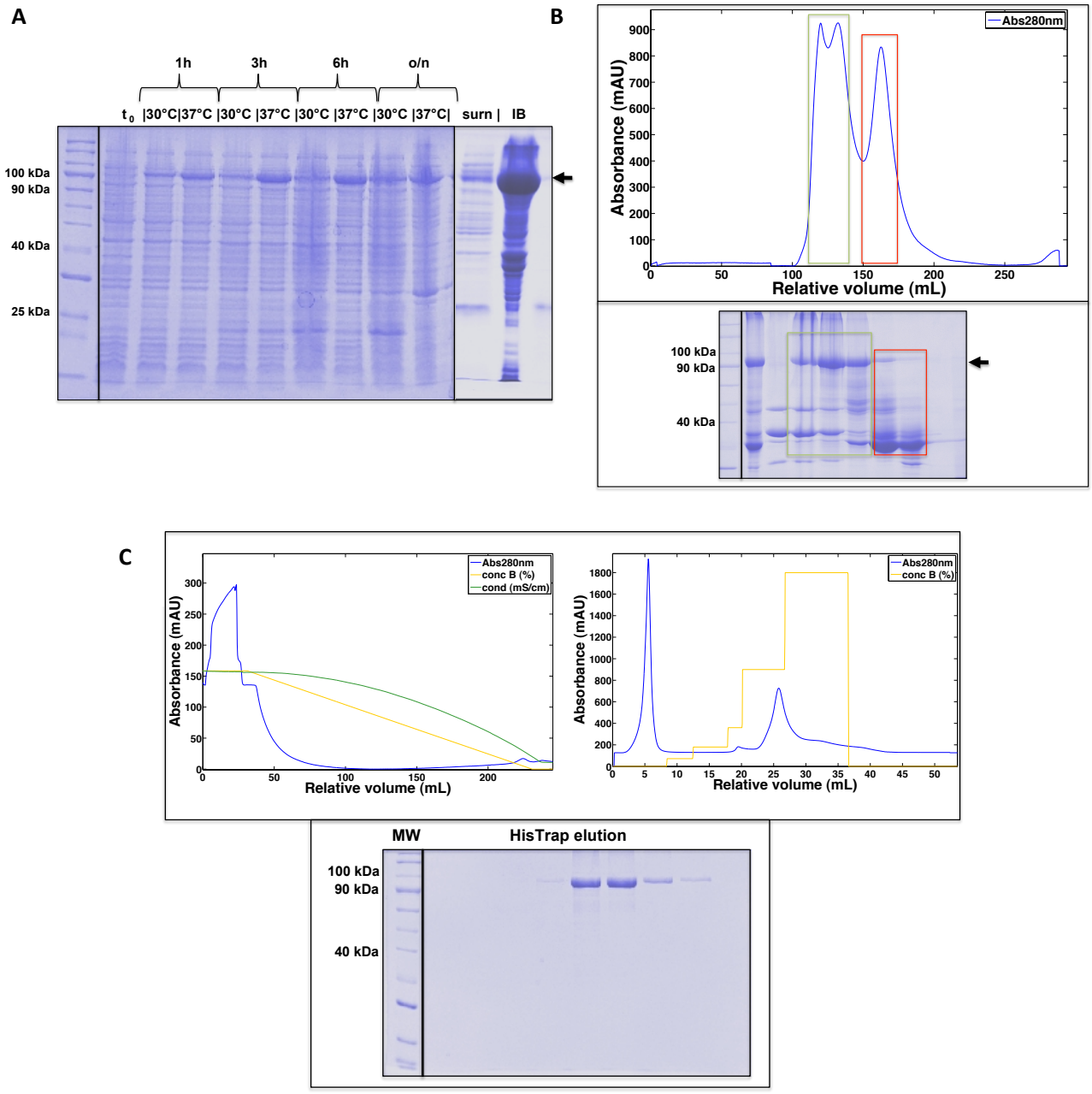

Figure 4.14: (**A**) Expression trials of MoPrP Tr_{x4} at different times and temperature, on the right supernatant and inclusion bodies (IB) of lysed bacteria culture. (**B**) HiLoad S200 HiPrep of solubilized inclusion bodies and relative SDS-PAGE of highlighted fractions. (**C**) On the top left panel loading and refolding by linear gradient of MoPrP Tr_{x4}, on top right elution of the refolded protein and relative SDS-PAGE gel on the bottom panel.

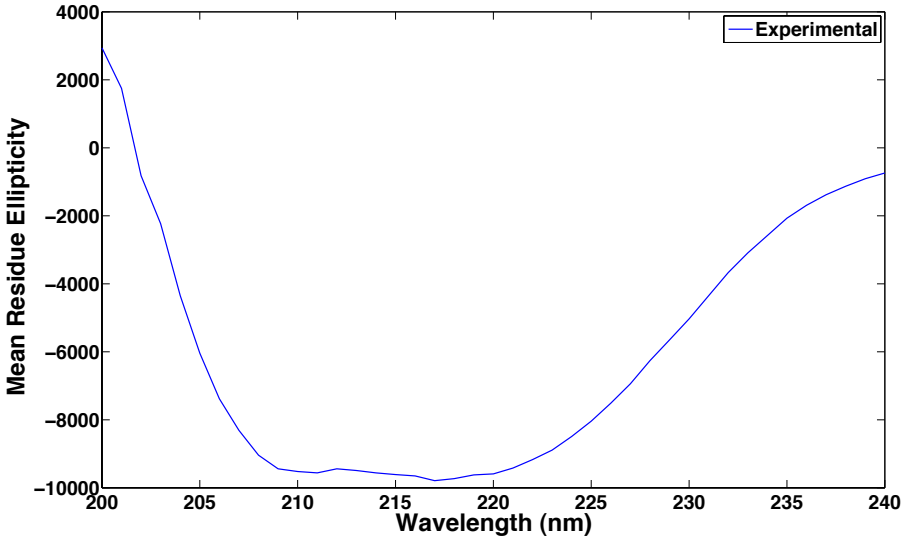

Figure 4.15: Normalized far-UV CD spectra of MoPrP Tr_{x4} shows a αβ mixed structure similar to previous purified proteins.

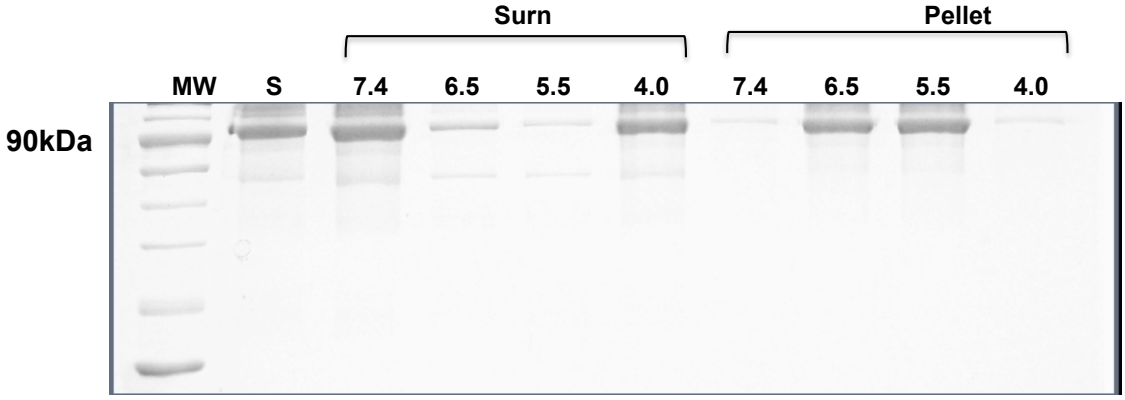

Figure 4.16: MoPrP Tr_{x4} solubility at different pH values. Marker (MW), protein sample at pH 8.0 (S). Surnatant (Surn) and unsoluble fraction (Pellet) from buffer exchange at different pH values are loaded.

4.5 Expression and purification of MoPrP for optical tweezers

Expression of MoPrP(89-230) cys92, cys229 and $MoPrP_{23\text{-}230}$ cys25, cys229 was carried out in 10L of Zym5052 auto-induction medium. Purification was performed starting from recombinant protein in the inclusion bodies using a first step of size-exclusion, followed by cation exchange chromatography (**figure 4.17**). Reducing conditions were critical to obtain a monomeric protein, which spontaneously dimerized via terminal cysteine residues in absence of DTT, generating high-molecular weight products. Protein purity was very high (~ 97%) even if some multimers could be detected by WB even in presence of reducing agents.
Proteins were refolded under reducing conditions and reacted with DTDP, therefore analysis of secondary structure content was necessary to prove that refolding occurred correctly (**figure 4.18**). After refolding and DTDP reaction, both proteins showed a typical α-helical structure, like respective WT proteins.

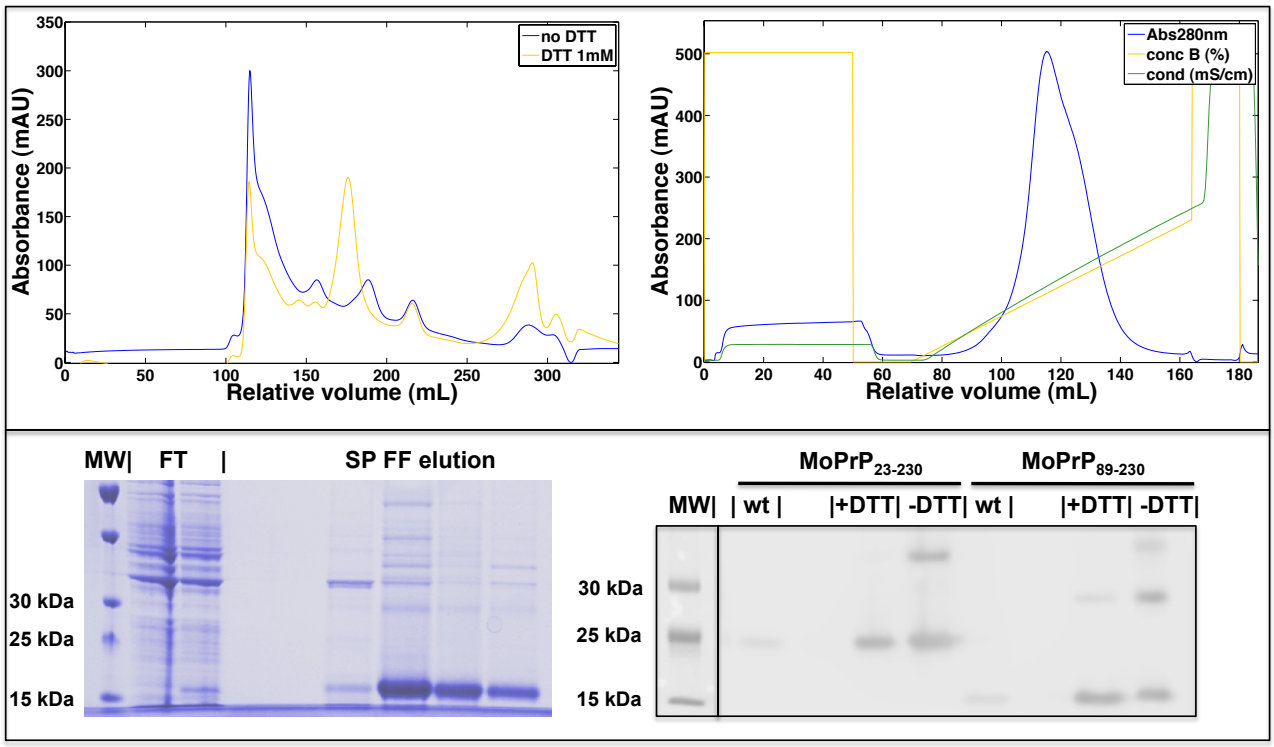

Figure 4.17: On top left panel HiLoad S200 26/60 column loaded with inclusion bodies, the blue trace shows the chromatogram without DTT in equilibration buffer, the yellow trace with DTT 1mM in equilibration buffer: notice the presence of a peak at ~170 ml typical of WT MoPrP; on top right panel HiLoad SP FF column loading and elution of MoPrP(89-230) cys92,cys229 from previous size-exclusion step. On bottom panel on the left SDS-PAGE relative to the cation exchange column: it is possible to notice several bands of multimers above the theoretical MW of truncated MoPrP; on the right WB with purified samples: wild type (wt), double cysteine construct with DTT (+DTT) and without DTT (-DTT).

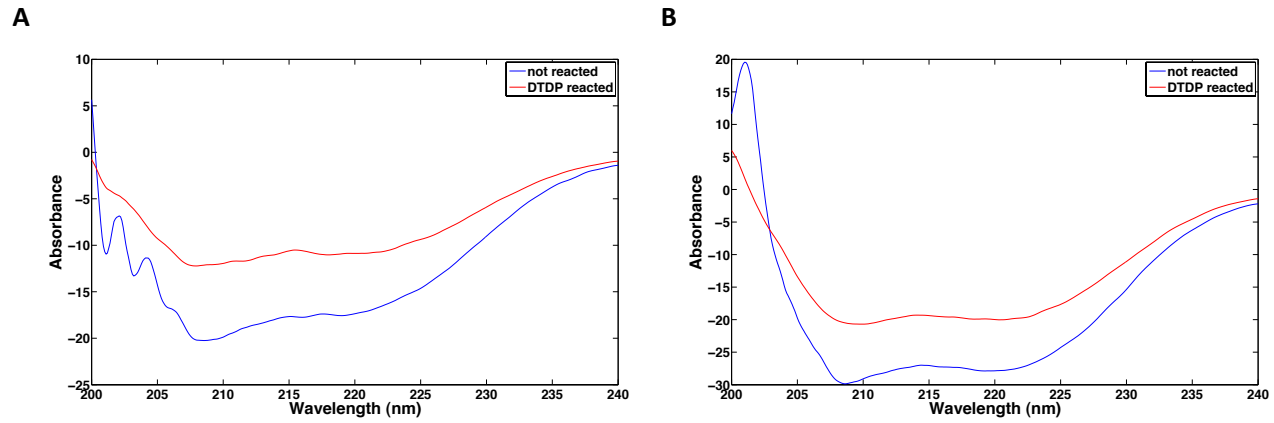

Figure 4.18: Far-UV CD spectra of (**A**) MoPrP(89-230) cys92,229 and (**B**) MoPrP(23-230) cys25,229 after refolding in reducing conditions (not reacted) and after DTDP reaction (DTDP reacted) of the same sample. After DTDP reaction absorbance diminished due to partial protein precipitation.

4.6 Protein-protein and DNA-protein interaction experiments

Different sets of experiments were carried out in order to identify possible interactions between MoPrP proteins and their corresponding handles for AFM (GB1 domains) and OT (dsDNA) .

4.6.1 Interaction analyses of MoPrP(89-230) with GB1

Initially co-immunoprecipitation experiments were performed by immunoprecipitating $GB1_{x4}$ incubated with MoPrP(89-230) and developing using Fab D18 antibody. Results showed that full-length seems to immunoprecipitate with the bacterial protein domain, while a faint band was detectable for the truncated form (**figure 4.19**). A band was detected when GB1 was not incubated with the prion protein and GB1 positive control without IP, indicating that the protein was able to bind secondary antibody Fc region. The same band was present in the full-length sample incubated with GB1, but it could not be detected in the truncated one.

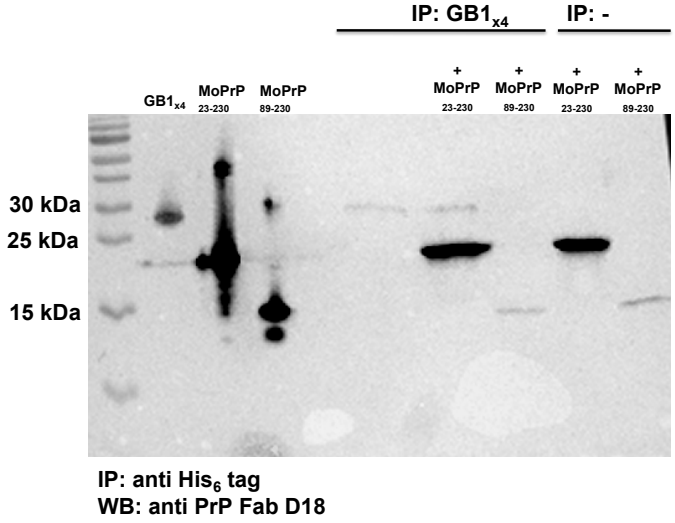

Figure 4.19: western blot developed with Fab D18 antibody. First three lanes were loaded with recombinant proteins only, immunoprecipitated samples GB1, GB1 and MoPrP(23-230) and GB1 and MoPrP(89-230); in the last two lanes negative controls are loaded.

ELISA experiments were performed by adsorbing truncated MoPrP on the wells. $GB1_{x4}$ was then added to the wells and developed using Anti His_6 tag antibody. Results showed that incubating MoPrP(89-230) with different increasing concentrations of GB1 did not result in significant increases in alkaline phosphatase signal (**figure 4.20**).

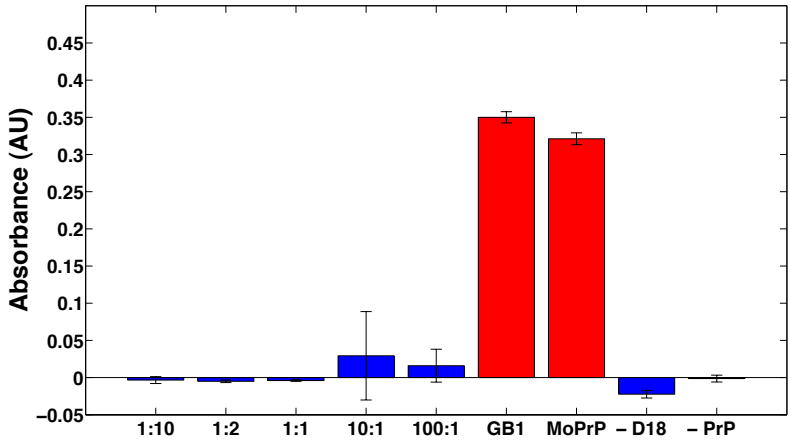

Figure 4.20: in blue the samples with increasing molar concentrations of $GB1_{x4}$, in red the two positive controls for PrP and $GB1_{x4}$; in magenta the negative controls without PrP coating (-D18) and PrP coating with Anti Histag (- αHis).

Non-equilibrium "small zone" [283] size-exclusion chromatography experiments were performed to check protein interactions without antibody related techniques. Firstly $GB1_{x4}$ construct only was loaded on the column and eluted with two peaks corresponding to the monomeric (15 ml) and the dimeric form (13 ml) (**figure 4.21**). Loading MoPrP(89-230) only resulted in appearance of a major elution peak at 18ml and a smaller peak at 15 mL. Incubating MoPrP(89-230) and $GB1_{x4}$ in a 10:1 stoichiometry at pH 7.4 significantly increased the 13 ml GB1 elution peak intensity (**figure 4.21**). Analyzing these fractions by western blot did not reveal the presence of MoPrP, suggesting that the peak was due to $GB1_{x4}$ terminal cysteine dimer. At pH 5.5 the 13 mL GB1 peak was still present even though it was less pronounced.

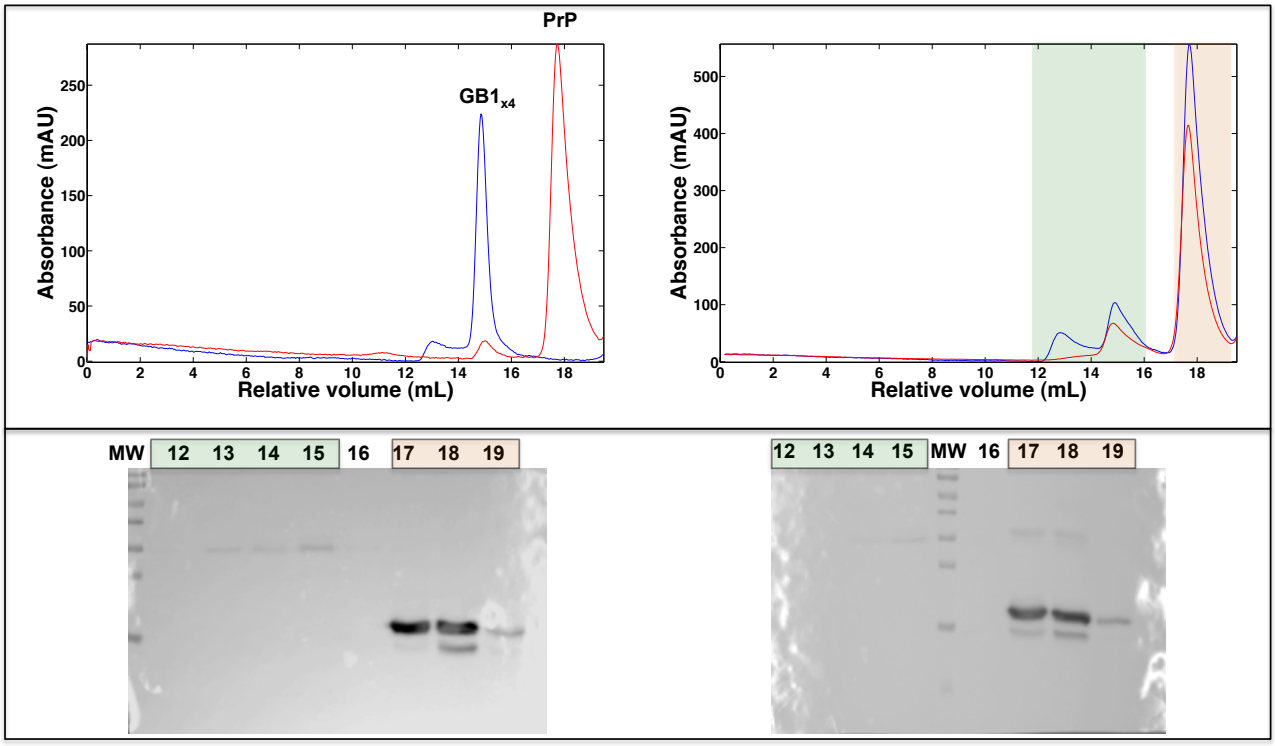

Figure 4.21: On top left panel S200 Increase 10/300 GL of $GB1_{x4}$ (blue trace) and MoPrP(89-230) (red trace) only, while on the right both protein mixed in 1:4 proportion at pH 7.4 (blue trace) and pH 5.5 (red trace); on bottom panel two WB of the two chromatographic experiments: numbers are referred to relative volume fractions, which are highlighted in green and orange for simplification. It is possible to notice that PrP is not present in GB1 fractions.

4.6.2 Interaction analyses of MoPrP(89-230) with dsDNA

Analysis of interaction between DNA and MoPrP for optical tweezers experiments was performed. EMSA experiments (**figure 4.22**) did not reveal any significant electrophoretic shift of the dsDNA handle band incubated with truncated recombinant PrP, while a small shift occurred with the full-length at 20:1 molar concentration ratio.

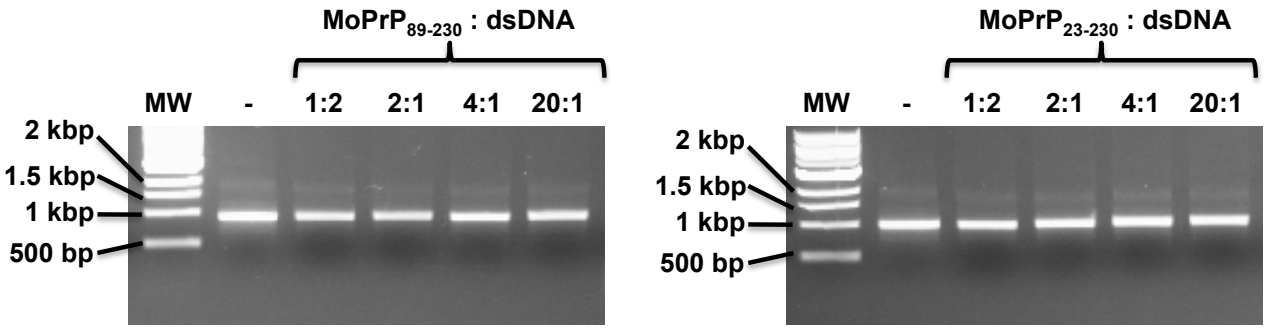

Figure 4.22: agarose 1% gel of MoPrP mixed with dsDNA OT handles: handles as negative control (-) and mixture proportions indicated as MoPrP:handle molar concentrations. Since the handles exposed a thiol group at 5', dimers could be observed at ~ 2 kbp.

5.1 SMFS experiments on $GB1_{x8}$ reference system

First of all analysis of GB1 fingerprint domain polyprotein was achieved, in order to compare data from literature and confirm the robustness of our system. Simple unfolding experiments were performed at three different pH: neutral (7.4), acidic (5.5) and highly acidic (4.0). Typical sawtooth pattern curves were obtained (**figure 5.1, A**) where every peak corresponds to a single GB1 domain unfolding event from a single molecule. Peaks were characterized by a typical exponential increase of the force, followed by a sudden drop to near to zero values at lower extensions. Not all the force-extension curves (FEC) showed a final peak with forces typical of covalent bond breakage (500 pN – 2nN), nevertheless, such curves where included in the analysis. Noticeably, some FEC showed more than eight GB1 unfolding events (up to fifteen) suggesting the presence of dimers, probably due to C-terminal cysteine oxidation events, which were not detected in protein preparation (**paragraph 4.1**). Fitting the overall events with a single gaussian distribution, showed a mean Δ_{cl} = 18.3 ± 1.4 nm with an average force F = 226.25 ± 45.85 pN at a loading rate of 2180 nm/s (**figure 5.2**). These values fit those reported in the literature for a two-state native-to-unfolding transition of the GB1 domain [256,284,285].

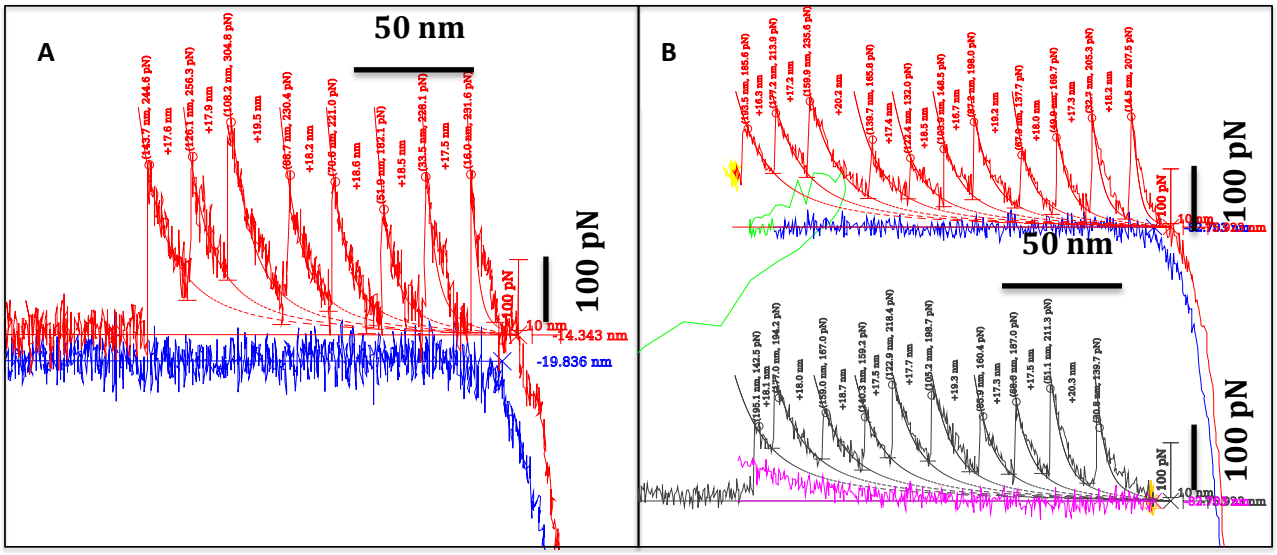

Figure 5.1: (**A**) Typical $GB1_{x8}$ FEC obtained from unfolding experiments. (**B**) FEC from double-pulse experiments on a $GB1_{x8}$ sample: the two superimposable unfolding pulses in red and black are separated for clarity.

Even if the majority of GB1 unfolding events were found inside a well-defined interval of contour length, some spurious events at different Δ_{cl} were detected. More in detail, events in the intervals between 0-15 nm, 23-30 nm and > 30 nm showed a frequency of 3.8%, 1.6% and 0.1% respectively. This data indicated that every unfolding event inside 15 to 23 nm range can be safely associated to a GB1 unfolding event.
No significant differences were found between experiments at three different pH in terms of Δ_{cl} distribution, average unfolding force and spurious events located outside the GB1 $\Delta_{cl\ N->U}$ window.

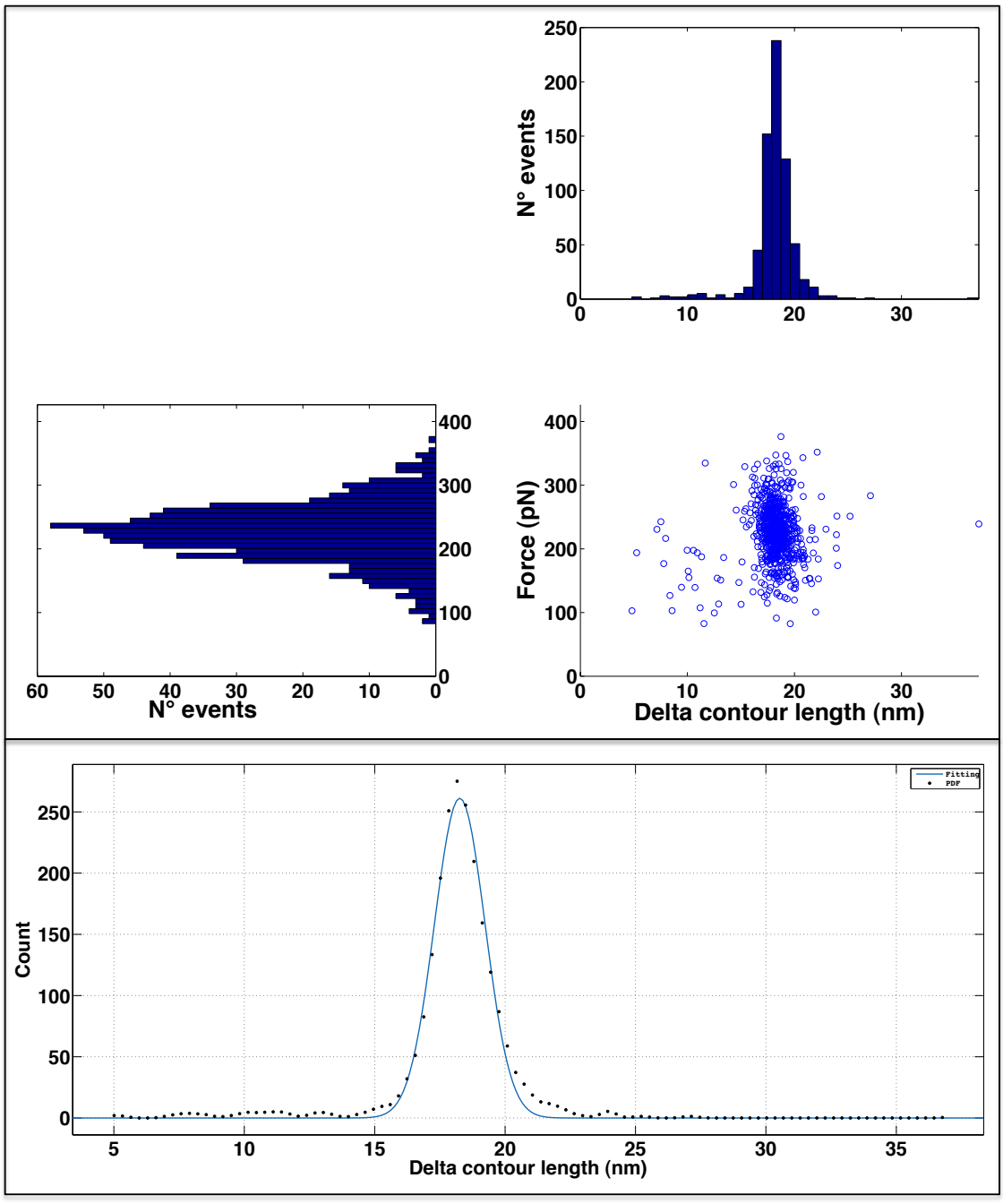

Figure 5.2: on top scatterplot from unfolding experiments carried out at pH 7.4. On bottom, fitting with one gaussian distribution of the PDF function calculated on Δ_{cl} experimental data; RMSD = 0.9903.

Double-pulse refolding experiments showed that GB1 domains were able to refold after 50 ms of refolding time, as indicated by the appearance of peaks during the second pulse that were

perfectly superposable to the first unfolding pulse (**figure 5.1, B**). Even if a small number of curves were obtained, all unfolding events had a length between 15 and 23 nm interval. This was confirmed using multi-pulse refolding experiments. Therefore in refolding experiments, unfolding peaks shorter than 15 nm and longer than 23 nm were not associated to GB1 unfolding events.

5.2 SMFS experiments on MoPrP Tr_{x1}

Unfolding experiments of MoPrP Tr_{x1} at three different pH were characterized by FEC (**figure 5.3**) with typical GB1 unfolding events with Δ_{cl} = 18 ± 1.7 nm and F = 208.56 ± 52.13 pN. Unlike the $GB1_{x8}$ construct, a higher frequency of rupture events with delta contour lengths between 23 and 30 nm (23.8%) and between 30 and 39 nm (3%) was observed. FEC with such rupture events showed only one peak with these lengths.

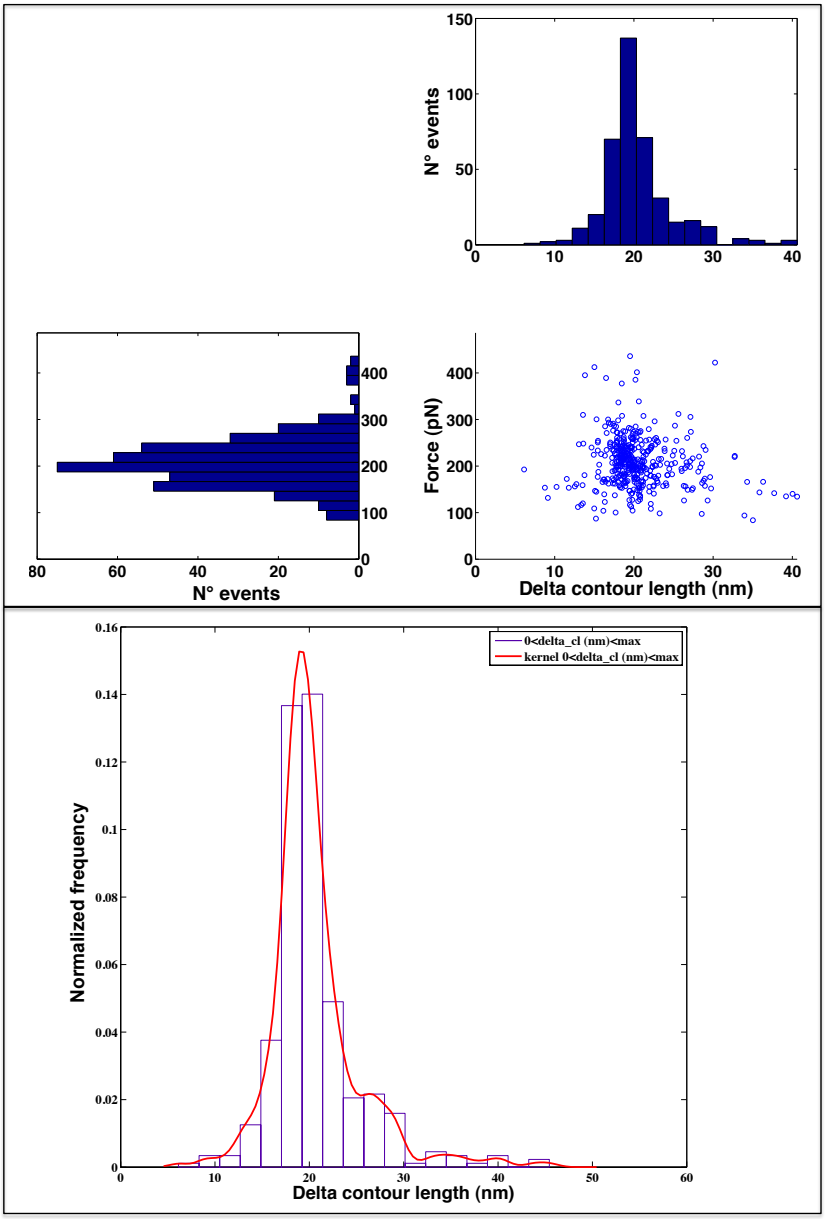

Figure 5.3: On top scatterplot from unfolding experiments carried out at pH 7.4. On bottom the fitting of delta delta contour length data with kernel density estimator.

Unfolding events with Δ_{cl} > 30 nm were present in about 18% of the overall curves almost independently on the pH of the buffer (**figure 5.4**).

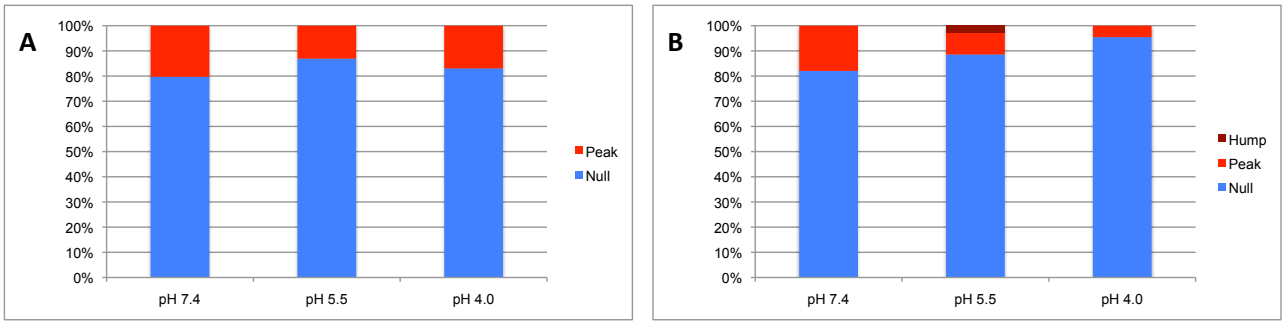

Figure 5.4: Frequency of MoPrP Tr_{x1} FEC with a peak Δ_{cl} > 30 nm ("Peak") or "hump" mechanical feature ("Hump") respect to the total. (**A**) Unfolding experiments, N=64, 107, 177. (**B**) Double-pulse refolding experiments, N=39, 35, 22.

In order to rule out that these additional events were not due to non-specific interactions between the tip and the surface, two methods where employed.
First, we prepared a construct (MoPrP Tr_{x1}-PEG) with additional PEG linkers at the N and C termini, in order to start the unfolding of the protein molecules farther away from the surface. In spite of a successful production of the protein, a very low efficiency of unfolding experiments was obtained. A total of three interpretable FEC (**figure 5.5, A**) were obtained from 2 million FECs, recorded from ten independent experimental setups, therefore an appropriate statistic analysis could not be built up.
Second, the reduction of non-specific signals by double-pulse refolding experiments. This latter approach was more useful since a higher number of curves could be obtained, with a drastically decreased number of non-specific interaction signals (**figure 5.5, B**). Obviously the main disadvantage was that 50 ms refolding time could not be sufficient to refold the additional events. Results showed that the frequency of FEC showing peaks with Δ_{cl} > 30 nm at pH 7.4 and 5.5 was comparable to the frequency observed in unfolding experiments in the same experimental conditions. At pH 4.0 instead the frequency was lower in double-pulse refolding respect to unfolding experiments. One curve showed an unusual mechanical feature (**figure 5.5, C**), which was characterized by a profile that couldn't be fitted using the WLC model; such curves were named "hump".

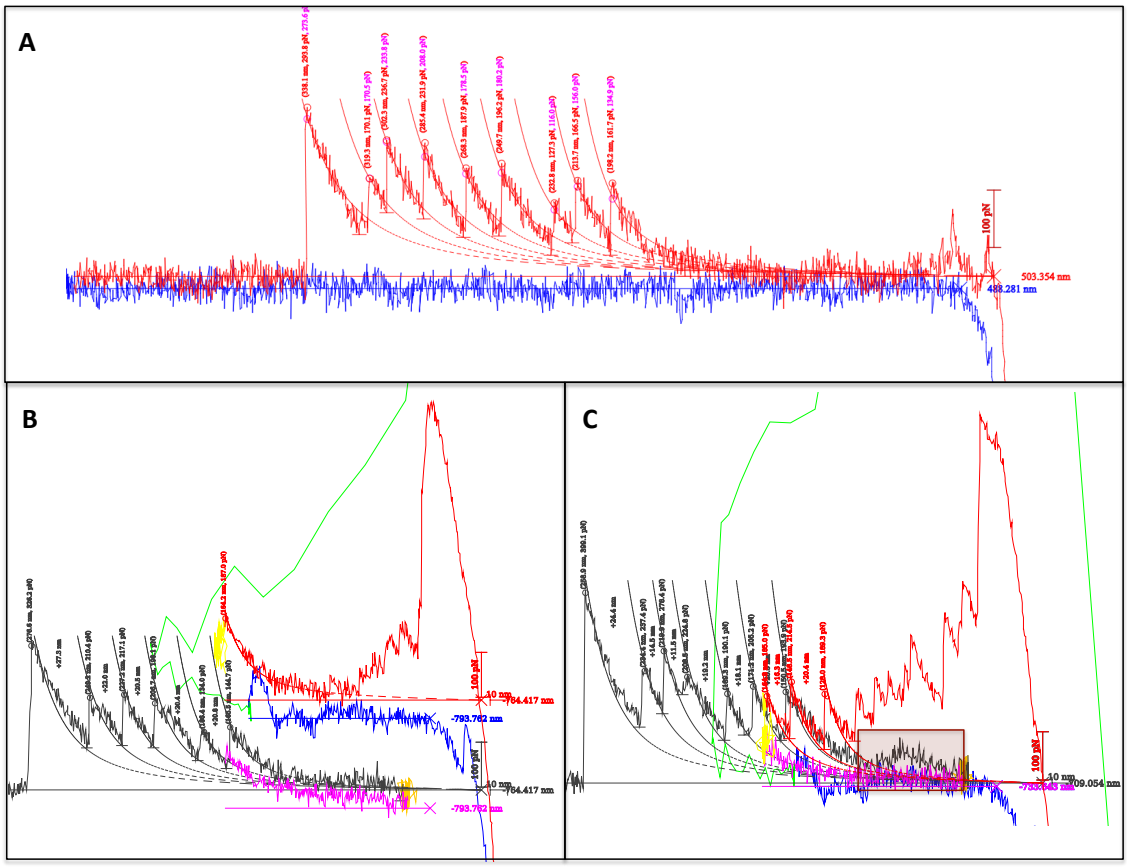

Figure 5.5: (**A**) PEG MoPrP Tr_{x1} unfolding curve: the first WLC starts 150 nm from the contact point, which correspond to the extension of 1.5 PEG 10k moieties. In the lower panels double-pulse refolding of MoPrP Tr_{x1} showing (**B**) a 27 nm peak before molecule detachment or (**C**) a "hump" mechanical feature inside the brown box.

Multi-pulse refolding experiments were carried out at pH 7.4, since experiment efficiency was higher under these conditions. Only one molecule was refolded 60 times and two types of signals could be detected (**figure 5.6**): low force events that could not be fitted with WLC model and GB1 unfolding peaks. Low force events where present only in 8% of the unfolding traces, prior to any GB1 unfolding event. No pushing on the surface during refolding traces was observed, therefore it is possible to exclude that such events were due to non-specific interaction between the tip and the surface.

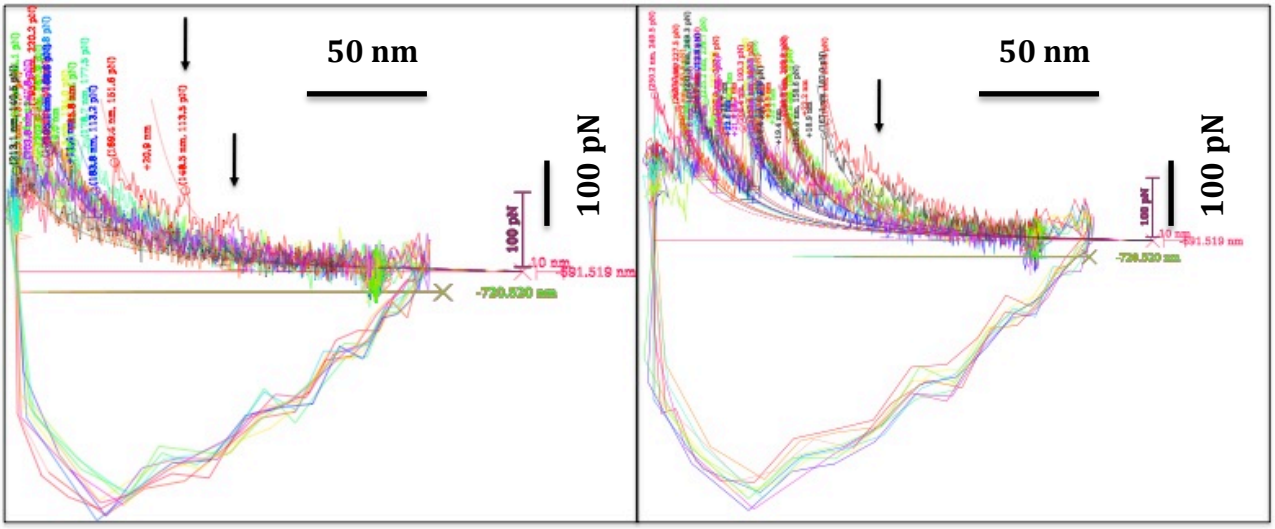

Figure 5.6: two refolding cycles of MoPrP Tr_{x1} composed by 10 unfolding/refolding iterations, with low force events indicated by black arrows. Contact point position is calculated from the first fetching curve.

5.3 SMFS experiments on MoPrP Tr_{x2} H-T and MoPrP Tr_{x2} H-H

We next analyzed the behavior of two dimeric Head-to-Tail and Head-to-Head constructs: MoPrP Tr_{x1} H-T ("Head-to-Tail") with the C-terminal globular of the first MoPrP moiety linked to the residue 89 of the N-terminal unstructured domain from the second MoPrP moiety; MoPrP Tr_{x2} H-H with both C-terminal globular domain of MoPrP moieties linked by a disulfide bridge.

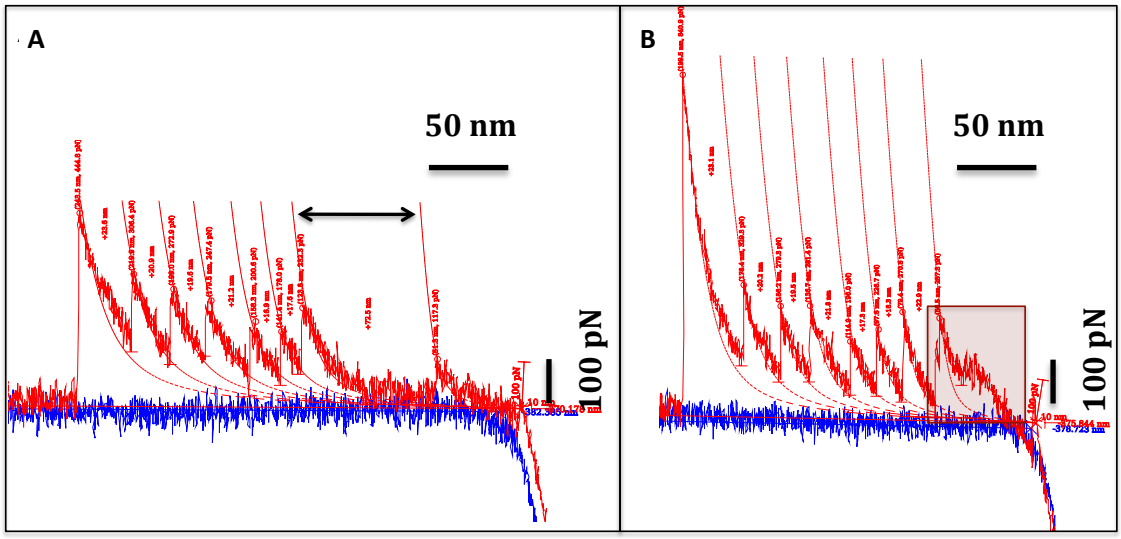

Figure 5.7: FEC from unfolding experiments on MoPrP Tr_{x2} H-T. (**A**) FEC with a peak of 72 nm preceding GB1 rupture peaks (indicated by the black arrow). (**B**) FEC with the hump mechanical feature highlighted in the brown box.

Unfolding experiments on MoPrP Tr_{x2} H-T and MoPrP Tr_{x2} H-H at neutral pH where characterized by FEC with a typical sawtooth pattern of GB1 unfolding events (**figure 5.7, A**). Differently from MoPrP Tr_{x1}, more than 40 % of the curves presented up to two peaks with Δ_{cl} between 30 and 80 nm length; the position of these peaks inside the FECs was mainly localized at the beginning of the curve and, less frequently, between GB1 unfolding events or previous the molecule's detachment. Decreasing the pH to more acidic values increased the number of such curves up to 20% for both constructs (**figure 5.8**). The "hump" mechanical feature was present in a small percentage of the curves (~ 2 %), showing up in two different ways: preceding the unfolding of GB1 domains as showed in **paragraph 5.2** or as an enthalpic contribution during the entropic force increase of a peak (**figure 5.7, B**).

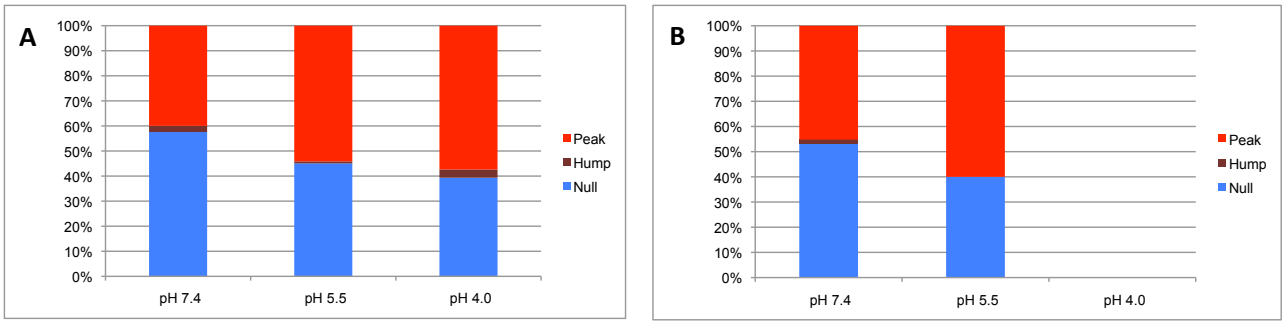

Figure 5.8: Frequency of curves showing a peak longer than 30 nm ("Peak") or hump mechanical feature ("Hump") respect to the total. A) unfolding experiments of MoPrP Tr_{x2} H-T, N=403, 114, 71. B) unfolding experiments of MoPrP Tr_{x2} H-H, N=188, 40.

Analysis of Δ_{cl} total distribution confirmed the presence of GB1 unfolding events cluster, characterized by $\Delta_{cl(N->U)}$ = 18.5 ± 2 nm ,with average unfolding force F = 233.3 ± 50.1 pN and F = 240.8 ± 53.3 pN for MoPrP Tr_{x2} H-T and MoPrP Tr_{x2} H-H constructs respectively. The frequency of peaks within the 23-30 nm interval was 7 % for MoPrP Tr_{x2} H-T and 3.7 % for the MoPrP Tr_{x2} H-H, both values were significantly lower compared to MoPrP Tr_{x1}. The distribution of peaks with delta contour length longer than 30 nm was similar for both proteins (**figure 5.9**): events with lower lengths were more frequent with respect to longer ones, but no clear clusters were present. Therefore, estimation of conformer populations by Gaussian mixture distribution could not be performed.

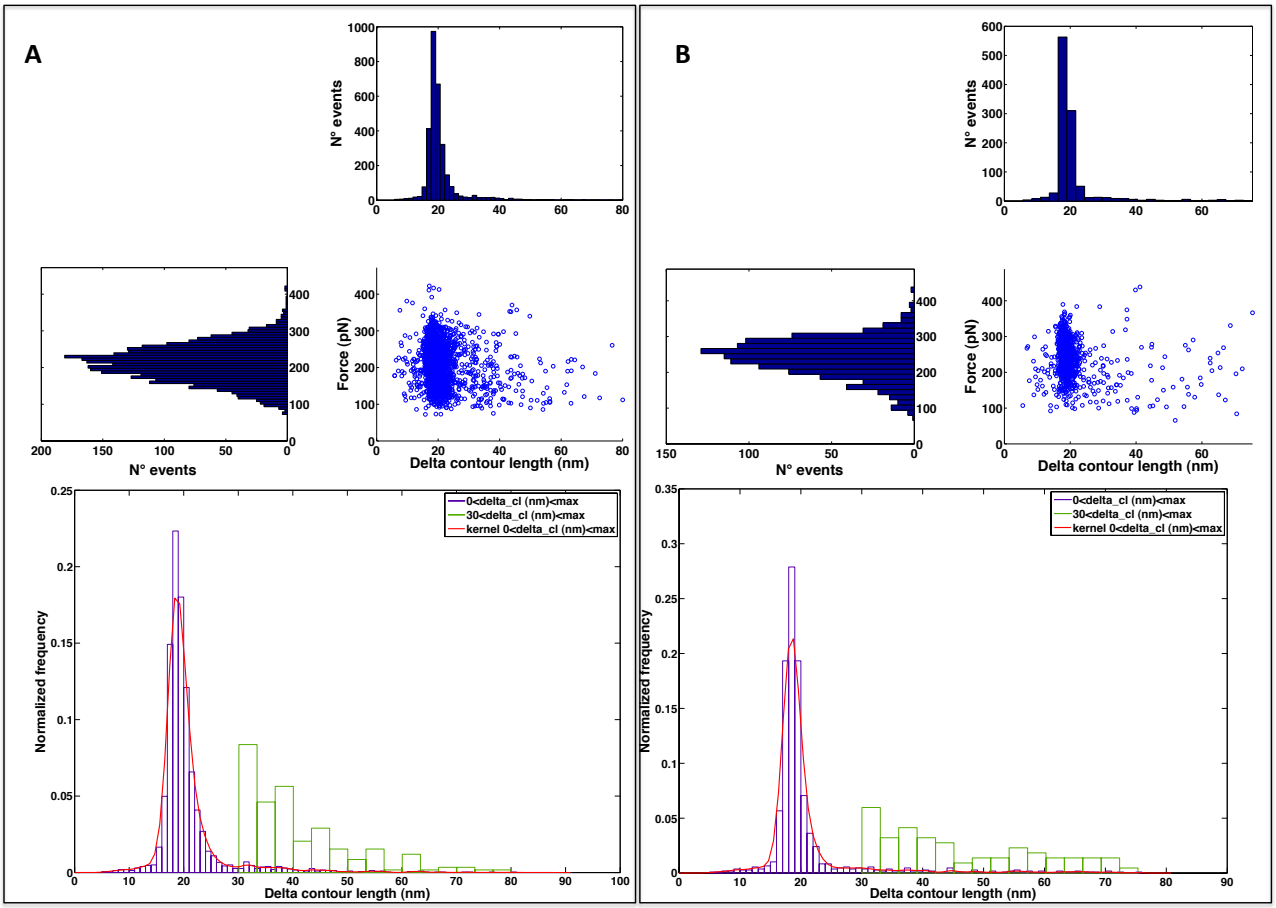

Figure 5.9: Analysis of (**A**) MoPrP Tr_{x2} H-T and (**B**) MoPrP Tr_{x2} H-H respectively. On top the scatterplot of unfolding experiments at pH 7.4. On bottom the overall Δ_{cl} distribution (blue bars) with calculated kernel density function (red line) and distribution of Δ_{cl} > 30 nm.

Since quantity and concentration of MoPrP Tr_{x2} H-H samples were not sufficient for refolding experiments, double-pulse refolding experiments were carried out on the Head-to-Tail heteropolymeric protein. Such experiments were performed at neutral pH to confirm that the presence of peaks with Δ_{cl} > 30 nm was not related to tip/surface non-specific interaction signals (**figure 5.10**).

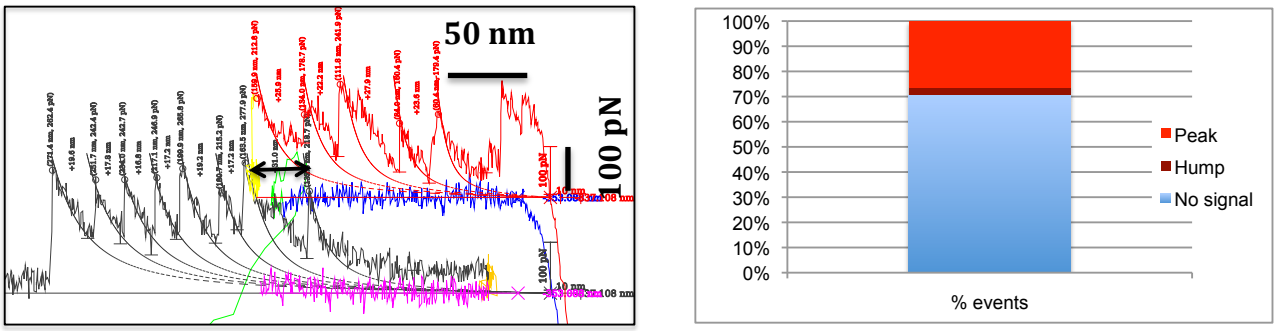

Figure 5.10: On left panel an example of double-pulse refolding curve of MoPrP Tr_{x2} H-T at pH 7.4. The first unfolding peak in the *break-away* curve (black trace) has a Δ_{cl} = 31 nm. On the right the frequency of curves with a peak with Δ_{cl} > 30 nm and curves showing the "hump" mechanical feature, respect to total curves. N = 34.

FEC with such peaks were similar to those observed in unfolding experiments, but their frequency was lower compared to unfolding experiments (**figure 5.10**). Nevertheless their frequency was ~ 12% higher compared to the same type of experiments carried out on MoPrP Tr_{x1} protein construct.

5.4 SMFS experiments on MoPrP Tr_{x3}

In order to gain insights in the oligomerization processes of MoPrP(89-230), single-molecule force spectroscopy experiments were performed using MoPrP Tr_{x3} construct.
FEC from unfolding experiments at neutral pH showed a more complex pattern of peaks compared to previous analyzed proteins (**figure 5.11, A and B**), with GB1 unfolding events preceded or followed by peaks with Δ_{cl} up to 90 nm. Scatterplot resulting from all unfolding experiments confirmed the presence of GB1 domain unfolding transition, with typical $\Delta_{cl(N->U)}$ = 18.5 ± 1.9 nm and an average force F = 234 ± 54 pN (**figure 5.13**). Unfolding events in the 27-30 nm interval had a frequency of 5%, similar to dimeric constructs discussed above. FEC showing peaks with Δ_{cl} > 30 nm were ~ 60% of the total recorded curves, but their number increased up to 70% at acidic pH values (**figure 5.12**). The distribution of such peaks was similar to dimeric constructs, without evident clusters (**figure 5.13**). The "hump" mechanical features were observed, showing similar patterns of previous analyzed constructs (**figure 5.11, C**).

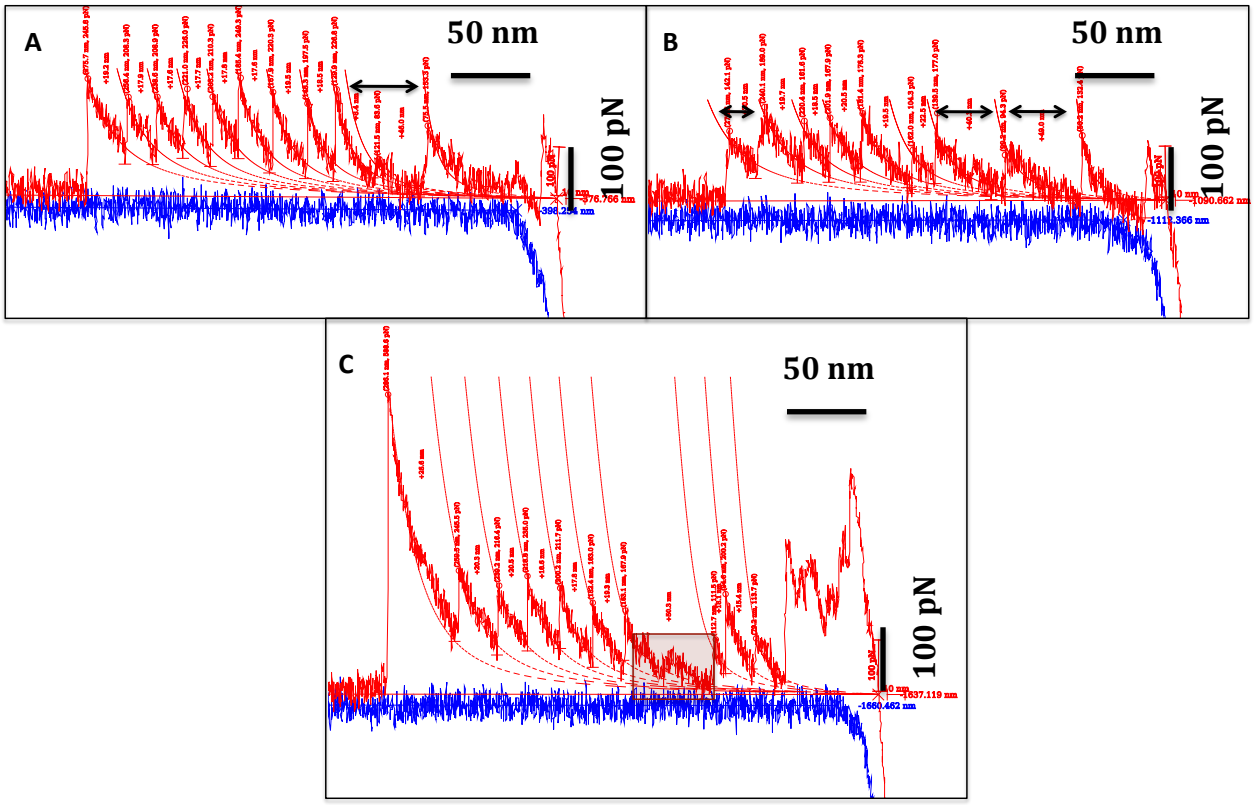

Figure 5.11: Typical FECs obtained from unfolding experiments on MoPrP Tr_{x3}. (**A**) FEC showing one peak with Δ_{cl} > 30 nm. The peak is highlighted with the black arrow. (**B**) FEC showing three peaks with Δ_{cl} > 30 nm, indicated by black arrows. (**C**) FEC with "hump" in brown box, following the rupture of a 51 nm peak.

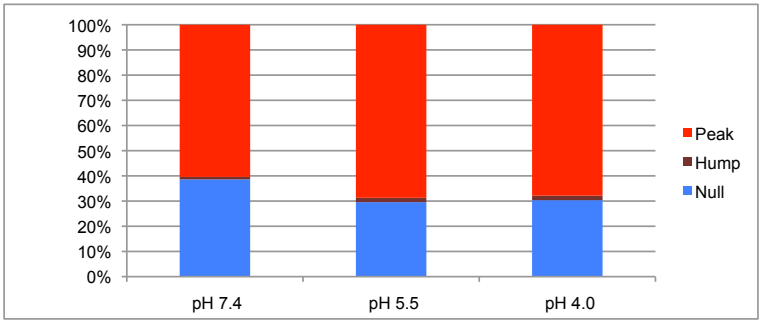

Figure 5.12: Frequency of FEC showing peaks with Δ_{cl} > 30 nm ("Peak") and with hump feature only ("Hump") respect to the total; N = 197, 115, 112.

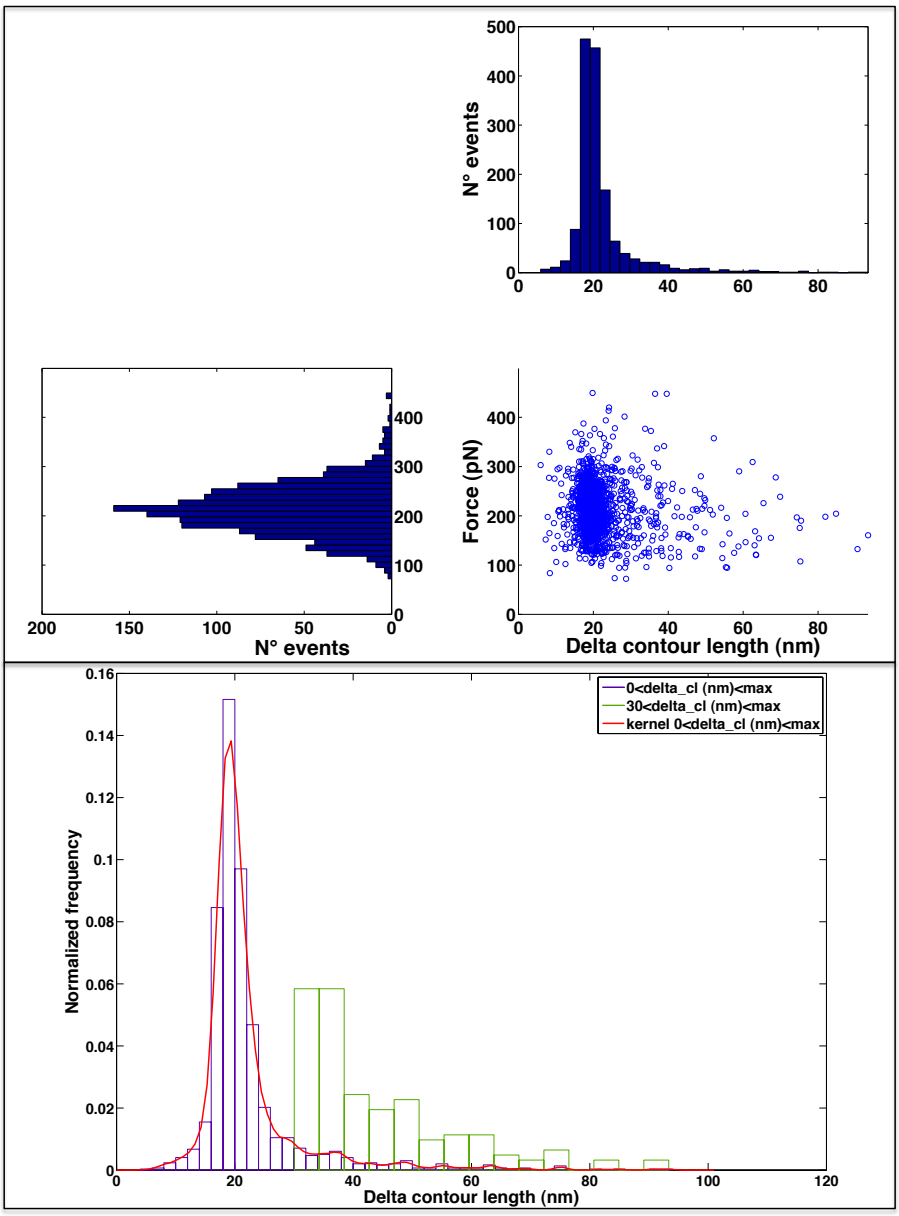

Figure 5.13: On top the scatterplot from unfolding experiments of MoPrP Tr_{x3} at pH 7.4; on bottom the overall Δ_{cl} distribution (blue bars) with calculated kernel density function (red line) and distribution of Δ_{cl} > 30 nm.

5.5 SMFS experiments on MoPrP Tr_{x4}

Experiments using four tandem repeats of MoPrP(89-230) moiety were performed in a similar fashion to previous recombinant proteins. As expected, FEC from unfolding experiments at pH 7.4 showed a minor number of GB1 unfolding events, consistent with the presence of only four domains flanking the MoPrP moieties. Peaks with Δ_{cl} > 30 nm were observed mainly at the beginning or at the end of the stretched molecule, and more rarely in the middle (**figure 5.14, inset A**). The frequency of FEC showing peaks with Δ_{cl} > 30 nm was higher compared to previous analyzed constructs. Their frequency was independent of the buffer pH, unlike the dimeric and trimeric constructs (**figure 5.15, inset A**). Experiments carried out using buffer with low ionic strength (NaCl 150 mM) did not change the frequency of the Δ_{cl} > 30 nm peaks in FECs.

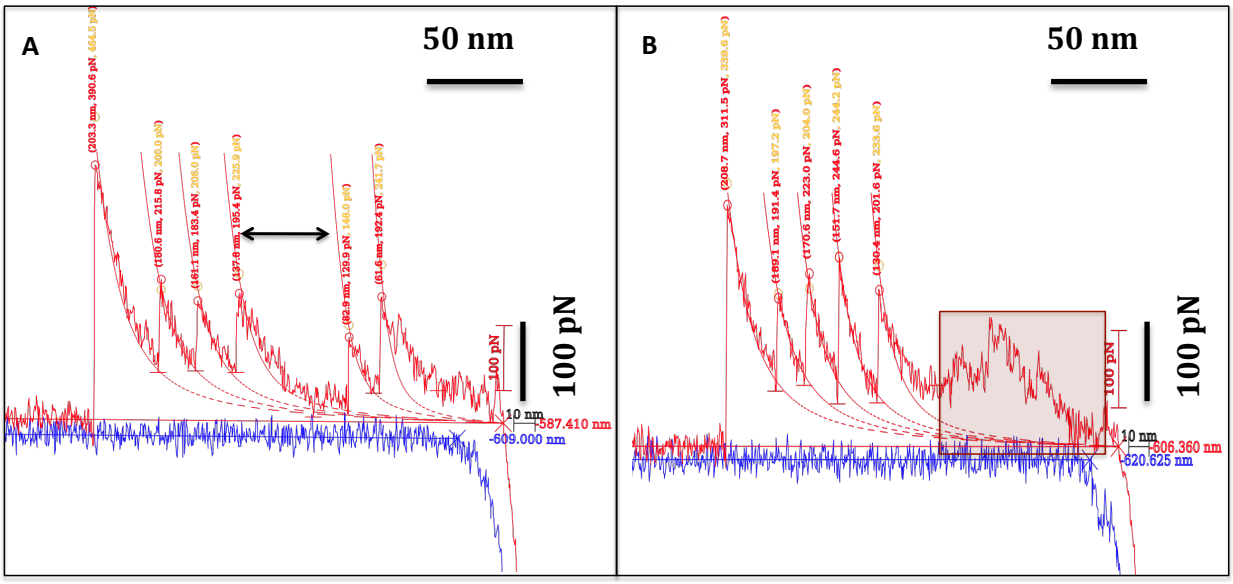

Figure 5.14: (**A**) FEC showing a peak with Δ_{cl} > 30 nm between GB1 unfolding events. (**B**) Example of a FEC with "hump" mechanical feature within the brown box. It is possible to notice that in this FEC no non-specific interaction could be observed.

The "hump" mechanical feature showed length and forces that were up to three times higher compared to the same features found in MoPrP Tr_{x1} but their frequency was 3-5%. Performing experiments at three different loading rates changed the frequency of the hump feature (**figure 5.15, inset B**).

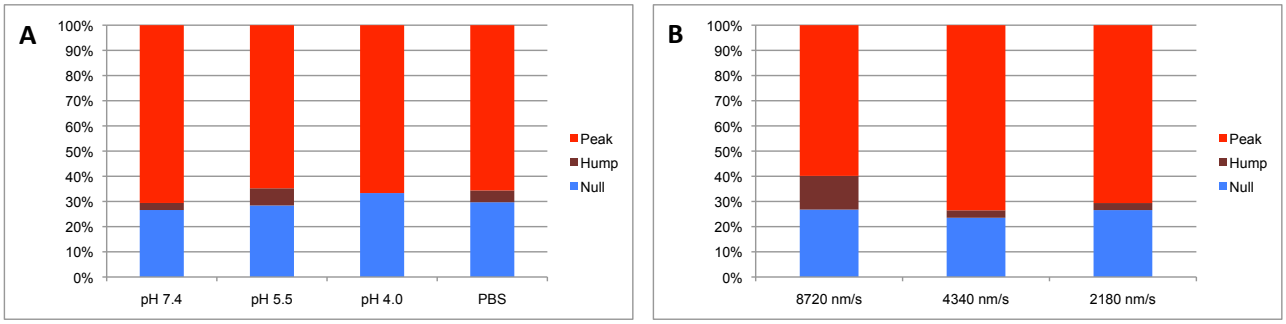

Figure 5.15: (**A**) Frequency of FEC showing a peak with Δ_{cl} > 30 nm ("Peak"), a "hump" ("hump") respect to the total. Data is obtained from unfolding experiments at 2180 nm/s under different buffering conditions. N=143, 88, 21, 64. (**B**) Frequency of FEC showing a peak with Δ_{cl} > 30 nm ("Peak"), a "hump" ("hump") respect to the total at different loading rates. N=127, 35, 143.

Analysis of length and forces revealed that GB1 native/unfolding transition showed $\Delta_{cl(N->U)}$ = 20.1 ± 1.3 nm and average F = 220.89 ± 54.03 pN at loading rate of 2180 nm/s. The distribution of peaks longer than 30 nm was more widespread than the trimeric construct, thus fitting with a single or multiple gaussians distributions could not be performed (**figure 5.16**).

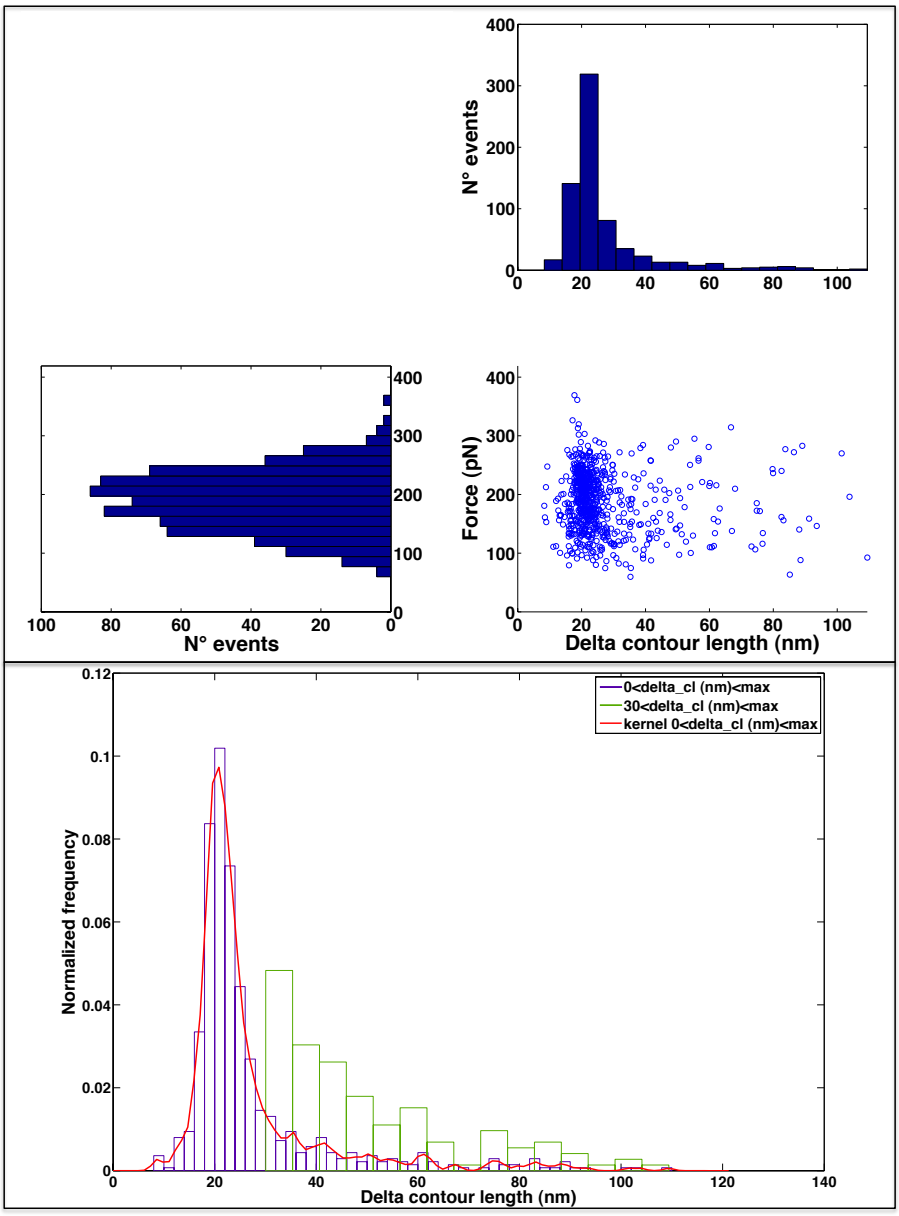

Figure 5.16: On top panel scatterplot from unfolding FEC at neutral pH of MoPrP Tr_{x4}. On bottom panel the distribution of all events (blue bars) with kernel fitting (red line) and peaks with Δ_{cl} > 30 nm (green bars).

Double-pulse refolding experiments at neutral pH confirmed the presence of peaks longer than 30 nm in 70% of the FEC (**figure 5.17, A and B**). Interestingly, performing the same experiments in presence of mild ionic strength the frequency of FEC with such peaks diminished to 42% (**figure 5.17, C**).

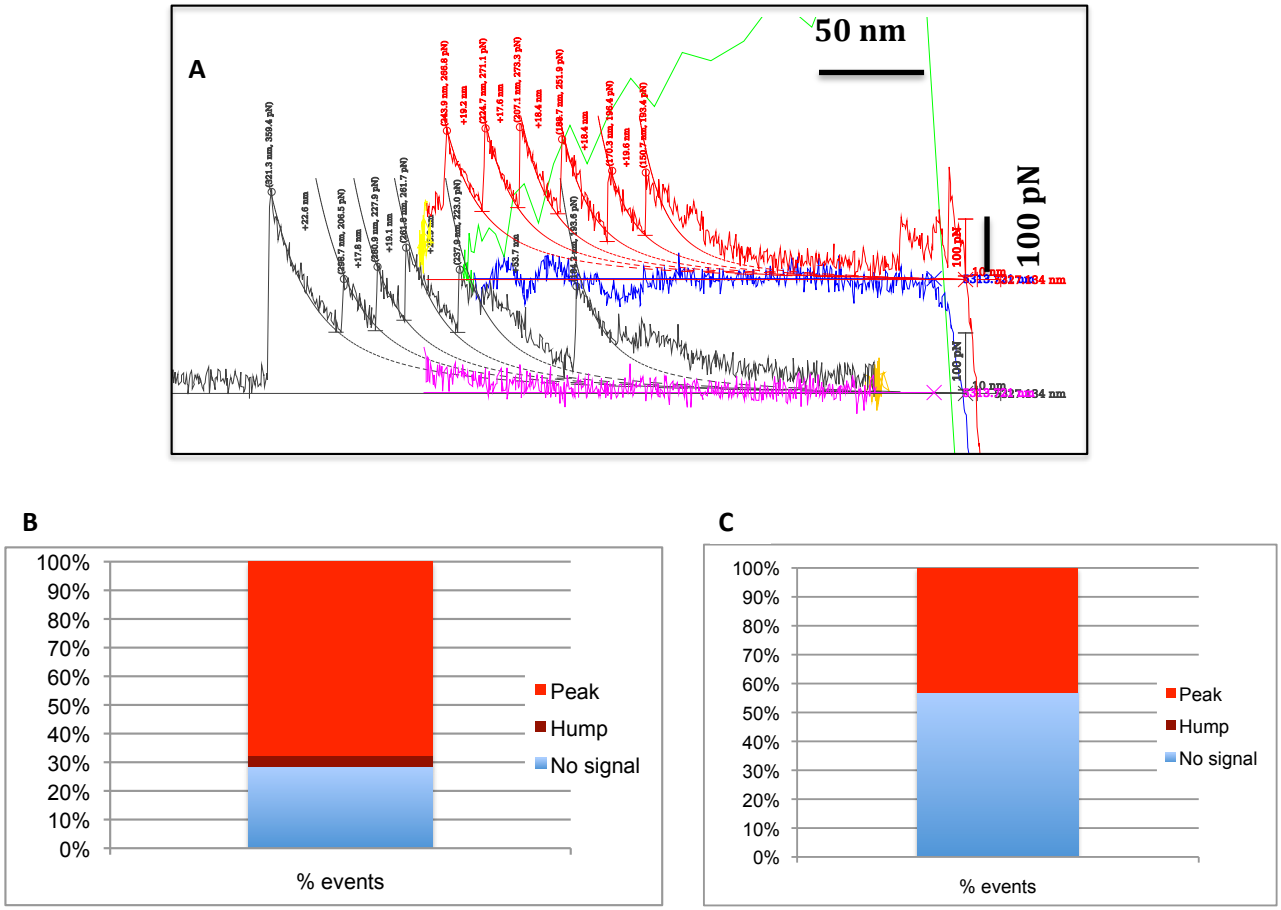

Figure 5.17: (**A**) Double-pulse refolding curve of MoPrP Tr_{x4}, it is possible to appreciate the presence of a 53 nm peak with a "hump" on the entropic force rising, before and after the peak. On bottom panels positive, "hump" and null curves from double-pulse experiments in (**B**) Tris 20 mM pH 7.4 (N=28) and (**C**) PBS pH 7.4 (N=34).

Multi-pulse refolding was performed on the construct at pH 7.4 and pH 5.5 (**figure 5.18**). Only one molecule in both experimental conditions was refolded 20 times before detaching from the tip. At neutral pH it was possible to detect low force (~ 90 - 100 pN) events preceding GB1 unfolding peaks in 20% of the unfolding pulses; after each refolding cycle the position and the force of these events changed. Differently, at acidic pH the events were present on 60% of the refolding cycles, with different lengths and force values up to 330 pN. In both cases the described peaks occurred before GB1 domain unfolding events.

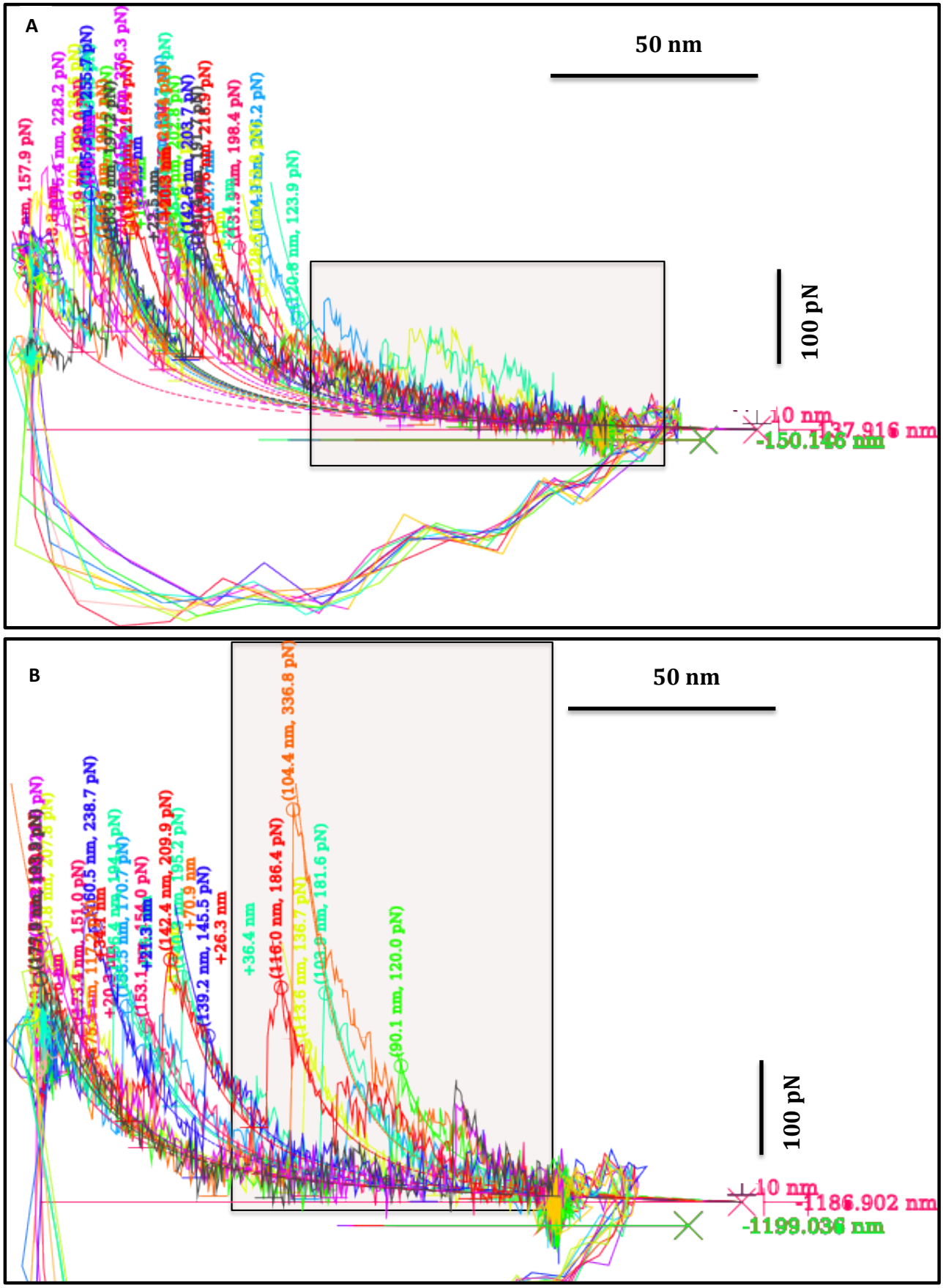

Figure 5.18: Multi-pulse refolding experiments on MoPrP Tr_{x4} in (**A**) Tris 20 mM pH 7.4 and (**B**) NaOAc 20 mM pH 5.5. In the brown box PrP association events are highlighted. The contact point is calculated from the fetching curve.

Part IV: Discussion

Transmissible Spongiform Encephalopathies (TSE) are diseases characterized by different incubation times, symptoms, biological phenotypes and etiology [77,286,287]. Stanley B. Prusiner proposed in 1982 that the infectious pathogen of TSEs is due to a proteinaceous infectious particle, named "prion" [173]. Through the years, much evidence has led the scientific community to accept the "protein-only" hypothesis. According to this hypothesis a misfolded form of PrP^{C}, a glycosylated GPI-anchored cellular protein [288] highly expressed in the brain, is the transmissible pathogen. The PrP^{C} structure is characterized by a large unstructured N-terminal domain and by a folded C-terminal domain with three α-helices and a small β-sheet [127,152,153,154,155]. Its infectious counterpart, PrP^{Sc}, is instead β-sheet rich [289].
The conversion between these two species was shown to take place *in vitro*, leading to the formation of amyloid species with distinct biochemical properties [188,290]. More recently the same type of structural heterogeneity was observed in other proteins involved in neurodegenerative disorders [291,292,293]. However the cause of this structural polymorphism has yet to be characterized. According to an emerging view, these proteins have an ensemble of amyloidogenic conformations. Therefore characterizing the monomer conformational space is required to better understand the aggregation processes.
Because of this structural heterogeneity, gaining structural insights on these conformers using "in-bulk" techniques is very challenging. Single-molecule methodologies instead are well suited for characterizing such poorly populated conformers, as they obtain structural information at the single-molecule level with atomic resolution. In our studies we employed single-molecule force spectroscopy (SMFS) techniques to gain further insights into the conformational equilibria of the mouse prion protein (MoPrP).
In fact, while several SMFS studies were performed on different proteins involved in neurodegenerative disorders [249,258,263,294], few were focused on the prion protein [248,270].

6.1 Interaction analyses of MoPrP proteins with handles

In SMFS techniques the analyte is usually tethered with specific handles, which are essential for molecule manipulation and recognition. Handles in AFM experiments are typically composed of tandem repetition of protein domains with well characterized mechanical features. In our studies we decided to use this approach as it could help us to unequivocally recognize the molecules picked by the AFM tip. More specifically, we flanked our analyte protein (MoPrP(89-230)) with multiple copies of streptococcal protein G domain B1 (GB1), which has been extensively characterized using "in-bulk" [278,284,285,295,296,297] and single-molecule [256,257,262,298,299,300] techniques. In OT SMFS experiments instead, we the tethered MoPrP(89-230) and MoPrP(23-230) to double stranded DNA (dsDNA), similar to previous works [208,301].
Since the handles are directly linked to the protein, their local concentration is very high due to kinetic constraints. This condition may lead to undesired interactions between the handles and the analyte. Therefore it is necessary to demonstrate that the two moieties do not interact each other.

In SMFS OT experiments we flanked MoPrP molecules with 1kbp dsDNA obtained by PCR from pET-11a plasmid. Previous studies have shown that recombinant PrP is able to interact

with nucleic acids [302,303,304], *via* electrostatic interactions in a sequence independent manner [305]. It has been observed that DNA had an anti-scrapie activity [306]. Also DNA was able to convert PrP to a β-rich conformation [307]. According to Lims *et al.* [305] the interaction is mediated by the C-terminal globular domain, which is able to bind short 18 bp long dsDNA sequences. Therefore at least 50 PrP molecules could bind 1000 bp dsDNA, decreasing its electrophoretic mobility by a factor of 2.3. The highest molar ratio used in our experiments was 20:1, thus a maximum decrease by a factor of 1.5 in the electrophoretic band mobility could be expected. Electrophoretic mobility shift assay (EMSA) showed that small migration shifts occurred only with the full-length prion protein at 20:1 dsDNA:MoPrP molar ratios, while no shift was observed with the truncated form. A possible explanation could be due to the theoretical isoelectric points of MoPrP(89-230) and MoPrP(23-230), which are 8.84 and 9.56 respectively. At neutral pH both molecules are positively charged, so it is likely that electrostatic interactions with dsDNA may occur [305]. In particular, the N-terminal unstructured domain of the full-length MoPrP presents the CC1 domain, with several basic residues that can interact strongly with nucleic acid phosphate groups. In our EMSA experiments the presence of ionic strength in running buffer likely disrupted the interaction between the C-terminal globular domain and dsDNA preventing the binding of the truncated MoPrP. The full-length form instead, was still able to bind dsDNA reducing its electrophoretic mobility, most probably *via* its N-terminal positively charged domain.

To confirm that the GB1 protein domain did not interact with MoPrP(89-230) moiety/ies in our AFM constructs, we employed three different experimental approaches. Initially we used the co-immunoprecipitation (Co-IP) technique, since it has been widely used to analyze protein-protein interactions *in vitro*, in cells and *in vivo* [308,309]. Our results showed that incubating GB1 with MoPrP(89-230) and MoPrP(23-230) resulted in co-immunoprecipiation of the target protein. The effect was more evident with the full-length form, which presented a clear band at the theoretical MW of $GB1_{x4}$ protein, indicating that the two proteins interacted. On the other hand MoPrP(89-230) and MoPrP(23-230) were detected in negative controls, suggesting that non-specific interactions between the prion protein and the resin occurred. A stronger band was observed for the full-length form indicating that the N-terminal charged domain was probably playing a major role in this interaction. Thus, it was not possible to conclude that the immunoprecipitation was due exclusively to protein-protein interactions or to protein-resin interactions.
For this reason further experiments were performed, using ELISA methodology. Incubating increasing amounts of GB1 in MoPrP adsorbed wells did not result in a significant increase of alkaline phosphatase signal, indicating that GB1 did not interact with PrP. In fact, if an interaction occurred, a titration curve with a saturation asymptote would have been expected. Positive and negative controls confirmed that under the experimental conditions antibodies worked correctly.
The major disadvantage of surface and antibody based methods is the possibility to cover the protein interacting surfaces with the antigene-antibody complex, hindering a possible interaction. These experimental limitations could be circumvented using free-solution methods such as size-exclusion chromatography [310,311]. This technique has several advantages: i) it is possible to use simple buffers, avoiding the use of detergents or salts that may interfere with the binding of the two proteins; ii) there is no steric hindrance due to a surface or antibody between the two analytes; iii) in case the two protein theoretical MW and experimental Stokes radius are similar, it is possible to check on SDS-PAGE the eluted fractions. Results showed that loading MoPrP(89-230) and $GB1_{x4}$ did not result in co-elution of the prion protein in GB1 fractions, while small amounts of the latter were detected in PrP fractions. This can be explained considering that typically the profile of elution peaks from

SEC experiments, present a sharper initial tail and a more prolonged tail in the end. No interaction was detected either at neutral or at slightly acidic pH values. However, it has to be noticed that developing WB with Fab D18 antibody resulted in a band at the MW of $GB1_{x4}$, indicating that the bacterial protein domain is able to bind the Fc region of the secondary antibody.
Nevertheless, these techniques required that GB1 and MoPrP proteins were free in solution, while in AFM constructs these proteins are covalently tethered to each other. Thus, it is possible that interactions occurred only in the heteropolymeric protein constructs.

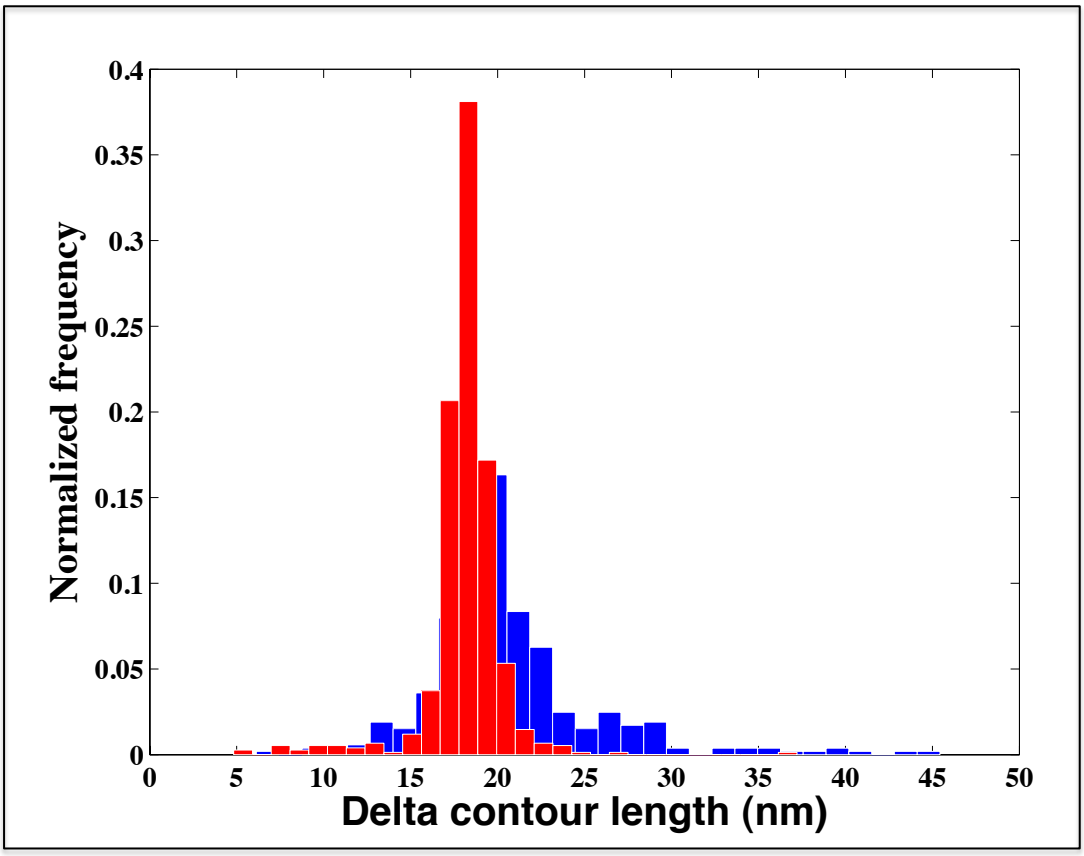

Figure 6.1: overlay between Δ_{cl} distributions of unfolding experiments at pH7.4 from $GB1_{x8}$ (red bars) and MoPrP Tr_{x1} (blue bars) overall rupture events.

In AFM SMFS experiments a possible GB1 and PrP interaction could be observed as a different Δ_{cl} or force distribution of their corresponding unfolding transitions. Since MoPrP(89-230) was never characterized previously using such technique, we compared GB1 unfolding with or without one MoPrP moiety in unfolding experiments. **Figure 6.1** shows the overlay of Δ_{cl} distribution of unfolding events at neutral pH from $GB1_{x8}$ and MoPrP Tr_{x1} constructs. Both distributions match each other, without any shift in the average Δ_{cl} values of the GB1 unfolding transition. Average unfolding forces were comparable, indicating that no mechanical variations of the GB1 moieties occurred. On the other hand, MoPrP Tr_{x1} Δ_{cl} distribution was less sharp in the interval between 22 and 30 nm, due to the presence of more rupture events, which were absent in the $GB1_{x8}$ construct. This aspect will be discussed in **paragraph 6.2**.
It has to be noted that in the MoPrP Tr_{x1} construct the GB1:MoPrP moieties ratio was 8:1. Thus if interactions between the two protein moieties occurred, only one or two GB1 modules unfolding transitions would have changed due to the possible interaction. As a result, only a

small fraction of the overall recorded rupture events would have been changed, without modifying significantly the average unfolding parameters values. Also with unfolding experiments it has been possible to analyze only native to unfolding (N->U) transitions, while it could be possible that structures generated from protein-protein interactions were accessible only from their U state. Double-pulse and multi-pulse refolding experiments clearly showed that GB1 domains within one molecule were able to refold independently (**figure 5.6**). WLC fitting of each rupture event were superimposable after each unfolding/refolding cycle, without any change in peak rupture lengths. This confirmed that interaction between the mouse prion protein and GB1 domain did not occur even from U->N pathway.

6.2 Conformational ensemble of MoPrP(89-230) at the monomeric level

The first part of the work was gaining insights into the conformational ensemble of the murine prion protein at the monomeric level. Multiple Gaussian fitting of Δ_{cl} distribution from overall FEC showed the presence of two major distributions: the first one centred at 19.3 ± 1.5 nm, which is relative to the unfolding of GB1 domains, and a second one at 27.2 ± 2.1 nm (**figure 6.2**). A possible third small population at ~ 13 nm seem to be present but data was not sufficient for a statistically significant characterization.

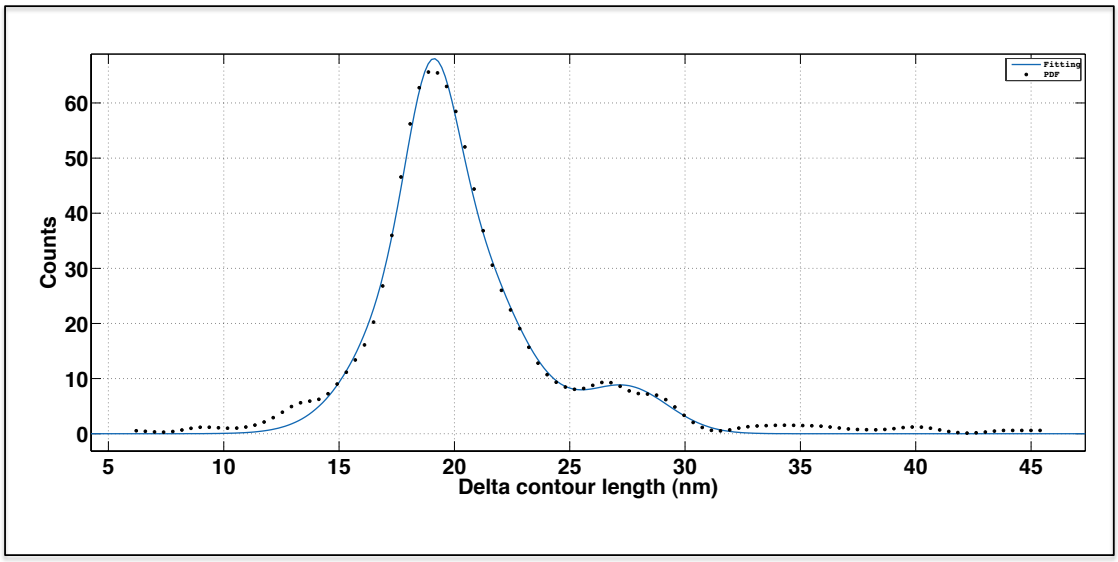

Figure 6.2: fitting with two Gaussian distributions of the PDF function calculated on Δ_{cl} experimental data of MoPrP Tr_{x1}; RMSD = 0.9833.

The 27 nm distribution could be associated to the native/unfolding (N->U) transition of the C-terminal globular domain of MoPrP. Considering Met128 and Ser229 as the first and last residues involved in the structure of the C-terminal globular domain [152], the average theoretical unfolding length is 26.3 nm. If we consider instead that GB1 unfolding events could not be longer than 23 nm, reducing the fitting window of the GB1 Gaussian distribution, the fitting of the PrP unfolding distribution is $\Delta_{cl(N->U)}$ = 26.12 ± 2.01 nm. This distribution represents almost 15% of the overall rupture events, one event for every six of GB1. The average unfolding force of these events was 198.13 ± 45.42 pN. Previous studies on $ShaPrP_{91-231}$ using OT [270,271] found that $ShaPrP_{(N->U)}$ = 34 nm, but the protein oxidation state was not confirmed. Since the production of such a construct required protein refolding under reducing conditions, it is likely that the native disulfide bridge of Cys178 and Cys213 (mouse

numeration) was reduced under pulling experiments. This hypothesis is supported by observations of the same group on ShaPrP construct with Cys->Ala mutations, which led to the identification of the same transition length.
The N->U transition observed in our experiments showed up as a single peak, therefore the unfolding of the three α-helices and the β-sheet occurred in a cooperative manner, without visible unfolding intermediates. These results pointed out that C-terminal domain PrP unfolding is a two state transition. This hypothesis is in agreement with previous studies using urea unfolding CD studies and tryptophan fluorescence techniques [156,157,171].
In 17% of the FEC, we observed peaks longer than 30 nm but shorter than the total unfolding length of the oxidized molecule (39.7 nm). These events could not be considered MoPrP(89-230) $_{(N->U)}$ transition of the folded domain, rather conformers with structures that encompassed also residues from 89 to 127. Structural studies have been carried out on truncated prion proteins from different species, showing that they share a common structure [154,155]. The folded domain encompassed residues 129 to 230, however residues 89-127 (in mouse numeration) were always observed as intrinsically disordered. Considering that the 30-40 nm unfolding transitions were present only when the C-terminal domain unfolding transition was not identified, we conclude that these two structures are competitive one with the other. Even if the data points relative to peaks in the 30-40 nm intervals are few, it is possible to notice that they have different lengths and the average unfolding force is 152.38 ± 47.86 pN, indicating that such structures are more heterogeneous and weaker compared to the native structure.
Such long conformers could represent extended conformers of the MoPrP(89-230) protein moiety, which could be involved in protein aggregation. This data is consistent with previous works where the unstructured region of the truncated protein could adopt β-sheets secondary structures [166]. H/D exchange experiments showed that this region may be exchanging between structured or collapsed states [158]. Moreover, the amyloid core of PrP^{Sc} encompasses all the truncated prion protein sequence [148,312]. On the other hand, previous studies shown that monomeric truncated HuPrP is not able to adopt extended structures, but rather partially unfolded structures [313] after its unfolding [158,270]. Some of these were thermodynamically more stable than the native state, showing a classical β-sheet rich spectra [314]. Recently, Yu *et al.* [270] shown by force-clamp OT force spectroscopy that three misfolded conformations of ShaPrP are accessible only from the U state. These conformers possessed a shorter structure compared to the native one and they were poorly populated, which is not consistent with our data, since the frequency of such events in our construct was higher. These misfolded forms were thermodynamically less stable compared to the native structure, similarly to what we observed. It may be pointed out that the events we observed were due to tip/surface non-specific interaction or interaction between GB1 domains and MoPrP moieties. We exclude the first possibility because double-pulse refolding experiments showed that these conformers could be observed after refolding the protein molecules. We also rule out the latter, considering that no interaction between GB1 and MoPrP moieties has been detected, as discussed in **paragraph 6.1**.
Lowering pH during unfolding experiments did not change significantly the percentage of curves with peaks $\Delta_{cl} > 30$ nm, while in double-pulse experiments a decrease was observed only at pH 4.0 (**figure 5.4**). A possible explanation of this behaviour could be due to the lower stability of such extended conformers at acidic pH values. During these latter experiments we observed one FEC with a mechanical feature characterized by a non-entropic increase and decrease of force, before GB1 rupture events. This type of mechanical feature was named "hump" and it could not be fitted with the WLC model. Since only one curve showed this feature, a more detailed analysis could not be performed.

Finally, using multi-pulse refolding protocol we could not detect signals related to PrP structures. A possible explanation could be that, the contact point was calculated in the fetch curve, so it was possible that during refolding cycles the piezoelectric stage drifted. In this manner the tethered molecule would have been kept under tension with forces in the order of tens of piconewtons, below our force resolution limit. PrP has a fast two-state folding mechanism [156], with folding rate k_{fold} at zero force of $5\times10^{3\pm1}$ s^{-1} [271], while at 10 pN force the k_{fold} is 3.67 $\times10^{-1}$ s^{-1}. GB1 instead is able to fold efficiently even at residual forces of 10 pN (k_{fold} = 720 s^{-1}) [256]. Therefore if residual forces acted on the protein molecules during refolding, GB1 domains were still able to refold while the MoPrP moiety could not.
From the data discussed above, we conclude that the monomeric MoPrP(89-230) inside the hetero-polymeric construct is folded in the native state. This is supported by the presence of an unfolding transition of 27 nm, which was present in almost 83% of the interpretable FEC. In ~ 17% of the remaining FEC, the prion protein adopts a more extended folded structure, which requires a conformational rearrangement of the unstructured region from residues 89 to 128. The length of these structures is very heterogeneous and their average force is lower compared to the native structure, indicating a lower stability. These conformers might be related to subsequent protein aggregation processes.

6.3 Complex conformational equilibria between multiple PrP molecules

The second part of the work was focused on the first steps of prion protein aggregation processes. Aggregation into disordered or high-ordered structures requires protein oligomerization, meaning that two or more protein monomers generate a new structure *via* intermolecular bonds [315]. In order to build a model of such mechanisms for MoPrP aggregation, we used the same approach of heteropolymeric protein constructs, but in this case we cloned more than one PrP molecule on the same polypeptide sequence. We expressed two dimeric constructs with different MoPrP protein orientations on the polypeptide chain, to find out how their relative orientations may affect the formation of intermolecular associations. We also expressed one trimeric and one tetrameric constructs, to understand how the associations are influenced by the number of MoPrP moieties, similarly to recent studies on α-synuclein [267].

6.3.1 Protein orientation dependence on PrP oligomerization

In the first dimeric construct the two prion protein moieties were in a head-to-tail orientation (MoPrP Tr_{x2} H-T) with the C-terminal globular domain of the first one linked to the N-terminal unstructured domain of the second. In the second dimeric construct the two C-terminal globular domains of MoPrP moieties were adjacent instead (MoPrP Tr_{x2} H-H), linked *via* a disulfide bridge.
MoPrP Tr_{x2} H-T and MoPrP Tr_{x2} H-H unfolding scatterplots at neutral pH showed that both proteins had a more complex pattern of unfolding with respect to MoPrP Tr_{x1}. Two major difference were observed with respect to the monomeric construct: i) the 27 nm transition was less frequent, as these events in the 23-30 nm interval represented only 3.7 % and 7 % of the total events for the H-H and H-T constructs respectively; ii) the frequency of FEC showing events with $\Delta_{cl} > 30$ was two times higher with respect to the monomeric construct. The fact that at least 40% of these events with respect to the total, were longer than the total length of the unfolded monomer (39.7 nm), suggests that these structures could have been generated only from the association of the two prion protein moieties. More interestingly, lowering the pH value resulted in the increase of the frequency of FEC with $\Delta_{cl} > 30$ nm events. This data

confirmed that PrP behaviour is strongly related to the surrounding environment; in fact upon lowering the pH the protein aggregation propensity increases. As discussed in **paragraph 1.2.4**, PrP native structure stability is lower at acidic pH [163,164,316], therefore the protein can more easily unfold and subsequently aggregate under these conditions. This type of pH-dependent behaviour has been observed in other proteins involved in neurodegenerative disorders [250,317].

An increase in the number of MoPrP(89-230) molecules could lead to a more evident interaction with GB1 handles, since in this case the GB1:MoPrP moieties ratio is 4:1. It is also possible that prion protein associations could involve GB1 domains. To rule out this possibility, we compared the GB1 unfolding events from FEC with and without unfolding events that showed a $\Delta_{cl} > 30$ nm. As shown in **figure 6.3** the Δ_{cl} and force distributions of the two types of curves are comparable. Moreover, these two distributions are comparable to the distribution of GB1 unfolding events from $GB1_{x8}$ construct, confirming that intermolecular PrP associations did not involve GB1 domains as a result of a possible interaction.

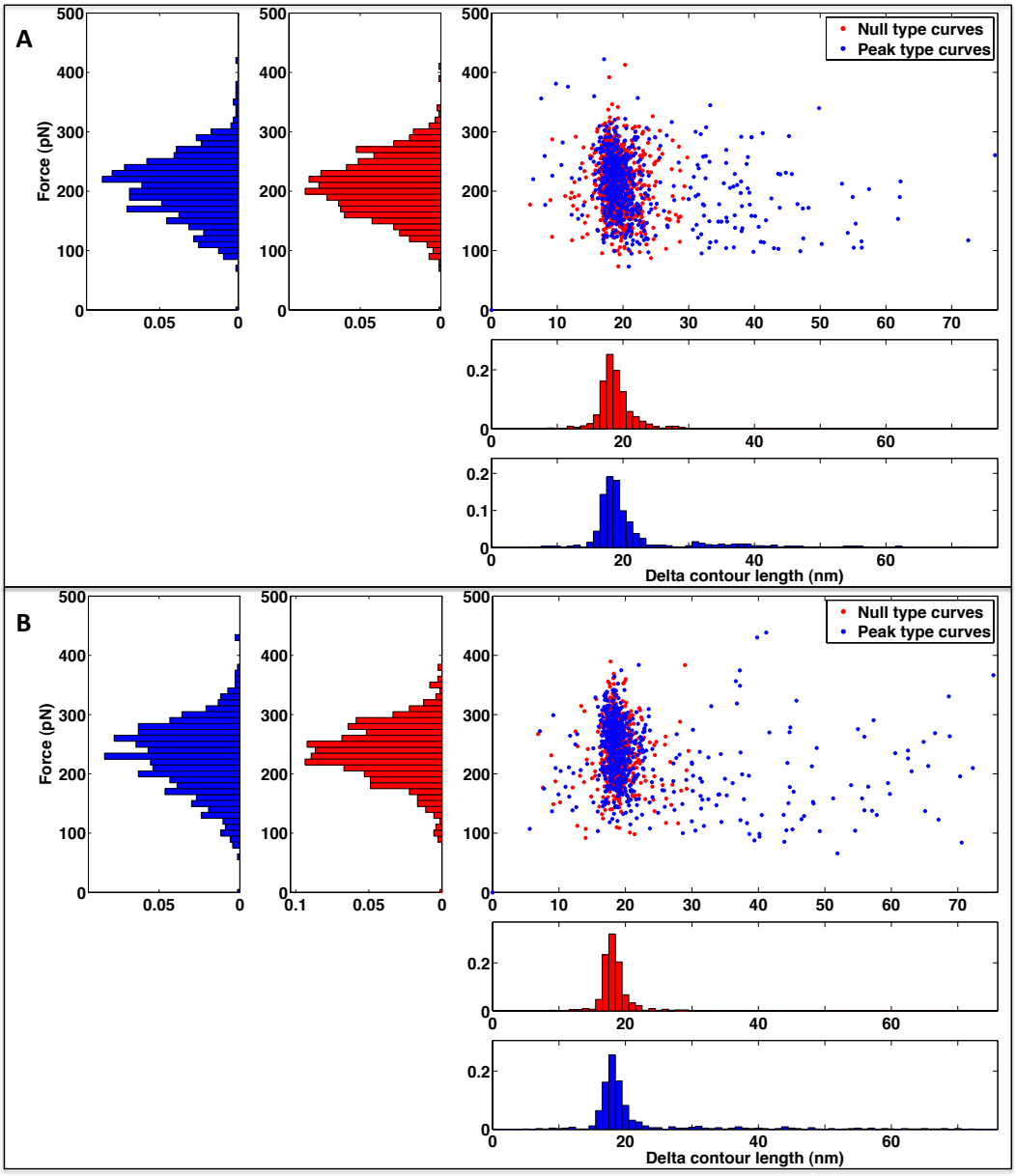

Figure 6.3: Unfolding events from FEC showing peaks with $\Delta_{cl} > 30$ nm (blue) or without them (in red). Data is referred to (**A**) MoPrP Tr_{x2} H-T and (**B**) MoPrP Tr_{x2} H-H proteins.

A more detailed analysis was performed considering only FEC showing unfolding events with Δ_{cl} > 30 nm. In ~ 85 % of these curves only one peak with Δ_{cl} > 30 nm was detected ("single peak curves"), while in the remaining 15 % of the curves two peaks ("double peak curves") were observed (**figure 6.4, panel 1**). As expected, the maximum lengths of these unfolding events from single and double peak curves were lower than the total length of the two PrP moieties of the construct (79.4 nm). In order to gain more detailed structural information of PrP conformers, it is important to remember that the measured contour length extensions cannot be related to the absolute position of the residues of the unfolded structures. It is possible that an association between two PrP molecules can be shorter or equal to the theoretical unfolding length of a PrP monomer. Therefore, associations between two PrP molecules can be unequivocally identified only if their unfolding Δ_{cl} is longer than the fully stretched monomer length (39.7 nm).
Unfolding events were counted inside the 30-40 nm and 40-80 nm length intervals (**figure 6.4, panel 2**). Interestingly, the H-T construct showed a major propensity to adopt "short" conformers (30-40 nm interval), while the H-H showed a prevalence of associations between two PrP molecules (40-80 nm interval). Considering that the sample size of H-T construct FECs was two times larger than the H-H one, bootstrapping was performed in order to obtain comparable data sets. This procedure was also used to confirm that the sub-population sample was statistically representative of the total population. Results from 500 iterations showed that in the H-T construct, unfolding events in the two intervals were maintained, with a frequency of 60.7 ± 3.7 % in the 30-40 nm and 38.7 ± 3.7 % in the 40-80 nm intervals. This confirms the difference in the association processes between the two dimeric protein constructs.
Considering that the number of FEC showing peaks with Δ_{cl} > 30 nm with respect to the total interpretable curves is identical for both constructs, it can be inferred that the orientation does not affect the frequency of PrP associations, but rather their length.
Focusing on the 27 nm transition, its frequency was 3.7 % and 7 % for the H-H and H-T constructs respectively. These unfolding transition frequencies were significantly lower compared to the one observed from MoPrP Tr_{x1} (15%). Moreover in the dimeric H-H construct, the frequency of the native state unfolding transition was almost half with respect to the H-T construct. Considering the associations between the two PrP moieties were more frequent in the H-H construct, it might be possible that they required the structural rearrangement of the C-terminal folded domain.
Double-pulse refolding experiments at neutral pH showed that even PrP associations were able to refold but with a lower frequency. A possible explanation could be that 50 ms refolding time may not be sufficient for the formation of some of these associations.

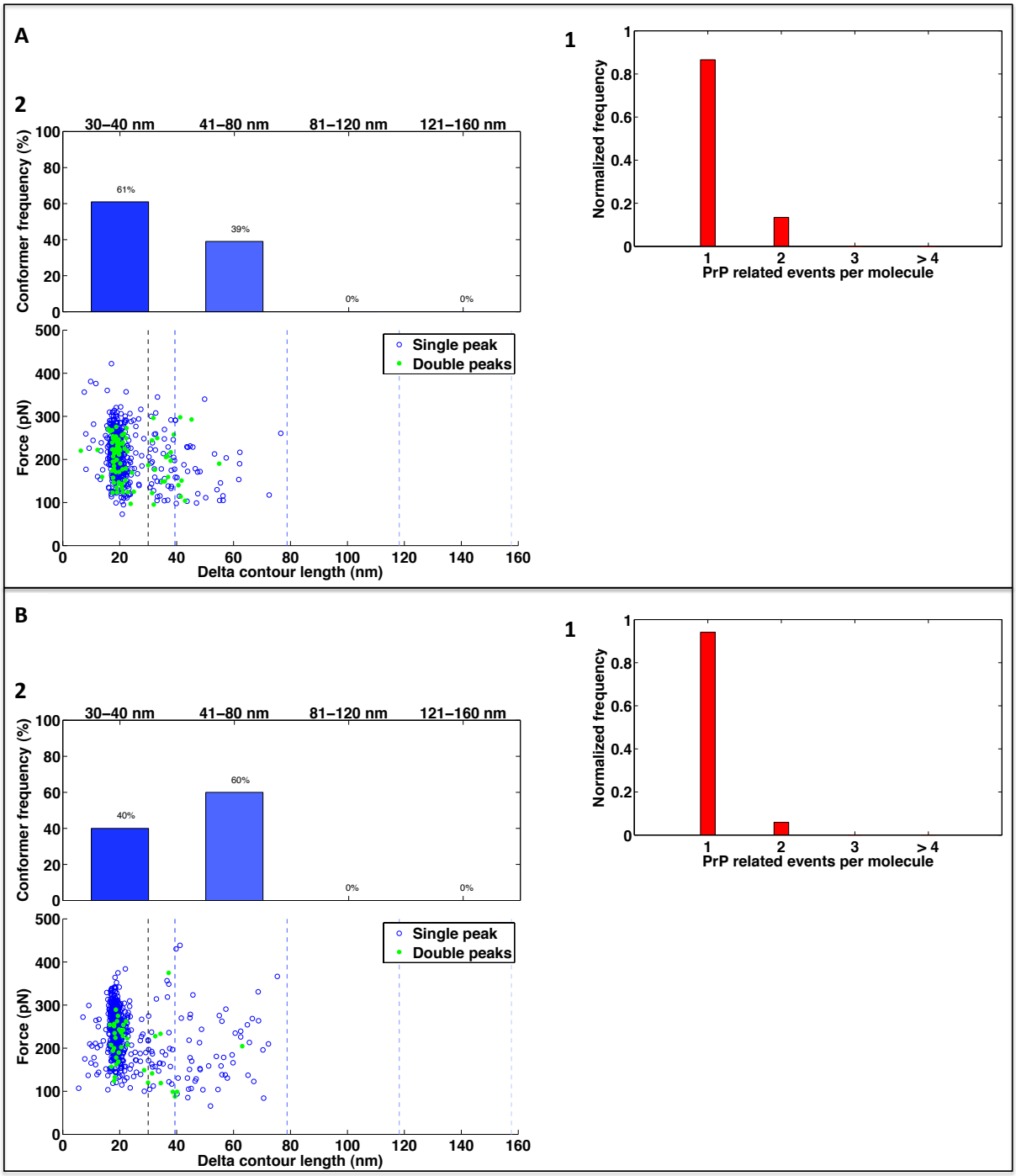

Figure 6.4: Analysis of curves showing associations peaks from (**A**) MoPrP Tr_{x2} H-T and (**B**) MoPrP Tr_{x2} H-H. (**1**) Frequency of curves with one or more peaks with $\Delta_{cl} > 30$ nm. (**2**) Scatterplot of FEC only with one or two peaks from MoPrP unfolding events and relative frequency inside intervals. Intervals are indicated in integer values for clarity.

Finally statistical analysis was performed by calculating the median and interquartile range (IQR) of force and Δ_{cl} values from the unfolding events within the two Δ_{cl} intervals. As shown in **figure 6.5** differences between the two protein constructs with conformers in the 30-40 nm range cannot be detected, while in the 40-80 nm interval the H-H protein shows longer structures. Median values of forces are comparable for both proteins at both intervals, but higher force events are more frequent in the H-H protein. This indicates that H-H orientation

of the C-terminal folded domain leads to longer and mechanically more resistant structures with respect to the H-T orientation.

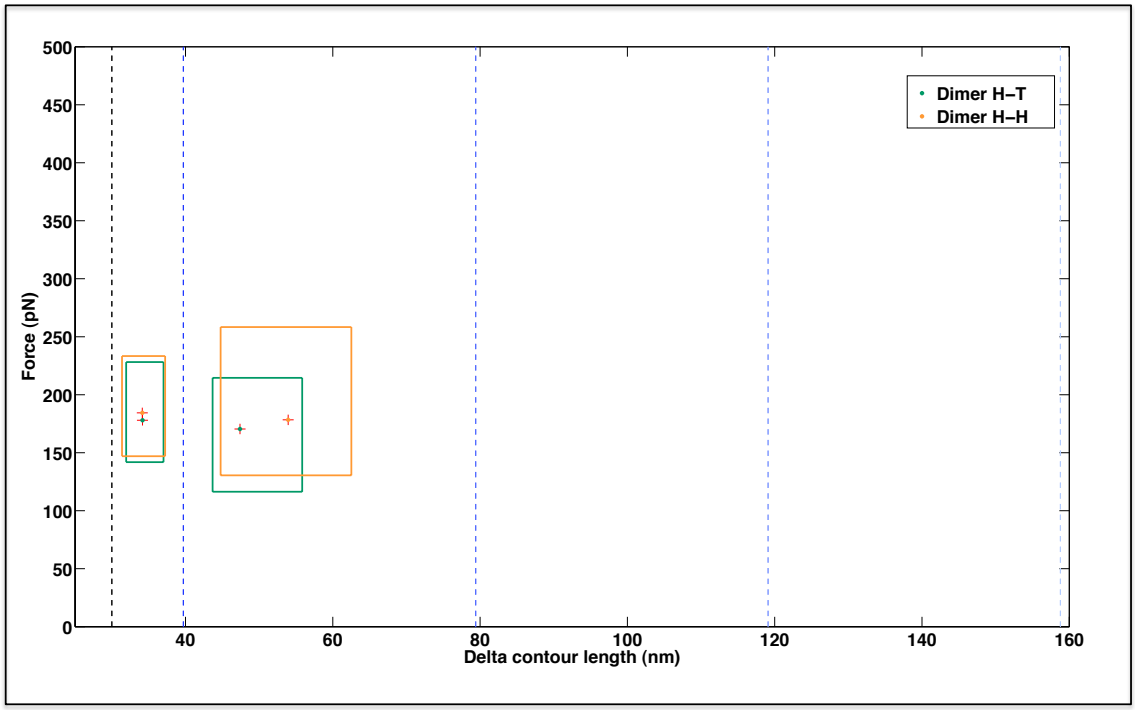

Figure 6.5: Median and IQR for events from MoPrP Tr_{x2} H-T (green) and MoPrP Tr_{x2} H-H (orange) within the 30-40 nm and 40-80 nm intervals. The cross indicates the median values, while IQR was calculated from the 1st and 3rd quartile. Whiskers are not shown.

6.3.2 Protein number affects PrP oligomerization

The formation of large oligomers requires the associations of more than two MoPrP monomers, therefore we increased the number of tandem MoPrP(89-230) molecules inside our AFM constructs up to four to simulate this phenomenon.
In order to rule out that increasing the number of PrP moieties and their associations did not involved also GB1 domains, FEC without events with Δ_{cl} >30 nm were separated from the ones that presented them. Comparing these curves from MoPrP Tr_{x3} unfolding events at neutral pH, showed that the GB1 unfolding Δ_{cl} and force distributions were similar, regardless the formation of structures with Δ_{cl} > 30 nm. This confirms that an interaction between the two protein domains did not occur (**figure 6.6, A**). PrP related events which had a Δ_{cl} > 30 nm usually presented in FECs as one (76%), two (22%) or three (2%) unfolding peaks, as a result of prion protein intra-molecular associations (**figure 6.6, B, panel 1**). The curves that showed only one of these events were also the ones with the longest peaks (up to 97 nm). As expected, increasing their number on the same FEC decreased their related length (**figure 6.6, B, panel 2**).
The frequency of the 30-40 nm conformers was higher (54%) compared to the 40-80 nm conformers (43%). These values are comparable with those obtained from MoPrP Tr_{x2} H-T. This is expected, as the orientations of MoPrP moieties in the two constructs are the same. A small percentage of 80-120 nm conformers (3%) in the trimeric construct were observed. These events correspond unequivocally to associations between all three PrP moieties.

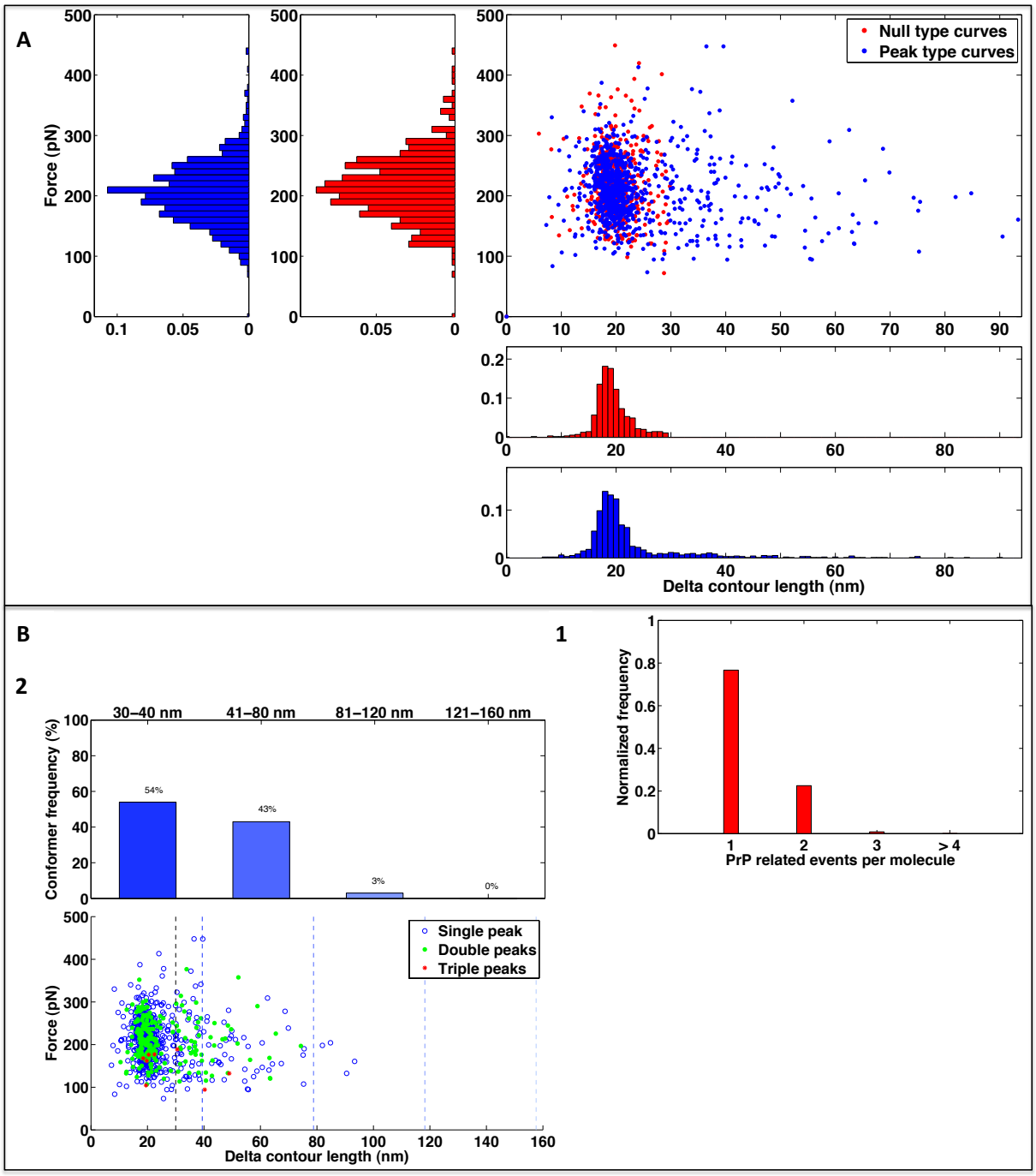

Figure 6.6: (**A**) Scatterplot with relative frequency histograms of FECs with (blue) and without (red) peaks with Δ_{cl} > 30 nm. Data is obtained from MoPrP Tr_{x3} unfolding experiments at neutral pH. (**B**) Analysis of FECs showing unfolding events with Δ_{cl} > 30 nm: (**1**) FECs with one or more PrP peaks with Δ_{cl} > 30 nm, (**2**) scatterplot with relative frequency of unfolding events inside intervals. Intervals are indicated in integer values for clarity.

Finally, tetrameric MoPrP construct was analyzed in the same manner. This construct has the lowest GB1:MoPrP moieties ratio (1:1) compared to previous analyzed proteins, therefore comparing FEC with or without PrP events with Δ_{cl} > 30 nm was necessary to prove that PrP interactions did not involve GB1 domains. As shown in **figure 6.7, A** no differences between the two type of curves was observed. On the other hand distributions of the GB1 delta contour length of MoPrP Tr_{x4} presented a slight shift of +1.8 nm of the average value with respect to the distribution obtained from $GB1_{x8}$ unfolding, while the force values instead were

comparable. Nevertheless the GB1 unfolding transition we observed was comparable to previous studies [226,256,257,262].

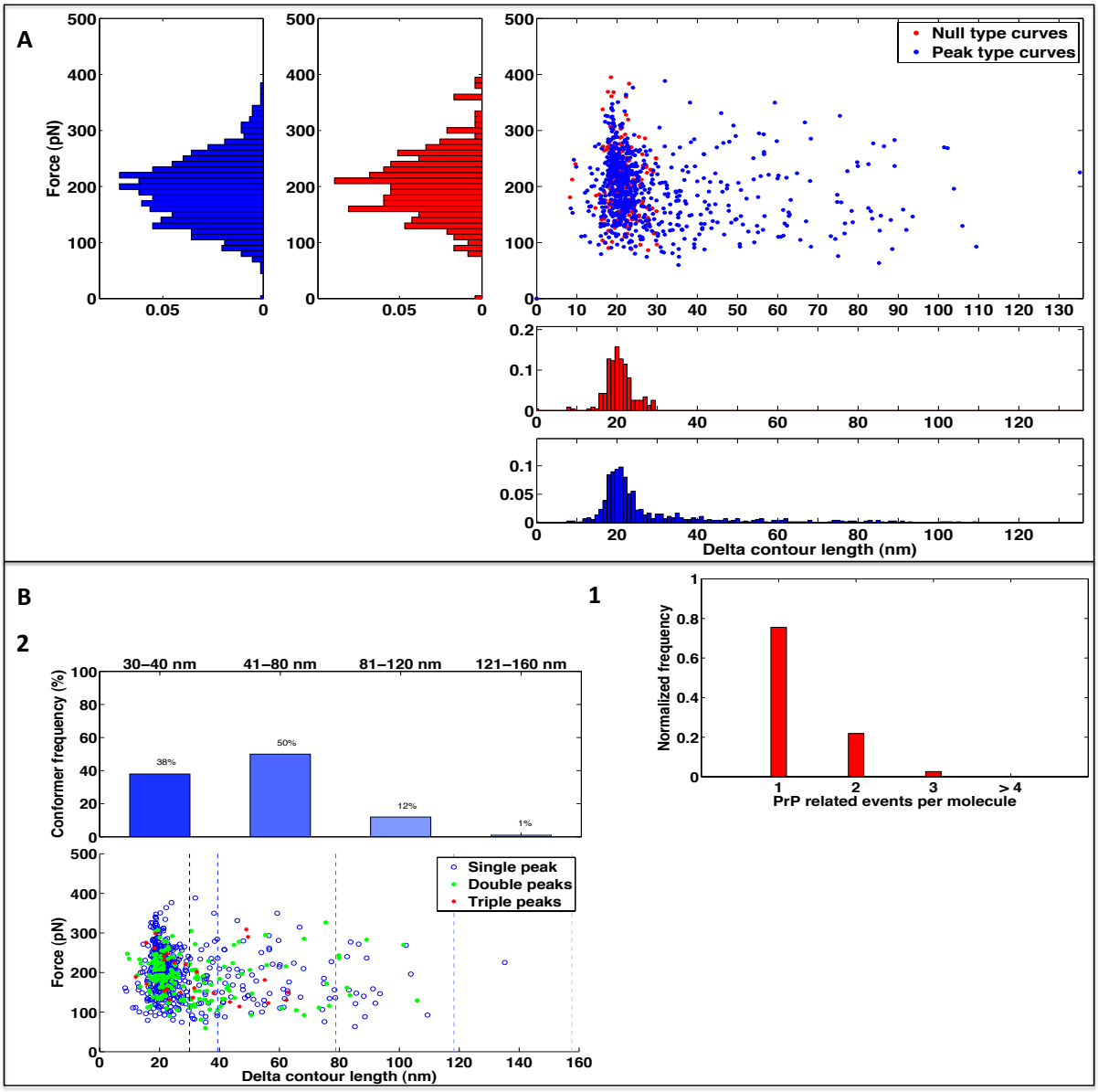

Figure 6.7: (**A**) Scatterplot and relative frequency histograms of FEC with (blue) and without (red) unfolding events with Δ_{cl} > 30 nm. Data is relative to MoPrP Tr_{x4} unfolding experiments at neutral pH. (**B**) Analysis of FECs showing unfolding events with Δ_{cl} > 30 nm: (**1**) FEC with one or more PrP peaks with Δ_{cl} > 30 nm, (**2**) scatterplot with relative frequency of unfolding events inside intervals. Intervals are indicated in integer values for clarity.

The number of MoPrP association unfolding peaks within one FEC was similar to previously analyzed proteins. A higher frequency of single PrP-related events was observed, followed by double and triple events (**figure 6.7, B, panel 1**). The frequency of double and triple peak FECs increased compared to MoPrP Tr_{x3}. Only one FEC showed a very long rupture event (up to 138 nm) indicating that the first and the last MoPrP moieties formed a stable structure. Strikingly the frequency of peaks in the 40-80 nm interval was higher compared to the 30-40 nm one, in a similar fashion of MoPrP Tr_{x2} H-H (**figure 6.7, B, panel 2**). Long range associations (Δ_{cl} > 80 nm) were more frequent compared to MoPrP Tr_{x3}. A possible explanation of this behaviour could be that elongation of the polypeptide chain upon a certain threshold, favours longer associations. As a result, bigger structures from PrP associations

could be established. MoPrP associations were strongly abolished in double-pulse refolding experiments in the presence of ionic strength (150mM) at neutral pH, respect to simple unfolding experiments in the same conditions. Therefore during the first 50 ms of folding, salt bridges play an important role in the stabilization of these associations. Subsequently, other type of interactions (*i.e* hydrophobic interactions) may contribute to further stabilize these structures. This result is corroborated by a wide array of literature that shows how ionic strength can influence strongly the stability [318] and solubility [319,320] of proteins. More in detail, experiments carried out on monomeric PrP have shown that its thermodynamic stability was strongly dependent on salt concentration [321]. It has also been shown that oligomerization and fibrillation can be modulated by ionic strength [322,323,324].
Finally, using multi-pulse refolding, the presence of rupture events from MoPrP associations was confirmed, excluding the possibility that these events were due to non-specific interactions. Also in this case the frequency of PrP related rupture events was lower compared to double-pulse and unfolding experiments. MoPrP association peaks had Δ_{cl} shorter than 60 nm both at neutral and acidic pH, but their frequency and unfolding force increased at acidic pH value.

6.3.3 Associations' complexity increases by increasing the number of MoPrP molecules

A more detailed comparison of all four "head-to-tail" constructs, including the monomeric one, can provide insights on PrP aggregation processes. First of all, increasing the number of MoPrP moieties results in a linear increase of the number of curves at neutral pH showing rupture events with $\Delta_{cl} > 30$ nm of $\sim 20\%$ for every MoPrP moiety added (**figure 6.8**). This type of behaviour is in sharp contrast with recent studies using the same approach to study α-synuclein oligomerization with OT SMFS, where increasing the number of α-synuclein moieties did not change the frequency of FEC showing association events [267]. A possible explanation of this difference could be related to the different association structures generated by the two proteins: while for α-synuclein associations were considered metastable, PrP associations are likely more stable.
Also, multimeric constructs display a strong pH dependence behaviour, increasing the association events upon lowering the pH. As a consequence, we observed a macroscopic aggregation of the tetrameric construct at pH values lower than 7.0 (**figure 4.16**). This data is in agreement with previous works, confirming that low pH is probably the most relevant environmental factor that induces PrP^{C} conversion to PrP^{Sc} both *in vitro* [165,176,325,326] and *in vivo* [327,328]. In fact it has been reported that low pH destabilizes the native structure of the PrP^{C} C-terminal globular domain [164], increasing its unfolding rate. Then, from the unfolded state, the protein can more easily access to misfolded states that are related to protein oligomerization and fibrillation [270]. We confirmed this using multi-pulse refolding experiments where, as respect to neutral pH, at pH 5.5 associations were more frequent and with a higher unfolding force.

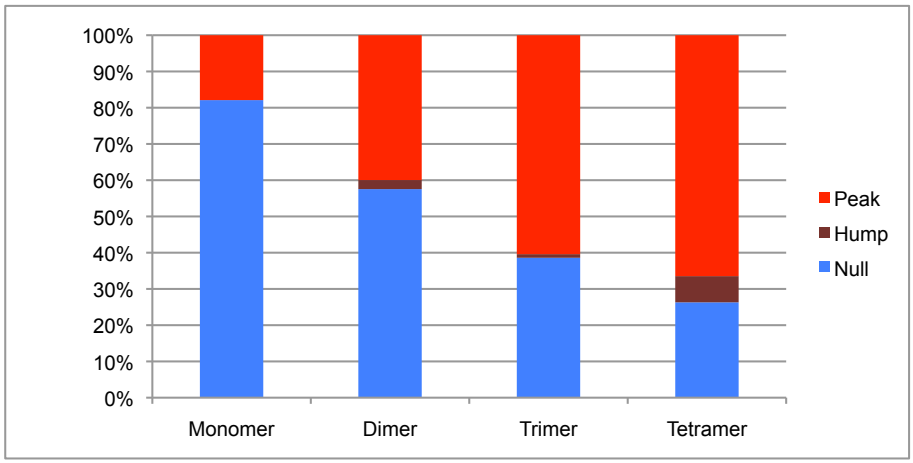

Figure 6.8: Frequency of FEC from all H-T constructs showing a "hump" mechanical feature, single or multiple PrP peaks with Δ_{cl} > 30 nm (peak) or no mechanical features except from GB1 unfolding events (null). Data is collected from unfolding experiments at neutral pH.

Increasing the number of PrP molecules along the protein construct results in an increase of the complexity of oligomeric structures [267], without any visible cluster, thus indicating that no favourite conformers are present (**figure 6.9**). Unfolding events from longer structures were less frequent compared to short ones. There are least two possible explanations for this phenomenon.

The first comes from previous studies which showed that upon closing a disordered loop within a folded structure, the latter decreases its mechanical stability [262]. The effect is related to the entropic contribution of the unstructured loop to the overall mechanical stability of the folded domain, accelerating the mechanical unfolding kinetics in a non linear manner with respect to loop length [262]. A similar effect was observed in AFM SMFS constructs with the "carrier/guest" approach (**paragraph 1.3.4**): when a long unstructured chain (an IDP in this case) was added within a loop of I27 or ubiquitin domain, it decreased strongly the stability of the latter [263].

The second explanation of this phenomenon could be that small structures occur more frequently due to local vicinity of their residues, compared to long ones.

Comparative analysis of IQRs of rupture events from all the constructs (**figure 6.10**) reveal that median Δ_{cl} values are similar in the 30-40 nm interval, while their force values positively correlate to the number of MoPrP moieties. The only exception is the tetramer, where the median force is similar to the monomer. In the 40-80 nm interval median Δ_{cl} values positively correlate to the number of MoPrP moieties, without significant differences in force values. Finally in the 80-120 nm interval the trimer and the tetramer median Δ_{cl} values are identical but higher force values are detected for the latter. Since the median force value of the structures in all the intervals is the same, the first hypothesis can be rejected. Regardless, further experiments are required to confirm the second hypothesis.

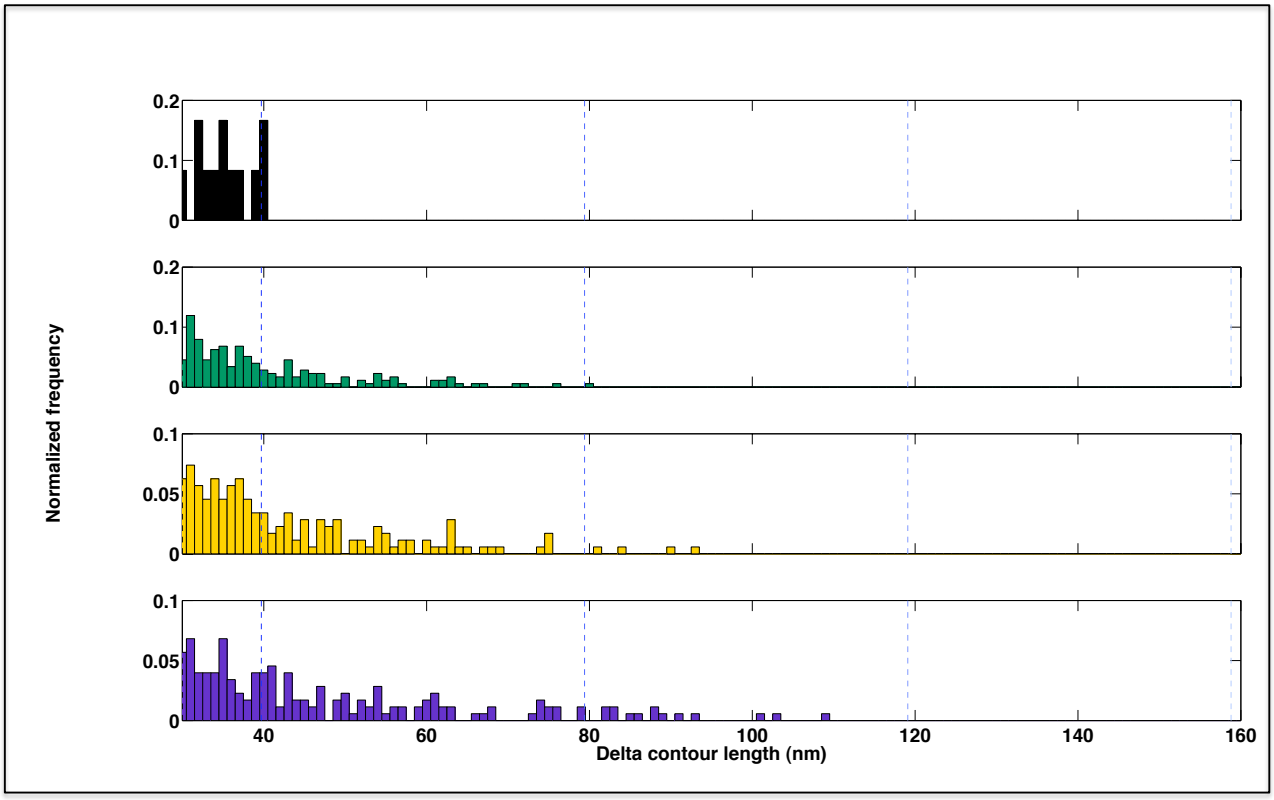

Figure 6.9: Comparison of peaks with Δ_{cl} > 30 nm from all analyzed constructs in unfolding experiments at neutral pH. In black the monomer, in green the dimer H-T, in yellow the trimer and in purple the tetramer constructs.

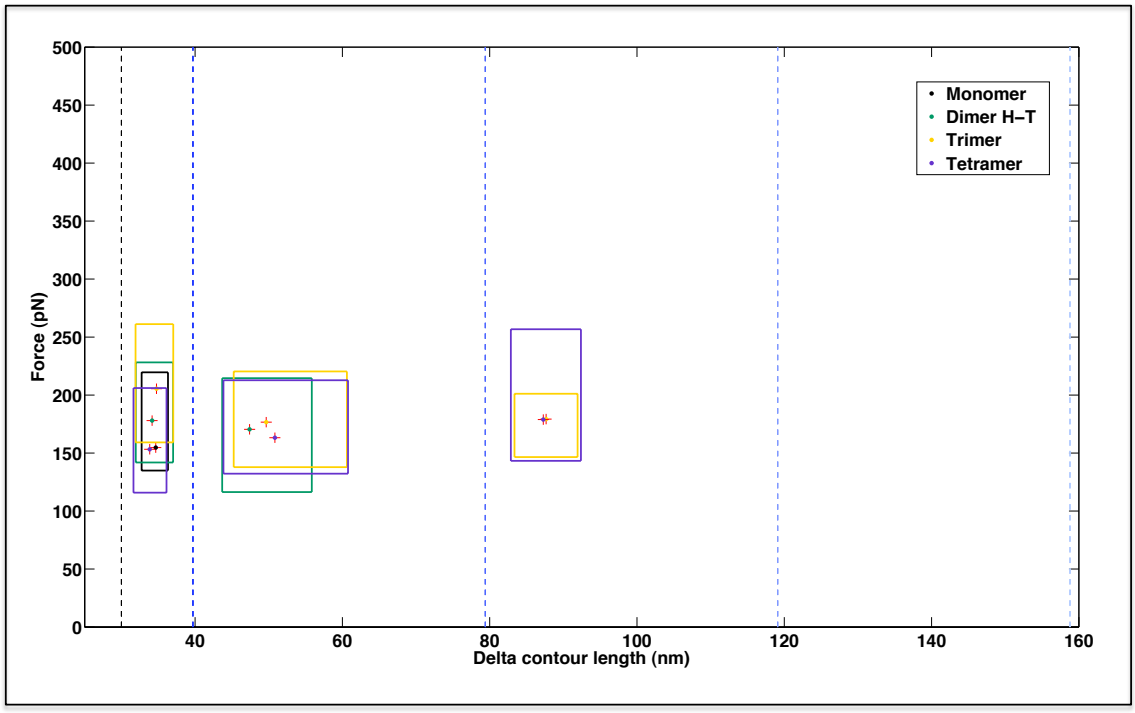

Figure 6.10: Median and IQR of events from MoPrP Tr_{x1} (black), Tr_{x2} H-T (green), Tr_{x3} (yellow) and Tr_{x4} (purple) within the intervals. The cross indicates the median values, while IQR was calculated from the 1st and 3rd quartile. Whiskers are not showed for clarity.

Correlating PrP association structures with models of oligomers or high ordered structures like amyloids is not feasible since no structural evidence at the atomic level are present for the oligomers. While for amyloids some structural data is present [63], it is debated whether oligomers are on-pathway intermediate for fibrils. However, some correlations can be found. PrP associations unfolding forces were in the order of magnitude of β-sheets rupture events [223], with antiparallel topology [224,225]. Models of amyloid fibrils from low resolution experiments of HuPrP [197] and from HET fungal prion domains [75], showed a common fold of stacked monomers with β-sheets orthogonal to the fibril axis. Moreover, our force values are lower but in the same order of magnitude of previous works of SMFS performed on amyloid fibrils [248,269]. Thus, it is possible that associations of PrP moieties in our constructs reflected the monomer interactions within amyloid fibrils with beta-like structures. On the other hand, it has to be considered that rupture force is dependent on loading rate and on tertiary structures. Therefore it is not possible to demonstrate that PrP association unfolding transitions came exclusively from β-sheet rich structures.

Finally, we observed an unusual family of mechanical transition that we called "hump". It comprised of a very heterogeneous group of signals, which were not observed on $GB1_{x8}$ construct, indicating that their nature was PrP dependent. Curves of this type were more frequent in multimeric PrP constructs rather than monomeric ones, showing higher forces and longer lengths by increasing the number of PrP moieties on the construct. The "hump" feature was first observed experimentally in AFM SMFS by Marszalek *et al.* [221], as an unfolding intermediate of I27 protein domain. The same type of transition was observed on GFP [246]. In both cases the "hump" preceded the unfolding of the protein domain. In our case this transition occurred mainly in three ways: i) on the entropic force rise of a GB1 peak, ii) on the entropic force rise of a peak with $\Delta_{cl} > 30$ nm, or iii) before GB1 unfolding events, as a non-exponential increase of force followed by an identical decrease. Regarding the first two, their similarity with previous works suggests that they may be unfolding intermediates of GB1 and of PrP associations, respectively. This can be possible for the latter, while for GB1 it has been suggested that the domain present unfolding intermediates [295], but evidences at the single molecule level are still lacking. Finally, regarding the third type of "hump", we exclude that such feature can be due to systematic instrumental noise since it would have appeared with the same frequency in FEC from all the experiments that have been performed. Nevertheless, more data is required to build up a model for such a feature.

A final important consideration is that dimeric, trimeric and tetrameric constructs had a very high local concentration of the prion protein due to bond constraints, suggesting that this model is very dissimilar to PrP^C in physiological conditions. Nonetheless it is important to remember that the cellular environment is very crowded, with an estimated protein concentration in the order of hundreds of mg/mL. In these conditions it has been estimated that the diffusion coefficient of molecules is 10 fold lower with respect to non-concentrated aqueous solutions and, as a consequence, it increases the tendency of protein oligomerization [1]. Furthermore it has been shown that molecular crowding is strongly correlated to protein aggregation, increasing its propensity [329,330]. Finally, another important aspect is that in its biological environment, PrP^C is highly concentrated in lipid rafts [331]. This limits the diffusion of the protein to two dimensions in a limited space (20-100 nm), increasing its local concentration. For the above cited reasons we can conclude that the constructs we employed in our research can be considered valuable models to characterize the early steps of prion protein aggregation.

Conclusions

Understanding the initial oligomerization steps of proteins involved in neurodegenerative diseases is crucial for gaining insights into the pathological mechanisms underlying these disorders. These maladies are characterized by the presence of oligomers and amyloid fibrils possessing high biochemical heterogeneity. Their biochemical charateristics reflect the protein monomer heterogeneous structural ensembles. Thus, gaining insights into this structural heterogeneity at the monomeric level is critical for understanding the molecular basis of these pathologies. However obtaining structural information on heterogeneous ensembles of protein conformers using classical "in-bulk" techniques can be very challenging. In fact, these techniques can only provide an enseble-averaged structural information. Instead, single-molecule methods provide powerful tools for probing complex folding pathways because they allow detection of rare and transient events.

The work described in this thesis has been focused on recombinant MoPrP(89-230) conformational equilibria at the monomeric and oligomeric levels using atomic force microscopy (AFM) single-molecule force spectroscopy (SMFS). This technique has been previously employed to study conformational equilibrium of other amyloidogenic proteins such as α-synuclein, Aβ 1-42 and Sup35 NM[258, 259, 263, 264].
To achieve this aim we designed, expressed and purified six different heteropolyprotein constructs, with one or multiple MoPrP moiety/moieties flanked by GB1 domains.
The first critical step was to show that PrP folding was not perturbed by the presence of the flanking GB1 domains. Using standard biochemical techniques, we showed that interactions between the two protein moieties were not present. Furthermore, unfolding experiments with AFM SMFS confirmed this hypothesis, since the average unfolding parameters of GB1 domains were not altered by the presence of one or more PrP moieties.

We then focused our attention on PrP monomeric construct in order to obtain structural information on its conformational equilibrium. Our results showed that the protein inside the construct was natively folded and the C-terminal globular domain N->U transition was characterized in terms of force and length. The unfolding of the secondary structures occurred in a cooperative manner, without any intermediate. However, a fraction of the analyzed molecules presented longer rupture events (Δ_{cl} > 30 nm) which could not be related to GB1 or to MoPrP N->U transitions alone. The length of these conformers was longer than the unfolding length of the C-terminal folded domain. Therefore these structures encompassed also residues of the N-terminal unstructured region. The unfolding lengths of these strutures were extremely heterogeneous and their unfolding force showed that they were less mechanically stable compared to the native structure. We concluded that these conformers could be related to PrP aggregation processes. To confirm this hypothesis, we purified and produced MoPrP constructs for optical-tweezers (OT) force spectroscopy experiments. By OT force-clamp force spectroscopy we will confirm whether these conformers are on-folding or off-folding pathway intermediates.

Analysis of dimeric constructs with MoPrP(89-230) moieties arranged in two different orientations, showed that associations between the two PrP moieties occurred, due to the presence of rupture events longer than the theoretical unfolding length of a monomer (39.7 nm). The different orientation of the PrP moieties shifted the conformational equilibria to longer associations (40-80 nm interval) with higher unfolding forces in the head-to-head dimer, compared to the head-to-tail one. Nevertheless, in both cases we could not identify preferred conformers, as a result of the absence of Δ_{cl} clusters. Interestingly the presence of such conformers correlated to the absence of the N->U transition of the C-terminal globular

domain, indicating that these structures required the unfolding of the native structure, and its subsequent conformational rearrangement. Decreasing pH led to increased frequency of associations between the two PrP moietes. These results showed for the first time that protein orientation could induce different structural rearrangements during protein aggregation processes.

Further analysis carried out on trimeric and tetrameric constructs revealed a more complex behaviour, increasing the frequency of associations between two or more prion protein molecules. The trimer showed a distribution of unfolding peaks from force-extension curves similar to the dimer in the head-to-tail orientation, with short associations more frequent than long ones. The tetramer resembled the dimer in the head-to-head orientation instead, with more events in the 40-80 nm interval. This indicated that increasing the number of MoPrP moieties to four made long range contacts surprisingly more favourable than short ones. Lowering the pH gave similar results compared to dimeric constructs, increasing the frequency of force-extension curves with PrP moieties associations. On the other hand, ionic strength was able to modulate the formation of PrP associations, by decreasing their occurrence only at early stages (50 ms). Our results showed that salt bridges play an important role in early oligomerization processes.

Comparing the monomeric and the multimeric constructs with head-to-tail orientation we observed that increasing the number of PrP moieties resulted in a higher frequency inter-PrP structures. Thus, the local concentration of PrP molecules may play an important role during the initial stages of aggregation also *in vivo*. The common effect of pH on the multimeric constructs identified its importance in PrP oligomerization steps, confirming that prion protein aggregation occurs most likely in the endosomal compartment. The force required to unfold inter-PrP structures was in the same order of magnitude of monomer unfolding in synthetic amyloid fibrils. This suggests that inter-PrP structures observed in our constructs could be on-pathway in the formation of high ordered oligomeric molecules.

Concluding, we managed to directly observe the high intrinsic structural heterogeneity of MoPrP both at the monomeric and at the oligomeric level. These data corroborated the hypothesis that the conformational heterogeneity of the monomer is responsible for the structural diversity of PrP aggregation species. Thus, single-molecule methodologies represent very powerful tools to unravel amyloidogenic protein complex energy landscapes, with the possibility to build models of their early mechanisms of aggregation.

Further experiments will be performed to better understand these observations. We will also investigate how the inter-PrP structures changes with pH and ionic strength. Finally, the role of the N-terminal unstructured domain in MoPrP conformational equilibrium will be investigate.

Author contributions

Cloning, expression, purification, characterization, AFM experiments and analysis was performed by Andrea Raspadori. The author also developed Matlab software for the analysis of AFM data.

Dr. Gabriele Giachin helped the author in the optimization of the plasmid sequences and in the purification optimization processes.

Dr. Daniel Aionaei wrote the software for the initial analysis of the AFM force-extension curves. He also developed the software that controlled the refolding-experiments.

Valentina Vignali helped the author to perform AFM experiments.

This work was funded by the Human Fronteer Science Program, as a result of a collaboration between:

-Laboratory of Single Molecule Biophysics of Prof. Carlos Bustamante (Berkeley University, Berkeley, U.S.A)

-Prion Biology laboratory of Prof. Giuseppe Legname (SISSA, Trieste, Italy)

-Laboratory of Nanobiosciences of Prof. Bruno Samorì (University of Bologna, Bologna, Italy)

-Laboratory of Protein Conformation diseases of Prof. Motomasa Tanaka (RIKEN Brain institute, Tokyo, Japan)

Acknowledgments

Finally, here I come! As usual I have to write the most important part of an experience in the last few hours available. For this reason, the english will be even worse!

First of all, I wish to thank Prof. Giuseppe Legname for accepting me in his group and giving me the possibility to carry out my research activity in a independent and critical manner. I would also thank him for reassuring and trusting me when the situation was difficult (and this happen not only once…).
However this work could not be possible without the help of my co-supervisor Prof. Bruno Samorì. I would like to thank him for showing me how to think positive and follow your lead, until you reach your objective. I would also like to thank Prof. Giampaolo Zuccheri for the important discussions on the experimental data, seeing it from a different point of view, and for other more important discussions, where my point of view didn't change (to appreciate coffee you MUST drink it without sugar).

During these last four years I've met extraordinary people who accompanied me in this looong journey. I would like thank ALL the people of the Prion Biology lab, present and past (this will be long): Lisa (aka "ever-tired Stachanov"), Gimli (get used to it Giulia…), Elisa (aka "The Rock" for her climbing and swimming abilites), Stefano, Suzana (but she doesn't understand as she speaks another language), Hoa, Nhat, Thao, Silvia, Elena, Irene Giulia, Lara, Elisa I., Ilaria, Maura, Johanna, Erica, Paola, Kate, Ludovica and, last but not least, MICHAEL. Finally I have to thank my ever-sweating-nose, not-anxious mentor and friend: Gabriele (aka GG). Thanks to you GG for supporting me, laughing with me and standing all my pranks.
I would like also to thank the Bologna's lab members, expecially Guido, Valentina and Daniel for sharing with me this experience. Indeed I cannot forget the (alcoholic) time passed with Cell Dynamics guys: Gazzo, Simo, Ilaria and gg-Zambo!

SISSA is a pool of weird and strange people (me included), baiting and attracting them in misterious ways that even researchers will never understand. But as time passes by, these people slowly become your "family". For this reason I have to thank my room-mates: Dario (the one who knows everything that is utterly useless), Gian (the reflexive-guy-with-the-thumb-in-the-mouth), Lisa (the girl who eats 30% of the worldwide apple, kiwi and fennel crops) and Stefano (the missing guy who completed our LAN party). Thanks to Roby, Katia, Elisuccia, Mix (our personal house-haunting poltergeist) and Stefano (il carabiniere) for the days spent together talking, drinking, eating and laughing! To all of you my deepest thanks!

New friends come but old ones still remains. Thanks again to my "B-friends of fire": Botte, Daniek, Elfo, Ferri, Filo, Folla, Ghembo, Giulia, Martina, Miki, Vale. Even if we spend less time together, because of someone who had a child or because you moved far away, every time we see each others it seems that only few days have passed!

And if old friends remains, older ones will never leave. Daniele my stupid beer-mate, Davide (the major abuser of the "…I have to think…" sentence), Eugi the scarlet (you know what I mean) nerd, Luciano the long-speared dwarf, Bea, Bianca, Giò, Denna, Iolev…I know it's not easy for you to stay near to me, so her's my deepest thanks to all of you guys!
Ah! I forgot Ste…Ste you stink! But without you life would be too boring.

Finally my family. Lella, Mauro (Udirfem), Mordicchis, Martina, Diego, Osanna and Enzo. I would never be here without you, who believed in me, loved me and taught me what being honest means. No matter how far away I will go, you will always be with me. And special thanks to Deborah. Thanks for loving me, for walking together in these years, for waiting me when I was far away and for giving me every day a small smile. Thanks.

To everyone who reads this: thanks for showing me what being happy means.

Andrea Raspadori

Bibliography

1. Ellis RJ (2001) Macromolecular crowding: an important but neglected aspect of the intracellular environment. Curr Opin Struct Biol. pp. 114-119.
2. Hammond C, Helenius A (1995) Quality control in the secretory pathway. Curr Opin Cell Biol. pp. 523-529.
3. Bence NF, Sampat RM, Kopito RR (2001) Impairment of the ubiquitin-proteasome system by protein aggregation. Science. pp. 1552-1555.
4. Kaufman RJ, Scheuner D, Schröder M, Shen X, Lee K, et al. (2002) The unfolded protein response in nutrient sensing and differentiation. Nat Rev Mol Cell Biol. pp. 411-421.
5. Dyson HJ, Wright PE (2005) Intrinsically unstructured proteins and their functions. Nat Rev Mol Cell Biol. pp. 197-208.
6. Uversky VN, Dunker AK (2010) Understanding protein non-folding. Biochimica et biophysica acta. pp. 1231-1264.
7. Dill KA, Ozkan SB, Shell MS, Weikl TR (2008) The protein folding problem. Annu Rev Biophys. pp. 289-316.
8. Eisenberg D, Jucker M (2012) The amyloid state of proteins in human diseases. Cell. pp. 1188-1203.
9. Haass C, Selkoe DJ (2007) Soluble protein oligomers in neurodegeneration: lessons from the Alzheimer's amyloid beta-peptide. Nat Rev Mol Cell Biol. pp. 101-112.
10. Bloomer AC, Champness JN, Bricogne G, Staden R, Klug A (1978) Protein disk of tobacco mosaic virus at 2.8 A resolution showing the interactions within and between subunits. Nature. pp. 362-368.
11. Bode W, Schwager P, Huber R (1978) The transition of bovine trypsinogen to a trypsin-like state upon strong ligand binding. The refined crystal structures of the bovine trypsinogen-pancreatic trypsin inhibitor complex and of its ternary complex with Ile-Val at 1.9 A resolution. J Mol Biol. pp. 99-112.
12. Knowles TPJ, Vendruscolo M, Dobson CM (2014) The amyloid state and its association with protein misfolding diseases. Nat Rev Mol Cell Biol. pp. 384-396.
13. Thomas PJ, Qu BH, Pedersen PL (1995) Defective protein folding as a basis of human disease. Trends Biochem Sci. pp. 456-459.
14. Uversky VN (2003) Protein folding revisited. A polypeptide chain at the folding-misfolding-nonfolding cross-roads: which way to go? Cell Mol Life Sci. pp. 1852-1871.
15. Eliezer D, Chiba K, Tsuruta H, Doniach S, Hodgson KO, et al. (1993) Evidence of an associative intermediate on the myoglobin refolding pathway. Biophysical Journal. pp. 912-917.
16. Semisotnov GV, Kihara H, Kotova NV, Kimura K, Amemiya Y, et al. (1996) Protein globularization during folding. A study by synchrotron small-angle X-ray scattering. J Mol Biol. pp. 559-574.
17. Kataoka M, Kuwajima K, Tokunaga F, Goto Y (1997) Structural characterization of the molten globule of alpha-lactalbumin by solution X-ray scattering. Protein Sci. pp. 422-430.
18. Uversky VN, Karnoup AS, Segel DJ, Seshadri S, Doniach S, et al. (1998) Anion-induced folding of Staphylococcal nuclease: characterization of multiple equilibrium partially folded intermediates. J Mol Biol. pp. 879-894.
19. Tcherkasskaya O, Uversky VN (2001) Denatured collapsed states in protein folding: example of apomyoglobin. Proteins. pp. 244-254.

20. Tcherkasskaya O, Uversky VN (2003) Polymeric aspects of protein folding: a brief overview. Protein Pept Lett. pp. 239-245.
21. Buchanan LE, Dunkelberger EB, Tran HQ, Cheng P-N, Chiu C-C, et al. (2013) Mechanism of IAPP amyloid fibril formation involves an intermediate with a transient β-sheet. Proc Natl Acad Sci USA. pp. 19285-19290.
22. Zerovnik E (2002) Amyloid-fibril formation. Proposed mechanisms and relevance to conformational disease. Eur J Biochem. pp. 3362-3371.
23. Sunde M, Serpell LC, Bartlam M, Fraser PE, Pepys MB, et al. (1997) Common core structure of amyloid fibrils by synchrotron X-ray diffraction. J Mol Biol. pp. 729-739.
24. Uversky VN, Li J, Fink AL (2001) Evidence for a partially folded intermediate in alpha-synuclein fibril formation. The Journal of biological chemistry. pp. 10737-10744.
25. Pavlov NA, Cherny DI, Heim G, Jovin TM, Subramaniam V (2002) Amyloid fibrils from the mammalian protein prothymosin alpha. FEBS Letters. pp. 37-40.
26. Booth DR, Sunde M, Bellotti V, Robinson CV, Hutchinson WL, et al. (1997) Instability, unfolding and aggregation of human lysozyme variants underlying amyloid fibrillogenesis. Nature. pp. 787-793.
27. Kelly JW (1998) The alternative conformations of amyloidogenic proteins and their multi-step assembly pathways. Curr Opin Struct Biol. pp. 101-106.
28. Gidalevitz T, Ben-Zvi A, Ho KH, Brignull HR, Morimoto RI (2006) Progressive disruption of cellular protein folding in models of polyglutamine diseases. Science. pp. 1471-1474.
29. David DC, Ollikainen N, Trinidad JC, Cary MP, Burlingame AL, et al. (2010) Widespread protein aggregation as an inherent part of aging in C. elegans. PLoS Biol. pp. e1000450.
30. Koga H, Kaushik S, Cuervo AM (2011) Protein homeostasis and aging: The importance of exquisite quality control. Ageing Res Rev. pp. 205-215.
31. Calamai M, Chiti F, Dobson CM (2005) Amyloid fibril formation can proceed from different conformations of a partially unfolded protein. Biophys J. pp. 4201-4210.
32. Yoshimura Y, Lin Y, Yagi H, Lee Y-H, Kitayama H, et al. (2012) Distinguishing crystal-like amyloid fibrils and glass-like amorphous aggregates from their kinetics of formation. Proc Natl Acad Sci USA. pp. 14446-14451.
33. Prabhu NV, Sharp KA (2005) Heat capacity in proteins. Annu Rev Phys Chem. pp. 521-548.
34. Stathopulos PB, Rumfeldt JAO, Karbassi F, Siddall CA, Lepock JR, et al. (2006) Calorimetric analysis of thermodynamic stability and aggregation for apo and holo amyotrophic lateral sclerosis-associated Gly-93 mutants of superoxide dismutase. The Journal of biological chemistry. pp. 6184-6193.
35. Lumry R, Eyring H (1954) Conformation changes of proteins. The Journal of physical chemistry. pp. 110-120.
36. Carrió M, González-Montalbán N, Vera A, Villaverde A, Ventura S (2005) Amyloid-like properties of bacterial inclusion bodies. J Mol Biol. pp. 1025-1037.
37. Kang H, Sun A-Y, Shen Y-L, Wei D-Z (2007) Refolding and structural characteristic of TRAIL/Apo2L inclusion bodies from different specific growth rates of recombinant Escherichia coli. Biotechnol Prog. pp. 286-292.
38. Ami D, Natalello A, Gatti-Lafranconi P, Lotti M, Doglia SM (2005) Kinetics of inclusion body formation studied in intact cells by FT-IR spectroscopy. FEBS Letters. pp. 3433-3436.
39. Ami D, Natalello A, Taylor G, Tonon G, Maria Doglia S (2006) Structural analysis of protein inclusion bodies by Fourier transform infrared microspectroscopy. Biochimica et biophysica acta. pp. 793-799.
40. Przybycien TM, Dunn JP, Valax P, Georgiou G (1994) Secondary structure characterization of beta-lactamase inclusion bodies. Protein Eng. pp. 131-136.

41. Doglia SM, Ami D, Natalello A, Gatti-Lafranconi P, Lotti M (2008) Fourier transform infrared spectroscopy analysis of the conformational quality of recombinant proteins within inclusion bodies. Biotechnol J. pp. 193-201.
42. Harper JD, Wong SS, Lieber CM, Lansbury PT (1997) Observation of metastable Abeta amyloid protofibrils by atomic force microscopy. Chem Biol. pp. 119-125.
43. Serio TR, Cashikar AG, Kowal AS, Sawicki GJ, Moslehi JJ, et al. (2000) Nucleated conformational conversion and the replication of conformational information by a prion determinant. Science. pp. 1317-1321.
44. Morozova-Roche LA, Zamotin V, Malisauskas M, Ohman A, Chertkova R, et al. (2004) Fibrillation of carrier protein albebetin and its biologically active constructs. Multiple oligomeric intermediates and pathways. Biochemistry. pp. 9610-9619.
45. Gosal WS, Morten IJ, Hewitt EW, Smith DA, Thomson NH, et al. (2005) Competing pathways determine fibril morphology in the self-assembly of beta2-microglobulin into amyloid. J Mol Biol. pp. 850-864.
46. Eakin CM, Attenello FJ, Morgan CJ, Miranker AD (2004) Oligomeric assembly of native-like precursors precedes amyloid formation by beta-2 microglobulin. Biochemistry. pp. 7808-7815.
47. El Moustaine D, Perrier V, Smeller L, Lange R, Torrent J (2008) Full-length prion protein aggregates to amyloid fibrils and spherical particles by distinct pathways. FEBS J. pp. 2021-2031.
48. Malisauskas M, Zamotin V, Jass J, Noppe W, Dobson CM, et al. (2003) Amyloid protofilaments from the calcium-binding protein equine lysozyme: formation of ring and linear structures depends on pH and metal ion concentration. J Mol Biol. pp. 879-890.
49. Sherman MY, Goldberg AL (2001) Cellular defenses against unfolded proteins: a cell biologist thinks about neurodegenerative diseases. Neuron. pp. 15-32.
50. Kayed R, Sokolov Y, Edmonds B, McIntire TM, Milton SC, et al. (2004) Permeabilization of lipid bilayers is a common conformation-dependent activity of soluble amyloid oligomers in protein misfolding diseases. The Journal of biological chemistry. pp. 46363-46366.
51. Harper JD, Lansbury PT (1997) Models of amyloid seeding in Alzheimer's disease and scrapie: mechanistic truths and physiological consequences of the time-dependent solubility of amyloid proteins. Annu Rev Biochem. pp. 385-407.
52. Knowles TPJ, Waudby CA, Devlin GL, Cohen SIA, Aguzzi A, et al. (2009) An analytical solution to the kinetics of breakable filament assembly. Science. pp. 1533-1537.
53. Eanes ED, Glenner GG (1968) X-ray diffraction studies on amyloid filaments. J Histochem Cytochem. pp. 673-677.
54. Sawaya MR, Sambashivan S, Nelson R, Ivanova MI, Sievers SA, et al. (2007) Atomic structures of amyloid cross-beta spines reveal varied steric zippers. Nature. pp. 453-457.
55. Fitzpatrick AWP, Debelouchina GT, Bayro MJ, Clare DK, Caporini MA, et al. (2013) Atomic structure and hierarchical assembly of a cross-β amyloid fibril. Proc Natl Acad Sci USA. pp. 5468-5473.
56. Wiltzius JJW, Landau M, Nelson R, Sawaya MR, Apostol MI, et al. (2009) Molecular mechanisms for protein-encoded inheritance. Nat Struct Mol Biol. pp. 973-978.
57. Apostol MI, Sawaya MR, Cascio D, Eisenberg D (2010) Crystallographic studies of prion protein (PrP) segments suggest how structural changes encoded by polymorphism at residue 129 modulate susceptibility to human prion disease. The Journal of biological chemistry. pp. 29671-29675.

58. Sievers SA, Karanicolas J, Chang HW, Zhao A, Jiang L, et al. (2011) Structure-based design of non-natural amino-acid inhibitors of amyloid fibril formation. Nature. pp. 96-100.
59. Bauer HH, Aebi U, Häner M, Hermann R, Müller M, et al. (1995) Architecture and polymorphism of fibrillar supramolecular assemblies produced by in vitro aggregation of human calcitonin. J Struct Biol. pp. 1-15.
60. Sunde M, Blake C (1997) The structure of amyloid fibrils by electron microscopy and X-ray diffraction. Adv Protein Chem. pp. 123-159.
61. Saiki M, Honda S, Kawasaki K, Zhou D, Kaito A, et al. (2005) Higher-order molecular packing in amyloid-like fibrils constructed with linear arrangements of hydrophobic and hydrogen-bonding side-chains. J Mol Biol. pp. 983-998.
62. Petkova AT, Leapman RD, Guo Z, Yau W-M, Mattson MP, et al. (2005) Self-propagating, molecular-level polymorphism in Alzheimer's beta-amyloid fibrils. Science. pp. 262-265.
63. Wille H, Michelitsch MD, Guenebaut V, Supattapone S, Serban A, et al. (2002) Structural studies of the scrapie prion protein by electron crystallography. Proc Natl Acad Sci USA. pp. 3563-3568.
64. Del Mar C, Greenbaum EA, Mayne L, Englander SW, Woods VL (2005) Structure and properties of alpha-synuclein and other amyloids determined at the amino acid level. Proc Natl Acad Sci USA. pp. 15477-15482.
65. Chen M, Margittai M, Chen J, Langen R (2007) Investigation of alpha-synuclein fibril structure by site-directed spin labeling. The Journal of biological chemistry. pp. 24970-24979.
66. Ladner CL, Chen M, Smith DP, Platt GW, Radford SE, et al. (2010) Stacked sets of parallel, in-register beta-strands of beta2-microglobulin in amyloid fibrils revealed by site-directed spin labeling and chemical labeling. The Journal of biological chemistry. pp. 17137-17147.
67. Benzinger TL, Gregory DM, Burkoth TS, Miller-Auer H, Lynn DG, et al. (1998) Propagating structure of Alzheimer's beta-amyloid(10-35) is parallel beta-sheet with residues in exact register. Proc Natl Acad Sci USA. pp. 13407-13412.
68. Oyler NA, Tycko R (2004) Absolute structural constraints on amyloid fibrils from solid-state NMR spectroscopy of partially oriented samples. Journal of the American Chemical Society. pp. 4478-4479.
69. Paravastu AK, Leapman RD, Yau W-M, Tycko R (2008) Molecular structural basis for polymorphism in Alzheimer's beta-amyloid fibrils. Proc Natl Acad Sci USA. pp. 18349-18354.
70. Tycko R, Savtchenko R, Ostapchenko VG, Makarava N, Baskakov IV (2010) The α-helical C-terminal domain of full-length recombinant PrP converts to an in-register parallel β-sheet structure in PrP fibrils: evidence from solid state nuclear magnetic resonance. Biochemistry. pp. 9488-9497.
71. Lansbury PT, Costa PR, Griffiths JM, Simon EJ, Auger M, et al. (1995) Structural model for the beta-amyloid fibril based on interstrand alignment of an antiparallel-sheet comprising a C-terminal peptide. Nat Struct Biol. pp. 990-998.
72. Balbach JJ, Ishii Y, Antzutkin ON, Leapman RD, Rizzo NW, et al. (2000) Amyloid fibril formation by A beta 16-22, a seven-residue fragment of the Alzheimer's beta-amyloid peptide, and structural characterization by solid state NMR. Biochemistry. pp. 13748-13759.
73. Petkova AT, Buntkowsky G, Dyda F, Leapman RD, Yau W-M, et al. (2004) Solid state NMR reveals a pH-dependent antiparallel beta-sheet registry in fibrils formed by a beta-amyloid peptide. J Mol Biol. pp. 247-260.

74. Tycko R, Sciarretta KL, Orgel JPRO, Meredith SC (2009) Evidence for novel beta-sheet structures in Iowa mutant beta-amyloid fibrils. Biochemistry. pp. 6072-6084.
75. Wasmer C, Lange A, Van Melckebeke H, Siemer AB, Riek R, et al. (2008) Amyloid fibrils of the HET-s(218-289) prion form a beta solenoid with a triangular hydrophobic core. Science. pp. 1523-1526.
76. Knight RSG, Will RG (2004) Prion diseases. J Neurol Neurosurg Psychiatr. pp. i36-42.
77. Prusiner SB (1998) Prions. Proc Natl Acad Sci USA. pp. 13363-13383.
78. Borchelt DR, Scott M, Taraboulos A, Stahl N, Prusiner SB (1990) Scrapie and cellular prion proteins differ in their kinetics of synthesis and topology in cultured cells. J Cell Biol. pp. 743-752.
79. Caughey B, Raymond GJ (1991) The scrapie-associated form of PrP is made from a cell surface precursor that is both protease- and phospholipase-sensitive. The Journal of biological chemistry. pp. 18217-18223.
80. Stahl N, Baldwin MA, Teplow DB, Hood L, Gibson BW, et al. (1993) Structural studies of the scrapie prion protein using mass spectrometry and amino acid sequencing. Biochemistry. pp. 1991-2002.
81. Pan KM, Baldwin M, Nguyen J, Gasset M, Serban A, et al. (1993) Conversion of alpha-helices into beta-sheets features in the formation of the scrapie prion proteins. Proc Natl Acad Sci USA. pp. 10962-10966.
82. Windl O, Dempster M, Estibeiro P, Lathe R (1995) A candidate marsupial PrP gene reveals two domains conserved in mammalian PrP proteins. Gene. pp. 181-186.
83. Harris DA, Lele P, Snider WD (1993) Localization of the mRNA for a chicken prion protein by in situ hybridization. Proc Natl Acad Sci USA. pp. 4309-4313.
84. Puckett C, Concannon P, Casey C, Hood L (1991) Genomic structure of the human prion protein gene. Am J Hum Genet. pp. 320-329.
85. Westaway D, Cooper C, Turner S, Da Costa M, Carlson GA, et al. (1994) Structure and polymorphism of the mouse prion protein gene. Proc Natl Acad Sci USA. pp. 6418-6422.
86. Saeki K, Matsumoto Y, Hirota Y, Matsumoto Y, Onodera T (1996) Three-exon structure of the gene encoding the rat prion protein and its expression in tissues. Virus Genes. pp. 15-20.
87. Horiuchi M, Ishiguro N, Nagasawa H, Toyoda Y, Shinagawa M (1998) Genomic structure of the bovine PrP gene and complete nucleotide sequence of bovine PrP cDNA. Anim Genet. pp. 37-40.
88. Premzl M, Delbridge M, Gready JE, Wilson P, Johnson M, et al. (2005) The prion protein gene: identifying regulatory signals using marsupial sequence. Gene. pp. 121-134.
89. Choi S-H, Kim I-C, Kim D-S, Kim D-W, Chae S-H, et al. (2006) Comparative genomic organization of the human and bovine PRNP locus. Genomics. pp. 598-607.
90. Basler K, Oesch B, Scott M, Westaway D, Wälchli M, et al. (1986) Scrapie and cellular PrP isoforms are encoded by the same chromosomal gene. Cell. pp. 417-428.
91. Saeki K, Matsumoto Y, Matsumoto Y, Onodera T (1996) Identification of a promoter region in the rat prion protein gene. Biochem Biophys Res Commun. pp. 47-52.
92. Baybutt H, Manson J (1997) Characterisation of two promoters for prion protein (PrP) gene expression in neuronal cells. Gene. pp. 125-131.
93. Lieberburg I (1987) Developmental expression and regional distribution of the scrapie-associated protein mRNA in the rat central nervous system. Brain Res. pp. 363-366.
94. McKinley MP, Hay B, Lingappa VR, Lieberburg I, Prusiner SB (1987) Developmental expression of prion protein gene in brain. Dev Biol. pp. 105-110.
95. Lazarini F, Deslys JP, Dormont D (1991) Regulation of the glial fibrillary acidic protein, beta actin and prion protein mRNAs during brain development in mouse. Brain Res Mol Brain Res. pp. 343-346.

96. Benvegnu S, Poggiolini I, Legname G (2010) Neurodevelopmental expression and localization of the cellular prion protein in the central nervous system of the mouse. J Comp Neurol. pp. 1879-1891.
97. Agostini F, Dotti CG, Pérez-Cañamás A, Ledesma MD, Benetti F, et al. (2013) Prion protein accumulation in lipid rafts of mouse aging brain. PLoS One. pp. e74244.
98. Poggiolini I, Legname G (2012) Mapping the prion protein distribution in marsupials: insights from comparing opossum with mouse CNS. PLoS One. pp. e50370.
99. Hegde RS, Mastrianni JA, Scott MR, DeFea KA, Tremblay P, et al. (1998) A transmembrane form of the prion protein in neurodegenerative disease. Science. pp. 827-834.
100. Hegde RS, Voigt S, Lingappa VR (1998) Regulation of protein topology by trans-acting factors at the endoplasmic reticulum. Mol Cell. pp. 85-91.
101. Stewart RS, Drisaldi B, Harris DA (2001) A transmembrane form of the prion protein contains an uncleaved signal peptide and is retained in the endoplasmic Reticulum. Mol Biol Cell. pp. 881-889.
102. Lawson VA, Collins SJ, Masters CL, Hill AF (2005) Prion protein glycosylation. J Neurochem. pp. 793-801.
103. Rudd PM, Wormald MR, Wing DR, Prusiner SB, Dwek RA (2001) Prion glycoprotein: structure, dynamics, and roles for the sugars. Biochemistry. pp. 3759-3766.
104. Haraguchi T, Fisher S, Olofsson S, Endo T, Groth D, et al. (1989) Asparagine-linked glycosylation of the scrapie and cellular prion proteins. Archives of Biochemistry and Biophysics. pp. 1-13.
105. Pan T, Wong B-S, Liu T, Li R, Petersen RB, et al. (2002) Cell-surface prion protein interacts with glycosaminoglycans. Biochem J. pp. 81-90.
106. Beringue V, Mallinson G, Kaisar M, Tayebi M, Sattar Z, et al. (2003) Regional heterogeneity of cellular prion protein isoforms in the mouse brain. Brain. pp. 2065-2073.
107. Naslavsky N, Stein R, Yanai A, Friedlander G, Taraboulos A (1997) Characterization of detergent-insoluble complexes containing the cellular prion protein and its scrapie isoform. The Journal of biological chemistry. pp. 6324-6331.
108. Sunyach C, Jen A, Deng J, Fitzgerald KT, Frobert Y, et al. (2003) The mechanism of internalization of glycosylphosphatidylinositol-anchored prion protein. EMBO J. pp. 3591-3601.
109. Taylor DR, Hooper NM (2007) The low-density lipoprotein receptor-related protein 1 (LRP1) mediates the endocytosis of the cellular prion protein. Biochem J. pp. 17-23.
110. Taylor DR, Watt NT, Perera WSS, Hooper NM (2005) Assigning functions to distinct regions of the N-terminus of the prion protein that are involved in its copper-stimulated, clathrin-dependent endocytosis. J Cell Sci. pp. 5141-5153.
111. Peters PJ, Mironov A, Peretz D, van Donselaar E, Leclerc E, et al. (2003) Trafficking of prion proteins through a caveolae-mediated endosomal pathway. J Cell Biol. pp. 703-717.
112. Porto-Carreiro I, Février B, Paquet S, Vilette D, Raposo G (2005) Prions and exosomes: from PrPc trafficking to PrPsc propagation. Blood Cells Mol Dis. pp. 143-148.
113. Büeler H, Fischer M, Lang Y, Bluethmann H, Lipp HP, et al. (1992) Normal development and behaviour of mice lacking the neuronal cell-surface PrP protein. Nature. pp. 577-582.
114. Brandner S, Isenmann S, Raeber A, Fischer M, Sailer A, et al. (1996) Normal host prion protein necessary for scrapie-induced neurotoxicity. Nature. pp. 339-343.
115. Mallucci GR, Ratté S, Asante EA, Linehan J, Gowland I, et al. (2002) Post-natal knockout of prion protein alters hippocampal CA1 properties, but does not result in neurodegeneration. EMBO J. pp. 202-210.

116. Mallucci G, Dickinson A, Linehan J, Klöhn P-C, Brandner S, et al. (2003) Depleting neuronal PrP in prion infection prevents disease and reverses spongiosis. Science. pp. 871-874.
117. Herms J, Tings T, Gall S, Madlung A, Giese A, et al. (1999) Evidence of presynaptic location and function of the prion protein. J Neurosci. pp. 8866-8875.
118. Haeberlé AM, Ribaut-Barassin C, Bombarde G, Mariani J, Hunsmann G, et al. (2000) Synaptic prion protein immuno-reactivity in the rodent cerebellum. Microsc Res Tech. pp. 66-75.
119. Kardos J, Kovács I, Hajós F, Kálmán M, Simonyi M (1989) Nerve endings from rat brain tissue release copper upon depolarization. A possible role in regulating neuronal excitability. Neurosci Lett. pp. 139-144.
120. Pauly PC, Harris DA (1998) Copper stimulates endocytosis of the prion protein. The Journal of biological chemistry. pp. 33107-33110.
121. Lee KS, Magalhães AC, Zanata SM, Brentani RR, Martins VR, et al. (2001) Internalization of mammalian fluorescent cellular prion protein and N-terminal deletion mutants in living cells. J Neurochem. pp. 79-87.
122. Perera WS, Hooper NM (2001) Ablation of the metal ion-induced endocytosis of the prion protein by disease-associated mutation of the octarepeat region. Curr Biol. pp. 519-523.
123. Mironov A, Latawiec D, Wille H, Bouzamondo-Bernstein E, Legname G, et al. (2003) Cytosolic prion protein in neurons. J Neurosci. pp. 7183-7193.
124. Bouzamondo-Bernstein E, Hopkins SD, Spilman P, Uyehara-Lock J, Deering C, et al. (2004) The neurodegeneration sequence in prion diseases: evidence from functional, morphological and ultrastructural studies of the GABAergic system. J Neuropathol Exp Neurol. pp. 882-899.
125. Jeffrey M, Halliday WG, Bell J, Johnston AR, MacLeod NK, et al. (2000) Synapse loss associated with abnormal PrP precedes neuronal degeneration in the scrapie-infected murine hippocampus. Neuropathol Appl Neurobiol. pp. 41-54.
126. López Garcia F, Zahn R, Riek R, Wüthrich K (2000) NMR structure of the bovine prion protein. Proc Natl Acad Sci USA. pp. 8334-8339.
127. Hornemann S, Schorn C, Wüthrich K (2004) NMR structure of the bovine prion protein isolated from healthy calf brains. EMBO Rep. pp. 1159-1164.
128. Wopfner F, Weidenhöfer G, Schneider R, von Brunn A, Gilch S, et al. (1999) Analysis of 27 mammalian and 9 avian PrPs reveals high conservation of flexible regions of the prion protein. J Mol Biol. pp. 1163-1178.
129. Kim Y, Lee J, Lee C (2008) In silico comparative analysis of DNA and amino acid sequences for prion protein gene. Transbound Emerg Dis. pp. 105-114.
130. Riek R, Hornemann S, Wider G, Glockshuber R, Wüthrich K (1997) NMR characterization of the full-length recombinant murine prion protein, mPrP(23-231). FEBS Letters. pp. 282-288.
131. Hornemann S, Korth C, Oesch B, Riek R, Wider G, et al. (1997) Recombinant full-length murine prion protein, mPrP(23-231): purification and spectroscopic characterization. FEBS Letters. pp. 277-281.
132. Donne DG, Viles JH, Groth D, Mehlhorn I, James TL, et al. (1997) Structure of the recombinant full-length hamster prion protein PrP(29-231): the N terminus is highly flexible. Proc Natl Acad Sci USA. pp. 13452-13457.
133. Zahn R (2003) The octapeptide repeats in mammalian prion protein constitute a pH-dependent folding and aggregation site. J Mol Biol. pp. 477-488.
134. Burns CS, Aronoff-Spencer E, Dunham CM, Lario P, Avdievich NI, et al. (2002) Molecular features of the copper binding sites in the octarepeat domain of the prion protein. Biochemistry. pp. 3991-4001.

135. Jones CE, Abdelraheim SR, Brown DR, Viles JH (2004) Preferential Cu2+ coordination by His96 and His111 induces beta-sheet formation in the unstructured amyloidogenic region of the prion protein. The Journal of biological chemistry. pp. 32018-32027.
136. Gabus C, Auxilien S, Péchoux C, Dormont D, Swietnicki W, et al. (2001) The prion protein has DNA strand transfer properties similar to retroviral nucleocapsid protein. J Mol Biol. pp. 1011-1021.
137. Derrington E, Gabus C, Leblanc P, Chnaidermann J, Grave L, et al. (2002) PrPC has nucleic acid chaperoning properties similar to the nucleocapsid protein of HIV-1. C R Biol. pp. 17-23.
138. Brown DR, Qin K, Herms JW, Madlung A, Manson J, et al. (1997) The cellular prion protein binds copper in vivo. Nature. pp. 684-687.
139. Hornshaw MP, McDermott JR, Candy JM, Lakey JH (1995) Copper binding to the N-terminal tandem repeat region of mammalian and avian prion protein: structural studies using synthetic peptides. Biochem Biophys Res Commun. pp. 993-999.
140. Viles JH, Cohen FE, Prusiner SB, Goodin DB, Wright PE, et al. (1999) Copper binding to the prion protein: structural implications of four identical cooperative binding sites. Proc Natl Acad Sci USA. pp. 2042-2047.
141. Aronoff-Spencer E, Burns CS, Avdievich NI, Gerfen GJ, Peisach J, et al. (2000) Identification of the Cu2+ binding sites in the N-terminal domain of the prion protein by EPR and CD spectroscopy. Biochemistry. pp. 13760-13771.
142. Choi CJ, Kanthasamy A, Anantharam V, Kanthasamy AG (2006) Interaction of metals with prion protein: possible role of divalent cations in the pathogenesis of prion diseases. Neurotoxicology. pp. 777-787.
143. Millhauser GL (2007) Copper and the prion protein: methods, structures, function, and disease. Annu Rev Phys Chem. pp. 299-320.
144. Jackson GS, Murray I, Hosszu LL, Gibbs N, Waltho JP, et al. (2001) Location and properties of metal-binding sites on the human prion protein. Proc Natl Acad Sci USA. pp. 8531-8535.
145. Jones CE, Klewpatinond M, Abdelraheim SR, Brown DR, Viles JH (2005) Probing copper2+ binding to the prion protein using diamagnetic nickel2+ and 1H NMR: the unstructured N terminus facilitates the coordination of six copper2+ ions at physiological concentrations. J Mol Biol. pp. 1393-1407.
146. Wells MA, Jackson GS, Jones S, Hosszu LLP, Craven CJ, et al. (2006) A reassessment of copper(II) binding in the full-length prion protein. Biochem J. pp. 435-444.
147. D'Angelo P, Della Longa S, Arcovito A, Mancini G, Zitolo A, et al. (2012) Effects of the pathological Q212P mutation on human prion protein non-octarepeat copper-binding site. Biochemistry. pp. 6068-6079.
148. Gasset M, Baldwin MA, Lloyd DH, Gabriel JM, Holtzman DM, et al. (1992) Predicted alpha-helical regions of the prion protein when synthesized as peptides form amyloid. Proc Natl Acad Sci USA. pp. 10940-10944.
149. Forloni G, Angeretti N, Chiesa R, Monzani E, Salmona M, et al. (1993) Neurotoxicity of a prion protein fragment. Nature. pp. 543-546.
150. Brown DR, Herms J, Kretzschmar HA (1994) Mouse cortical cells lacking cellular PrP survive in culture with a neurotoxic PrP fragment. Neuroreport. pp. 2057-2060.
151. Peretz D, Williamson RA, Matsunaga Y, Serban H, Pinilla C, et al. (1997) A conformational transition at the N terminus of the prion protein features in formation of the scrapie isoform. J Mol Biol. pp. 614-622.
152. Riek R, Hornemann S, Wider G, Billeter M, Glockshuber R, et al. (1996) NMR structure of the mouse prion protein domain PrP(121-231). Nature. pp. 180-182.

153. Zahn R, Liu A, Lührs T, Riek R, von Schroetter C, et al. (2000) NMR solution structure of the human prion protein. Proc Natl Acad Sci USA. pp. 145-150.
154. Lysek DA, Schorn C, Nivon LG, Esteve-Moya V, Christen B, et al. (2005) Prion protein NMR structures of cats, dogs, pigs, and sheep. Proc Natl Acad Sci USA. pp. 640-645.
155. Calzolai L, Lysek DA, Pérez DR, Güntert P, Wüthrich K (2005) Prion protein NMR structures of chickens, turtles, and frogs. Proc Natl Acad Sci USA. pp. 651-655.
156. Hornemann S, Glockshuber R (1996) Autonomous and reversible folding of a soluble amino-terminally truncated segment of the mouse prion protein. J Mol Biol. pp. 614-619.
157. Wildegger G, Liemann S, Glockshuber R (1999) Extremely rapid folding of the C-terminal domain of the prion protein without kinetic intermediates. Nat Struct Biol. pp. 550-553.
158. Hosszu LL, Baxter NJ, Jackson GS, Power A, Clarke AR, et al. (1999) Structural mobility of the human prion protein probed by backbone hydrogen exchange. Nat Struct Biol. pp. 740-743.
159. Jenkins DC, Pearson DS, Harvey A, Sylvester ID, Geeves MA, et al. (2009) Rapid folding of the prion protein captured by pressure-jump. Eur Biophys J. pp. 625-635.
160. Maiti NR, Surewicz WK (2001) The role of disulfide bridge in the folding and stability of the recombinant human prion protein. J Biol Chem. pp. 2427-2431.
161. Baldwin RL (1999) Structure and Mechanism in Protein Science: A Guide to
Enzyme Catalysis and Protein Folding. Protein Science. pp. 1-1.
162. Younan ND, Klewpatinond M, Davies P, Ruban AV, Brown DR, et al. (2011) Copper(II)-induced secondary structure changes and reduced folding stability of the prion protein. J Mol Biol. pp. 369-382.
163. Sang JC, Lee C-Y, Luh FY, Huang Y-W, Chiang Y-W, et al. (2012) Slow spontaneous alpha-to-beta structural conversion in a non-denaturing neutral condition reveals the intrinsically disordered property of the disulfide-reduced recombinant mouse prion protein. Prion.
164. Calzolai L, Zahn R (2003) Influence of pH on NMR structure and stability of the human prion protein globular domain. J Biol Chem. pp. 35592-35596.
165. Hornemann S, Glockshuber R (1998) A scrapie-like unfolding intermediate of the prion protein domain PrP(121-231) induced by acidic pH. Proc Natl Acad Sci USA. pp. 6010-6014.
166. DeMarco ML, Daggett V (2007) Molecular mechanism for low pH triggered misfolding of the human prion protein. Biochemistry. pp. 3045-3054.
167. Liemann S, Glockshuber R (1999) Influence of amino acid substitutions related to inherited human prion diseases on the thermodynamic stability of the cellular prion protein. Biochemistry. pp. 3258-3267.
168. Ilc G, Giachin G, Jaremko M, Jaremko L, Benetti F, et al. (2010) NMR structure of the human prion protein with the pathological Q212P mutation reveals unique structural features. PLoS One. pp. e11715.
169. Biljan I, Ilc G, Giachin G, Plavec J, Legname G (2012) Structural rearrangements at physiological pH: nuclear magnetic resonance insights from the V210I human prion protein mutant. Biochemistry. pp. 7465-7474.
170. Rossetti G, Giachin G, Legname G, Carloni P (2010) Structural facets of disease-linked human prion protein mutants: A molecular dynamic study. Proteins.
171. Thaa B, Zahn R, Matthey U, Kroneck PMH, Bürkle A, et al. (2008) The deletion of amino acids 114-121 in the TM1 domain of mouse prion protein stabilizes its conformation but does not affect the overall structure. Biochim Biophys Acta. pp. 1076-1084.
172. Surewicz WK, Apostol MI (2011) Prion protein and its conformational conversion: a structural perspective. Top Curr Chem. pp. 135-167.

173. Prusiner SB (1982) Novel proteinaceous infectious particles cause scrapie. Science. pp. 136-144.
174. Jarrett JT, Lansbury PT (1993) Seeding "one-dimensional crystallization" of amyloid: a pathogenic mechanism in Alzheimer's disease and scrapie? Cell. pp. 1055-1058.
175. Prusiner SB (1991) Molecular biology of prion diseases. Science. pp. 1515-1522.
176. Swietnicki W, Petersen R, Gambetti P, Surewicz WK (1997) pH-dependent stability and conformation of the recombinant human prion protein PrP(90-231). The Journal of biological chemistry. pp. 27517-27520.
177. Jackson GS, Hosszu LL, Power A, Hill AF, Kenney J, et al. (1999) Reversible conversion of monomeric human prion protein between native and fibrilogenic conformations. Science. pp. 1935-1937.
178. Baskakov I, Legname G, Gryczynski Z, Prusiner S (2004) The peculiar nature of unfolding of the human prion protein. Protein Sci. pp. 586-595.
179. Redecke L, von Bergen M, Clos J, Konarev PV, Svergun DI, et al. (2007) Structural characterization of beta-sheeted oligomers formed on the pathway of oxidative prion protein aggregation in vitro. J Struct Biol. pp. 308-320.
180. Yang M, Liu D, Bolen DW (1999) The peculiar nature of the guanidine hydrochloride-induced two-state denaturation of staphylococcal nuclease: a calorimetric study. Biochemistry. pp. 11216-11222.
181. Bolen DW, Yang M (2000) Effects of guanidine hydrochloride on the proton inventory of proteins: implications on interpretations of protein stability. Biochemistry. pp. 15208-15216.
182. Torrent J, Alvarez-Martinez MT, Heitz F, Liautard J-P, Balny C, et al. (2003) Alternative prion structural changes revealed by high pressure. Biochemistry. pp. 1318-1325.
183. Cordeiro Y, Kraineva J, Ravindra R, Lima LMTR, Gomes MPB, et al. (2004) Hydration and packing effects on prion folding and beta-sheet conversion. High pressure spectroscopy and pressure perturbation calorimetry studies. The Journal of biological chemistry. pp. 32354-32359.
184. Hosszu LLP, Trevitt CR, Jones S, Batchelor M, Scott DJ, et al. (2009) Conformational properties of beta-PrP. J Biol Chem. pp. 21981-21990.
185. Gerber R, Tahiri-Alaoui A, Hore PJ, James W (2007) Oligomerization of the human prion protein proceeds via a molten globule intermediate. J Biol Chem. pp. 6300-6307.
186. Larda ST, Simonetti K, Al-Abdul-Wahid MS, Sharpe S, Prosser RS (2013) Dynamic Equilibria between Monomeric and Oligomeric Misfolded States of the Mammalian Prion Protein Measured by 19F NMR. J Am Chem Soc. pp. 10533-10541.
187. Sokolowski F, Modler AJ, Masuch R, Zirwer D, Baier M, et al. (2003) Formation of critical oligomers is a key event during conformational transition of recombinant syrian hamster prion protein. The Journal of biological chemistry. pp. 40481-40492.
188. Baskakov I, Legname G, Baldwin M, Prusiner S, Cohen F (2002) Pathway complexity of prion protein assembly into amyloid. J Biol Chem. pp. 21140-21148.
189. Breydo L, Bocharova OV, Makarava N, Salnikov VV, Anderson M, et al. (2005) Methionine oxidation interferes with conversion of the prion protein into the fibrillar proteinase K-resistant conformation. Biochemistry. pp. 15534-15543.
190. Colby DW, Prusiner SB (2011) Prions. Cold Spring Harb Perspect Biol. pp. a006833.
191. McKinley MP, Meyer RK, Kenaga L, Rahbar F, Cotter R, et al. (1991) Scrapie prion rod formation in vitro requires both detergent extraction and limited proteolysis. J Virol. pp. 1340-1351.
192. Govaerts C, Wille H, Prusiner SB, Cohen FE (2004) Evidence for assembly of prions with left-handed beta-helices into trimers. Proc Natl Acad Sci USA. pp. 8342-8347.

193. Schuler B, Rachel R, Seckler R (1999) Formation of fibrous aggregates from a non-native intermediate: the isolated P22 tailspike beta-helix domain. The Journal of biological chemistry. pp. 18589-18596.
194. Junker M, Schuster CC, McDonnell AV, Sorg KA, Finn MC, et al. (2006) Pertactin beta-helix folding mechanism suggests common themes for the secretion and folding of autotransporter proteins. Proc Natl Acad Sci USA. pp. 4918-4923.
195. DeMarco ML, Silveira J, Caughey B, Daggett V (2006) Structural properties of prion protein protofibrils and fibrils: an experimental assessment of atomic models. Biochemistry. pp. 15573-15582.
196. DeMarco ML, Daggett V (2004) From conversion to aggregation: protofibril formation of the prion protein. Proc Natl Acad Sci USA. pp. 2293-2298.
197. Cobb NJ, Sönnichsen FD, McHaourab H, Surewicz WK (2007) Molecular architecture of human prion protein amyloid: a parallel, in-register beta-structure. Proc Natl Acad Sci USA. pp. 18946-18951.
198. Smirnovas V, Baron GS, Offerdahl DK, Raymond GJ, Caughey B, et al. (2011) Structural organization of brain-derived mammalian prions examined by hydrogen-deuterium exchange. Nat Struct Mol Biol. pp. 504-506.
199. Castilla J, Saá P, Hetz C, Soto C (2005) In vitro generation of infectious scrapie prions. Cell. pp. 195-206.
200. Wille H, Bian W, McDonald M, Kendall A, Colby DW, et al. (2009) Natural and synthetic prion structure from X-ray fiber diffraction. Proc Natl Acad Sci USA. pp. 16990-16995.
201. KENDREW JC (1961) The three-dimensional structure of a protein molecule. Sci Am. pp. 96-110.
202. Williamson MP, Havel TF, Wüthrich K (1985) Solution conformation of proteinase inhibitor IIA from bull seminal plasma by 1H nuclear magnetic resonance and distance geometry. J Mol Biol. pp. 295-315.
203. Milhiet P-E, Gubellini F, Berquand A, Dosset P, Rigaud J-L, et al. (2006) High-resolution AFM of membrane proteins directly incorporated at high density in planar lipid bilayer. Biophysical Journal. pp. 3268-3275.
204. Moreno-Herrero F, Colchero J, Gómez-Herrero J, Baró AM (2004) Atomic force microscopy contact, tapping, and jumping modes for imaging biological samples in liquids. Phys Rev E Stat Nonlin Soft Matter Phys. pp. 031915.
205. Lamour G, Yip CK, Li H, Gsponer J (2014) High Intrinsic Mechanical Flexibility of Mouse Prion Nanofibrils Revealed by Measurements of Axial and Radial Young's Moduli. ACS Nano. pp. 3851-3861.
206. Evans E, Ritchie K (1997) Dynamic strength of molecular adhesion bonds. Biophysical Journal. pp. 1541-1555.
207. Hummer G, Szabo A (2001) Free energy reconstruction from nonequilibrium single-molecule pulling experiments. Proc Natl Acad Sci USA. pp. 3658-3661.
208. Cecconi C, Shank EA, Dahlquist FW, Marqusee S, Bustamante C (2008) Protein-DNA chimeras for single molecule mechanical folding studies with the optical tweezers. Eur Biophys J. pp. 729-738.
209. Neuman KC, Block SM (2004) Optical trapping. Rev Sci Instrum. pp. 2787-2809.
210. Neuman KC, Nagy A (2008) Single-molecule force spectroscopy: optical tweezers, magnetic tweezers and atomic force microscopy. Nat Methods. pp. 491-505.
211. Yu H, Dee DR, Woodside MT (2013) Single-molecule approaches to prion protein misfolding. Prion. pp. 140-146.
212. Bustamante C, Chemla YR, Forde NR, Izhaky D (2004) Mechanical processes in biochemistry. Annu Rev Biochem. pp. 705-748.

213. Smith SB, Cui Y, Bustamante C (1996) Overstretching B-DNA: the elastic response of individual double-stranded and single-stranded DNA molecules. Science. pp. 795-799.
214. Mendels D-A, Lowe M, Cuenat A, Cain MG, Vallejo E, et al. (2006) Dynamic properties of AFM cantilevers and the calibration of their spring constants J Micromech Microeng. pp. 1-15.
215. Bergkvist M, Cady NC (2011) Chemical functionalization and bioconjugation strategies for atomic force microscope cantilevers. Methods Mol Biol. pp. 381-400.
216. Bowers CM, Carlson DA, Shestopalov AA, Clark RL, Toone EJ (2012) A general and efficient cantilever functionalization technique for AFM molecular recognition studies. Biopolymers. pp. 761-765.
217. Barattin R, Voyer N (2011) Chemical Modifications of Atomic Force Microscopy Tips. Methods Mol Biol. pp. 457-483.
218. Žoldák G, Rief M (2013) Force as a single molecule probe of multidimensional protein energy landscapes. Curr Opin Struct Biol. pp. 48-57.
219. Zoldák G, Rief M (2013) Force as a single molecule probe of multidimensional protein energy landscapes. Curr Opin Struct Biol. pp. 48-57.
220. Best RB, Fowler SB, Herrera JLT, Steward A, Paci E, et al. (2003) Mechanical unfolding of a titin Ig domain: structure of transition state revealed by combining atomic force microscopy, protein engineering and molecular dynamics simulations. J Mol Biol. pp. 867-877.
221. Marszalek PE, Lu H, Li H, Carrion-Vazquez M, Oberhauser AF, et al. (1999) Mechanical unfolding intermediates in titin modules. Nature. pp. 100-103.
222. Sułkowska JI, Cieplak M (2008) Stretching to understand proteins - a survey of the protein data bank. Biophysical Journal. pp. 6-13.
223. Rohs R, Etchebest C, Lavery R (1999) Unraveling proteins: a molecular mechanics study. Biophysical Journal. pp. 2760-2768.
224. Keten S, Buehler MJ (2008) Geometric confinement governs the rupture strength of H-bond assemblies at a critical length scale. Nano Lett. pp. 743-748.
225. Brockwell DJ, Paci E, Zinober RC, Beddard GS, Olmsted PD, et al. (2003) Pulling geometry defines the mechanical resistance of a beta-sheet protein. Nat Struct Biol. pp. 731-737.
226. Peng Q, Li H (2008) Atomic force microscopy reveals parallel mechanical unfolding pathways of T4 lysozyme: evidence for a kinetic partitioning mechanism. Proc Natl Acad Sci USA. pp. 1885-1890.
227. Dey A, Szoszkiewicz R (2012) Complete noise analysis of a simple force spectroscopy AFM setup and its applications to study nanomechanics of mammalian Notch 1 protein. Nanotechnology. pp. 175101.
228. Schwaiger I, Sattler C, Hostetter DR, Rief M (2002) The myosin coiled-coil is a truly elastic protein structure. Nat Mater. pp. 232-235.
229. Bustamante C, Marko JF, Siggia ED, Smith S (1994) Entropic elasticity of lambda-phage DNA. Science. pp. 1599-1600.
230. Law R, Harper S, Speicher DW, Discher DE (2004) Influence of lateral association on forced unfolding of antiparallel spectrin heterodimers. The Journal of biological chemistry. pp. 16410-16416.
231. Wolny M, Batchelor M, Knight PJ, Paci E, Dougan L, et al. (2014) Stable single alpha helices are constant-force springs in proteins. The Journal of biological chemistry.
232. Carl P, Kwok CH, Manderson G, Speicher DW, Discher DE (2001) Forced unfolding modulated by disulfide bonds in the Ig domains of a cell adhesion molecule. Proc Natl Acad Sci USA. pp. 1565-1570.

233. Bustanji Y, Samorì B (2002) The mechanical properties of human angiostatin can be modulated by means of its disulfide bonds: a single-molecule force-spectroscopy study. Angew Chem Int Ed Engl. pp. 1546-1548.
234. Grandi F, Sandal M, Guarguaglini G, Capriotti E, Casadio R, et al. (2006) Hierarchical mechanochemical switches in angiostatin. Chembiochem. pp. 1774-1782.
235. Ainavarapu SRK, Wiita AP, Huang HH, Fernandez JM (2008) A single-molecule assay to directly identify solvent-accessible disulfide bonds and probe their effect on protein folding. J Am Chem Soc. pp. 436-437.
236. Wiita AP, Ainavarapu SRK, Huang HH, Fernandez JM (2006) Force-dependent chemical kinetics of disulfide bond reduction observed with single-molecule techniques. Proc Natl Acad Sci USA. pp. 7222-7227.
237. Liang J, Fernández JM (2011) Kinetic measurements on single-molecule disulfide bond cleavage. J Am Chem Soc. pp. 3528-3534.
238. Leake MC, Grützner A, Krüger M, Linke WA (2006) Mechanical properties of cardiac titin's N2B-region by single-molecule atomic force spectroscopy. J Struct Biol. pp. 263-272.
239. Li H, Oberhauser AF, Redick SD, Carrion-Vazquez M, Erickson HP, et al. (2001) Multiple conformations of PEVK proteins detected by single-molecule techniques. Proc Natl Acad Sci USA. pp. 10682-10686.
240. Urry DW, Hugel T, Seitz M, Gaub HE, Sheiba L, et al. (2002) Elastin: a representative ideal protein elastomer. Philos Trans R Soc Lond, B, Biol Sci. pp. 169-184.
241. Bell GI (1978) Models for the specific adhesion of cells to cells. Science. pp. 618-627.
242. Bullerjahn JT, Sturm S, Kroy K (2014) Theory of rapid force spectroscopy. Nat Commun. pp. 4463.
243. Pauling L, Corey RB (1951) The pleated sheet, a new layer configuration of polypeptide chains. Proc Natl Acad Sci USA. pp. 251-256.
244. Williams MC, Rouzina I, McCauley MJ (2009) Peeling back the mystery of DNA overstretching. Proc Natl Acad Sci USA. pp. 18047-18048.
245. Marszalek PE, Li H, Fernandez JM (2001) Fingerprinting polysaccharides with single-molecule atomic force microscopy. Nat Biotechnol. pp. 258-262.
246. Dietz H, Rief M (2004) Exploring the energy landscape of GFP by single-molecule mechanical experiments. Proc Natl Acad Sci USA. pp. 16192-16197.
247. Mariano Carrión-Vázquez, Andrés F. Oberhauser, Héctor Díez, Rubén Hervás, Javier Oroz, et al. (2006) Protein Nanomechanics — as Studied by AFM Single-Molecule Force Spectroscopy. In: Biophysics SSi, editor. Advanced Techniques in Biophysics. pp. pp 163-245
248. Ganchev DN, Cobb NJ, Surewicz K, Surewicz WK (2008) Nanomechanical properties of human prion protein amyloid as probed by force spectroscopy. Biophys J. pp. 2909-2915.
249. Lv Z, Roychaudhuri R, Condron MM, Teplow DB, Lyubchenko YL (2013) Mechanism of amyloid β-protein dimerization determined using single-molecule AFM force spectroscopy. Sci Rep. pp. 2880.
250. Yu J, Malkova S, Lyubchenko YL (2008) alpha-Synuclein misfolding: single molecule AFM force spectroscopy study. J Mol Biol. pp. 992-1001.
251. Li H, Linke WA, Oberhauser AF, Carrion-Vazquez M, Kerkvliet JG, et al. (2002) Reverse engineering of the giant muscle protein titin. Nature. pp. 998-1002.
252. Rief M, Gautel M, Schemmel A, Gaub HE (1998) The mechanical stability of immunoglobulin and fibronectin III domains in the muscle protein titin measured by atomic force microscopy. Biophys J. pp. 3008-3014.

253. Jollymore A, Lethias C, Peng Q, Cao Y, Li H (2009) Nanomechanical properties of tenascin-X revealed by single-molecule force spectroscopy. J Mol Biol. pp. 1277-1286.
254. Schlierf M, Li H, Fernandez JM (2004) The unfolding kinetics of ubiquitin captured with single-molecule force-clamp techniques. Proc Natl Acad Sci USA. pp. 7299-7304.
255. Kotamarthi HC, Sharma R, Koti Ainavarapu SR (2013) Single-molecule studies on PolySUMO proteins reveal their mechanical flexibility. Biophysical Journal. pp. 2273-2281.
256. Cao Y, Li H (2007) Polyprotein of GB1 is an ideal artificial elastomeric protein. Nat Mater. pp. 109-114.
257. Cao Y, Kuske R, Li H (2008) Direct observation of markovian behavior of the mechanical unfolding of individual proteins. Biophysical Journal. pp. 782-788.
258. Sandal M, Valle F, Tessari I, Mammi S, Bergantino E, et al. (2008) Conformational equilibria in monomeric alpha-synuclein at the single-molecule level. PLoS Biol. pp. e6.
259. Brucale M, Sandal M, Di Maio S, Rampioni A, Tessari I, et al. (2009) Pathogenic mutations shift the equilibria of alpha-synuclein single molecules towards structured conformers. Chembiochem. pp. 176-183.
260. Oberhauser AF, Badilla-Fernandez C, Carrion-Vazquez M, Fernandez JM (2002) The mechanical hierarchies of fibronectin observed with single-molecule AFM. J Mol Biol. pp. 433-447.
261. Oroz J, Hervás R, Carrión-Vázquez M (2012) Unequivocal single-molecule force spectroscopy of proteins by AFM using pFS vectors. Biophysical Journal. pp. 682-690.
262. Li H, Wang H-C, Cao Y, Sharma D, Wang M (2008) Configurational entropy modulates the mechanical stability of protein GB1. J Mol Biol. pp. 871-880.
263. Hervás R, Oroz J, Galera-Prat A, Goñi O, Valbuena A, et al. (2012) Common features at the start of the neurodegeneration cascade. PLoS Biol. pp. e1001335.
264. Yu J, Warnke J, Lyubchenko YL (2011) Nanoprobing of α-synuclein misfolding and aggregation with atomic force microscopy. Nanomedicine. pp. 146-152.
265. Lv Z, Condron MM, Teplow DB, Lyubchenko YL (2013) Nanoprobing of the effect of Cu(2+) cations on misfolding, interaction and aggregation of amyloid β peptide. J Neuroimmune Pharmacol. pp. 262-273.
266. Dougan L, Li J, Badilla CL, Berne BJ, Fernandez JM (2009) Single homopolypeptide chains collapse into mechanically rigid conformations. Proc Natl Acad Sci USA. pp. 12605-12610.
267. Neupane K, Solanki A, Sosova I, Belov M, Woodside MT (2014) Diverse metastable structures formed by small oligomers of α-synuclein probed by force spectroscopy. PLoS One. pp. e86495.
268. Apetri AC, Vanik DL, Surewicz WK (2005) Polymorphism at residue 129 modulates the conformational conversion of the D178N variant of human prion protein 90-231. Biochemistry. pp. 15880-15888.
269. Dong J, Castro CE, Boyce MC, Lang MJ, Lindquist S (2010) Optical trapping with high forces reveals unexpected behaviors of prion fibrils. Nat Struct Mol Biol. pp. 1422-1430.
270. Yu H, Liu X, Neupane K, Gupta AN, Brigley AM, et al. (2012) Direct observation of multiple misfolding pathways in a single prion protein molecule. Proc Natl Acad Sci USA.
271. Yu H, Gupta AN, Liu X, Neupane K, Brigley AM, et al. (2012) Energy landscape analysis of native folding of the prion protein yields the diffusion constant, transition path time, and rates. Proc Natl Acad Sci USA. pp. 14452-14457.
272. Hoffmann A, Woodside MT (2011) Signal-Pair Correlation Analysis of Single-Molecule Trajectories. Angew Chem Int Ed. pp. n/a-n/a.
273. Studier FW (2005) Protein production by auto-induction in high density shaking cultures. Protein Expr Purif 41: 207-234.

274. Mehlhorn I, Groth D, Stöckel J, Moffat B, Reilly D, et al. (1996) High-level expression and characterization of a purified 142-residue polypeptide of the prion protein. Biochemistry. pp. 5528-5537.
275. Zahn R, Schroetter Cv, Wüthrich K (1998) Human prion proteins expressed in Escherichia coli and purified by high-affinity column refolding. FEBS Letters. pp. 400-404.
276. Florin E-L, Rief M, Lehmann H, Ludwig M, Dornmair C, et al. (1995) Sensing specific molecular interactions with the atomic force microscope. Biosensors & Bioelectronics. pp. 1-7.
277. Aioanei D, Brucale M, Samorí B (2011) Open source platform for the execution and analysis of mechanical refolding experiments. Bioinformatics. pp. 423-425.
278. Bauer MC, Xue W-F, Linse S (2009) Protein GB1 folding and assembly from structural elements. Int J Mol Sci. pp. 1552-1566.
279. Wong BS, Vénien-Bryan C, Williamson RA, Burton DR, Gambetti P, et al. (2000) Copper refolding of prion protein. Biochem Biophys Res Commun. pp. 1217-1224.
280. Bogomolovas J, Simon B, Sattler M, Stier G (2009) Screening of fusion partners for high yield expression and purification of bioactive viscotoxins. Protein Expr Purif. pp. 16-23.
281. Cheng Y, Patel DJ (2004) An efficient system for small protein expression and refolding. Biochem Biophys Res Commun. pp. 401-405.
282. Sørensen HP, Mortensen KK (2005) Advanced genetic strategies for recombinant protein expression in Escherichia coli. J Biotechnol. pp. 113-128.
283. Phizicky EM, Fields S (1995) Protein-protein interactions: methods for detection and analysis. Microbiol Rev. pp. 94-123.
284. Kuszewski J, Clore GM, Gronenborn AM (1994) Fast folding of a prototypic polypeptide: the immunoglobulin binding domain of streptococcal protein G. Protein Sci. pp. 1945-1952.
285. Frank MK, Clore GM, Gronenborn AM (1995) Structural and dynamic characterization of the urea denatured state of the immunoglobulin binding domain of streptococcal protein G by multidimensional heteronuclear NMR spectroscopy. Protein Sci. pp. 2605-2615.
286. Collinge J (2001) Prion diseases of humans and animals: their causes and molecular basis. Annu Rev Neurosci. pp. 519-550.
287. Weissmann C (2004) The state of the prion. Nat Rev Microbiol. pp. 861-871.
288. Stahl N, Borchelt DR, Prusiner SB (1990) Differential release of cellular and scrapie prion proteins from cellular membranes by phosphatidylinositol-specific phospholipase C. Biochemistry. pp. 5405-5412.
289. Caughey BW, Dong A, Bhat KS, Ernst D, Hayes SF, et al. (1991) Secondary structure analysis of the scrapie-associated protein PrP 27-30 in water by infrared spectroscopy. Biochemistry. pp. 7672-7680.
290. Peretz D, Williamson R, Legname G, Matsunaga Y, Vergara J, et al. (2002) A change in the conformation of prions accompanies the emergence of a new prion strain. Neuron. pp. 921-932.
291. Danzer KM, Krebs SK, Wolff M, Birk G, Hengerer B (2009) Seeding induced by alpha-synuclein oligomers provides evidence for spreading of alpha-synuclein pathology. J Neurochem. pp. 192-203.
292. Masuda-Suzukake M, Nonaka T, Hosokawa M, Oikawa T, Arai T, et al. (2013) Prion-like spreading of pathological α-synuclein in brain. Brain. pp. 1128-1138.
293. Holmes BB, Diamond MI (2014) Prion-like Properties of Tau Protein: The Importance of Extracellular Tau as a Therapeutic Target. The Journal of biological chemistry. pp. 19855-19861.

294. Wegmann S, Schöler J, Bippes CA, Mandelkow E, Muller DJ (2011) Competing interactions stabilize pro- and anti-aggregant conformations of human Tau. J Biol Chem. pp. 20512-20524.
295. Morrone A, Giri R, Toofanny RD, Travaglini-Allocatelli C, Brunori M, et al. (2011) GB1 is not a two-state folder: identification and characterization of an on-pathway intermediate. Biophys J. pp. 2053-2060.
296. Tcherkasskaya O, Knutson JR, Bowley SA, Frank MK, Gronenborn AM (2000) Nanosecond dynamics of the single tryptophan reveals multi-state equilibrium unfolding of protein GB1. Biochemistry. pp. 11216-11226.
297. Park SH, O'Neil KT, Roder H (1997) An early intermediate in the folding reaction of the B1 domain of protein G contains a native-like core. Biochemistry. pp. 14277-14283.
298. Zheng P, Cao Y, Bu T, Straus Suzana K, Li H (2104) Single Molecule Force Spectroscopy Reveals that Electrostatic Interactions Affect the Mechanical Stability of Proteins. Biophysj. pp. 1534-1541.
299. Aioanei D, Tessari I, Bubacco L, Samorì B, Brucale M (2011) Observing the osmophobic effect in action at the single molecule level. Proteins. pp. 2214-2223.
300. Aioanei D, Lv S, Tessari I, Rampioni A, Bubacco L, et al. (2011) Single-molecule-level evidence for the osmophobic effect. Angew Chem Int Ed Engl. pp. 4394-4397.
301. Cecconi C, Shank EA, Bustamante C, Marqusee S (2005) Direct observation of the three-state folding of a single protein molecule. Science. pp. 2057-2060.
302. Bera A, Roche A-C, Nandi PK (2007) Bending and unwinding of nucleic acid by prion protein. Biochemistry. pp. 1320-1328.
303. Marques AF, Cordeiro Y, Silva JL, Lima LMTR (2009) Enhanced prion protein stability coupled to DNA recognition and milieu acidification. Biophys Chem. pp. 135-139.
304. Nandi PK (1997) Interaction of prion peptide HuPrP106-126 with nucleic acid. Arch Virol. pp. 2537-2545.
305. Lima LMTR, Cordeiro Y, Tinoco LW, Marques AF, Oliveira CLP, et al. (2006) Structural insights into the interaction between prion protein and nucleic acid. Biochemistry. pp. 9180-9187.
306. Kocisko DA, Vaillant A, Lee KS, Arnold KM, Bertholet N, et al. (2006) Potent antiscrapie activities of degenerate phosphorothioate oligonucleotides. Antimicrob Agents Chemother. pp. 1034-1044.
307. Cordeiro Y, Machado F, Juliano L, Juliano MA, Brentani RR, et al. (2001) DNA converts cellular prion protein into the beta-sheet conformation and inhibits prion peptide aggregation. J Biol Chem. pp. 49400-49409.
308. Phee B-K, Shin DH, Cho J-H, Kim S-H, Kim J-I, et al. (2006) Identification of phytochrome-interacting protein candidates in Arabidopsis thaliana by co-immunoprecipitation coupled with MALDI-TOF MS. Proteomics. pp. 3671-3680.
309. Ren L, Emery D, Kaboord B, Chang E, Qoronfleh MW (2003) Improved immunomatrix methods to detect protein:protein interactions. J Biochem Biophys Methods. pp. 143-157.
310. Hadwiger JA, Wittenberg C, Richardson HE, de Barros Lopes M, Reed SI (1989) A family of cyclin homologs that control the G1 phase in yeast. Proc Natl Acad Sci USA. pp. 6255-6259.
311. Herberg FW, Taylor SS (1993) Physiological inhibitors of the catalytic subunit of cAMP-dependent protein kinase: effect of MgATP on protein-protein interactions. Biochemistry. pp. 14015-14022.
312. Robakis NK, Sawh PR, Wolfe GC, Rubenstein R, Carp RI, et al. (1986) Isolation of a cDNA clone encoding the leader peptide of prion protein and expression of the homologous gene in various tissues. Proc Natl Acad Sci USA. pp. 6377-6381.

313. Hosszu LLP, Wells MA, Jackson GS, Jones S, Batchelor M, et al. (2005) Definable equilibrium states in the folding of human prion protein. Biochemistry. pp. 16649-16657.
314. Baskakov I, Legname G, Prusiner S, Cohen F (2001) Folding of prion protein to its native alpha-helical conformation is under kinetic control. J Biol Chem. pp. 19687-19690.
315. Doyle CM, Rumfeldt JA, Broom HR, Broom A, Stathopulos PB, et al. (2013) Energetics of oligomeric protein folding and association. Archives of Biochemistry and Biophysics. pp. 44-64.
316. van der Kamp MW, Daggett V (2010) Influence of pH on the human prion protein: insights into the early steps of misfolding. Biophys J. pp. 2289-2298.
317. Xu W, Zhang C, Morozova-Roche L, Zhang JZH, Mu Y (2013) pH-dependent conformational ensemble and polymorphism of amyloid-β core fragment. J Phys Chem B. pp. 8392-8399.
318. Lindman S, Xue W-F, Szczepankiewicz O, Bauer MC, Nilsson H, et al. (2006) Salting the Charged Surface: pH and Salt Dependence of Protein G B1 Stability. Biophysical Journal. pp. 2911-2921.
319. Foster PR, Dunnill P, Lilly MD (1976) The kinetics of protein salting-out: precipitation of yeast enzymes by ammonium sulfate. Biotechnol Bioeng. pp. 545-580.
320. Baldwin RL (1996) How Hofmeister ion interactions affect protein stability. Biophysical Journal. pp. 2056-2063.
321. Apetri AC, Surewicz WK (2003) Atypical effect of salts on the thermodynamic stability of human prion protein. The Journal of biological chemistry. pp. 22187-22192.
322. Jain S, Udgaonkar JB (2008) Evidence for stepwise formation of amyloid fibrils by the mouse prion protein. J Mol Biol. pp. 1228-1241.
323. Jain S, Udgaonkar JB (2010) Salt-induced modulation of the pathway of amyloid fibril formation by the mouse prion protein. Biochemistry. pp. 7615-7624.
324. Jain S, Udgaonkar JB (2011) Defining the pathway of worm-like amyloid fibril formation by the mouse prion protein by delineation of the productive and unproductive oligomerization reactions. Biochemistry. pp. 1153-1161.
325. Alonso DO, DeArmond SJ, Cohen FE, Daggett V (2001) Mapping the early steps in the pH-induced conformational conversion of the prion protein. Proc Natl Acad Sci USA. pp. 2985-2989.
326. Zou W-Q, Cashman NR (2002) Acidic pH and detergents enhance in vitro conversion of human brain PrPC to a PrPSc-like form. The Journal of biological chemistry. pp. 43942-43947.
327. Arnold JE, Tipler C, Laszlo L, Hope J, Landon M, et al. (1995) The abnormal isoform of the prion protein accumulates in late-endosome-like organelles in scrapie-infected mouse brain. J Pathol. pp. 403-411.
328. Marijanovic Z, Caputo A, Campana V, Zurzolo C (2009) Identification of an intracellular site of prion conversion. PLoS Pathog. pp. e1000426.
329. van den Berg B, Ellis RJ, Dobson CM (1999) Effects of macromolecular crowding on protein folding and aggregation. EMBO J. pp. 6927-6933.
330. van den Berg B, Wain R, Dobson CM, Ellis RJ (2000) Macromolecular crowding perturbs protein refolding kinetics: implications for folding inside the cell. EMBO J. pp. 3870-3875.
331. Madore N, Smith KL, Graham CH, Jen A, Brady K, et al. (1999) Functionally different GPI proteins are organized in different domains on the neuronal surface. EMBO J. pp. 6917-6926.